

学校代码：10246
学号：19110190003

復旦大學

博士 学位 论文 (学术学位)

利用 X 射线观测数据研究黑洞吸积系统

Probing the inner accretion flow around black holes with
X-ray observations

院 系：物理系

专 业：物理学

姓 名：刘鸿辉

指 导 教 师：Cosimo Bambi 教授

完 成 日 期：2024 年 05 月 13 日

指导小组成员

Cosimo Bambi 教 授

Contents

List of Figures	v
摘要	xiii
Abstract	xv
List of Symbols	xvii
Chapter 1 Introduction	1
1.1 Black hole accretion systems	2
1.1.1 Eddington limit	3
1.1.2 Active galactic nucleus	3
1.1.3 Black hole X-ray binary	5
1.2 Accretion structure and spectral components	6
1.2.1 Cold standard disk	6
1.2.2 Corona	8
1.2.3 Reflection	10
1.2.4 Outflow	10
1.3 Outburst of X-ray binaries	12
1.3.1 Hard state	13
1.3.2 Intermediate states	14
1.3.3 Soft state	15
1.3.4 Open questions	15
1.4 X-ray reflection spectroscopy	16
1.4.1 Local reflection	16
1.4.2 Relativistic reflection	19
1.4.3 Reflection models	22
1.5 Thesis outline	24
Chapter 2 The hard to soft transition of GX 339–4 as seen by <i>Insight</i>–HXMT	25
2.1 Introduction	25

2.2 Observation and data reduction	26
2.3 Spectral analysis	27
2.3.1 Relativistic reflection features	27
2.3.2 Spectral fitting with reflection models	28
2.4 Discussion	37
2.4.1 Evolution of the disc-corona system	37
2.4.2 Measurement of system parameters	40
2.5 Conclusion	42
 Chapter 3 Rapidly alternating flux states of GX 339–4 during its 2021 outburst	
captured by <i>Insight</i>–HXMT	49
3.1 Introduction	49
3.2 Observations and data reduction	50
3.3 Alternating X-ray Flux States	51
3.4 Spectral Analysis	52
3.4.1 Spectral models	53
3.4.2 Spectral variability	55
3.5 Discussion	56
3.5.1 The inner radius of the disk	59
3.5.2 The geometry of the corona during the state transition	60
3.5.3 The power of the corona	61
3.5.4 The reflection component	62
3.5.5 Compare with other sources	63
3.6 Conclusions	63
3.7 Appendix	64
 Chapter 4 High-density reflection spectroscopy of black hole X-ray binaries in	
the hard state	67
4.1 Introduction	67
4.2 Observations and data reduction	68
4.2.1 <i>NuSTAR</i>	70
4.2.2 <i>Swift</i>	70
4.3 Spectral analysis	70
4.4 Results and Discussion	72
4.4.1 Comparisons with the low density model	72
4.4.2 Disk densities	76

4.4.3	Disk inner radius	80
4.4.4	Inclination angle	81
4.4.5	Reflection strength	83
4.4.6	Photon index	83
4.4.7	The corona properties in the compactness-temperature plane . .	84
4.5	Conclusion	86
4.6	Appendix	88
4.6.1	Modeling with <code>relxillcp</code>	88
4.6.2	Spectral analysis results for individual sources	89
Chapter 5	The disk wind in GRS 1915+105 as seen by <i>Insight</i>–HXMT	99
5.1	Introduction	99
5.2	Observations and data reduction	100
5.3	Data analysis	102
5.3.1	The light curve	102
5.3.2	The continuum and absorption lines	102
5.3.3	The absorption wind	105
5.4	Discussion and conclusions	109
5.4.1	Long timescale variability of the disk wind	109
5.4.2	Short timescale variability of the disk wind	112
5.4.3	Driving mechanism and mass outflow	112
Chapter 6	Summary and future work	115
6.1	Summary of previous research	115
6.2	Future work	117
6.2.1	Spectral-timing study of the state transition	117
6.2.2	Disk density at soft state	117
6.2.3	Improving reflection models	118
6.2.4	Spectra-polarimetric study of accreting systems	119
Bibliography		121
Acknowledgements		159

List of Figures

1-1	Trajectories of stars in the Galactic center. The orbits indicate a central mass of $\sim 4 \times 10^6 M_\odot$. Image created by Prof. Andrea Ghez's team at UCLA using data from the W. M. Keck Telescopes. Download link: https://galacticcenter.astro.ucla.edu/images.html .	2
1-2	A schematic picture of the AGN unification model. A supermassive black hole is surrounded by an accretion disk with a sub-pc length scale. The broad line region consists of high-density (i.e., the electron density $n_e > 10^8 \text{ cm}^{-3}$) and dust-free gas clouds at a distance of 0.01–1 pc from the BH. Outside the broad line region, there is a dusty torus structure at a scale of 0.1–10 pc. The narrow line region has low-density ($n_e < 10^6 \text{ cm}^{-3}$) and ionized gas extending up to 100 pc.	4
1-3	An artist's impression of an X-ray binary system in which a stellar-mass black hole is accreting matter from its companion star (courtesy of JPL/NASA). The accreted matter form a disk-like structure around the black hole. A relativistic jet is launched in the direction perpendicular to the disk.	6
1-4	MAXI lightcurve (2–20 keV) of a prototype low mass black hole X-ray binary, GX 339-4, that show recurrently outbursts every a few years.	7
1-5	(Left) Artist's impression of the inner accretion flow near a black hole (courtesy of JPL/NASA). Arrows with different colors represent emission components: (red) the disk thermal emission; (blue) the coronal emission; (green) the reflected emission of the disk. (Right) The <i>Insight</i> –HXMT observation of the low mass black hole XRB GX 339–4 in the intermediate state on 2021 March 27. The red, blue and green lines show spectral components corresponding to the left panel. The sum is shown as the black solid line.	9
1-6	A cartoon to show the disk wind in the soft state and the jet in the hard state. Image adapted from Ponti et al. 2021 ^[1] .	11

1-7 Hardness-intensity diagram for outbursts of three black hole XRBs with <i>MAXI</i> data. Grey arrows are used to indicate the evolution of a typical outburst on the diagram. The dashed lines denote the launch of powerful jets.	13
1-8 A sketch of the hardness-intensity diagram which shows temporal evolution for a typical outburst of black hole low mass XRBs. Representative energy spectrum and power spectrum for each state are plotted. Image adapted from Wang et al. 2022 ^[2]	14
1-9 Solid lines: rest-frame reflection spectra for different ionization states of the disk. The grey dashed line represent the incident energy spectrum which is a cutoff power-law with $\Gamma = 2$ and $E_{\text{cut}}=300$ keV. The reflection spectra are generated with the <code>xillver</code> model assuming an iron abundance three times of the solar value and an electron density $n_e=10^{15}$ cm $^{-3}$	17
1-10 rest-frame reflection spectra for different electron density of the disk. The reflection spectra are generated with the <code>xillvercp</code> model assuming an iron abundance three times of the solar value and an ionization parameter $\xi=100$ erg cm s $^{-1}$. The incident spectrum is a Comptonized continuum with $\Gamma = 2$ and $kT_e=60$ keV.	18
1-11 A sketch of the disk corona system with the parameters that are relevant to the reflection spectrum.	20
1-12 Sketch of how a narrow line with energy at ν_{em} is broadened by the relativistic effects. Image adapted from Fabian et al. 2000 ^[3]	21
1-13 (Left) The broad iron line profile as a function of the inner disk radius (R_{in}). The line profiles are generated with the <code>relline</code> model. The other parameter required to make the plot are: line energy (6.4 keV), index for a power-law emissivity profile ($q = 3$), black hole spin ($a_* = 0.998$) and inclination ($i = 30^\circ$). (Right) The ISCO radius in Boyer-Lindquist coordinates as a function of black hole spin (a_*).	22

1-14 rest-frame reflection (black) and relativistic reflection (red) spectra for an accretion disk extending to the innermost circular orbit. The red spectrum is shifted vertically for visual clarity. The reflection spectra are generated by convolving the relativistic broadening kernel <code>rel-conv</code> with the <code>xillver</code> model. An iron abundance three times of the solar value and an ionization parameter $\xi=100 \text{ erg cm s}^{-1}$ are assumed. The incident spectrum is a Comptonized continuum with $\Gamma = 2$ and $kT_e=60 \text{ keV}$.	23
1-15 The observed relativistic reflection features in AGN (top), black hole XRB (middle) and neutron star XRB (bottom) with <i>NuSTAR</i> observations. In each case, we fit the data with a simple absorbed continuum model and plot the data to model ratio. The broad iron line around 7 keV and the Compton hump peaked around 30 keV are clearly seen.	24
2-1 (left): The observation log of GX 339-4 from <i>Insight-HXMT</i> Low Energy (LE) instruments. The hardness is defined as the ratio between count rates in 4–10 keV and 2–4 keV. (right): The hardness intensity diagram of GX 339-4 from <i>Insight-HXMT</i> . Each point represents data from one day and is marked with the epoch number. The red color denotes the observations analyzed in this work. Figures adapted from Liu et al. 2023a ^[4] .	27
2-2 Data to model ratios for an absorbed continuum model <code>tbabs * (diskbb+cutoffpl)</code> for the seven epochs. The vertical line marks the position of 6.4 keV. Data are rebinned for visual clarity.	28
2-3 The best-fit model components for the seven epochs and the corresponding residuals with the model <code>tbabs * (diskbb+relxilllp+cutoffpl)</code> . The black solid line represents the total model. The magenta, red and green dashed lines are for the corona emission, the disk component and the reflected component respectively.	33

2-4	The evolution of spectral parameters along with X-ray hardness of the source. The definition of the hardness is the same as in Fig. 2-1. Lower and upper limits are marked with arrows. Panels in the left show the parameters from Model 1A except the scattering fraction (f_{sc} , from Model 3). In the third panel in the left, the red color represents estimation of the inner disk radius from the normalization parameter of <code>diskbb</code> of Model 3 and the size of the ISCO is chosen for a black hole with $a_* = 0.95$. The reflection strength (R_s) is defined as the ratio between the observed flux of the reflected and the direct corona emission in the 0.1–100 keV band. Parameters from Model 4 with the <code>refhiden</code> model are shown in the right panels.	36
2-5	The χ^2 contours for the black hole spin and the inclination parameters for the lamppost geometry and broken power-law emissivity. The horizontal lines represent the 1σ , 2σ and 3σ confidence levels for a single parameter of interest.	42
3-1	The hardness intensity diagram of the 2021 outburst of GX 339–4. Data are extracted from <i>Insight</i> –HXMT observations. Each point represents data from one day. The two observations analyzed in this work are marked with red stars. The hardness is defined using the count rate.	50
3-2	Lightcurves of GX 339–4 by <i>Insight</i> –HXMT in 4–10 keV (panel 1) and 2–4 keV (panel 2). The evolution of the hardness ratio is shown in panel 3. The source enters a low flux state at 52 ks that lasts for about 100 ks. Two brief high flux states emerge from the low flux interval on a timescale less than one orbit. The flux change is more prominent in 4–10 keV. Different colors mark the four spectra extracted from the observation (see Sec. 3.4).	51
3-3	(Left): Spectra of the four intervals as defined in Fig 3-2. The LE (2–9 keV) and ME (8–15 keV) data are marked with filled circle and diamond respectively. The spectra are obtained using <code>setplot area</code> command in <code>xspec</code> and are only shown for demonstration purposes. (Right): Data to model ratio of Spec 1 to a simple absorbed continuum model. Data are binned for visual clarity.	56

3-4 Left panel: The $\Delta\chi^2$ confidence contours of the inner disk radius for the two models. The orange vertical lines mark the radius of ISCO for $a_* = 0.998, 0.99, 0.98$ and 0.95 respectively (from left to right). Right panel: The $\Delta\chi^2$ confidence contours for the corona height (h) of the four spectra. In both panels, the horizontal dashed lines represent the $1, 2$ and 3σ confidence levels. Colors are coded as in Fig 3-5, while the magenta line represents the result when linking h between the four spectra.	58
3-5 (Left): The best-fit models and the corresponding residuals to the four spectra with model <code>tbabs*(diskbb+nthcomp+relconv*reflionx)</code> . The LE and ME data are marked with filled circle and diamond markers respectively. (Right): The same as the left plot but with the relativistic broadening kernel replaced by <code>relconv_lp</code> . The full models are plotted in solid lines. The disk, power-law and reflection components are plotted in dashed, dotted and dash-dotted lines respectively.	58
3-6 Relations of the some spectral parameters with the total X-ray flux in the energy range 2–15 keV. Lower and upper limits are marked with arrows.	59
3-7 Lightcurves of GX 339–4 by <i>Insight–HXMT</i> , <i>NuSTAR</i> and <i>Swift</i>	64
4-1 Data to model ratio when fitting with a simple absorbed continuum model: <code>constant * tbabs * (diskbb + nthcomp)</code> . Only one observation is shown for each source. The black and red colors represent data from FPMA and FPMB respectively. Data are rebinned for visual clarity.	74
4-2 Upper: The black solid line shows the best-fit reflection component for GRS 1739–278 with a disk density of 10^{19} cm^{-3} . The red dashed and magenta dotted lines represent the cases when the density is set to 10^{15} cm^{-3} and 10^{22} cm^{-3} respectively without changing the other parameters. Lower three panels: The data to model ratios for the three cases in the upper panel. The blue, black and red data represent <i>Swift</i> -XRT, <i>NuSTAR</i> -FPMA and <i>NuSTAR</i> -FPMB respectively.	75

4-6 (Left) The temperature at the Thomson depth of $\tau = 1$ of the corona-illuminated disk as a function of the density. The coronal emission component and the disk properties are assumed to be the mean values from our samples ($\Gamma = 1.7$, $E_{\text{cut}}=100$ keV, $\xi=100$ erg cm s $^{-1}$ and $A_{\text{Fe}}=1$). The calculation is conducted with the <code>reflionx</code> code. (Right) The relation between the incident radiation pressure and the gas thermal pressure from this work. The grey line marks where $P_{\text{rad}} = P_{\text{th}}$	80
4-7 The evolution of the inner disk radius with the Eddington-scaled luminosity. Our results are color-coded as in Fig. 4-5. The data in black and grey are from previous measurements of GX 339–4 ^[12–22] where the grey stars mark the measurements with data in the timing mode of <i>XMM-Newton</i> EPIC/pn. The grey and magenta dashed horizontal lines represent the ISCO radii for $a_* = 0.998$ and 0.2 respectively.	82
4-8 (Left) The relation between the reflection strength parameter (R_{str} , defined as the flux ratio between the reflected component and the power-law component in 0.1–100 keV band) and the Eddington-scaled luminosity. (Middle) The relation between R_{str} and the photon index Γ . (Right) The variation between the photon index Γ and Eddington-scaled luminosity. The line in green represents the statistical relation in AGNs found by ^[23]	84
4-9 The relation between the coronal temperature and and the dimensionless compactness parameter from our analysis. The grey dashed lines are theoretical predictions of a hybrid plasma with $\ell_h/\ell_s = 1$, where ℓ_h is the total heating parameter and ℓ_s is the compactness of the soft photons. From right to left, the lines represent solutions with a non-thermal fraction (ℓ_{nth}/ℓ_h) of 0, 0.01, 0.05, 0.1, 0.2, 0.3, 0.4 and 0.6 respectively.	87
4-10 The best-fit model components (top panels) and the corresponding residual plots (bottom panels) for observations analyzed in this work.	95
4-11 Figure 4-10 continued.	96
4-12 Figure 4-10 continued.	97
4-13 Figure 4-10 continued.	98

5-1	Light curves of GRS 1915+105 in Crab units by MAXI/GSC (2–20 keV) and Swift/BAT (15–50 keV). The hardness in the lower panel is defined as the ratio between the Swift and MAXI count rate in Crab units (Swift/MAXI). The vertical lines mark the three <i>Insight</i> –HXMT observations analyzed in this work.	101
5-2	The LE (1–10 keV) light curve and the hardness ratio of GRS 1915+105 for the three epochs. For every epoch, only 1000 s (bin size 1 s) data are shown. The hardness ratio is defined as ratio between the count rates in the range of 4–10 keV and 1–4 keV. The red dashed line in the panel for Epoch 1 denotes the threshold used to divide this observation to low and high flux states (see Sec. 5.4.2).	103
5-3	(Left 1): Residuals to an absorbed continuum model <code>tbabs * (diskbb + nthcomp)</code> for the three epochs. The two vertical grey lines mark the positions of absorption by Fe XXVI Ly α and Fe XXVI Ly β . (Left 2): Residuals to the model <code>tbabs * (diskbb + nthcomp + relxill)</code> with absorption lines fitted with two extra negative gaussian. (Left 3): Residuals to the model <code>tbabs * pcfabs * (nthcomp + gaussian)</code> with two additional absorption gaussian lines. (Right): A zoomed in version of panel 1 on the left with the three observations plotted separately. Data are rebinned for visual clarity.	104
5-4	Spectra and residuals for the best-fit model <code>tbabs * xstar * pcfabs (nthcomp + gauss)</code> for the three epochs. The spectra are corrected for the effective area of the instruments but not unfolded from the response. Data are rebinned for visual clarity.	106
5-5	Spectra and residuals for the low and high flux data of epoch 1. The spectra are corrected for the effective area and are only shown for demonstration purposes. Data are rebinned for visual clarity.	110

摘要

黑洞吸积过程与宇宙中的一系列高能天体物理现象相关。此过程能有效地把被吸积物质的引力势能转化为电磁辐射或动能。吸积过程控制着黑洞的质量增长和演化，并通过辐射和外流对吸积环境产生较强的反馈。例如，超大质量黑洞的吸积能够显著地影响宿主星系的恒星形成，并由此影响以星系为基本单位的大尺度结构。利用空间 X 射线望远镜，我们可以观测到吸积流产生的 X 射线辐射，从而研究吸积物理以及黑洞周围强引力场的时空性质。自从 X 射线天文学诞生以来，我们对包括活动星系核以及黑洞 X 射线双星在内的黑洞吸积系统的观测研究取得了一系列进展。然而目前还存在一些关于吸积流结构以及黑洞基本性质的问题亟待解决。

在此论文中，我将分析对几个 X 射线双星的近期观测。观测数据主要来自没有光子堆积效应的 X 射线望远镜，如 *Insight-HXMT* 和 *NuSTAR*。通过分析光谱中的反射成分，我发现 X 射线双星的吸积盘内缘在硬态或者中间态时已达到最内层稳定圆周轨道。对 GX 339-4 中“flip-flop”现象的研究表明冕的辐射功率可以在几分钟的时间尺度上变化达到 3 倍以上。这对理解冕的加热机制有重要的启示作用。更进一步地，利用高密度反射光谱模型，我系统性地研究了黑洞 X 射线双星样本中的吸积盘密度，补充了前人的研究。最后，我研究了著名的黑洞 X 射线双星，GRS 1915+105，中的盘风的性质，证明了盘风在吸积过程中的重要性。

关键词：黑洞；吸积盘；X 射线双星；X 射线反射光谱；盘风

中图分类号：O413.1

Abstract

Accretion onto black holes is a fundamental process responsible for many high-energy phenomena in the Universe. The process is highly efficient at converting the gravitational potential energy of the matter into radiation and kinetic energy. It plays a vital role in shaping the Universe by governing the growth and evolution of black holes and driving strong feedback to the environment (e.g., host galaxies of supermassive black holes) in the form of radiation or outflows. X-ray emission from accretion flows, observed by space X-ray missions, serves as a powerful tool to probe the properties of the accretion flow and the innermost spacetime region near the central black hole. The study of accreting black holes, including active galactic nuclei and black hole X-ray binaries, has been active since the early days of X-ray astronomy. However, important open questions remain regarding the structure of the accretion flow and fundamental properties of black holes.

In this thesis, I present the study of recent X-ray observations of a few black hole X-ray binaries (XRBs), primarily using pile-up free X-ray telescopes such as *Insight-HXMT* and *NuSTAR*. Analysis of X-ray reflection spectra provides evidence that the inner edge of the accretion disk of XRBs extends to the innermost stable circular orbit in their luminous hard state and intermediate states. The “flip-flop” variability observed in GX 339–4 indicates that the coronal power can change by a factor of 3 on timescales as short as a few minutes, providing new insight into the mechanism powering the corona. Additionally, I conducted a systematic study of high-density reflection effects on a sample of black hole X-ray binaries in the hard state, complementing previous research. I investigated the properties of disk winds in the famous black hole XRB GRS 1915+105, demonstrating the significant role of the wind in regulating the accretion process.

Keywords: Black hole; accretion disk; X-ray binary; X-ray reflection spectroscopy; disk wind

CLC code: O413.1

List of Symbols

M_\odot Solar mass

a_* Black hole spin parameter

G Gravitational constant

c Speed of light

η Accretion efficiency or mass to radiation conversion efficiency

Publications during Ph. D:

- **Liu, H.**, Jiang, J., Zhang, Z., Bambi, C., Fabian, A. C., Garcia, J. A., Ingram, A., Kara, E., Steiner, J. F., Tomsick, J. A., Walton, D. J., Young, A. J., (2023), High-density reflection spectroscopy of black hole X-ray binaries in the hard state. *The Astrophysical Journal*, 951, 145.
- **Liu, H.**, Bambi, C., Jiang, J., Garcia, J., Ji, L., Kong, L., Ren, X., Zhang, S., Zhang, S. N. (2023). The hard to soft transition of GX 339–4 as seen by Insight-HXMT. *The Astrophysical Journal*, 950, 5.
- **Liu, H.**, Fu, Y., Bambi, C., Jiang, J., Parker, M., Ji, L., Kong, L., Zhang, L., Zhang, S., Zhang, Y. (2022). The disk wind in GRS 1915+105 as seen by Insight-Hard X-ray Modulation Telescope. *The Astrophysical Journal*, 933, 122.
- **Liu, H.**, Jiang, J., Zhang, Z., Bambi, C., Ji, L., Kong, L., Zhang, S. (2022). Rapidly alternating flux states of GX 339-4 during its 2021 outburst captured by Insight-HXMT. *Monthly Notices of the Royal Astronomical Society*, 513(3), p.4308.
- **Liu, H.**, Parker, M. L., Jiang, J., Kara, E., Bambi, C., Grupe, D., Komossa, S. (2021). A systematic study of photoionized and warm absorption signatures of the NLS1 Mrk 335. *Monthly Notices of the Royal Astronomical Society*, 506(4), p.5190.
- **Liu, H.**, Ji, L., Bambi, C., Jain, P., Misra, R., Rawat, D., ... & Zhang, Y. (2021). Testing evolution of LFQPOs with mass accretion rate in GRS 1915+105 with Insight-HXMT. *The Astrophysical Journal*, 909(1), p.63.
- **Liu, H.**, Wang, H., Abdikamalov, A.B., Ayzenberg, D. and Bambi, C., 2020. Reflection features in the X-ray spectrum of Fairall 9 and implications for tests of general relativity. *The Astrophysical Journal*, 896(2), p.160.

Chapter 1

Introduction

Black holes (BHs) are the most extreme predictions of Einstein's general theory of relativity^[24]. From a purely mathematical point of view, a black hole is a vacuum solution of Einstein's field equations. In this solution, all mass is concentrated in the central singularity which is surrounded by an *event horizon*, a closed surface from within which nothing can escape, not even light. By this definition, it is not hard to imagine that isolated black holes are difficult to see. Indeed black holes are mostly found in actively interacting systems where a lot of energy is released.

Black holes are probably the simplest objects in the Universe. According to the “No-hair Theorem”, a black hole is fully characterized by three parameters^[25]: the mass (M), the angular momentum (J) and the electric charge (Q). Since matters that form black holes are supposed to be mostly neutral, the electric charge for astrophysical black holes is often thought to be negligible. The spin angular momentum is often represented by the dimensionless spin parameter $a_* = cJ/GM^2$ where c is the speed of light and G is the gravitational constant. In 1916, the first solution of Einstein's vacuum field equation was obtained by Karl Schwarzschild^[26]. It describes the spacetime of a non-spinning ($a_* = 0$), spherically symmetric black hole. The spinning black hole solution was given nearly half a century later by Roy Kerr in 1963^[27], known as the Kerr solution (or Kerr metric). The Kerr solution sets a limit for the black hole spin parameter: $-1 < a_* < 1$.

From an observational point of view, black holes in the Universe can be classified into two categories based on their masses. Supermassive black holes (SMBH) have masses 10^5 - 10^{10} times of the solar mass (M_\odot). The strongest evidence of SMBHs is the measurements of trajectories of stars in the Galactic center (Figure 1-1). These measurements indicate a hidden mass around $4 \times 10^6 M_\odot$ within 100 AU radius. It is now generally believed that SMBHs exist at the center of nearly all galaxies. The other kind

of black holes are stellar-mass black holes with masses usually below $100 M_{\odot}$. These black holes are mostly found in binary systems, either in binary black hole systems detected by gravitational wave measurements^[28] or in black hole-star systems detected via electromagnetic radiation, primarily in the X-ray band^[29]. Black holes with an intermediate mass ($\sim 1000 M_{\odot}$) have never been firmly detected but there are candidates and may form a third class of objects.

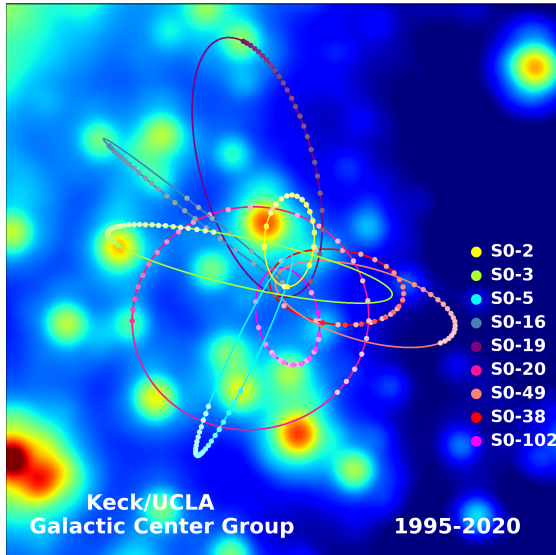


Figure 1-1 Trajectories of stars in the Galactic center. The orbits indicate a central mass of $\sim 4 \times 10^6 M_{\odot}$. Image created by Prof. Andrea Ghez's team at UCLA using data from the W. M. Keck Telescopes. Download link: <https://galacticcenter.astro.ucla.edu/images.html>.

From Isaac Newton to Albert Einstein, the study of gravity has continued to revolutionize our understanding of the Universe. Black holes, as the most extreme prediction of Einstein's general theory of relativity, are potentially ideal objects to explore for new physics. Furthermore, as will be discussed in later sections, black holes, being the simplest objects, act as the engine for the complex accretion-ejection process, which can significantly influence the evolution of galaxies and the Universe. Hence, their study is of greater interest than mere curiosity.

1.1 Black hole accretion systems

Before the detection of gravitational wave (GW) in 2015 by the LIGO-Virgo collaboration, the only way to study black holes is through electromagnetic radiation. Black holes do not emit observable electromagnetic radiation themselves. However, if a black

hole sits in a gas-rich environment, matters can overflow to and be swallowed by the black hole due to gravity. This process is called accretion. The accretion process is efficient at converting the gravitational energy of the accreted matter into radiation. The accretion efficiency is defined as the ratio of the produced energy to the rest-mass energy ($E = Mc^2$) it consumes, e.g. $L_{\text{acc}} = \eta \dot{M}c^2$ where \dot{M} is the mass accretion rate. Depending on the spin of the black hole, the accretion efficiency (η) for a thin disk is between 5%-42%^[30]. In comparison, the efficiency of nuclear fusion reactions that power the Sun and stars are around 0.3%.

1.1.1 Eddington limit

For accretion to happen, the gravity exerted on the matter must exceed the outward radiation pressure. This sets a limit of the highest luminosity a source can have. Under the assumption that the system is spherically symmetric, this limit is known as the “Eddington luminosity”:

$$L_{\text{Edd}} = \frac{4\pi GM_{\text{BH}}m_p c}{\sigma_e} = 1.26 \times 10^{38} (M/M_\odot) \text{ erg s}^{-1} \quad (1.1)$$

where m_p is the proton mass, G is the gravitational constant, c is the speed of light and $\sigma_e = 6.65 \times 10^{-25} \text{ cm}^2$ is the cross-section for Thomson scattering. Note that the equation is valid for a plasma of electrons and protons. The “Eddington accretion rate”, \dot{M}_{Edd} is the mass accretion rate required to produce L_{Edd} :

$$\dot{M}_{\text{Edd}} = \frac{L_{\text{Edd}}}{\eta c^2} \quad (1.2)$$

An “Eddington ratio”, which is the ratio between the source bolometric luminosity and the Eddington luminosity ($\lambda_{\text{Edd}} = L_{\text{bol}}/L_{\text{Edd}}$), is often defined to indicate the accretion rate. This parameter is independent of the black hole mass and is a useful measure to compare black hole accretion rates over a wide range of black hole masses. This thesis will focus on “high-accretion” rate systems (i.e., $\lambda_{\text{Edd}} > 0.001$).

1.1.2 Active galactic nucleus

Supermassive black holes can accrete matter from their host galaxies. When the mass accretion rate is high enough, the radiation emitted by the accretion flow can outshine the light from stars in the entire galaxy. In this case, the central SMBH is called active galactic nucleus (AGN). AGNs are among the most luminous steady radiation

sources in the Universe. Two classes of AGNs have been established: (1) type 1 AGNs that present broad permitted emission lines and narrow emission lines in their optical spectra (2) type 2 AGNs that show only narrow emission lines^[31]. These classes have been unified using a simple model that postulates all AGNs are fundamentally similar and different types result from the viewing angle^[32].

Figure 1-2 shows a sketch of the AGN unification model that consists of a central SMBH, an accretion disk, a broad line region (BLR), a narrow line region (NLR) and a dusty torus. If the angle between our line of sight and the symmetry axis is too large (i.e. more edge on), the emission from the accretion disk and the broad line region will be blocked by the dusty torus. In this case, broad permitted emission lines are not seen. The narrow lines can still be observed because the narrow line region is more extended. With a lower inclination angle (i.e. more face on), both the broad line region and the narrow line region can be observed.

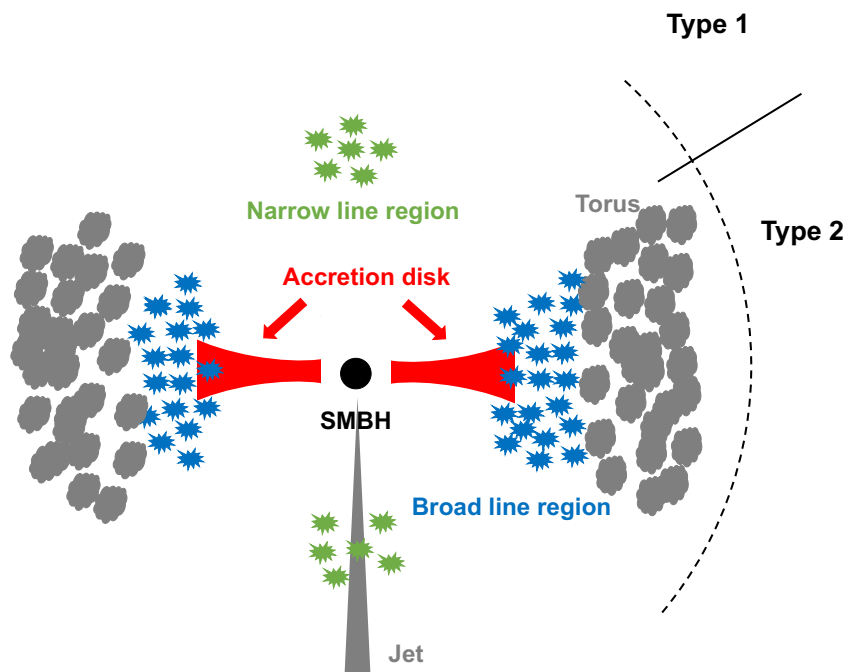


Figure 1-2 A schematic picture of the AGN unification model. A supermassive black hole is surrounded by an accretion disk with a sub-pc length scale. The broad line region consists of high-density (i.e., the electron density $n_e > 10^8 \text{ cm}^{-3}$) and dust-free gas clouds at a distance of 0.01–1 pc from the BH. Outside the broad line region, there is a dusty torus structure at a scale of 0.1–10 pc. The narrow line region has low-density ($n_e < 10^6 \text{ cm}^{-3}$) and ionized gas extending up to 100 pc.

The very well known correlations between mass of SMBHs (M_{BH}) and their host galaxy properties (e.g., galaxy bulge luminosity L_{bulge} ^[33], galaxy bulge mass M_{bulge} ^[34] and stellar velocity dispersion of the galaxy bulge σ ^[35–36]) suggest that the growth of SMBHs and galaxies are intrinsically linked^[37]. Accretion is an important channel for the growth of SMBHs. During the accretion period, SMBHs release vast amounts of energy in the form of radiation or kinetic energy (e.g., outflows, winds and jets) into the surroundings^[38], which can regulate the star formation in host galaxies. This is called AGN feedback and is likely the cause of the above relations^[37].

1.1.3 Black hole X-ray binary

For stellar-mass black holes, accretion happens when a companion star is in a close orbit. The system is identified as X-ray binary (XRB). Black holes in these systems have mass 4–20 M_{\odot} ^[39] and are formed due to collapse of massive stars^[40]. Depending on the mass of the companion star, XRBs can be divided into low mass and high mass XRBs.

In low mass XRBs, the companion star has a mass less than 1 solar mass. If the volume of the star exceeds the Roche lobe, matter will overflow from the star to the black hole through the inner Lagrangian point (Figure 1-3). For high mass XRBs in which the companions are O/B stars with masses ten times heavier than the Sun, the black hole can accrete from both the Roche lobe overflow and the strong stellar wind from the star.

In both cases, matter from the companion star forms a disk-like structure around the central black hole because of the angular momentum. Materials at the outer disk gradually lose their angular momentum due to viscosity (friction) and spiral inward slowly towards the black hole. The angular momentum is transported outwards. The viscous process makes the gas lose energy and angular momentum. This, in turn, makes the gas fall onto the gravitational well of the BH, so potential energy is converted into kinetic energy of the gas.

Most black hole X-ray binaries in the Galaxy are transient sources that go into recurrent outbursts. Figure 1-4 shows the lightcurve of a prototype low mass XRB, GX 339-4, obtained by the Monitor of All-sky X-ray Image (MAXI) in the 2–20 keV band^[41]. The source stays at a quiescent state for most of the time during which the luminosity is low ($\sim 10^{33} \text{ erg s}^{-1}$, $\lambda_{\text{Edd}} \sim 10^{-6}$)^[42]. Every few years (the timescale significantly depends

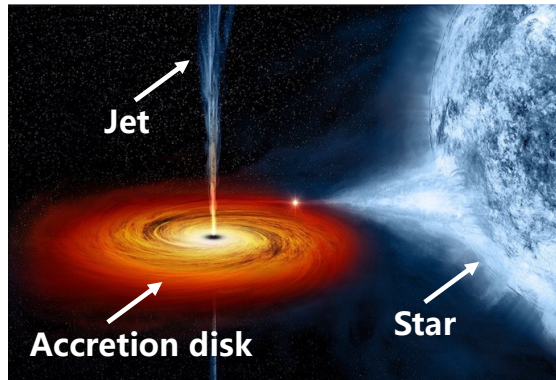


Figure 1-3 An artist’s impression of an X-ray binary system in which a stellar-mass black hole is accreting matter from its companion star (courtesy of JPL/NASA). The accreted matter form a disk-like structure around the black hole. A relativistic jet is launched in the direction perpendicular to the disk.

on particular systems), GX 339-4 undergoes an outburst, with the luminosity increasing by several orders of magnitude (10^{37-39} erg s $^{-1}$). These outbursts typically last for a few months, making it convenient to track the evolution of the accretion flow across a wide range of accretion rates. When scaling this timescale to AGNs, the outburst duration exceeds 10^4 years, rendering it inaccessible for human observation.

Generally, it is believed that the physics governing the accretion flow in AGNs and XRBs is very similar^[43]. It is only necessary to scale the properties (such as temperature and variability timescale) of the accretion flow according to the mass of the central black hole^[44]. Both types of systems show signatures of an optically thick disk, an energetic corona and jet (see Sec. 1.2). It has been shown that the X-ray and radio emission of both systems follow the same correlation on the fundamental plane^[45]. Therefore, studying black hole XRBs helps to understand the general accretion process onto black holes. During the outburst phase, BH XRBs in the Galaxy are often orders of magnitude brighter than most AGNs in the sky, and more photons can be collected within a certain exposure time. This makes XRBs ideal sources to study the accretion process onto black holes.

1.2 Accretion structure and spectral components

1.2.1 Cold standard disk

When the accretion rate is below some critical value (i.e., $\lambda_{\text{Edd}} < 0.001$), the accretion flow is geometrically thick and optically thin. The accretion flow has very high

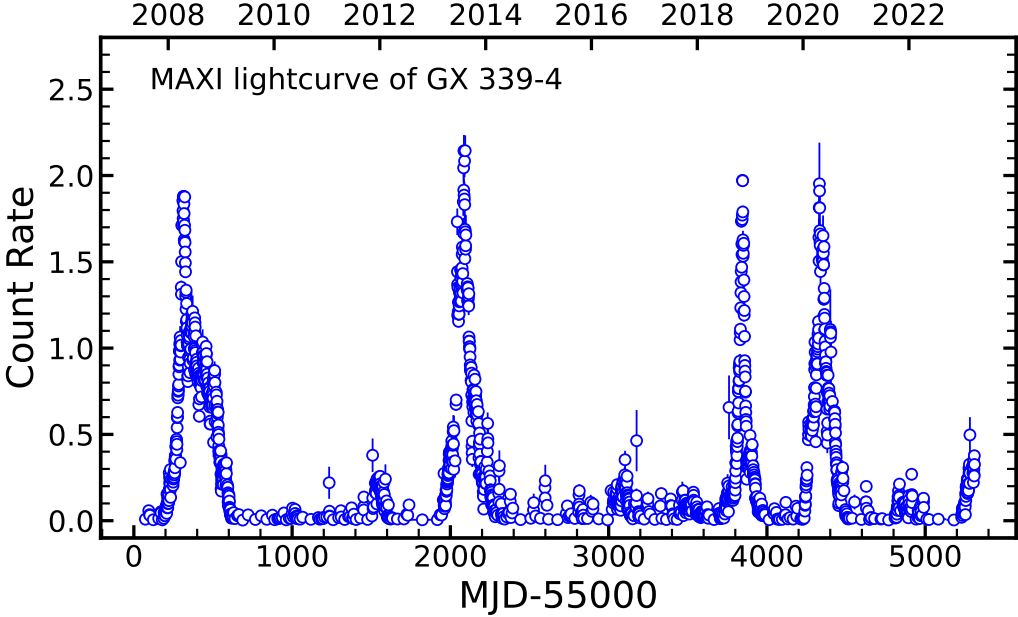


Figure 1-4 MAXI lightcurve (2–20 keV) of a prototype low mass black hole X-ray binary, GX 339-4, that show recurrently outbursts every a few years.

temperature (~ 100 keV for electrons) because the density is too low to have efficient cooling through radiation and the energy is stored internally as thermal energy. This is known as the radiatively inefficient accretion flow (RIAF), or advection-dominated accretion flow (ADAF)^[46–47]. This hot flow is supposed to be present in low luminosity AGNs (LLAGNs) and XRBs in the low-hard/quiescent state^[48].

If the accretion rate increases but remains within the sub-Eddington regime (i.e., $\lambda_{\text{Edd}} < 0.3$), a geometrically thin and optically thick accretion disk will form. In such cases, the accretion disk is radiatively efficient, indicating that at every point on the disk, gas can effectively cool down by radiating energy away. Since the disk is optically thick, photons will have many interactions before leaving the disk. Therefore, the local spectrum is a blackbody, and the spectrum of the entire disk is a multi-temperature blackbody, with higher temperature if closer to the central black hole. The temperature profile of such disk is given by (i.e., Equation (5.43) in Frank et al. 2002^[49]):

$$T(r) = \left[\frac{3GM_{\text{BH}}\dot{M}}{8\pi\sigma r^3} [1 - (\frac{r_{\text{in}}}{r})^{\frac{1}{2}}] \right]^{\frac{1}{4}} \quad (1.3)$$

where r_{in} is the inner disk radius and σ is the Stefan-Boltzmann constant. If defining the radius in units of the gravitational radius, $r_g = GM_{\text{BH}}/c^2$, and scaling the mass

accretion rate to the Eddington accretion rate, the temperature profile at $r \gg r_{\text{in}}$ is:

$$T(r) \propto M_8^{-1/4} \left[\frac{\dot{M}}{\dot{M}_{\text{Edd}}} \right]^{1/4} \left[\frac{r}{r_g} \right]^{-3/4} \quad (1.4)$$

where M_8 is the black hole mass in units of 10^8 solar masses.

Equation (1.4) shows that more massive black holes have a cooler disk. This is in agreement with observations that thin accretion disks around supermassive black holes in AGNs have temperature $\sim 10^5$ K. Such disks emit most of their energy in the UV band of the spectrum, known as the “big blue bump” in the spectral energy distribution of AGNs. The accretion disks around stellar-mass black holes in XRBs are much hotter ($\sim 10^7$ K) and emit primarily in the X-ray band. This component has frequently been observed at intermediate and high soft states of BH XRBs when the disk thermal emission dominates the spectrum (i.e., Figure 1-5).

1.2.2 Corona

It has long been known that the thermal emission from the accretion disk is not enough to explain the X-ray spectra of accreting black holes^[50]. An additional component that has an apparently non-thermal spectral shape, extending up to very high energy range (100 keV or even MeV), has been ubiquitously detected in AGNs^[51] and XRBs (i.e., the blue line in the right panel of Figure 1-5). This component takes a power-law-like shape with a high-energy cutoff. The currently most plausible explanation is that this power-law continuum is produced by a hot (~ 100 keV or 10^9 K), optically thin ($\tau \leq 1$) plasma, usually referred to as the *corona* (in analogy with the solar corona), near the central black hole. Seed photons from the disk can be up-scattered (inverse Compton scattering) to higher energies by hot electrons in the corona^[28,52]. The scattering can happen multiple times, with the probability decreasing with the number of scatterings. The sum of multiple scatterings results in a power-law spectrum with the specific photon flux takes the form $n(E) \sim E^{-\Gamma}$. The photon index, Γ , is determined by the optical depth (τ) and electron temperature (kT_e) of the corona. The power-law form is valid until the photon energy becomes comparable to the energy of thermal electrons in which case photons can no longer gain energy from scatterings. This causes a high-energy turn-over in the spectrum that can be roughly modeled as an exponential cutoff: $n(E) \sim E^{-\Gamma} e^{-E/E_{\text{cut}}}$. The cutoff energy, E_{cut} , is controlled by the coronal electron temperature via $E_{\text{cut}} \sim 2 - 3 kT_e$, assuming a slab-like geometry^[53]. This

simple phenomenological model fits well the hard X-ray emission of XRBs and AGNs, with E_{cut} often found in 30–300 keV^[54]. There are also self-consistently calculated models for the spectrum of thermal Comptonization (i.e., the `nthcomp`^[55–56] model) or Comptonization by a non-thermal corona (i.e., the `eqpair`^[57] model in which the distribution of electrons in the corona is not Maxwellian).

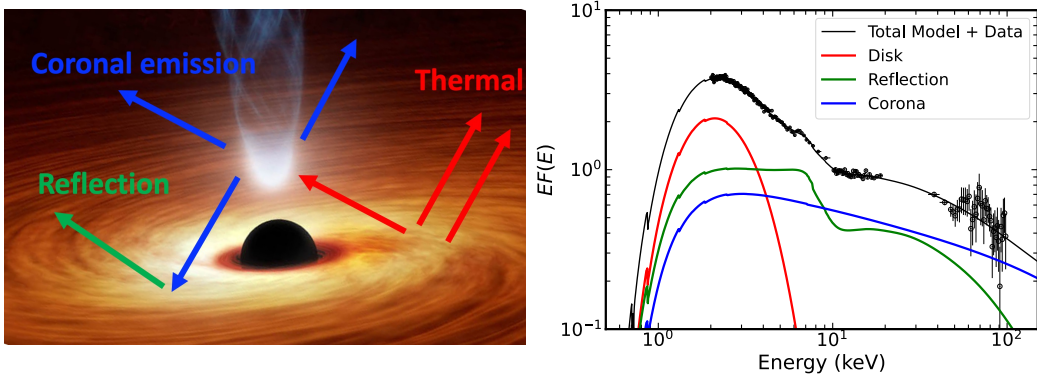


Figure 1-5 (Left) Artist’s impression of the inner accretion flow near a black hole (courtesy of JPL/NASA). Arrows with different colors represent emission components: (red) the disk thermal emission; (blue) the coronal emission; (green) the reflected emission of the disk. (Right) The *Insight*–HXMT observation of the low mass black hole XRB GX 339–4 in the intermediate state on 2021 March 27. The red, blue and green lines show spectral components corresponding to the left panel. The sum is shown as the black solid line.

Little has been known about the nature of the corona, including its formation mechanism and geometry. It is not fully understood how the accretion power is transported into the corona, although magnetic field seems to play an important role^[58]. There are a few speculations about the geometry of the corona. In the *lamppost model*, the corona is thought to be a point-like source located along the spin axis of the black hole at a certain height^[59–60]. Physically it might correspond to the base of the jet^[61] (e.g., Figure 1-5). This geometry has been widely used in analyzing the X-ray data of accreting black holes because of the simplicity for calculation and the success in interpreting the data. The hot inner flow (e.g., ADAF) between a truncated accretion disk and the black hole has also been proposed to be the corona^[62]. The mechanism to truncate the disk is still unclear (useful discussions can be found in Liu et al. 2022^[63]). In this scenario, the hot inner flow can Comptonize seed photons from the outer cold accretion disk. This radially extended coronal geometry is now supported by the recent X-ray polarization measurements of Cygnus X-1 in the hard state using the Imaging X-ray Polarimetry

Explorer (IXPE)^[64]. Another popular geometry assumes that the hot corona is lying above the cold geometrically thin disk, either in the form of a continuous layer embeds the disk (*sandwich corona*)^[28,65] or as individual active regions on the disk (*patchy corona*)^[66–67]. Illustrations of these geometries can be found in Reynolds & Nowak 2003^[68] or Bambi et al. 2021^[69]. Moreover, the corona might not be a static structure but be outflowing^[70–71].

1.2.3 Reflection

As shown in Figure 1-5, a fraction of the corona emission can reach the distant observer but the others will be captured and reprocessed by the accretion disk. This reprocessed emission is called *reflection* which is a misleading name because photons are not simply reflected but underwent complicate processes within the disk such as absorption, emission and scattering. As a consequence, unlike the featureless spectra of the disk thermal emission and the coronal emission, a number of atomic features are imprinted in the spectrum of the reflected component. These features will be altered by relativistic effects near the black holes because the atoms/ions that produce these features are rapidly orbiting the black hole, and reflected photons must lose energy to escape the gravitational potential well of the black hole before reaching the observer. In this way, information about the accretion flow properties (i.e. geometry, ionization state or element abundances) and the central black hole (i.e., spin) are encoded in the reflected spectrum. Modeling and analyzing the reflected spectrum serves as a powerful tool to extract these details^[69]. This technique, called *X-ray reflection spectroscopy*, is the main tool used in this thesis. More details for the reflection component and the reflection technique can be found in Sec. 1.4.

1.2.4 Outflow

In addition to the disk and corona, outflow is also an integral component of the accretion flow. For example, strong relativistic jets have been detected in both XRBs and AGNs. In addition to the jet, which moves perpendicular to the disk, there is another kind of outflow that travels along the radial direction of the disk with a much slower velocity. In XRBs, this kind of outflow is known as *disk wind* (Figure 1-6).

The disk wind manifests as blue-shifted narrow absorption lines by highly ionized material such as Fe XXV and Fe XXVI (~ 6.7 and 6.96 keV) in the X-ray spectrum.

These features are commonly found in high-inclination systems, indicating an equatorial geometry and an origin from the accretion disk^[1]. The disk wind is likely an important ingredient of the accretion process since it can carry a large amount of mass (often exceeding the mass accretion rate) away from the disk^[72–73]. The launch of disk winds might be related to state transitions of low-mass X-ray binaries^[74]. The anti-correlation between the jet and wind suggests the wind acts as a quenching mechanism of the jet^[75] but recent studies have found that the two kinds of outflows can coexist^[76].

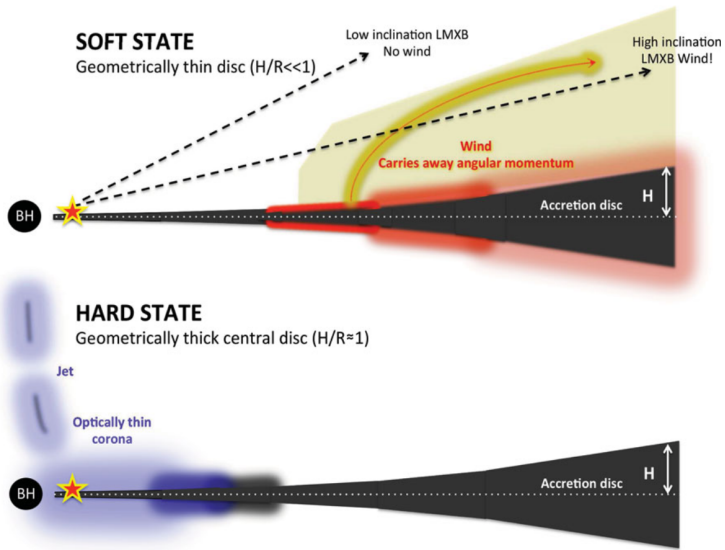


Figure 1-6 A cartoon to show the disk wind in the soft state and the jet in the hard state. Image adapted from Ponti et al. 2021^[1].

There are still open questions regarding the disk winds in low mass XRBs, such as its launching mechanism and state dependence. Based on the properties of the disk winds, it is believed that either thermal or magnetic pressure serves as the driving mechanism. Thermal winds are generated when the outer disk is Compton heated by irradiation from the central source and the thermal velocity exceeds the escape velocity^[77–78]. In this case, wind is only possible to be launched at radius larger than the Compton radius at which the thermal velocity equals the escape velocity. Magnetic field can generate winds without restriction on the launching radius and the outflow velocity. Therefore, if the launching radius is inside the Compton radius, the wind is generally thought to have a magnetic origin. However, it is hard to determine the launching radius because of the strong degeneracy between the density and the launching radius when fitting the reflection features. Methods based on geometrical considerations often yield mea-

surements with significant uncertainties^[79]. Absorption features from density-sensitive metastable levels, such as Fe XXII, serve as reliable indicators of wind density. Using this method, magnetic winds have been identified in GRO J1655–40^[80–81]. However, even this method has been challenged recently. It is found that the considering cascades from radiative excitation in accumulating metastable levels can significantly change the estimation of the wind density^[82].

The X-ray absorption signature of the disk wind is preferentially and consistently observed in the soft state of low mass XRBs^[1], disappearing in the hard state (see Sec. 1-4). This pattern underlines a link between the wind and the inner accretion process. One obvious explanation is that the ionizing spectrum in the hard state has more high energy photons than that of the soft state, so the wind is over-ionized^[83]. With detailed photoionization modeling, this scenario has been shown to fail at explaining the disappearance of absorption lines in a few cases^[84–85]. Therefore, the wind is either not launched or is thermally unstable^[86] in the hard state.

Understanding these open questions is crucial for comprehending the accretion-ejection paradigm. It might hold the key to understanding the long-lasting question of the state transition mechanism in low-mass BH XRBs. The mechanism driving disk winds in XRBs may also be applicable to AGNs. In such cases, the central supermassive black hole can generate feedback to the host galaxy, triggering black hole-galaxy coevolution^[38]. In this thesis, the disk wind signature in the famous BH XRB GRS 1915+105 will be studied.

1.3 Outburst of X-ray binaries

Some black hole X-ray binaries are persistent sources, which means they have been active in X-rays since their discovery (i.e., Cygnus X-1). Most Galactic black hole XRBs are transient sources that spend most of their time in quiescence and occasionally go into outburst. The outburst is thought to be caused by instabilities, e.g. thermal-viscous instability, at the outer part of the disk that result in an increased mass accretion rate^[87–88].

The outbursts of black hole X-ray binaries provide ideal observational data for studying accretion physics across several orders of magnitude of the mass accretion rate. It has long been found that typical outburst of BH XRBs follows a certain pattern that can be traced on the so-called *hardness-intensity diagram* (HID)^[89]. Figure 1-7 shows HIDs

for outbursts for three bright BH XRBs. To plot this diagram, the X-ray hardness is simply defined as the ratio between count rate in a hard X-ray band and a soft X-ray band and the intensity is the total count rate of the detector. Note that there is no rigid definition of the soft, hard X-ray bands or the intensity. It is not the exact numbers of the hardness or the intensity but the evolution trend (see the grey arrows in Figure 1-7) that matters. Other methods, such as the root mean square (rms)-intensity diagram^[90] and the “hue angle” based on the power spectrum^[91] have also been used to trace the evolution of the outburst. These tools share the same spirit as the HID, which is to understand how the sources transition among different *spectral states* during an outburst. Evolutions of spectral and timing properties along the track of HID are summarized below.

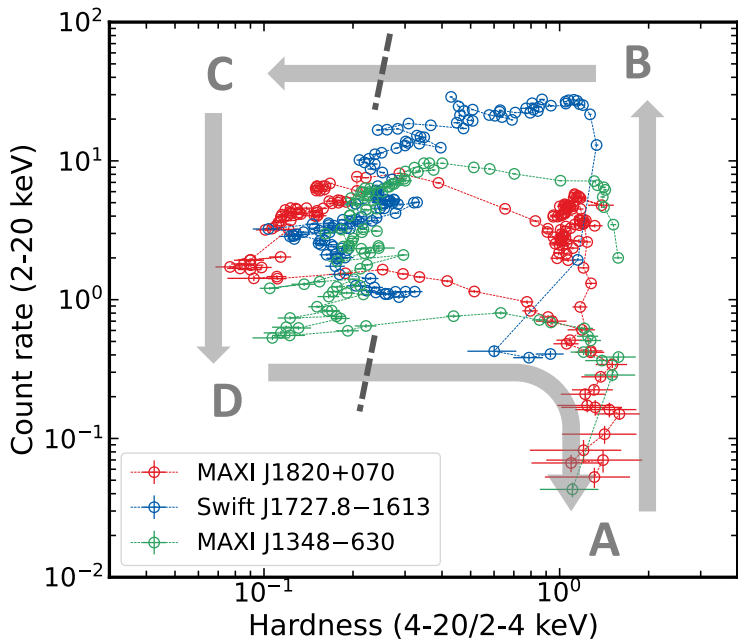


Figure 1-7 Hardness-intensity diagram for outbursts of three black hole XRBs with *MAXI* data. Grey arrows are used to indicate the evolution of a typical outburst on the diagram. The dashed lines denote the launch of powerful jets.

1.3.1 Hard state

At the initial phase of the outburst, the source first enters the *low hard* (LH) state after emerging from quiescence. This corresponds to region A in Figure 1-7 (low luminosity and high hardness). As the accretion rate gets higher, the source continues to get brighter but remains in the hard state (from A to B). As shown in Figure 1-8,

the energy spectrum for the hard state is dominated by the power-law like non-thermal emission (photon index ~ 1.7) from the corona, with minimal contribution from the thermal emission of the disk. The intrinsic variability is high, with root-mean-square (rms) up to 30%, as shown by the power density spectra (PDS). Moreover, in the PDS of hard state (and intermediate states), narrow peaks, known as quasi-periodic oscillations (QPOs), are frequently detected on top of the broadband noise. The central frequency of the QPO increases with the luminosity, along with slight softening of the photon index (Γ) of the coronal emission and the decreasing of the coronal temperature^[92]. Compact and optically thick jets are found in the hard state and the radio emission from the jet positively correlates with the X-ray luminosity^[93]. X-ray disk wind is rarely detected in the hard state but recently there is evidence for wind signatures in the UV, optical and infrared bands^[94–96].

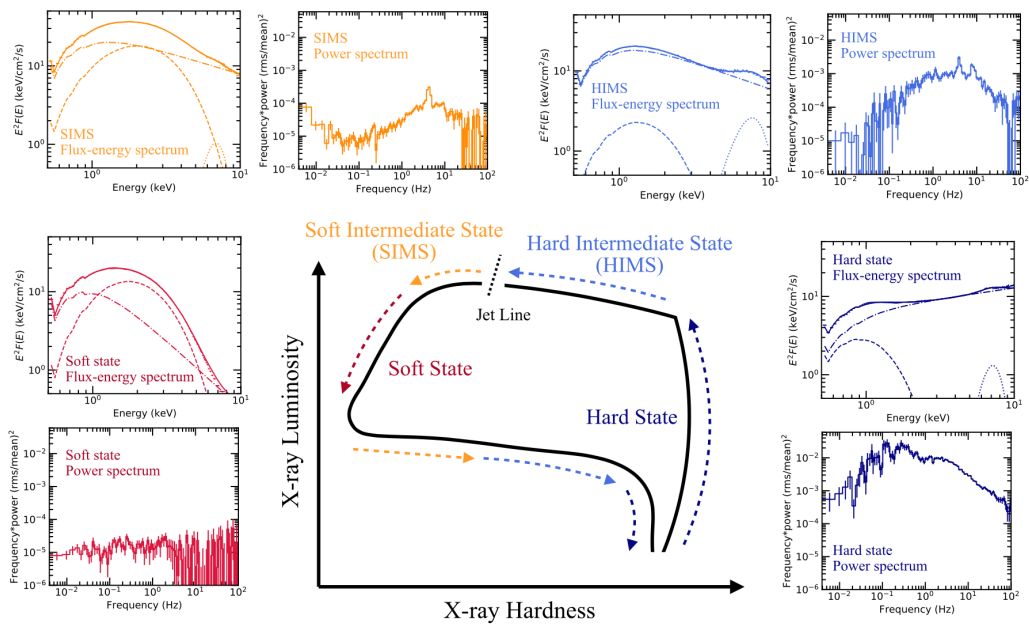


Figure 1-8 A sketch of the hardness-intensity diagram which shows temporal evolution for a typical outburst of black hole low mass XRBs. Representative energy spectrum and power spectrum for each state are plotted. Image adapted from Wang et al. 2022^[2].

1.3.2 Intermediate states

At a certain luminosity, which varies from source to source and may even differ from one outburst to another for the same source, the system undergoes a state transition. This transition spans from the hard state to the soft state (from B to C in Figure 1-7), passing through the hard intermediate state (HIMS) and the soft intermediate state (SIMS).

The transition is along with increasing contribution from the disk thermal emission and steepening of the coronal power-law emission. After the turn (B), the source enters HIMS, with its energy spectrum continuing to soften. Meanwhile, the QPO frequency also keeps increasing. HIMS and SIMS are difficult to distinguish from the energy spectrum, the transition from HIMS to SIMS is defined by the appearance of type-B QPOs in the PDS^[89]. There are three types of QPOs (type A, B and C) for BH XRBs^[97–98], but a detailed explanation is out of the scope of this thesis. During the hard-to-soft state transition, the compact slower-moving jet becomes unstable, and a ballistic powerful optically-thin radio jet appears^[99].

1.3.3 Soft state

At the end of the SIMS, the disk thermal emission dominates the source spectrum. However, before entering the soft state, an anomalous very high state (VHS) sometimes appears, with an amplified steep ($\Gamma \sim 2.5$) power-law component. The luminosity of this power-law component is comparable to the strong disk thermal emission.

The soft state energy spectrum is dominated by thermal emission ($> 75\%$) from the disk with the characteristic temperature of ~ 1 keV. This state is often observed when the source is bright, hence earning the the name *high soft* (HS) state. The variability is suppressed (rms $< 5\%$) and QPOs are absent or very weak in the soft state. Radio jet emission from the core often disappears while X-ray wind is ubiquitously detected in high inclination systems. UV and optical winds are not found but infrared wind still exists in the soft state^[100].

The source usually stays a large fraction of the time in the soft state, during which its luminosity gradually decreases. Then the source transitions back to LH via SIMS and HIMS (from D to A in Figure 1-7) at a lower luminosity than the hard-to-soft transition.

1.3.4 Open questions

It is generally believed that the optically thick accretion disk is truncated at large radius in the LH state when the luminosity is low. In between the truncation radius and the black hole is an optically thin hot flow that can serve as the corona to Comptonize seed photons from the disk. The disk moves towards the black hole as the accretion rate increases. This *disk truncation scenario* has commonly been used to explain the state transition of low mass BH XRBs^[62]. Observationally, there is evidence to show that

the accretion disk is indeed truncated at larger radius ($> 100 R_g$) at LH state ($\lambda_{\text{Edd}} < 0.001$)^[15]. In the HS state, the disk is believed to reach the ISCO^[101–102].

Significant debates still exist regarding whether the disk is truncated at the luminous hard state (region B in Figure 1-7) or in the intermediate states. Measurements of the inner disk radius from spectral and timing properties in these states can yield significantly controversial results^[103–104]. Consequently, the mechanism that triggers the state transition remains unclear. Understanding the evolution of the inner disk radius is of broader importance since it is related to the radiative efficiency of the accretion process. One of the topics of this thesis is to study the state transition of the low mass X-ray binary GX 339–4 using X-ray reflection spectroscopy.

1.4 X-ray reflection spectroscopy

1.4.1 Local reflection

Photons incident to the disk can undergo photoelectric absorption by the material in the disk atmosphere^[105–106]. For example, photons with energy higher than 7.1 keV can be absorbed by a neutral iron atom (Fe I), removing an electron from the K shell ($n = 1$). This causes a photoelectric absorption edge in the reflection spectrum. In the meantime, an electron from the L shell ($n = 2$) can transition to the K shell, emitting an X-ray photon with energy of 6.4 keV (iron K α). The photon can escape, producing a *fluorescence* line in the reflection spectrum or be reabsorbed and eject an electron from a higher level (*Auger* de-excitation). This process happens for not only iron, but all other elements in the disk. However, the fluorescent probability increases with atomic number ($\sim Z^4$ for neutral matter). Given iron’s large atomic number, high abundance, and the fact that the X-ray continuum flux often decreases with energy, the iron K α line at 6.4 keV stands out to be the strongest fluorescent line. The other reason that iron lines are important is that there are not many other lines around 6.4 keV, while there are a lot of lines below 4 keV. When the spectrum gets blurred (Sec. 1.4.2), these lines below 4 keV all merge together. Due to the spin-orbit interaction, the iron K α line has two components, K α_1 at 6.404 keV and K α_2 at 6.391 keV, that cannot be resolved by the spectrometers used in this thesis. Associated with the K α line, there is also a iron K β line at 7.06 keV. Iron fluorescent lines have been detected since 1980s by instruments like *Ginga* and *EXOSAT*^[107–109]. With modern instruments such as *Suzaku*, *XMM*-

Newton or *NuSTAR*, the narrow iron K α line is found to be almost omnipresent in the X-ray spectra of type 1 and type 2 AGNs^[110].

For ionized iron, less electrons are available to screen the inner K shell, the energy for both the photoelectric absorption threshold and the iron K α line are increased. The iron K α line energy is 6.45 keV in Fe XVII, 6.7 keV in Fe XXV and 6.9 keV in Fe XXVI. The energy for the K shell absorption edge also increase from 7.1 keV in Fe I to 7.8 keV for Fe XVIII and 9.3 keV for Fe XXVI. Therefore, the ionization state of the disk atmosphere is an importance parameter controlling the shape of the reflection spectrum.

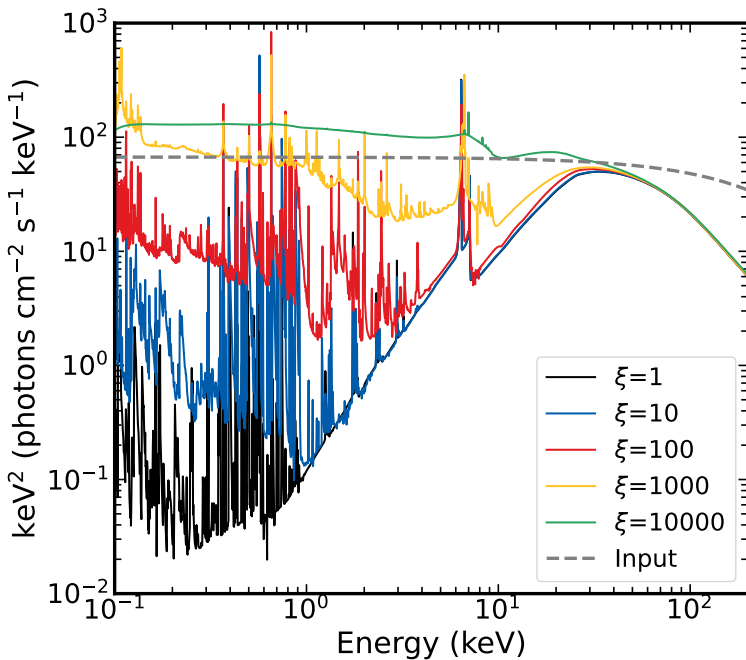


Figure 1-9 Solid lines: rest-frame reflection spectra for different ionization states of the disk. The grey dashed line represent the incident energy spectrum which is a cutoff power-law with $\Gamma = 2$ and $E_{\text{cut}} = 300$ keV. The reflection spectra are generated with the `xillver` model assuming an iron abundance three times of the solar value and an electron density $n_e = 10^{15}$ cm $^{-3}$.

The photoelectric absorption cross-section (σ_{abs}) decreases with energy ($\sim E^{-3}$) while the cross-section for electron scattering (σ_{es}) is nearly constant with energy. The electron scattering cross-section (σ_{es}) is equivalent to σ_{abs} at $E \approx 12$ keV for cosmic abundances. Above this energy, the scattering process starts to dominate, thus high-energy photons tend to be Compton scattered back out of the disk. Since the disk temperature is low, the high-energy photons will lose energy for this scattering process (Compton down-scattering). The combination of the iron absorption edge (7.1–9.3 keV,

depending on the ion) and the Compton down-scattering of high-energy photons leads to *Compton hump* peaked around 20–30 keV that appears above the power-law continuum from the corona^[111]. This hump feature was observed not long after the detection of the iron line emission^[112].

The ionization state of the material can be described by the ionization parameter:

$$\xi = \frac{4\pi F}{n_e} \quad (1.5)$$

where F (in units of $\text{erg cm}^{-2} \text{s}^{-1}$) is the incident flux (from the corona) integrated between 13.6 eV and 13.6 keV and n_e is the electron density (in units of cm^{-3}). Figure 1-9 shows how the reflection spectrum in the local rest-frame can be impacted by the ionization parameter. The spectra in Figure 1-9 are generated with one of the most advanced reflection models, `xillver`^[106]. At lower ionization, there are more bounded electrons, therefore strong absorption and prominent fluorescent lines are seen below 10 keV. Both the absorption and emission features get weak for highly ionized reflecting material as electrons for low-Z elements are almost fully stripped.

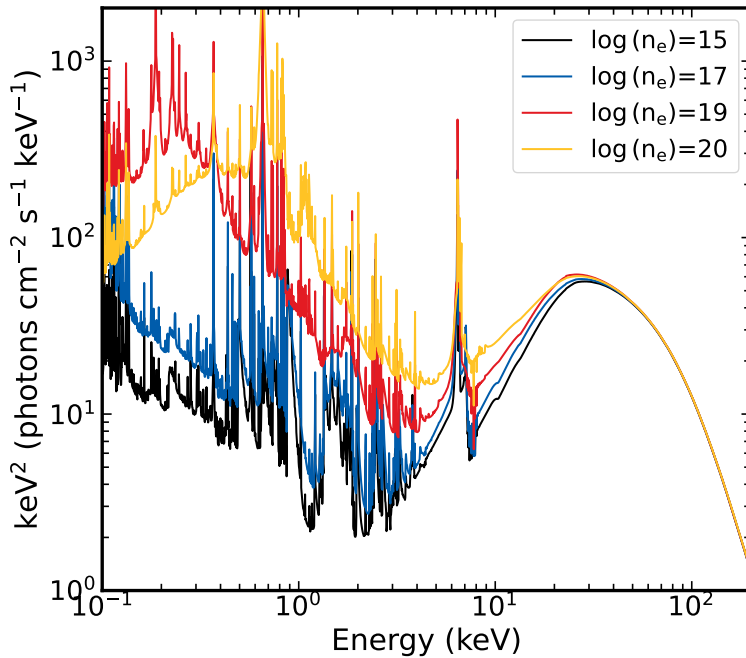


Figure 1-10 rest-frame reflection spectra for different electron density of the disk. The reflection spectra are generated with the `xillvercp` model assuming an iron abundance three times of the solar value and an ionization parameter $\xi=100 \text{ erg cm s}^{-1}$. The incident spectrum is a Comptonized continuum with $\Gamma = 2$ and $kT_e=60 \text{ keV}$.

The electron density, n_e , not only plays a role in defining the ionization parameter

but also has its own impact on the reflection spectrum. A higher density makes the free-free (i.e., bremsstrahlung) heating-cooling being dominant in the disk, therefore increasing the temperature of the disk surface^[113]. The main effect of increasing the density on the reflection spectrum is to boost the thermal continuum in the soft X-ray band (< 2 keV, see Figure 1-10). Previous reflection models assume an electron density of 10^{15} cm^{-3} ^[106,114], which is only appropriate for the disk of very massive black holes ($> 10^8 M_\odot$) according to the standard accretion disk model^[115–116]. It was recently founded that the disk for AGNs with less massive black holes indeed requires a higher density^[7,11]. Reflection by a high-density disk is a plausible explanation of the “soft excess” component in the X-ray spectra of some Seyfert galaxies^[117–118]. The disk in XRBs has a higher density than the of AGNs, therefore the high-density effect should be stronger. However, this effect has only been studied in a few individual XRBs. To completely study this effect, part of this thesis will focus on the high-density reflection spectra for BH XRBs.

The element abundances are critical parameters to calculate the local reflection spectrum. Current reflection models often assume the solar abundance for calculation with the exception of the iron abundance. The abundance of iron controls the strength of the Fe K α line and the absorption edge. It can be measured from the observed reflection spectrum. In some cases, the iron abundance has been found to be super high (e.g., 10 times of the solar iron abundance). The super-solar iron abundance is partly attributed to the previous models’ oversight of the high-density effect^[8]. More detailed discussions can be found in later sections.

1.4.2 Relativistic reflection

As shown in Figure 1-9, atomic lines are emitted at specific energies that correspond to the differences between energy levels in the atom. These correspond to the narrow emission lines in the spectrum in the *local rest-frame* of the reflecting material. The local reflection spectrum is determined by the incident coronal radiation (a power-law-like spectrum parameterized by the photon index Γ and the cutoff energy E_{cut}) and the physical properties of the disk (density, ionization state and element abundances). These parameters are illustrated in Figure 1-11. However, to understand the observed reflection spectrum, a number of other (relativistic) effects must be considered.

Figure 1-12 shows how a zero-width line (delta line) emitted by the accretion disk is

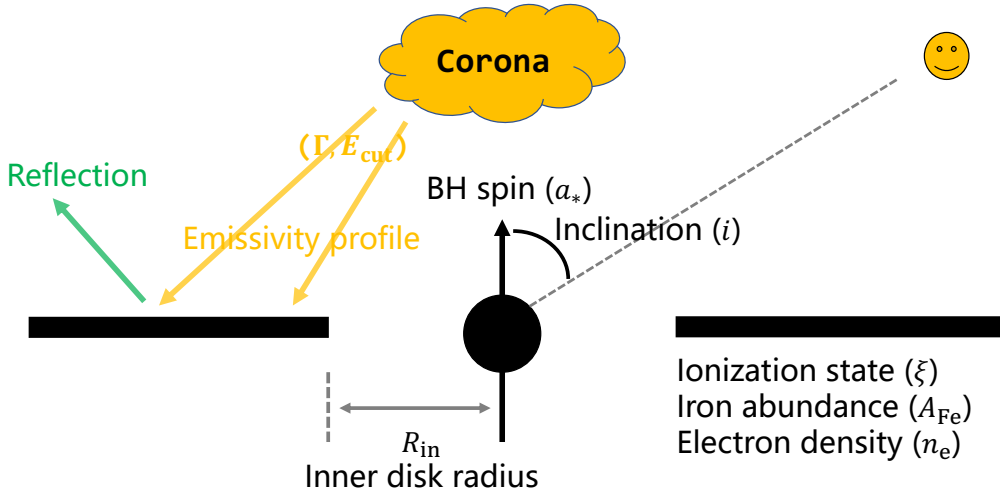


Figure 1-11 A sketch of the disk corona system with the parameters that are relevant to the reflection spectrum.

distorted and skewed into a broad line profile. The material that emit the line is orbiting the black hole so the line will be Doppler shifted due to be motion. This effect produces a double-peaked line profile since there is always material that move away from the observer (redshift) and move towards the observer (blueshift). Considering emission from the outer disk, the double-peaked line profile is symmetric about the rest-frame energy of the line. At the innermost region of the disk, the material is orbiting with a high velocity (up to half of the speed of light), so beaming effect will be significant, enhancing the blueshifted peak. Moreover, gravitational redshift also gets stronger when getting closer to the black hole, leading to a “red wing” in the line profile. Combining all these effects and integrating over the whole disk produces a relativistically broadened line profile shown at the bottom of Figure 1-12.

The inner disk radius (R_{in} , Figure 1-11) is an important parameter that controls the relativistic reflection spectrum. As explained above, a smaller R_{in} makes the broad line profile extends to lower energy (Figure 1-13). This makes it possible to measure R_{in} through analyzing the reflection spectrum. The innermost stable circular orbit (ISCO) is the last orbit that the disk can extend to. At radii smaller than the ISCO, the orbit is no longer stable and the material directly plunges into the event horizon instead of forming a disk. With the right observations when R_{in} is at ISCO, the relativistically broadened emission lines can be used to measure the size of ISCO (in units of R_g).

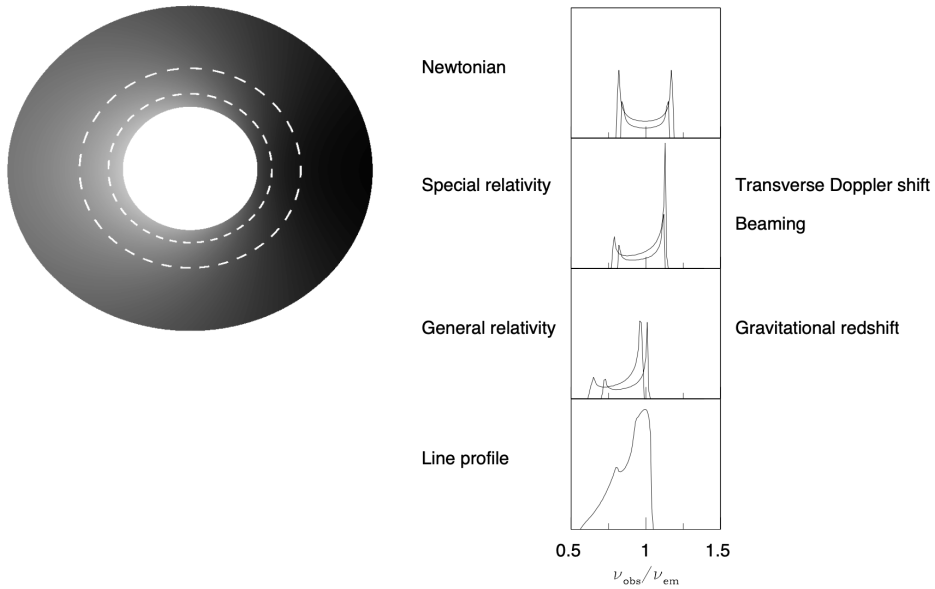


Figure 1-12 Sketch of how a narrow line with energy at ν_{em} is broadened by the relativistic effects.
Image adapted from Fabian et al. 2000^[3].

This is equivalent to measure the spin of the accreting black hole because the ISCO size is a monotonic function of black hole spin (Figure 1-13). Since the length scale measured by the reflection spectrum is in units of gravitational radius (R_g), so the black hole mass is not relevant. This property makes the relativistic reflection spectroscopy currently *the only method to measure black holes spins in both XRBs and AGNs*.

The inclination angle (i), which is the angle between the black hole spin axis and the line of sight (Figure 1-11), is another parameter that can be measured using the relativistically reflection spectrum. For a higher inclination angle (i.e., a more edge-on view), the separation between the peaks in the double-peaked profile will be larger.

The incident radiation from the corona is undoubtedly a critical factor in determining the reflection spectrum. The spectrum of the incident coronal emission can be parameterized by its photon index (Γ) and cutoff energy (E_{cut}) although current models usually allow a few “flavors” of the coronal spectrum. The other vital component is the *emissivity profile*, which is the radial dependence of the intensity of the reflected emission ($\epsilon(r)$, equal to the incident intensity given energy balance at each site of the disk). In principle the emissivity profile is determined by the coronal geometry. As explained in Sec. 1.2.2, this geometry is still unknown. Therefore, phenomenological emissivity profiles, e.g., a simple power-law or broken power-law ($\epsilon \propto 1/r^{q_{\text{in}}}$ for $R_{\text{in}} < r < R_{\text{br}}$ and $\epsilon \propto 1/r^{q_{\text{out}}}$ for

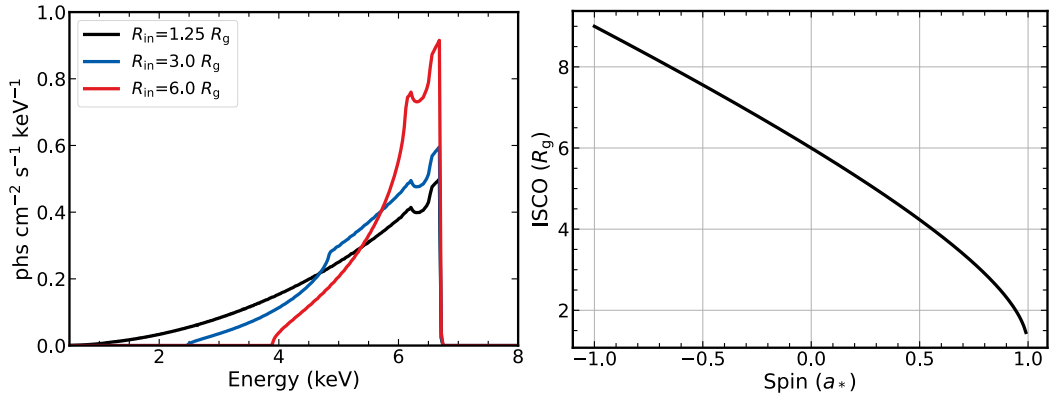


Figure 1-13 (Left) The broad iron line profile as a function of the inner disk radius (R_{in}). The line profiles are generated with the *relline* model. The other parameter required to make the plot are: line energy (6.4 keV), index for a power-law emissivity profile ($q = 3$), black hole spin ($a_* = 0.998$) and inclination ($i = 30^\circ$). (Right) The ISCO radius in Boyer-Lindquist coordinates as a function of black hole spin (a_*).

$R_{\text{br}} < r < R_{\text{out}}$ where R_{br} is the breaking radius), are often employed to fit the observed reflection spectrum. In practice, the measured emissivity profile with this method can be compared to theoretical predictions of different coronal geometries^[119–120]. Alternatively, a coronal geometry can be assumed (often a point source, or lamppost above the black hole) and the model can be directly fit to the full reflection spectrum to measure the coronal parameters (e.g., the height of the lamppost)^[60].

In reality, the relativistic broadening applies not only to emission lines but the entire local reflection spectrum. This can be simply done by convolving the relativistically broadened kernel for a single line to the rest-frame reflection spectrum because emission from each energy can essentially be treated at a single line. As shown in Figure 1-14, the Compton hump is still seen after considering relativistic effects. The strong, narrow Fe K α line is broadened into a broad line profile. Moreover, emission lines by lighter elements at lower energies are smoothed by relativistic effects. Therefore, prominent features for relativistic reflection spectrum are a broad iron line around 6–7 keV and a Compton hump peaked at 20–30 keV. These features have been ubiquitously found in various kinds of accretion systems such as AGNs and XRBs (see Figure 1-15).

1.4.3 Reflection models

In the early age of X-ray reflection spectroscopy, reflection models only consider relativistic effects on a single line (Fe K α). This is done by implementing the transfer

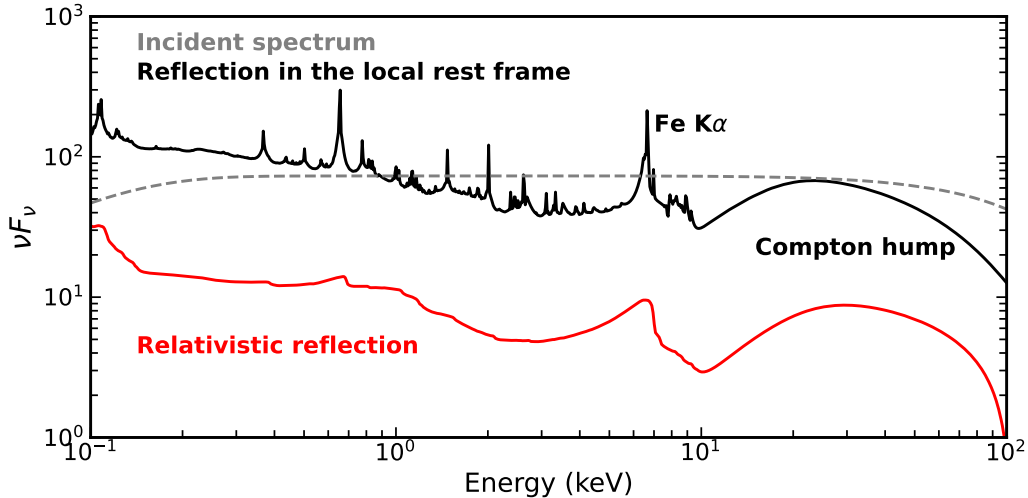


Figure 1-14 rest-frame reflection (black) and relativistic reflection (red) spectra for an accretion disk extending to the innermost circular orbit. The red spectrum is shifted vertically for visual clarity. The reflection spectra are generated by convolving the relativistic broadening kernel `relconv` with the `xillver` model. An iron abundance three times of the solar value and an ionization parameter $\xi=100 \text{ erg cm s}^{-1}$ are assumed. The incident spectrum is a Comptonized continuum with $\Gamma = 2$ and $kT_e=60 \text{ keV}$.

function mechanism proposed by Cunningham 1975^[121] that is still being used today. The first model of this kind is `diskline`^[122], which is only valid for $a_* = 0$. Others models valid for any spin were developed later. These include `laor`^[123], `kyrline`^[124], `kerrdisk`^[125] and `relline`^[126].

With data quality of current observations, it is necessary to consider relativistic broadening of the full local reflection model (as described in Sec. 1.4.1) instead of only the Fe K α line. The most advanced models for the local reflection spectrum are `reflionx`^[127] and `xillver`^[106]. The full relativistic reflection model can be calculated by applying the relativistic broadening kernels (e.g., `relconv`) to the local reflection model. This approach neglects the fact that the emission angle (θ_e) from the disk surface is different from the inclination angle (i) of the observer. Therefore, angle-resolved full relativistic reflection models have been developed such as `relxill`^[114], `relxill_nk`^[128], `relkerr`^[129–130], `kyn`^[124] and `reltrans`^[131]. Details of comparisons for these models can be found in Bambi et al. 2021^[69].

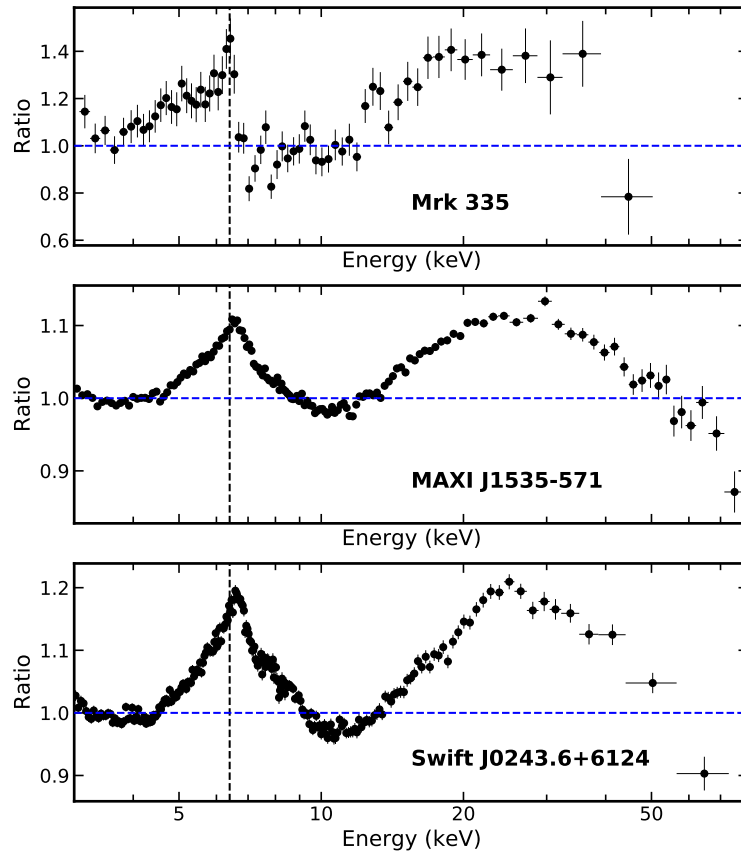


Figure 1-15 The observed relativistic reflection features in AGN (top), black hole XRB (middle) and neutron star XRB (bottom) with *NuSTAR* observations. In each case, we fit the data with a simple absorbed continuum model and plot the data to model ratio. The broad iron line around 7 keV and the Compton hump peaked around 30 keV are clearly seen.

1.5 Thesis outline

This thesis focuses on recent X-ray observations of black hole X-ray binaries using *Insight-HXMT*, *NuSTAR* and *Swift*. In Chapter 2, the hard-to-soft transition of GX 339–4 is studied using *Insight-HXMT* data. Following the state transition, the source shows a unique variability pattern (“flip-flop”), which is explored in Chapter 3. Chapter 4 delves into the high-density reflection effect in X-ray binaries. Additionally, Chapter 5 presents the analysis of disk wind absorption signatures in GRS 1915+105. Each chapter discusses detailed data analysis procedures and provides a physical interpretation of the observational data. Chapter 6 summarizes the research presented in this thesis and proposes future plans to strengthen our understanding of black hole accretion systems.

Chapter 2

The hard to soft transition of GX 339–4 as seen by *Insight*–HXMT

2.1 Introduction

The outbursts of BH XRBs are characterized by orders of magnitude changes in the X-ray luminosity and transitions between various spectral states^[132–133] (see Sec. 1.3). These states include the low hard (LH) state when the source spectrum is dominated by a non-thermal power-law-like continuum from the corona, and the high soft (HS) state, during which the thermal emission from the optically thick accretion disk dominates. The disk truncation scenario is commonly employed to explain the state transition^[19,62] but it remains to be known at which point the disk exactly reaches the ISCO and the mechanism triggering the state transition remain elusive.

Relativistic reflection component, namely the reprocessed coronal emission by the optically thick accretion disk near the black hole, is a powerful tool to probe the space-time properties^[69,134–136] and the geometry of the accreting system^[20,137–139]. One of the key features of the relativistic reflection component is the broad iron line around 6.4 keV, arising from the skewed iron K lines due to the strong relativistic effect near the black hole^[3,126]. This is why this broad line feature can be utilized to map the innermost regions surrounding the accreting black hole^[122] (see Sec. 1.4).

GX 339–4 is a classical low mass X-ray binary located at 8–12 kpc with a black hole mass estimated to be 4–11 M_{\odot} ^[140]. Strong relativistic reflection signatures have been identified in this source in both the hard and soft states^[20,141–142]. Previous studies have indicated that the black hole in GX 339–4 exhibits a very high spin ($a_* \sim 0.95$)^[20,143]. The inclination angle of the accretion disk should have an intermediate value^[143–144]. This source undergoes bright outbursts every few years, making it an ideal object for studying the accretion flow across different spectral states. Recently, the hard-

to-soft transition of GX 339–4 has been investigated by Sridhar et al. 2020^[145] using *RXTE*/PCA data, focusing on reflection analysis. The inner edge of the accretion disk was found to be close to ISCO during the transition. Beginning in February 2021, GX 339–4 entered a new outburst that lasted for several months. The hard to soft transition of this outburst was captured by the Chinese X-ray satellite Hard X-ray Modulation Telescope (dubbed *Insight*–HXMT^[146]). Therefore, we study the *Insight*–HXMT data to understand the evolution of the accretion geometry.

In this chapter, we aim at studying the relativistic reflection spectra of GX 339–4 during its 2021 outburst with *Insight*–HXMT data. In Sec. 2.2, we describe the data reduction process. The spectral fitting results are presented in Sec. 2.3. We discuss the results in Sec. 2.4.

2.2 Observation and data reduction

The *Insight*–HXMT satellite monitored the 2021 outburst of GX 339–4 with observations conducted nearly every day (refer to Fig. 2-1). Commencing from March 25, 2021, the source underwent a rapid transition from the hard state to the soft state within approximately one week. Unfortunately, the soft-to-hard transition, expected to occur at a lower luminosity, was not captured due to the high background levels of the *Insight*–HXMT. This study aims to examine the system’s evolution during the state transition. Therefore, we have selected observation data from the *Insight*–HXMT during this transition period and are investigating their broadband energy spectra. Further details regarding the chosen *Insight*–HXMT observations are provided in the appendix.

The low-energy (LE), medium-energy (ME) and high-energy (HE) detectors on-board *Insight*–HXMT cover the energy range of 1–250 keV^[147–150]. The energy spectra are extracted following the HXMT Data Reduction Guide v2.04^① and using the software HXMTDAS v2.04. The background spectra are estimated using the scripts `hebkmap`, `mebkmap` and `lebkmap`^[151–153]. As indicated in Tab. 2-3, short exposures on the same day are merged to increase the signal to noise ratio. Before merging the data, we first check the lightcurve and hardness ratio and confirm that there are no significant flares or dips. In the end, we obtain energy spectra for seven epochs. The spectra are

^① The guide can be found from here: <http://hxmtweb.ihep.ac.cn/SoftDoc/496.jhtml>. We follow the extraction approach provided here: <https://code.ihep.ac.cn/jldirac/insight-hxmt-code-collection/-/tree/master/version2.04>.

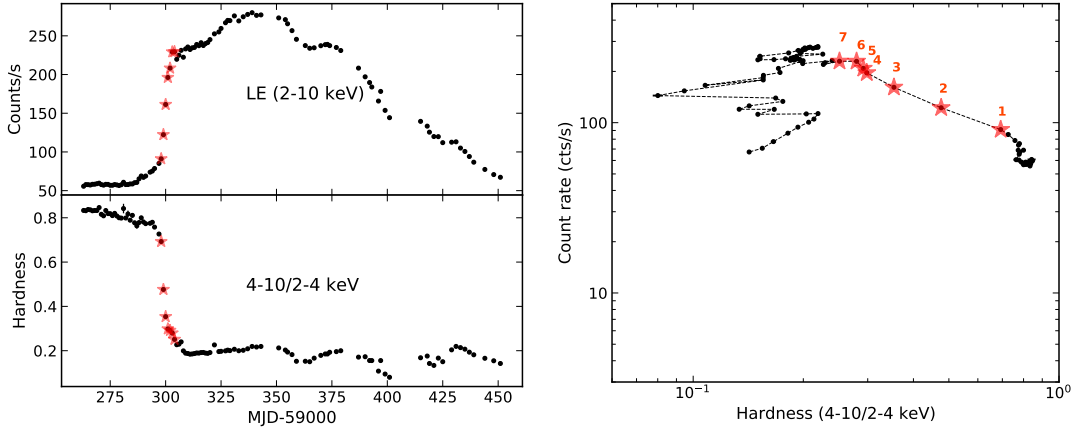


Figure 2-1 (left): The observation log of GX 339–4 from *Insight*–HXMT Low Energy (LE) instruments. The hardness is defined as the ratio between count rates in 4–10 keV and 2–4 keV. (right): The hardness intensity diagram of GX 339–4 from *Insight*–HXMT. Each point represents data from one day and is marked with the epoch number. The red color denotes the observations analyzed in this work. Figures adapted from Liu et al. 2023a^[4].

then binned using `ft grouppha` to ensure a minimal signal to noise ratio of 25 before fitting them to physical models. We use data in 2–10 keV, 10–25 keV and 30–100 keV bands for LE, ME and HE respectively.

2.3 Spectral analysis

Spectral fittings are conducted with XSPEC v12.11.1^[154]. We implement element abundances of Wilm et al. 2000^[155] for galactic absorption and cross-sections of Verner et al. 1996^[156]. χ^2 statistics are used to find the best-fit values and uncertainties (at 90% confidence level unless otherwise specified) of parameters.

2.3.1 Relativistic reflection features

As the initial step, we fit the seven spectra simultaneously using a simple absorbed continuum model which consists of a multicolor disk component (`diskbb`^[157]), a power-law component with a high energy cutoff (`cutoffpl`) and a Galactic absorption model (`tbabs`^[155]). In XSPEC notation, the model reads as `constant * tbabs * (diskbb + cutoffpl)`. The `constant` is required to fit the cross-normalization between the three instruments onboard *Insight*–HXMT. The column density (N_H) of the `tbabs` is tied across all spectra.

The ratios between the data and the best-fit models for the seven spectra are de-

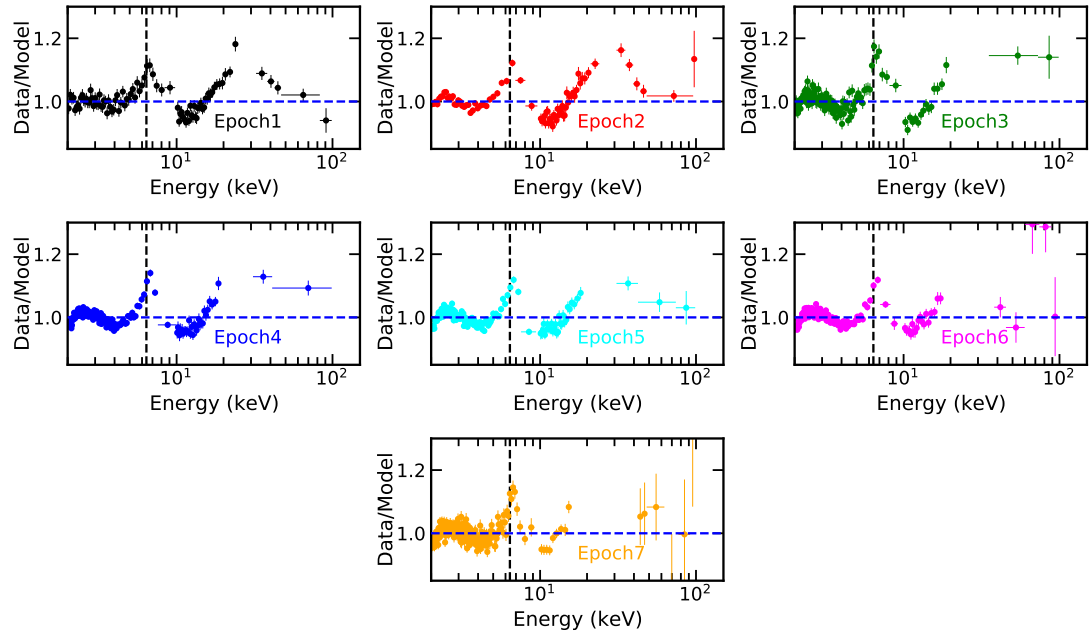


Figure 2-2 Data to model ratios for an absorbed continuum model `tbabs*(diskbb+cutoffpl)` for the seven epochs. The vertical line marks the position of 6.4 keV. Data are rebinned for visual clarity.

picted in Fig. 2-2, aiding in the identification of any missing model components. Notably, common features observed in Fig. 2-2 include a broad excess around 6–7 keV and a hump around 30 keV. These characteristics are frequently observed in the X-ray spectra of black hole X-ray binaries^[6,20,158] and can be explained by the reflection of corona emission by the optically thick accretion disk^[159] (see Sec. 1.4). The vertical dashed line in Fig. 2-2 indicates the position of the neutral iron K α fluorescent line (6.4 keV). The broad emission profile around this line arises from relativistically skewed iron K lines. Furthermore, the “Compton hump” around 30 keV results from the electron downscattering of high-energy photons and photoelectric absorption on the disk^[105].

2.3.2 Spectral fitting with reflection models

To fit the relativistic reflection features, we implement the widely used reflection model `relxill v1.4.3`^[114]. The full model in XSPEC is `constant * tbabs * (diskbb + relxill + cutoffpl)` (Model 1). With this model, we can measure parameters of the system, such as the black hole spin (a_*), the inclination angle (i) of the inner accretion disk with respect to our line of sight and the size of the disk inner edge (R_{in}). The seven spectra are fitted simultaneously. The column

density of the Galactic absorption (N_{H}), the black hole spin, the inclination angle and the iron abundance of the system should not change on the short timescale we are seeing. Therefore, these parameters are tied across all seven spectra during the spectral fitting. The reflection fraction parameter of `relxill` is set to -1 to make the model returns only the reflection component. The outer radius of the disk R_{out} is fixed at $400 R_g$ (where $R_g = GM/c^2$ is the gravitational radius, M is the black hole mass).

Lamppost geometry

The emissivity profile, which is the radial dependence of the intensity of the reflected emission, is a crucial component of the reflection model. In principle, if the corona geometry is known, the emissivity profile can be self-consistently calculated. Hence, we incorporate the `relxilllp` model (Model 1A), one of the models in the `relxill` package. This model assumes a lamppost geometry^[60], wherein the corona exists as a point source above the black hole at a certain height (h). Demonstrating a favorable fit with $\chi^2/\text{d.o.f}=3697.6/3384$, the model's best-fit values are presented in Tab. 2-1. The spectral components and residuals of the best-fit model are plotted in Fig. 2-3, where significant unresolved features are not seen. With this model, we can conduct fittings with both the spin parameter and the inner disk radius left free. Typically, there exists a strong degeneracy between these two parameters^[60]. However, our data have the potential to break this degeneracy as the disk extends very close to the ISCO^[160]. If we set the spin parameter at the maximum value allowed by the model ($a_* = 0.998$), R_{in} remains unconstrained for Epoch 1 but falls below twice the ISCO for Epoch 4 to 7 ($\chi^2/\text{d.o.f}=3697.6/3385$). Furthermore, if we fix R_{in} at the ISCO for all epochs, the spin is measured to be 0.93 ± 0.01 ($\chi^2/\text{d.o.f}=3704.0/3391$).

Broken power-law emissivity

Another approach commonly employed to treat the emissivity profile is to phenomenologically fit it with a broken power-law (i.e., $\epsilon \propto 1/r^{q_{\text{in}}}$ for $R_{\text{in}} < r < R_{\text{br}}$ and $\epsilon \propto 1/r^{q_{\text{out}}}$ for $R_{\text{br}} < r < R_{\text{out}}$ where R_{br} represents the breaking radius). We explore both the power-law emissivity ($q_{\text{in}} = q_{\text{out}}$) and the broken power-law emissivity (implemented with the model `relxill`) to seek a more suitable description of the data. In the latter scenario, we set the outer index at a fixed value of 3 ($q_{\text{out}} = 3$), consistent

Table 2-1 Best-fit values with the lamppost geometry (Model 1A).

Component	Parameter	Epoch 1	Epoch 2	Epoch 3	Epoch 4	Epoch 5	Epoch 6	Epoch 7
tbabs	N_{H} (10^{22} cm $^{-2}$)	$0.50^{+0.03}_{-0.03}$	$0.548^{+0.014}_{-0.01}$	$0.656^{+0.008}_{-0.008}$	$0.725^{+0.011}_{-0.008}$	$0.725^{+0.01}_{-0.009}$	$0.766^{+0.006}_{-0.007}$	$0.757^{+0.011}_{-0.007}$
diskbb	T_{in} (keV)	$0.50^{+0.03}_{-0.03}$	$0.548^{+0.014}_{-0.01}$	$0.656^{+0.008}_{-0.008}$	$0.725^{+0.011}_{-0.008}$	$0.725^{+0.01}_{-0.009}$	$0.766^{+0.006}_{-0.007}$	$0.757^{+0.011}_{-0.007}$
relxilllp	a_*	3.5^{+P}_{-P}	$3.1^{+0.5}_{-0.5}$	2.0^{+4}_{-P}	$2.20^{+0.21}_{-0.1}$	$2.06^{+0.18}_{-P}$	$2.35^{+0.28}_{-0.29}$	$2.03^{+0.24}_{-P}$
	$h(R_g)$							
	Incl				$42.0^{+1.3}_{-1.4}$			
	A_{Fe} (solar)				$10.0^{+P}_{-0.6}$			
	R_{in} (ISCO)	70^{+P}_{-P}	$1.4^{+0.7}_{-P}$	$3.2^{+1.2}_{-1.9}$	$1.56^{+0.08}_{-0.07}$	$1.44^{+0.08}_{-0.09}$	$1.62^{+0.12}_{-0.13}$	$1.6^{+0.1}_{-0.1}$
	$\log(\xi)$	$4.29^{+0.06}_{-0.06}$	$3.89^{+0.17}_{-0.23}$	$4.51^{+0.06}_{-0.11}$	$3.71^{+0.09}_{-0.08}$	$4.06^{+0.22}_{-0.2}$	$4.14^{+0.2}_{-0.19}$	$3.79^{+0.13}_{-0.12}$
cutoffpl	Γ	$1.696^{+0.018}_{-0.013}$	$2.087^{+0.028}_{-0.019}$	$2.260^{+0.06}_{-0.019}$	$2.460^{+0.021}_{-0.03}$	$2.451^{+0.024}_{-0.019}$	$2.511^{+0.028}_{-0.024}$	$2.55^{+0.1}_{-0.08}$
	E_{cut} (keV)	150^{+20}_{-20}	160^{+40}_{-20}	> 400	> 400	> 330	> 410	130^{+50}_{-60}
cflux	(10^{-8} erg cm $^{-2}$ s $^{-1}$)							
	F_{diskbb}	$0.23^{+0.03}_{-0.03}$	$0.552^{+0.019}_{-0.028}$	$0.935^{+0.019}_{-0.023}$	$1.314^{+0.03}_{-0.017}$	$1.355^{+0.021}_{-0.025}$	$1.603^{+0.019}_{-0.022}$	$1.85^{+0.03}_{-0.05}$
	$F_{\text{relxilllp}}$	$0.77^{+0.10}_{-0.06}$	$0.74^{+0.08}_{-0.08}$	$1.43^{+0.13}_{-0.11}$	$1.52^{+0.18}_{-0.12}$	$1.52^{+0.2}_{-0.12}$	$1.64^{+0.19}_{-0.14}$	$1.9^{+1.1}_{-0.5}$
	F_{cutoffpl}	$0.71^{+0.05}_{-0.07}$	$1.28^{+0.13}_{-0.15}$	$0.94^{+0.10}_{-0.20}$	$2.04^{+0.13}_{-0.21}$	$1.77^{+0.1}_{-0.12}$	$1.90^{+0.09}_{-0.27}$	$1.6^{+0.4}_{-0.3}$
	$L_{0.1-100\text{keV}}/L_{\text{Edd}}$ (%)	10.9	16.4	21.1	31.1	29.6	32.8	34.1
constant	ME/LE						$1.023^{+0.013}_{-0.014}$	
	HE/LE						$1.110^{+0.019}_{-0.023}$	
	$\chi^2/\text{d.o.f}$						3697.6/3384	

Note. Best-fit parameters for the model `tbabs*(diskbb+relxilllp+cutoffpl)`. Parameters with * are fixed during the fit and the symbol *P* denotes the upper or lower boundary. Parameters that are only shown for Epoch 4 are tied across all observations. The flux of each spectral components are calculated in the 0.1–100 keV band using the `cflux` model. The absorption corrected X-ray flux ($L_{0.1-100\text{keV}}$) is calculated with the `flux` command in `XSPEC`.

with the value predicted by the Newtonian limit for a compact corona. Additionally, for the initial three epochs, the inner index (q_{in}) and the breaking radius (R_{br}) cannot be constrained by the data. We fix q_{in} at 3 for these datasets. The broken power-law emissivity yields improved statistics ($\chi^2/\nu = 3673.1/3383$), with the χ^2 reduced by 13 with 2 additional free parameters. The best-fit values for the broken power-law emissivity (Model 1B) are presented in Tab. 2-4.

High-density reflection

The disk density (n_e) in the aforementioned models is fixed at 10^{15} cm^{-3} . While this value might be suitable for massive black holes, XRBs with stellar-mass black holes are known to exhibit higher densities^[6–7]. Therefore, we employ the `relxill1D` model (assuming a broken power-law emissivity, Model 1C) where $\log(n_e)$ is permitted to vary between 15 and 19^[113]. The best-fit parameters are outlined in Tab. 2-5. Compared to the previous model, the high-density model marginally enhances the χ^2 by 9 with 7 additional degrees of freedom and yields consistent constraints on the spin parameter and the inclination angle. Specifically, five out of the seven observations necessitate a higher density than 10^{15} cm^{-3} . The measurements of the ionization parameter are consistently lower. This outcome is anticipated as a higher density results in stronger soft X-ray emission, similar to the effect of a higher ionization parameter.

The Comptonized continuum

The models tested above yield satisfactory fits to the data. However, the column density of the `tbabs` component appears to be higher than previously reported in other spectral analyses (e.g., $7.7 \pm 0.2 \times 10^{21} \text{ cm}^{-2}$ in Parker et al. 2016^[143], using the same versions of abundances and cross-sections). This inconsistency is reconciled by substituting the `cutofffpl` model with a physically motivated Comptonization model, `nth-comp`^[55–56]. Furthermore, the reflection component is replaced with the corresponding variant, `relxillcp` (Model 2). We link the seed photon temperature for the `nth-comp` model to the T_{in} parameter in `diskbb`. The best-fit parameters for this model are shown in Tab. 2-6. Compared to `relxill`, this model improves the statistics by $\Delta\chi^2 = 64$ while reducing the column density of Galactic absorption to $7.3 \pm 0.6 \times 10^{21} \text{ cm}^{-2}$. This discrepancy arises because the Comptonization model incorporates cutoffs

at both low and high energy ends, rendering the X-ray luminosity estimates from the Comptonization model more realistic than those from the `cutoffpl` model. Additionally, it's noteworthy that our data are insufficient to accurately constrain the coronal temperature (or the high energy cutoff).

Distant reflector

The spectra of GX 339–4 might require a distant reflection component to accommodate a potential narrow-line feature^[22,145]. To explore this possibility, we add Model 1A with a `xillver` component^[106,161]. The relativistic reflection model assumes a broken power-law emissivity profile. We fix the ionization parameter of this distant reflection component at $\log(\xi) = 0$, while linking the other parameters of the distant reflector to their counterparts in the relativistic reflection component. Incorporating this component marginally improves the χ^2 by only 10 with 7 additional free parameters.

To evaluate whether our data quality enables the detection of a distant reflector, we conduct a simulation involving 1000 spectra. These spectra incorporate a model comprising a distant reflection component. We utilize the response files, exposure time, and model parameters from our Epoch 5, characterized by the longest exposure. The flux (0.1–100 keV) of the distant reflection component is set to 2%^[145] of the relativistic component. Subsequently, we perform fittings on the spectra using two models: one without the distant reflection and the other incorporating it. Remarkably, the latter model consistently yields better statistics with $\Delta\chi^2 > 50$ and one more degree of freedom, indicating the potential detectability of the distant component if present. Thus, we infer that, for the observation with the lengthiest exposure time, the distant reflection component can be identified if its flux exceeds 2% of the relativistic component. The absence of detection of the distant component in our analysis might be attributed to its flux being below the limit imposed by our data quality. Similarly, in^[6], no distant reflection is deemed necessary for the intermediate state of GX 339–4.

Comptonization of the reflection component

The power-law emission originates from the inverse Compton scattering of disk photons by the hot electrons (although alternative explanations have been proposed^[162–163]). It is notable that a portion of the reflected emission should also inter-

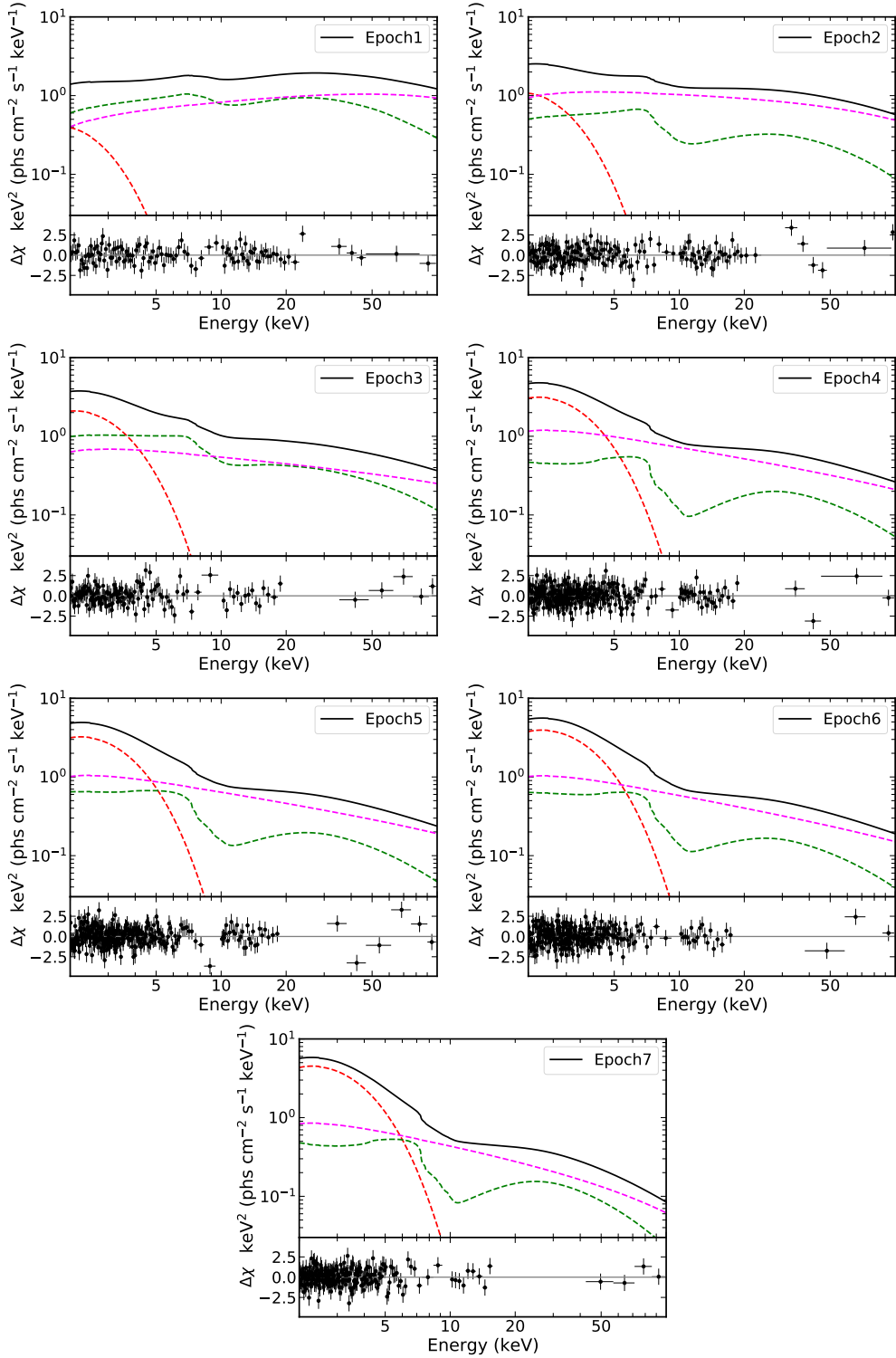


Figure 2-3 The best-fit model components for the seven epochs and the corresponding residuals with the model `tbabs*(diskbb+relxilllp+cutoffpl)`. The black solid line represents the total model. The magenta, red and green dashed lines are for the corona emission, the disk component and the reflected component respectively.

cept the corona and undergoes Comptonization. Therefore, a consistent model should incorporate the Comptonized reflection spectrum^[22,164]. We explore this scenario using the Compton scattering kernel `simplcut`^[164]. The complete model is denoted as `tbabs*simplcut*(diskbb+relxillcp)` (Model 3). The photon index (Γ) and electron temperature (kT_e) of `simplcut` are linked to the corresponding parameters in `relxillcp`. Additionally, the Compton scattering kernel introduces two more parameters: the reflection fraction R_f and the scattered fraction f_{sc} . We set the reflection fraction parameter to the flux ratio between the reflection and power-law components in the 20–40 keV band derived from Model 2 and allow the scattered fraction parameter to vary freely.

With this model, we assume an equal fraction of the disk photons and the reflected photons are scattered by the corona. The best-fit parameters are shown in Tab. 2–7. We observe that including the effect of Comptonization of the disk and reflection photons does not significantly alter the measurements of parameters such as T_{in} , Γ , and R_{in} . Similarly, the measurements of the spin and inclination parameters remain unaffected. However, the scattered fraction decreases from 0.12 to 0.07, potentially indicating changes in the disk-corona system during the transition.

The `refhidden` model

In the `relxill` model, the ionization balance on the disk is calculated using only the incident corona emission. However, in reality, we would expect that the thermal emission from the disk can also affect the ionization state. This is particularly important in XRBs since the disk temperature of XRBs can be very high (around 1 keV), and the thermal emission can dominate the X-ray spectra. In some cases, the disk emission has been found to contribute significantly to the ionization state, and models assuming the primary continuum to be only a blackbody have been successful in fitting the data^[165–167]. However, in the intermediate states, the strength of the disk and power-law components are comparable (see Fig. 2–3 and Tab. 2–1). Consequently, considering only one of the components (disk or corona) to ionize the disk atmosphere is not appropriate.

Therefore, we implement the `refhidden` model, which is specifically designed for accreting stellar-mass black holes^[168]. In this model, the disk atmosphere is ionized

by the combination of a power-law component from above and a blackbody from below. It is important to note that here the blackbody is assumed to be single-temperature, which differs from the multi-temperature disk blackbody component. The model also includes the effect of Comptonization in the accretion disk. The full model reads as `tbabs * simplcut * relconv * refhidden` (Model 4). The broadening kernel `relconv`^[126] is required to account for the relativistic effects. Since the disk thermal emission is already incorporated in `refhidden`, there is no need to add an additional disk component. The parameters in the `refhidden` model include: the hydrogen number density on the disk (H_{den}), the temperature of the blackbody from the disk (kT_{bb}), the flux ratio between the power-law and blackbody components, and the power-law index Γ (Illum/BB). We link Γ of the `refhidden` model to the same parameter in `simplcut`. To better constrain the evolution of other parameters, we fix the black hole spin at 0.998 for the fitting.

The model provides an acceptable fit ($\chi^2/\nu = 3788.8/3386$), and the best-fit parameters are shown in Tab. 2-8. The variations of spectral parameters from this model during the state transition are shown in the right panels of Fig. 2-4 and can be compared with those from Model 1A in the left panels. The `refhidden` model gives a blackbody temperature (kT_{bb}) that is systematically lower than the T_{in} found in other fits with the `diskbb` model. This is within expectation because the temperature in `refhidden` is the effective mid-plane temperature of the disk. The disk surface temperature would be higher after including the effect of color correction (see the discussion in Reis et al. 2008^[13]). Moreover, `diskbb` assumes a multi-temperature blackbody while a single temperature is used in `refhidden`. This is probably also affecting the value of the scattering fraction (f_{sc}) of `simplcut`, but the decreasing trend of this parameter along with the transition is retained. The number density of hydrogen is higher at the early phase of the transition (the first two epochs). One parameter of `refhidden` that clearly changes through the transition is the flux ratio between the illuminating power-law and the blackbody from the disk mid-plane.

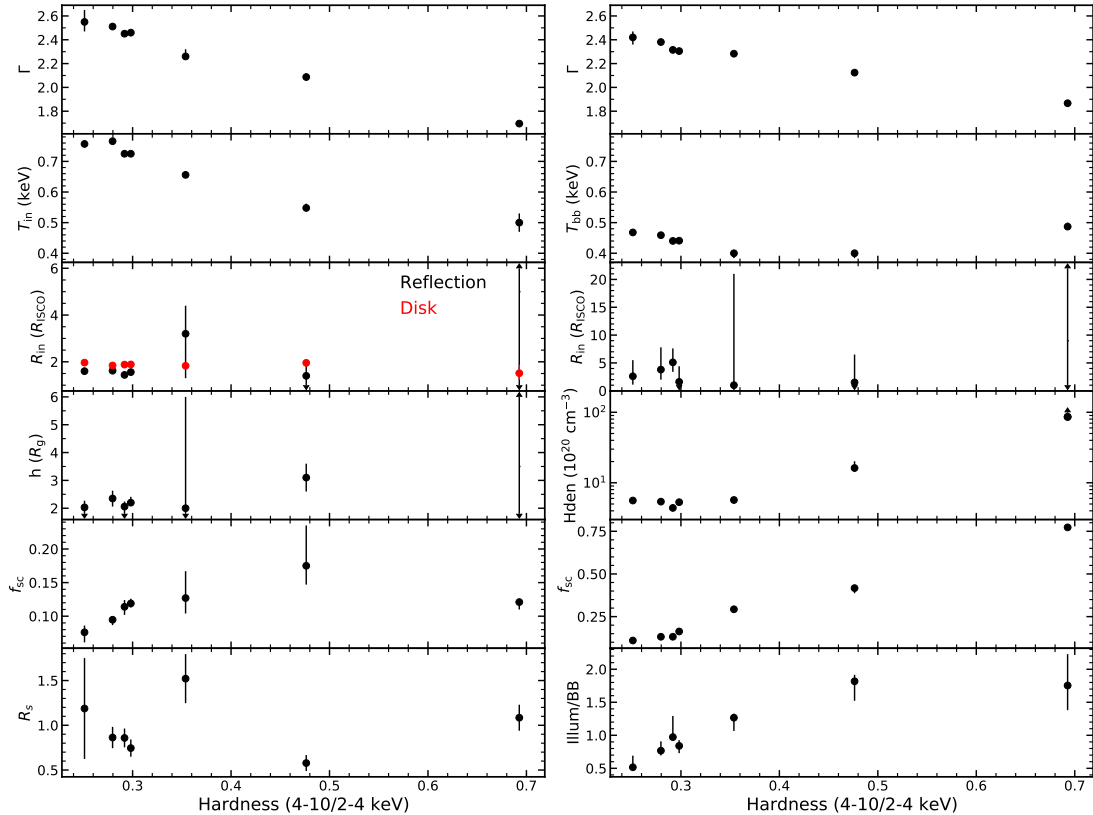


Figure 2-4 The evolution of spectral parameters along with X-ray hardness of the source. The definition of the hardness is the same as in Fig. 2-1. Lower and upper limits are marked with arrows. Panels in the left show the parameters from Model 1A except the scattering fraction (f_{sc} , from Model 3). In the third panel in the left, the red color represents estimation of the inner disk radius from the normalization parameter of `diskbb` of Model 3 and the size of the ISCO is chosen for a black hole with $a_* = 0.95$. The reflection strength (R_s) is defined as the ratio between the observed flux of the reflected and the direct corona emission in the 0.1–100 keV band. Parameters from Model 4 with the `refhidden` model are shown in the right panels.

2.4 Discussion

2.4.1 Evolution of the disc-corona system

During the transition from the hard to the soft state, GX 339–4 exhibits a progressive increase in X-ray brightness. Fig. 2-4 illustrates how the spectral parameters change with the X-ray hardness of the source. The state transition is marked by a decrease in hardness. This phenomenon appears to correlate with a steepening of the corona emission component, as evidenced by the evolution of the photon index (Γ) from 1.7 to 2.5 (refer to the top panel of Fig. 2-4). Concurrently, the X-ray luminosity rises from 10% to 20% of the Eddington limit, assuming a black hole mass of $10 M_{\odot}$ and a distance of 8 kpc (see Tab. 2-6). There is a notable trend of the inner disk temperature increasing from 0.5 to 0.76 keV. Additionally, the contribution of the disk component (in the 0.1–100 keV band) rises from 13% to 35%. This increase in soft cooling photons might account for the softening of the corona emission^[169].

Regarding the coronal temperature (kT_e), the data present challenges in constraining this parameter. Only lower limits are found for Epoch 2–7 (refer to Tab. 2-6), although these lower limits still exceed the measurement of Epoch 1. This subtle trend of an increasing coronal temperature during the state transition aligns with prior broadband spectral analyses of GX 339–4^[145,170] and other systems^[171]. It diverges from the trend of a decreasing coronal temperature with luminosity in the hard state^[20], believed to be a consequence of stronger cooling by the seed photons. The state transition dynamics might entail a reduction in optical depth^[169,172], leading to diminished scattering between the seed photons and corona electrons and subsequently increase the coronal temperature. Note that this rise in coronal temperature could be limited by the run-away electron-positron pair production process within the corona^[54].

Another parameter of significant interest is the inner radius of the accretion disk (R_{in}). Previous reflection-based investigations have already studied the accretion geometry of GX 339–4 during the hard state. In the study by Garcia et al. 2015^[20], which examined a luminosity range spanning from 1.7% to 17% of the Eddington limit (L_{Edd}) using data from *RXTE/PCA*, R_{in} was determined to be close to the ISCO ($< 5R_{\text{ISCO}}$). Conversely,^[19], studying similar luminosity levels with *XMM-Newton* data in timing mode, observed substantial disk truncation (see also Ref^[21]). This discrepancy might be attributed to the intricate pile-up effect in timing mode, which can impact the iron K

line^[173]. Investigations into luminosity levels below 1% of the Eddington luminosity have also been conducted using reflection models^[16,18,22,138]. These studies suggest that R_{in} tends to decrease with increasing luminosity, reaching approximately $20 R_g$ when the luminosity exceeds 1% of the Eddington limit (see Fig. 6 of Garcia et al. 2016^[174]).

Our investigation delves into the reflection spectra of GX 339–4 throughout the hard-to-soft transition, encompassing the luminosity spectrum from 10% to 20% L_{Edd} . The outcomes reveal that R_{in} lacks constraint in Epoch 1, likely owing to the limited statistics of the data, given that Epoch 1 has the shortest exposure time among all epochs. Subsequent to Epoch 2, R_{in} aligns with the ISCO in certain models and remains several times below the ISCO in others, indicative of the relative stability of the inner disk edge across the state transition. Additionally, the inner disc radius can be approximated using the normalization parameter of the `diskbb` model^[175]. Using values from Model 3, which considers both transmitted and scattered disk photons, the findings, depicted in Fig. 2-4 in red, presume a distance of 8 kpc, a black hole mass of $10 M_\odot$, an inclination of 40 deg, a color correction factor of 1.7, and a relativistic correction factor of 0.412. Once more, this illustrates the inner disk radius's constancy throughout the transition, although the absolute values warrant caution due to systematic uncertainties in mass, distance, and color correction assumptions.

Similar findings have been reported by Sridhar et al. 2020^[145], who studied the 2002–2003 and 2004–2005 outbursts of GX 339–4 employing data from *RXTE/PCA*. In their study, with the black hole spin set at 0.998, R_{in} was observed to approach proximity to the ISCO at the outset of the transition for both outbursts, despite the transition luminosity varying by a factor of 3. Additionally, the stability of the disk throughout the state transition has been observed in other systems as well, such as XTE J1550–564^[176] and MAXI J1820+070^[177].

The corona height exhibits a similar trend to R_{in} , remaining unconstrained in Epoch 1 and staying close to the black hole ($< 6 R_g$) in subsequent observations. When the primary source is in close proximity to the black hole, the light-bending effect causes its radiation to be concentrated towards the innermost region of the accretion disk^[60]. This phenomenon aligns with our findings, particularly evident with the broken power-law emissivity, yielding a steep inner emissivity index (see Tab. 2-4). Additionally, we

introduce an empirical reflection strength parameter (R_s), representing the ratio between the reflected and the power-law flux in the 0.1–100 keV band. This is similar to the reflection fraction parameter (R_f), which indicates the ratio between the corona intensity illuminating the disk and reaching the observer^[178]. Variations in the reflection strength may signify changes in the disk-corona system^[179]. The lowest panel on the left of Fig. 2-4 reveals no significant fluctuations in this parameter, aligning with the prediction of the stable inner disk radius.

We note that relativistic reflection analysis utilizing a single lamppost geometry may primarily probe the regions of the corona close to the black hole, as they predominantly contribute to the reflection emissivity see^[177]. In practice, two-lamppost reflection models have been used to mimic a vertically extended corona^[180]. The upper lamppost could potentially account for the narrow cores observed in the iron band, often attributed to a distant reflector^[174]. We do not explore further in this aspect since our data does not require the presence of a narrow iron line.

The scattering fraction parameter (f_{sc}) within `simplcut` is intricately linked to the geometry of the disk-corona system and the optical depth of the corona. Examining Fig. 2-4, we observe that, except for Epoch 1, f_{sc} derived from Model 3 exhibits a tentative decreasing trend throughout the transition, albeit with considerable uncertainties. This trend becomes more apparent in Model 4 (refer to the right panel of Fig. 2-4). In the fit employing `refhidden`, we see that the flux ratio between the illuminating power-law component and the blackbody component from the disk (Illum/BB) decreases notably by a factor of 3 from Epoch 1 to Epoch 7. Meanwhile, the temperature of the disk mid-plane (T_{bb}) undergoes only marginal changes within a narrow range (0.4–0.5 keV). Considering these patterns of variation and the stable nature of the inner disk radius, we posit that the state transition is more likely linked to the properties of the corona rather than the inner edge of the disk. This proposition finds support in recent studies on the reverberation lag of black hole transients^[2], where the elongation of the lag across the hard-to-soft transition is interpreted as indicative of a vertically expanding jet. Similar corona behaviors have also been observed in other sources through the analysis of lag spectra with Comptonization models^[171,181–184].

The ionization parameter ξ is defined as $\xi = L/nr^2$ where L is the ionizing luminosity, n is the density and r is the distance to the illuminating source. We do not observe

significant variations in the ionization parameter. This aligns with our expectations, considering that the source luminosity undergoes only a twofold change. If the density and distance remain constant, any variation in the ionization parameter would likely be comparable to the uncertainties in its fitting. Across all seven epochs, a high ionization parameter ($\log(\xi) > 3.6$) consistently emerges as necessary to adequately fit the reflection spectra. This high ionization state remains consistent with prior investigations of GX 339–4 at comparable luminosity levels^[145]. With the measured ionization parameter and the known source luminosity, we can calculate the disk density and compare it with our measurements (e.g. Tab. 2–5). Using the Equ. 9 of Zdziarski et al. 2020^[185], we calculate a disk density of $n_{\text{cal}} \sim 10^{22} \text{ cm}^{-3}$ with the averaged illuminating flux and ionization parameter in Tab. 2–5. This value is higher than what we measured with the `relxillD` model and exceeds the upper limit (10^{19} cm^{-3})^① allowed by the model. A similar discrepancy has been noted in other intermediate data sets of GX 339–4^[185]. This inconsistency could potentially be rationalized if the inner disk radius were 30 times larger than the ISCO, although this explanation would conflict with the presence of the broad iron line observed in our data. Further advancements in developing reflection models would be instrumental in gaining a deeper understanding of this issue.

2.4.2 Measurement of system parameters

By simultaneously fitting the seven spectra using relativistic reflection models, we are able to determine the black hole spin parameter of GX 339–4. Assuming a lamppost geometry, we obtain a constraint of $a_* > 0.95$. However, when employing a broken power-law emissivity in `relxill`, which yields the lowest χ^2 among all models, we obtain a constraint of $a_* > 0.86$ (see Fig. 2–5). This measurement reaffirms the high spin nature of the black hole in GX 339–4, consistent with previous studies conducted during both the hard^[13,20,186] and soft states^[143].

Previous reflection-based analyses have constrained the disk inclination angle of GX 339–4 to be between 30° and 60° ^[20,143]. Additionally, through the study of the near-infrared light curve of GX 339–4, Heida et al. 2017^[187] determined the orbital inclination to fall within 37° and 78° . A more recent study by Ref^[140], which incorpo-

^① Note that in the latest version of `relxill`, which was released after writing of this paper, the density is allowed to vary up to 10^{20} cm^{-3} . See <http://www.sternwarte.uni-erlangen.de/~dauser/research/relxill/>.

rated evolutionary models for the donor, updated the inclination to approximately 40°–60°. Our measurement of the inclination angle of the inner accretion disk ranges from 35 to 43 degrees, consistent with previous studies utilizing different methodologies. We also observe slight variations in the constraint on the inclination when considering different treatments of the emissivity profile, with values of $42.0^{+1.3}_{-1.4}$ for the lamppost geometry and $36.6^{+1.5}_{-1.3}$ for the broken power-law emissivity (see Fig. 2-5). These differences in parameter measurements due to systematic uncertainties are anticipated in reflection spectroscopy^[188–189], stemming from our incomplete understanding of the system. It is essential to consider these systematic uncertainties when reporting parameter measurements obtained with disk reflection models. Other sources of systematic uncertainties include model simplifications (e.g., discussed in Tripathi et al. 2021^[190]) or instrumental effects (see the review in Bambi et al. 2021^[69]).

We consistently observe a very high iron abundance in our analyses, typically approaching ten times the solar value. However, it is important to note that this measurement may not accurately reflect the true abundance of the system. The issue of a super-solar iron abundance in relativistic reflection modeling is well known^[191–193]. Studies have demonstrated that allowing the electron density (n_e) of the disk to exceed the assumed standard value in the reflection model ($\log(n_e/\text{cm}^{-3}) = 15$) could potentially alleviate the high iron abundance^[6,8]. However, even with a higher-density model, we still observe a very high iron abundance ($A_{\text{Fe}} > 8.6$). Another approach to address this high iron abundance issue involves permitting different photon indices for the directly observed primary emission and the reflection spectrum^[144]. However, this adjustment does not substantially lower the iron abundance, with $A_{\text{Fe}} > 9.0$ still observed. Note that the structure of the corona may be more complex than the simple configuration of two uniform plasma clouds^[194]. Additionally, previous studies have suggested that neglecting the effects of returning radiation could impact the measurement of the iron abundance, although more recent investigations have not found strong evidence for this effect^[195–197]. Alternatively, the possibility exists that the high iron abundance is genuine and is caused by radiative levitation of metal ions in the inner regions of the accretion disk^[198]. Further investigations and refinements in modeling techniques are needed to better understand and address this issue.

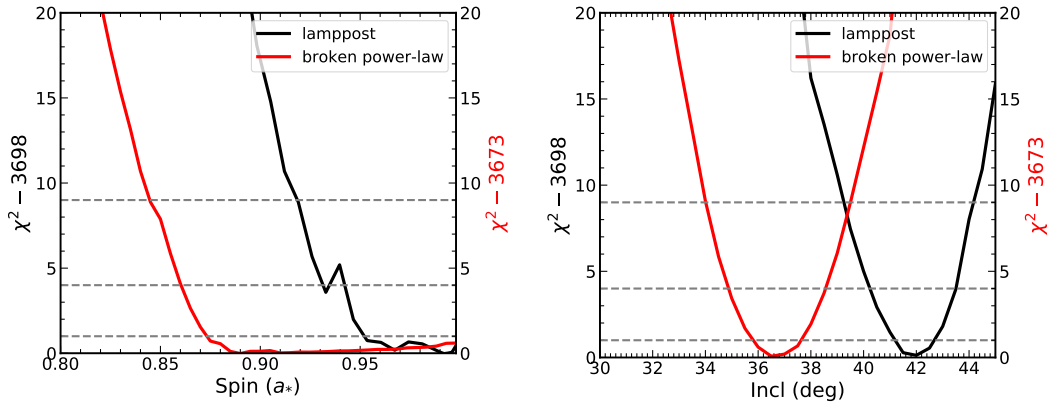


Figure 2-5 The χ^2 contours for the black hole spin and the inclination parameters for the lamppost geometry and broken power-law emissivity. The horizontal lines represent the 1σ , 2σ and 3σ confidence levels for a single parameter of interest.

2.5 Conclusion

In this work, we analyzed the broadband spectra (2–100 keV) of GX 339–4 during the bright state transition of its 2021 outburst observed by *Insight–HXMT*. Strong relativistic reflection features were found in the spectra, which allowed us to study the evolution of the disk-corona system during the transition. The main results are the following:

- The hard to soft transition is associated with a stronger contribution of the disk thermal component to the X-ray spectrum and a steepening of the power-law emission.
- The inner disk radius stays close to the ISCO during the transition. This is even true when we consider a reflection model that assumes the ionizing continuum to be a combination of the corona emission from above and a blackbody emission from below.
- If assuming a lamppost geometry, the measured corona height is always close to the black hole.
- The scattering fraction, which is the fraction of the disk photons that are scattered by the hot corona, decreases along with the transition.
- The data provide constraint on the black hole spin ($a_* > 0.86$) and the inclination parameter ($i \approx 35^\circ$ – 43°) of the system.

Table 2-3 *Insight-HXMT* observations of GX 339–4 analyzed in this paper

Reference name	Date ¹	obsID	Exposure (ks)			Start time MJD	Stop time MJD
			LE	ME	HE		
Epoch 1	20210325	P030402403702	1.86	3.31	2.30	59298.012	59298.151
		P030402403703				59298.151	59298.289
Epoch 2	20210326	P030402403801	3.46	5.75	7.95	59299.602	59299.776
		P030402403802				59299.776	59299.909
		P030402403803				59299.909	59300.003
Epoch 3	20210327	P030402403901	2.40	3.86	3.88	59300.796	59300.923
		P030402403902				59300.923	59301.059
Epoch 4	20210328	P030402403903	7.25	12.9	13.2	59301.059	59301.204
		P030402403904				59301.204	59301.343
		P030402403905				59301.343	59301.498
		P030402403906				59301.498	59301.634
		P030402403907				59301.634	59301.794
		P030402403908				59301.794	59301.916
		P030402403909				59301.916	59302.052
Epoch 5	20210329	P030402403910	7.46	13.3	13.6	59302.052	59302.189
		P030402403911				59302.189	59302.347
		P030402403912				59302.347	59302.515
		P030402403913				59302.515	59302.648
		P030402403914				59302.648	59302.787
		P030402403915				59302.787	59302.961
		P030402403916				59302.961	59303.120
Epoch 6	20210330	P030402403917	5.63	11.2	11.4	59303.120	59303.260
		P030402403918				59303.260	59303.399
		P030402403919				59303.399	59303.551
		P030402403920				59303.551	59303.684
		P030402403921				59303.684	59303.816
		P030402403922				59303.816	59303.949
		P030402403923				59303.949	59304.081
Epoch 7	20210331	P030402403924	4.57	9.95	10.2	59304.081	59304.214
		P030402403925				59304.214	59304.346
		P030402403926				59304.346	59304.479
		P030402403927				59304.479	59304.611
		P030402403928				59304.611	59304.743
		P030402403929				59304.743	59304.876
		P030402403930				59304.876	59305.037

Note. (1) The observation date is presented in the form of yyyyymmdd.

Table 2-4 Best-fit values with a broken power-law emissivity with $q_{\text{out}} = 3$ (Model 1B).

Component	Parameter	Epoch 1	Epoch 2	Epoch 3	Epoch 4	Epoch 5	Epoch 6	Epoch 7
tbabs	N_{H} (10^{22} cm^{-2})				$0.99^{+0.05}_{-0.06}$			
diskbb	T_{in} (keV)	$0.50^{+0.04}_{-0.04}$	$0.540^{+0.013}_{-0.012}$	$0.658^{+0.009}_{-0.009}$	$0.718^{+0.008}_{-0.011}$	$0.726^{+0.01}_{-0.011}$	$0.765^{+0.009}_{-0.008}$	$0.752^{+0.011}_{-0.009}$
relxill	a^*	3^*	3^*	3^*	10^{+P}_{-3}	10^{+P}_{-4}	9^{+P}_{-4}	$7.4^{+P}_{-1.7}$
	q_{in}				3^{*}	$3.5^{+0.5}_{-0.3}$	$3.6^{+0.8}_{-0.3}$	$4.2^{+0.9}_{-0.9}$
	R_{br} (R_g)	–	–	–	$36.6^{+1.5}_{-1.3}$			
	Incl				$10.0^{+P}_{-1.1}$			
	A_{Fe} (solar)				$1.0^{+0.8}_{-P}$			
	R_{in} (ISCO)	40^{+P}_{-33}	$3.6^{+4.0}_{-1.6}$	$2.3^{+1.4}_{-0.6}$	$1.0^{+0.6}_{-P}$	$1.1^{+0.9}_{-P}$	$1.0^{+0.7}_{-P}$	
	$\log(\xi)$	$4.29^{+0.05}_{-0.1}$	$4.54^{+0.05}_{-0.07}$	$4.60^{+0.07}_{-0.1}$	$4.02^{+0.21}_{-0.15}$	$4.35^{+0.12}_{-0.22}$	$4.31^{+0.14}_{-0.16}$	$4.1^{+0.3}_{-0.3}$
cutoffpl	Γ	$1.701^{+0.029}_{-0.025}$	$2.054^{+0.017}_{-0.013}$	$2.27^{+0.04}_{-0.06}$	$2.42^{+0.04}_{-0.04}$	$2.42^{+0.03}_{-0.04}$	$2.504^{+0.027}_{-0.027}$	$2.48^{+0.15}_{-0.1}$
	E_{cut} (keV)	140^{+30}_{-20}	> 450	> 400	> 220	> 330	> 410	130^{+70}_{-60}
cf lux								
	F_{diskbb}	$(10^{-8} \text{ erg cm}^{-2} \text{ s}^{-1})$	$0.219^{+0.03}_{-0.024}$	$0.556^{+0.020}_{-0.029}$	$0.93^{+0.04}_{-0.03}$	$1.310^{+0.023}_{-0.025}$	$1.360^{+0.03}_{-0.023}$	$1.597^{+0.022}_{-0.025}$
	F_{relxill}	$(10^{-8} \text{ erg cm}^{-2} \text{ s}^{-1})$	$0.73^{+0.16}_{-0.13}$	$1.26^{+0.07}_{-0.08}$	$1.44^{+0.17}_{-0.19}$	$1.38^{+0.14}_{-0.12}$	$1.45^{+0.11}_{-0.18}$	$1.62^{+0.2}_{-0.16}$
	F_{cutoffpl}	$(10^{-8} \text{ erg cm}^{-2} \text{ s}^{-1})$	$0.73^{+0.07}_{-0.20}$	$0.57^{+0.15}_{-0.12}$	$0.9^{+0.5}_{-0.3}$	$1.78^{+0.25}_{-0.24}$	$1.52^{+0.22}_{-0.25}$	$1.80^{+0.23}_{-0.24}$
constant	ME/LE					$1.035^{+0.014}_{-0.014}$		
	HE/LE					$1.158^{+0.018}_{-0.023}$		
	$\chi^2/\text{d.o.f}$					3673.1/3383		

Best-fit parameters for the model tbabs*(diskbb+relxill+cutoffpl). Parameters with * are fixed during the fit and the symbol P denotes the upper or lower boundary. Parameters that are only shown for Epoch 4 are tied across all observations.

Table 2-5 Best-fit values with `relxillD`.

Component	Parameter	Epoch 1	Epoch 2	Epoch 3	Epoch 4	Epoch 5	Epoch 6	Epoch 7
TBABS	N_{H} (10^{22} cm^{-2})				$0.98^{+0.04}_{-0.04}$			
DISKBB	T_{in} (keV)	$0.48^{+0.04}_{-0.04}$	$0.561^{+0.012}_{-0.014}$	$0.659^{+0.008}_{-0.008}$	$0.717^{+0.008}_{-0.01}$	$0.726^{+0.006}_{-0.007}$	$0.762^{+0.008}_{-0.007}$	$0.756^{+0.008}_{-0.006}$
RELXILL	a_*	3*	3*	3*	$7.3^{+P}_{-2.2}$	$7.3^{+P}_{-2.2}$	$7.2^{+P}_{-2.7}$	$6.5^{+P}_{-1.4}$
	q_{in}				3^{*}			
	q_{out}	-	-	-	$3.7^{+0.7}_{-0.4}$	$3.8^{+1.0}_{-0.6}$	$3.8^{+1.2}_{-0.6}$	$4.2^{+1.1}_{-0.8}$
	R_{br} (R_g)				$35.3^{+1.5}_{-1.5}$			
	Incl							
	A_{Fe}				> 8.6			
	R_{in} (ISCO)	11^{+P}_{-6}	$1.5^{+0.8}_{-P}$	$1.5^{+0.9}_{-P}$	$1.69^{+0.22}_{-0.23}$	$1.7^{+0.3}_{-0.4}$	$1.77^{+0.29}_{-0.26}$	$1.73^{+0.25}_{-0.18}$
	$\log(\xi)$	$3.97^{+0.17}_{-0.19}$	$3.69^{+0.17}_{-0.14}$	$4.2^{+0.1}_{-0.1}$	$3.49^{+0.13}_{-0.15}$	$4.00^{+0.22}_{-0.16}$	$4.0^{+0.2}_{-0.4}$	$4.01^{+0.27}_{-0.4}$
	$\log(n_e)$	16^{+P}_{-P}	$19.0^{+P}_{-0.6}$	$19.0^{+P}_{-0.6}$	$18.9^{+P}_{-0.9}$	$17.9^{+0.4}_{-1.3}$	$18.2^{+0.5}_{-0.5}$	$15.0^{+2.1}_{-P}$
CUTOFFPL	T	$1.724^{+0.026}_{-0.019}$	$2.042^{+0.024}_{-0.011}$	$2.166^{+0.04}_{-0.022}$	$2.369^{+0.019}_{-0.029}$	$2.387^{+0.023}_{-0.024}$	$2.43^{+0.04}_{-0.04}$	$2.54^{+0.09}_{-0.06}$
	E_{cut} (keV)	100^{+18}_{-14}	130^{+30}_{-20}	> 270	> 320	> 310	> 390	170^{+270}_{-90}
cflux								
	F_{diskbb} ($10^{-8} \text{ erg cm}^{-2} \text{ s}^{-1}$)	$0.22^{+0.04}_{-0.03}$	$0.556^{+0.027}_{-0.029}$	$0.965^{+0.017}_{-0.017}$	$1.346^{+0.028}_{-0.012}$	$1.390^{+0.027}_{-0.017}$	$1.634^{+0.029}_{-0.012}$	$1.82^{+0.05}_{-0.03}$
	F_{relxillD} ($10^{-8} \text{ erg cm}^{-2} \text{ s}^{-1}$)	$0.55^{+0.09}_{-0.08}$	$0.69^{+0.04}_{-0.1}$	$1.2^{+0.1}_{-0.1}$	$1.43^{+0.11}_{-0.1}$	$1.28^{+0.13}_{-0.11}$	$1.44^{+0.3}_{-0.3}$	$1.73^{+0.21}_{-0.22}$
	F_{cutoffpl} ($10^{-8} \text{ erg cm}^{-2} \text{ s}^{-1}$)	$1.00^{+0.09}_{-0.05}$	$1.21^{+0.11}_{-0.05}$	$0.75^{+0.07}_{-0.06}$	$1.54^{+0.1}_{-0.1}$	$1.53^{+0.08}_{-0.11}$	$1.51^{+0.11}_{-0.11}$	$1.6^{+0.6}_{-0.6}$
constant	ME/LE							
	HE/LE							
	$\chi^2/\text{d.o.f}$							
								3664.5/3376

Best-fit parameters for the model `tbbabs*(diskbb+relxillD+cutoffpl)`. Parameters with * are fixed during the fit and the symbol P denotes the upper or lower boundary. Parameters that are only shown for Epoch 4 are tied across all observations.

Table 2–6 Best-fit values with `relxillcp` (Model 2).

Component	Parameter	Epoch 1	Epoch 2	Epoch 3	Epoch 4	Epoch 5	Epoch 6	Epoch 7
tbabs	N_{H} (10^{22} cm^{-2})				$0.73^{+0.06}_{-0.06}$			
diskbb	T_{in} (keV)	$0.48^{+0.04}_{-0.04}$	$0.567^{+0.016}_{-0.016}$	$0.676^{+0.009}_{-0.01}$	$0.729^{+0.008}_{-0.009}$	$0.739^{+0.008}_{-0.009}$	$0.775^{+0.008}_{-0.009}$	$0.768^{+0.008}_{-0.009}$
relxillcp	a_*	3*	3*	3*	10^{+P}_{-3}	$8.0^{+P}_{-2.2}$	9^{+P}_{-4}	$7.3^{+P}_{-2.0}$
	q_{in}				3^{*}			
	q_{out}	-	-	-		$3.42^{+0.6}_{-0.12}$	$3.9^{+0.9}_{-0.7}$	$4.1^{+1.2}_{-0.9}$
	R_{br} (R_g)					$37.1^{+1.4}_{-1.3}$		
	Incl					$10.0^{+P}_{-0.3}$		
	A_{Fe}					$1.1^{+0.4}_{-0.7}$		
	R_{in} (ISCO)	> 12	$2.3^{+1.8}_{-0.8}$	$2.5^{+1.8}_{-1.1}$	$3.99^{+0.12}_{-0.15}$	$4.09^{+0.24}_{-0.18}$	$4.27^{+0.12}_{-0.12}$	$3.93^{+0.22}_{-0.3}$
	$\log(\xi)$	$4.56^{+0.05}_{-0.11}$	$4.46^{+0.13}_{-0.1}$	$4.66^{+P}_{-0.07}$				<i>Note.</i>
nthcomp	F	$1.773^{+0.04}_{-0.024}$	$2.092^{+0.019}_{-0.022}$	$2.215^{+0.03}_{-0.027}$	$2.339^{+0.02}_{-0.016}$	$2.360^{+0.022}_{-0.023}$	$2.391^{+0.024}_{-0.018}$	$2.42^{+0.12}_{-0.08}$
	kT_e (keV)	64^{+30}_{-21}	160^{+600}_{-70}	> 270	> 400	> 310	> 410	65^{+600}_{-30}
cflux								
	F_{diskbb}	$(10^{-8} \text{ erg cm}^{-2} \text{ s}^{-1})$	$0.183^{+0.03}_{-0.024}$	$0.506^{+0.024}_{-0.022}$	$0.938^{+0.025}_{-0.012}$	$1.370^{+0.022}_{-0.022}$	$1.421^{+0.024}_{-0.022}$	$1.665^{+0.023}_{-0.022}$
	$F_{\text{relxillcp}}$	$(10^{-8} \text{ erg cm}^{-2} \text{ s}^{-1})$	$0.94^{+0.15}_{-0.25}$	$0.85^{+0.12}_{-0.15}$	$1.10^{+0.12}_{-0.14}$	$1.04^{+0.09}_{-0.07}$	$1.05^{+0.09}_{-0.07}$	$1.09^{+0.11}_{-0.11}$
	F_{nthcomp}	$(10^{-8} \text{ erg cm}^{-2} \text{ s}^{-1})$	$0.50^{+0.24}_{-0.15}$	$0.67^{+0.11}_{-0.08}$	$0.46^{+0.08}_{-0.08}$	$0.528^{+0.022}_{-0.027}$	$0.50^{+0.03}_{-0.03}$	$0.43^{+0.04}_{-0.03}$
	$L_{0.1-100\text{keV}}/L_{\text{Edd}}$ (%)	10.4	12.9	15.9	18.8	19.0	20.3	21.1
constant	ME/LE					$1.022^{+0.014}_{-0.012}$		
	HE/LE					$1.147^{+0.034}_{-0.025}$		
	$\chi^2/\text{d.o.f}$					3737.3/3383		

Best-fit parameters for the model `tbabs*(diskbb+relxillcp+cutoffpl)`. Parameters with * are fixed during the fit and the symbol P denotes the upper or lower boundary. Parameters that are only shown for Epoch 4 are tied across all observations.

Table 2-7 Best-fit values with `simplcut` (Model 3).

Component	Parameter	Epoch 1	Epoch 2	Epoch 3	Epoch 4	Epoch 5	Epoch 6	Epoch 7
<code>tbabs</code>	N_{H} (10^{22} cm^{-2})				$0.75^{+0.04}_{-0.06}$			
<code>diskbb</code>	T_{in} (keV)	$0.50^{+0.04}_{-0.04}$	$0.575^{+0.018}_{-0.017}$	$0.682^{+0.008}_{-0.009}$	$0.735^{+0.007}_{-0.007}$	$0.743^{+0.007}_{-0.01}$	$0.777^{+0.007}_{-0.007}$	$0.769^{+0.008}_{-0.009}$
<code>relxillcp</code>	a_*				$0.92^{+0.05}_{-0.07}$			
	q_{in}	3^*	3^*		9.7^{+P}_{-3}	$7.8^{+P}_{-2.3}$	8.9^{+P}_{-5}	$7.0^{+P}_{-2.0}$
	q_{out}				3^{*}	$3.8^{+1}_{-0.4}$	$3.45^{+2.6}_{-0.28}$	$4.0^{+1.5}_{-0.7}$
	$R_{\text{br}} (R_g)$	-	-					
	Incl							
	A_{Fe}							
	R_{in} (ISCO)	50.0^{+P}_{-39}	$3.0^{+1.9}_{-0.9}$	$3.1^{+1.0}_{-0.9}$	$1.4^{+0.5}_{-P}$	$1.41^{+0.25}_{-0.30}$	$1.47^{+0.24}_{-0.29}$	$1.4^{+0.5}_{-0.3}$
	$\log(\xi)$	$4.62^{+0.03}_{-0.04}$	$4.59^{+0.09}_{-0.15}$	$4.70^{+P}_{-0.19}$	$3.99^{+0.12}_{-0.16}$	$4.13^{+0.22}_{-0.22}$	$4.28^{+0.13}_{-0.24}$	$3.94^{+0.6}_{-0.27}$
	Γ	$1.771^{+0.008}_{-0.012}$	$2.125^{+0.024}_{-0.022}$	$2.243^{+0.04}_{-0.029}$	$2.356^{+0.03}_{-0.018}$	$2.370^{+0.019}_{-0.022}$	$2.397^{+0.019}_{-0.016}$	$2.43^{+0.11}_{-0.07}$
	kT_e (keV)	90^{+35}_{-20}	> 80	> 240	> 280	> 200	> 270	60^{+230}_{-30}
<code>simplcut</code>	f_{sc}	$0.121^{+0.004}_{-0.011}$	$0.175^{+0.06}_{-0.028}$	$0.127^{+0.04}_{-0.023}$	$0.119^{+0.007}_{-0.006}$	$0.114^{+0.01}_{-0.012}$	$0.0947^{+0.0025}_{-0.008}$	$0.076^{+0.01}_{-0.015}$
<code>cflux</code>								
F_{diskbb}	($10^{-8} \text{ erg cm}^{-2} \text{ s}^{-1}$)	$0.215^{+0.03}_{-0.028}$	$0.60^{+0.06}_{-0.03}$	$1.066^{+0.06}_{-0.024}$	$1.547^{+0.022}_{-0.029}$	$1.60^{+0.05}_{-0.04}$	$1.838^{+0.021}_{-0.029}$	$2.009^{+0.025}_{-0.04}$
$F_{\text{relxillcp}}$	($10^{-8} \text{ erg cm}^{-2} \text{ s}^{-1}$)	$1.278^{+0.017}_{-0.014}$	$1.17^{+0.1}_{-0.11}$	$1.34^{+0.05}_{-0.21}$	$1.21^{+0.11}_{-0.09}$	$1.18^{+0.09}_{-0.09}$	$1.20^{+0.08}_{-0.09}$	$1.2^{+0.7}_{-0.4}$
	$L_{0.1-100\text{keV}/L_{\text{Edd}} (\%)}$	10.5	13.7	16.8	19.7	19.7	21.0	21.7
constant	ME/LE					$1.018^{+0.017}_{-0.007}$		
	HE/LE					$1.141^{+0.020}_{-0.027}$		
$\chi^2/\text{d.o.f}$						3734.8/3383		

Best-fit parameters for the model `tbabs*simplcut (diskbb+relxillcp)` with a broken power-law emissivity. Parameters with * are fixed during the fit and the symbol *P* denotes the upper or lower boundary. Parameters that are only shown for Epoch 4 are tied across all observations. The model flux is before Comptonization by `simplcut`. The absorption corrected X-ray flux is calculated with the `flux` command in XSPEC.

Table 2-8 Best-fit values with `refhidden` (Model 4).

Component	Parameter	Epoch 1	Epoch 2	Epoch 3	Epoch 4	Epoch 5	Epoch 6	Epoch 7
tbabs	N_{H} (10^{22} cm $^{-2}$)				$0.36^{+0.09}_{-0.06}$			
relconv	a_*	$2.0^{+2.0}_{-2.2}$	$2.17^{+0.21}_{-0.16}$	$1.7^{+0.5}_{-0.6}$	$2.35^{+0.14}_{-0.14}$	$3.3^{+0.7}_{-0.6}$	$2.7^{+0.5}_{-0.3}$	$2.5^{+0.8}_{-0.3}$
	q_{in}				0.998*			
	q_{out}				$= q_{\text{in}}$			
Incl					$33.2^{+2.4}_{-1.4}$	$5.1^{+2.5}_{-1.7}$	$3.8^{+4}_{-1.8}$	$2.6^{+2.9}_{-1.5}$
	R_{in} (ISCO)	9^{+P}_{-P}	1.5^{+5}_{-P}	1.0^{+20}_{-P}				
refhidden	kT_{bb} (keV)	$0.487^{+0.013}_{-0.008}$	$0.400^{+0.007}_{-P}$	$0.400^{+0.005}_{-P}$	$0.441^{+0.004}_{-0.004}$	$0.4403^{+0.004}_{-0.0027}$	$0.459^{+0.004}_{-0.004}$	$0.468^{+0.005}_{-0.004}$
	H_{den} (10^{20} cm $^{-3}$)	> 86	$16.2^{+4.0}_{-1.8}$	$5.7^{+0.6}_{-0.7}$	$5.3^{+0.4}_{-0.5}$	$4.4^{+0.5}_{-0.3}$	$5.4^{+0.3}_{-0.4}$	$5.6^{+0.4}_{-0.4}$
	Illum/BB	$1.8^{+0.5}_{-0.4}$	$1.82^{+0.1}_{-0.29}$	$1.27^{+0.06}_{-0.2}$	$0.84^{+0.09}_{-0.09}$	$0.97^{+0.3}_{-0.11}$	$0.77^{+0.14}_{-0.14}$	$0.52^{+0.18}_{-0.18}$
	Norm	$0.39^{+0.03}_{-0.03}$	$0.70^{+0.06}_{-0.05}$	$0.89^{+0.04}_{-0.04}$	$0.86^{+0.15}_{-0.04}$	$0.99^{+0.19}_{-0.09}$	$0.92^{+0.07}_{-0.07}$	$0.73^{+0.2}_{-0.2}$
simplcut	f_{sc}	$0.773^{+0.011}_{-0.015}$	$0.417^{+0.015}_{-0.03}$	$0.293^{+0.009}_{-0.017}$	$0.163^{+0.005}_{-0.004}$	$0.132^{+0.006}_{-0.009}$	$0.132^{+0.003}_{-0.003}$	$0.110^{+0.013}_{-0.011}$
	Γ	$1.867^{+0.013}_{-0.009}$	$2.124^{+0.015}_{-0.018}$	$2.283^{+0.013}_{-0.025}$	$2.305^{+0.012}_{-0.016}$	$2.315^{+0.026}_{-0.013}$	$2.381^{+0.014}_{-0.021}$	$2.42^{+0.05}_{-0.06}$
	kT_{e} (keV)	$26.4^{+1.6}_{-2.1}$	50^{+10}_{-10}	> 200	> 100	> 100	> 360	70^{+500}_{-30}
	$L_{0.1-100\text{keV}}/L_{\text{Edd}}$ (%)	8.2	9.3	11.0	12.2	12.5	13.3	12.8
constant	ME/LE				$0.985^{+0.008}_{-0.006}$			
	HE/LE				$1.057^{+0.016}_{-0.019}$			
	$\chi^2/\text{d.o.f}$				3788.8/3386			

Note. Best-fit parameters for the model `tbabs*simplcut*relconv*refhidden` with a power-law emissivity. Parameters with * are fixed during the fit and the symbol P denotes the upper or lower boundary. Parameters that are only shown for Epoch 4 are tied across all observations.

The absorption corrected X-ray flux is calculated with the `flux` command in XSPEC.

Chapter 3

Rapidly alternating flux states of GX 339–4 during its 2021 outburst captured by *Insight*–HXMT

3.1 Introduction

The outbursts of XRBs typically last for weeks to months (with extreme cases lasting years to decades)^[42]. This suggests that the geometry of the disk-corona system can undergo changes on these timescales^[4]. The coronal emission is known to exhibit faster variability, such as low-frequency quasi-periodic oscillations in the range of 0.05 to 30 Hz (corresponding to timescales from milliseconds to tens of seconds)^[199]. Studying these variability enables to understand the interaction within the disk-corona system^[183] and changes of the structures of the system^[103,200].

GX 339–4 entered a new outburst in 2021, which was captured by *Insight*–HXMT. Fig. 3-1 shows the HID of this outburst. The source spent some time in the hard state followed by a fast transition (around a week) to the soft state. The spectra for the hard-to-soft transition have been investigated in Chapter 2. At the end of this transition, marked by the red stars on the HID (April 01, 2020), the source was found to exhibit rapid changes of flux in the hard X-ray band as shown in Fig. 3-2. This variability happens on a timescale of less than one orbit of *Insight*–HXMT (1.5 hours). This kind of variability is different from the state transition we have seen, with a shorter timescale and smaller amplitude. Moreover, it is apparently not the kind of variability seen for QPOs and broadband noise in PDS. Similar patterns have only been reported in a few cases and are identified as “flip-flop” (see Bogensberger et al. 2020^[201]). The mechanism that drives this kind of variability is still poorly understood.

In this Chapter, we investigate the hard X-ray alternating states by analyzing its

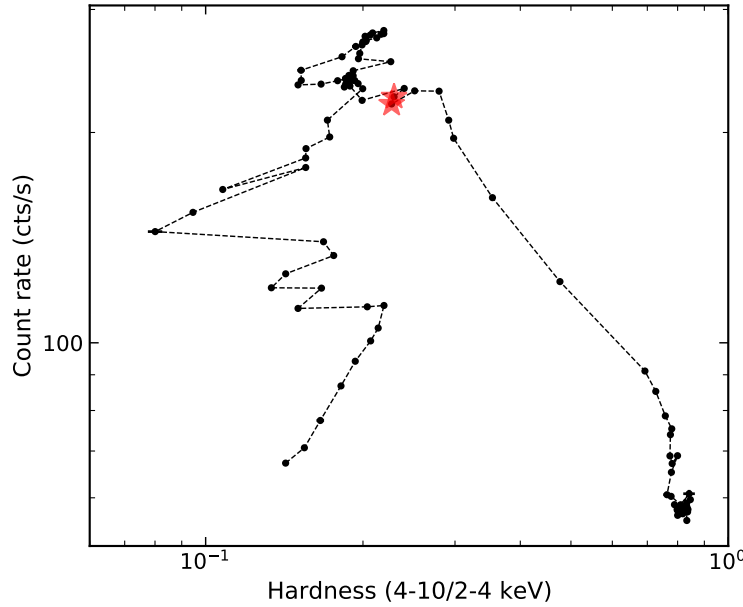


Figure 3-1 The hardness intensity diagram of the 2021 outburst of GX 339–4. Data are extracted from *Insight–HXMT* observations. Each point represents data from one day. The two observations analyzed in this work are marked with red stars. The hardness is defined using the count rate.

Table 3-1 *Insight–HXMT* observations of GX 339–4 analyzed in this paper.

Date	obsID	Exposure (ks) ¹	
		LE	ME
2021-04-01	P0304024043 01-07	5.4	15.0
2021-04-02	P0304024043 08-15	5.9	15.0

Note. (1) We show the total exposure time of all observations in one day.

time-resolved broadband spectra from *Insight–HXMT*. We present the data reduction procedure in Sec. 3.2. Overview of the alternating X-ray flux states is presented in Sec. 3.3. The spectral fitting results are described in Sec. 3.4. We discuss the results in Sec. 3.5.

3.2 Observations and data reduction

The procedures to extract lightcurves and spectra for *Insight–HXMT* are explained in Chapter 2. The LE data in the 2–9 keV band and ME data in the 8–15 keV band are used in this work. Data above 15 keV are ignored because of the very high background. For the use of χ^2 statistics, spectra are binned to ensure a minimal counts of 30 for every energy bin.

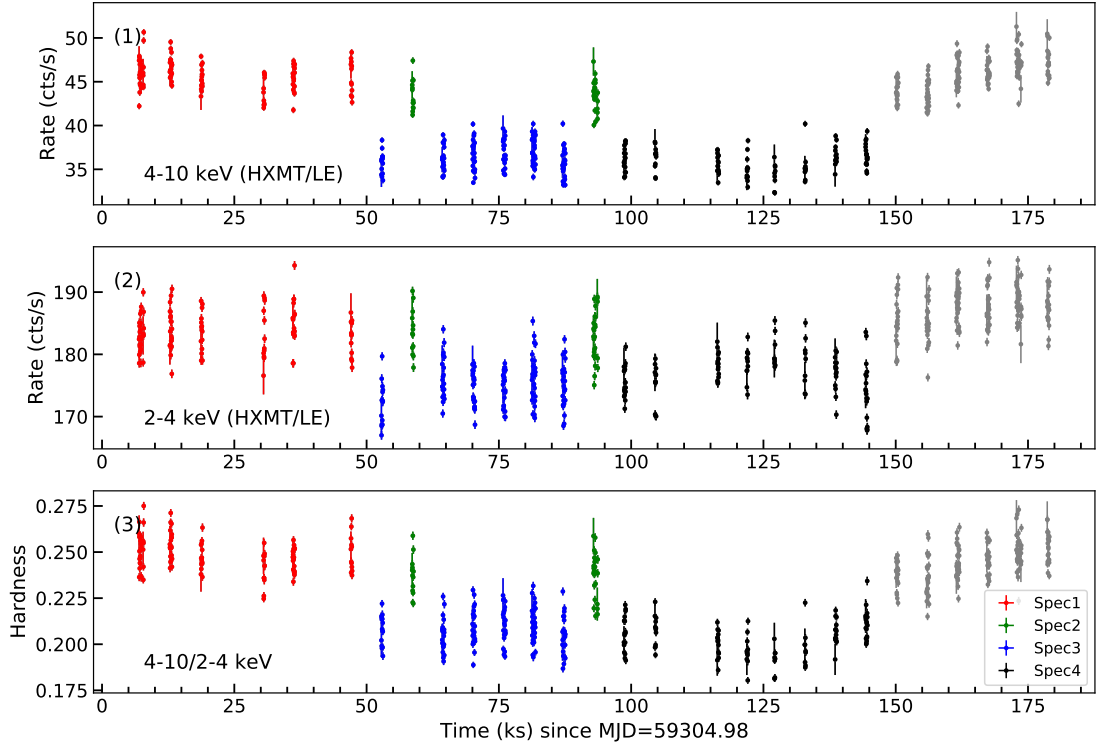


Figure 3-2 Lightcurves of GX 339-4 by *Insight*-HXMT in 4–10 keV (panel 1) and 2–4 keV (panel 2). The evolution of the hardness ratio is shown in panel 3. The source enters a low flux state at 52 ks that lasts for about 100 ks. Two brief high flux states emerge from the low flux interval on a timescale less than one orbit. The flux change is more prominent in 4–10 keV. Different colors mark the four spectra extracted from the observation (see Sec. 3.4).

3.3 Alternating X-ray Flux States

In Fig. 3-2, we present the light curves of GX 339-4 on the 1st and 2nd of April 2021. The corresponding hardness and intensity plotted on the HID are indicated in Fig. 3-1. Instances of data gaps in the light curves are attributed to the telescope’s low Earth orbit or traversing the South Atlantic Anomaly (SAA).

Panel (1) illustrates that the observed 4–10 keV count rate of GX 339-4 experienced a sudden decrease by a factor of 1.28 at 52 ks since the onset of observations. Subsequently, GX 339-4 reverted to its original high flux level during the subsequent orbit of observation at 58 ks. Another brief period of high flux state occurred around 93 ks. Both the initial and subsequent high flux states, highlighted in yellow in Fig. 3-2, exhibited similar observed X-ray flux levels.

The 4–10 keV count rate exhibited a change by a factor of 1.28, indicating a more pronounced alteration in the hard X-ray flux compared to the soft X-ray flux. Consis-

tently, the X-ray hardness of GX 339–4, defined as the count rate ratio between the 4–10 keV and 2–4 keV bands, remained higher during the high flux state than in the low flux state.

The two brief high flux states endured for periods shorter than the orbital period of the telescope. Given their rapid transition, occurring in less than the orbital period, *Insight–HXMT* did not capture the shift from the high to low flux states^①.

To ensure that unknown instrumental issues did not spur the observed high flux states, we cross-checked observations from other missions in the archive. Notably, the second rise in flux was captured by other missions, including *NuSTAR* and *Swift* (refer to Fig 3-7). Our analysis focuses solely on the *Insight–HXMT* observations of GX 339–4, while detailed spectral analysis of *NuSTAR* and *Swift* data is deferred to future work by Garcia et al.

In summary, we observe that GX 339–4 swiftly oscillated between two flux states in the X-ray band during the intermediate state. The high flux states endured for brief periods comparable to the orbital period of the telescope. Throughout these alternating flux states, the 4–10 keV count rate of GX 339–4 escalated by a factor of 1.28, whereas the 2–4 keV count rate rose by a factor of 1.05.

3.4 Spectral Analysis

In this section, we conduct an analysis of the X-ray spectra observed during both the high and low flux states. To explore how the spectral components evolve alongside the X-ray flux, we extract spectra from four distinct intervals as indicated in panel (3) of Fig. 3-2. These intervals correspond to: before the flux drop (Spec 1), two alternating high flux periods during the extended dip (Spec 2), and the low flux intervals before (Spec 3) and after (Spec 4) the second brief high flux state.

The four spectra are depicted in the left panel of Fig. 3-3. Notably, all spectra are soft with a pronounced blackbody-like component in the soft energy band. Comparing Spec 1 and Spec 2, there are no discernible differences. However, transitioning from the high flux (Spec 1/2) to the low flux (Spec 3/4) state, the spectra primarily vary in the hard X-ray range (> 4 keV).

We conduct spectral analysis using `xspec v12.11.1`. Elemental abundances

^① The *Swift* observation of GX 339–4 captured the state transition from the high to low flux states. Refer to Appendix 3-7 for further details.

are adopted from Anders et al. (1989)^[202], and cross-sections from Verner et al. (1996)^[156]. Unless explicitly stated otherwise, errors in this study are quoted at the 90% confidence level.

3.4.1 Spectral models

We begin by focusing on Spec 1 to establish a baseline model applicable to all spectra. X-ray spectra from LMXRBs typically exhibit contributions from thermal emission originating from the accretion disk and a power-law component from a hot corona. Therefore, as a preliminary step, we fit Spec 1 using the model `tbabs * (diskbb + nthcomp)`. The `tbabs` model^[155] accounts for Galactic absorption and involves only one free parameter (N_{H}). The `diskbb` model^[157] characterizes the thermal emission from a multi-color accretion disk, while `nthcomp`^[55–56] represents the power-law component. Given that the reflection component from an optically thick accretion disk often contributes significantly to the spectrum within the energy range of the iron K emission, we exclude data in the 4–8 keV band when fitting the continuum model. The residuals of the data to the best-fit continuum model are depicted in the right panel of Fig.3-3. Notably, there is evidence of a prominent and broad Fe K emission line around 6–7 keV, indicating the presence of a relativistic reflection component originating from the accretion disk.

Therefore, we incorporate a reflection component into the model and simultaneously fit the four spectra. Given the potential variability in the electron density of the disk of GX 339–4 during the outburst^[6], we employ the reflection model `reflionx`^[168], which allows for variable electron density. However, it is important to note that `reflionx` describes only non-relativistic reflection from the accretion disk. To adequately capture relativistic effects, we include the broadening kernel `relconv`^[60,126]. Therefore, the full model is expressed as `tbabs * (diskbb + nthcomp + relconv * reflionx)` in XSPEC notation.

The spin of the black hole is set at the maximum value to estimate the inner radius of the disk using the reflection model. This assumption of a high black hole spin aligns with previous measurements^[143]. In this model, the iron abundance is fixed at the solar value. The electron temperature (kT_e) of the power-law component is also fixed at 100 keV, as this parameter cannot be constrained reliably. We assume a power-law emissivity profile and allow the index (q) to vary freely. This model yields a satisfactory fit for

Spec 1 ($\chi^2/\nu=846/884$). We explored the possibility of a broken power-law emissivity profile by fixing the outer index at 3 and letting the breaking radius (R_{br}) vary freely. However, this adjustment only marginally improved the χ^2 by 2, with no significant impact on the best-fit parameters. Hence, we conclude that a power-law emissivity profile is sufficient to describe the data adequately. Note that there is a narrow peak in the iron line profile (visible in the right panel of Fig. 3-3). The narrow core, centered at 6.7 keV, rules out the possibility of reprocessing by a distant neutral reflector. Additionally, including a non-relativistic reflection component did not lead to a better fit. The line energy aligns with the emission of Fe XXV, suggesting it may originate from highly ionized material in the system, such as the accretion disk wind outside the line of sight. However, it's currently impossible to ascertain its precise origin with the available data. Moreover, the narrow line is unlikely to significantly impact the analysis of the relativistically broadened iron line profile.

We measure an inner disk temperature of 0.73 keV for the `diskbb` component, which dominates the soft X-ray band (accounting for 60% of the flux in the 2–15 keV range). Additionally, the fit requires a very soft power-law component ($\Gamma > 2.9$). Using the relativistic reflection model, we infer an inclination angle of approximately 40 degrees for the inner disk. Furthermore, we find evidence of slight truncation of the inner disk edge at around $2 R_g$ ($R_g = GM/c^2$, the gravitational radius) assuming a maximum black hole spin ($a_* = 0.998$).

The index in the emissivity profile, which is steeper than the canonical value in the Newtonian limit ($q = 3$), may result from light bending effects when the corona is in close proximity to the black hole. To account for this, we replace the kernel `rel-conv` with `relconv_lp`. In this model, the corona is assumed to be a point source positioned at a certain height (h) above the black hole, and the emissivity profile is self-consistently calculated. This modified model yields a fit statistic of $\chi^2/\nu=844/884$. Additionally, we find that the corona height is constrained to within $3 R_g$ of the black hole at a 90% confidence level.

We will further discuss the geometry of the innermost accretion region, including R_{in} and h , in the following section.

3.4.2 Spectral variability

Having achieved a satisfactory model for Spec 1, incorporating both the thermal emission and reflection from the accretion disk, we extend this model to analyze Spec 2–4 and investigate the spectral variability of GX 339–4. Given the short timescale of observation, we anticipate that the inclination of the disk and the column density of Galactic absorption remain constant; therefore, we link these parameters across the spectra. Additionally, we link the electron density and the inner radius of the disk among the spectra.

The best-fit parameters are summarized in Tab. 3-2. Notably, the temperature of the inner disk remains relatively stable at around 0.7 keV across both the low and high flux states. The inclination angle of the inner disk is around 40 degrees, consistent with findings from previous investigations^[20,186]. Although the electron density parameter (n_e) exhibits a loose constraint ($\log(n_e) < 20$), its value aligns with prior studies conducted during the very high state (e.g., $18.93^{+0.12}_{-0.16}$ as reported by Jiang et al. 2019^[6]). The limited energy range of the *Insight*–HXMT LE data contributes to the weak constraint on the density parameter, with its impact confined primarily to the soft X-ray band (e.g., < 3 keV^[113,168]). Additionally, the inner disk is observed to be slightly truncated at approximately $2 R_g$. In Fig. 3-4, we depict the $\Delta\chi^2$ contour of the inner disk radius alongside the location of the innermost stable circular orbit (ISCO) for various spin values. Remarkably, this measurement of the inner radius is consistent with the ISCO ($3 - \sigma$) assumption under a black hole spin value of 0.95.

Employing the `reconv_lp` model, we observe that the estimated corona heights from the four spectra exhibit consistency within uncertainties. Furthermore, we investigated a scenario wherein the corona height remains constant. The constraint on h after linking it across the four spectra is shown by the black line on the right side of Fig. 3-4. Evidently, this analysis suggests that the corona must be situated proximate to the black hole, with a distance of less than $3 R_g$.

The best-fit model and corresponding spectral components are illustrated in Fig. 3-5, accompanied by the residuals. It is apparent that the changes in the `diskbb` component are minimal. However, noticeable alterations occur in the reflection and power-law components, which primarily contribute to the variance observed in the hard X-ray band across the four spectra. In Fig. 3-6, we depict the evolution of several spectral param-

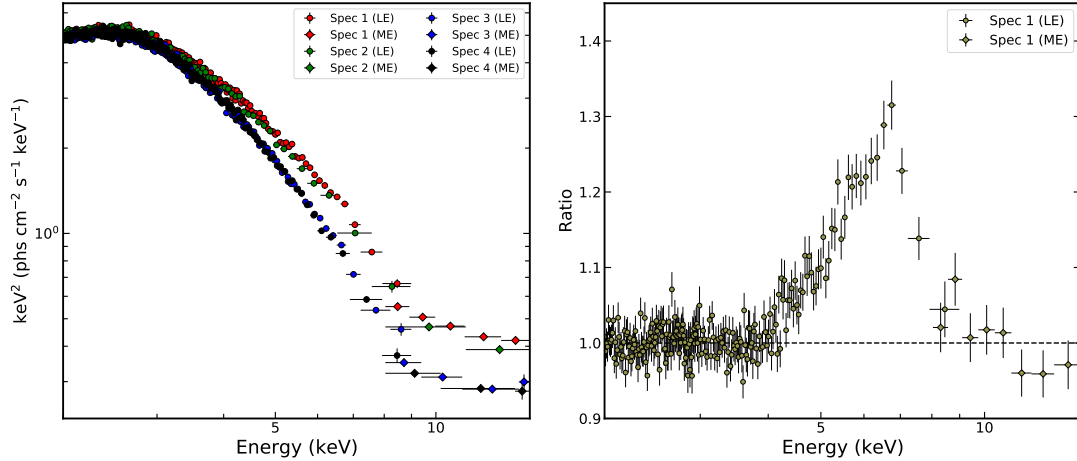


Figure 3-3 (Left): Spectra of the four intervals as defined in Fig 3-2. The LE (2–9 keV) and ME (8–15 keV) data are marked with filled circle and diamond respectively. The spectra are obtained using `setplot area` command in `xspec` and are only shown for demonstration purposes. (Right): Data to model ratio of Spec 1 to a simple absorbed continuum model. Data are binned for visual clarity.

eters with the X-ray flux of the source. The data indicate a requirement for a very soft ($\Gamma > 2.5$) index for the power-law component, although it is challenging to discern how Γ fluctuates due to considerable uncertainty. Notably, the flux of the power-law emission decreases by a factor of 4 from the high flux to the low flux states. Similarly, the flux of the reflection component also decreases, albeit by a factor of 1.6. While the reflection strength, defined as the ratio between the reflection and power-law components, exhibits tentative evidence of increasing from the high to low flux states, this trend lacks significance when considering the associated uncertainty.

3.5 Discussion

At the end of the hard to soft transition during the 2021 outburst of GX 339–4, *Insight–HXMT* detected two brief high flux states (Fig. 3-2) lasting for a duration comparable to the orbital period of the telescope. This indicates rapid alternation between two distinct flux states. Particularly noteworthy is the more pronounced change in flux observed in the hard X-ray band (Fig. 3-3), which rules out variable local absorption as the primary cause of these fluctuations.

In our investigation to discern which emission components are varying alongside the source flux, we segmented the two-day observation into four intervals based on alternating properties and analyzed the spectral components within each interval. To model the

Table 3-2 Best-fit values of the four spectra.

Model	Parameter	relconv				relconv_1p			
		Spec 1	Spec 2	Spec 3	Spec 4	Spec1	Spec2	Spec3	Spec 4
tbabs	N_{H} (10^{22} cm^{-2})		$0.66^{+0.08}_{-0.07}$				$0.68^{+0.08}_{-0.07}$		
diskbb	T_{in} (keV)	$0.729^{+0.015}_{-0.019}$	$0.729^{+0.016}_{-0.021}$	$0.714^{+0.012}_{-0.017}$	$0.728^{+0.012}_{-0.014}$	$0.724^{+0.014}_{-0.018}$	$0.722^{+0.016}_{-0.021}$	$0.711^{+0.013}_{-0.015}$	$0.725^{+0.013}_{-0.014}$
	Norm	3000^{+350}_{-300}	3200^{+400}_{-300}	3700^{+400}_{-300}	3600^{+350}_{-300}	3100^{+320}_{-300}	3300^{+350}_{-350}	3800^{+400}_{-330}	3650^{+360}_{-300}
relconv (1p)	q	$4.6^{+0.9}_{-0.6}$	$4.3^{+1.0}_{-0.7}$	$4.7^{+0.9}_{-0.7}$	$4.3^{+0.9}_{-0.9}$	-	-	-	-
	$h(R_e)$	-	-	-	-	< 2.5	< 3.2	< 2.3	< 2.8
	a_*		0.998^*			0.998^*			
	i (deg)	41^{+3}_{-5}				37^{+3}_{-3}			
	$R_{\text{in}}(R_e)$		$2.01^{+0.26}_{-0.18}$			$2.18^{+0.22}_{-0.18}$			
reflionx	$\log(n_e)$		$17.3^{+2.7}_{-1.3}$				< 20		
	ξ	480^{+370}_{-300}	230^{+1300}_{-80}	480^{+480}_{-300}	480^{+2500}_{-350}	480^{+500}_{-300}	330^{+1100}_{-150}	530^{+2100}_{-300}	490^{+1300}_{-400}
	Γ	> 2.9	> 2.8	> 2.7	> 2.5	> 2.9	> 2.8	> 2.7	> 2.5
	Norm	63^{+290}_{-40}	100^{+100}_{-90}	44^{+40}_{-30}	36^{+160}_{-24}	65^{+220}_{-40}	76^{+78}_{-60}	41^{+80}_{-22}	37^{+100}_{-21}
nthcomp	Norm	$0.38^{+0.13}_{-0.13}$	$0.24^{+0.21}_{-0.2}$	$0.18^{+0.09}_{-0.11}$	$0.08^{+0.08}_{-0.08}$	$0.39^{+0.12}_{-0.14}$	$0.29^{+0.17}_{-0.19}$	$0.2^{+0.1}_{-0.1}$	< 0.17
	F_{ref}	$2.4^{+0.4}_{-0.3}$	$2.4^{+1.2}_{-0.5}$	$1.67^{+1.0}_{-0.5}$	$1.49^{+0.4}_{-0.18}$	$2.47^{+0.6}_{-0.11}$	$2.4^{+0.5}_{-0.3}$	$1.78^{+0.5}_{-0.23}$	$1.53^{+0.4}_{-0.14}$
	$F_{\text{power-law}}$	$1.3^{+0.4}_{-0.4}$	$0.8^{+0.6}_{-0.6}$	$0.6^{+0.27}_{-0.3}$	$0.32^{+0.28}_{-0.28}$	$1.3^{+0.3}_{-0.4}$	$0.9^{+0.5}_{-0.7}$	$0.53^{+0.14}_{-0.5}$	$0.34^{+0.26}_{-P}$
	F_{total}	$9.18^{+0.13}_{-0.12}$	$8.98^{+0.13}_{-0.12}$	$8.21^{+0.12}_{-0.11}$	$8.25^{+0.13}_{-0.11}$	$9.21^{+0.11}_{-0.12}$	$9.00^{+0.11}_{-0.15}$	$8.24^{+0.12}_{-0.11}$	$8.27^{+0.12}_{-0.12}$
Fraction	ref/power-law	1.8 ± 0.6	3.0 ± 2.5	2.8 ± 1.7	5.0 ± 4	1.9 ± 0.6	2.7 ± 1.8	3.4 ± 2.1	4.5 ± 4
Fraction	(ref+power-law)/total	0.40 ± 0.06	0.36 ± 0.11	0.28 ± 0.08	0.22 ± 0.05	0.41 ± 0.05	0.37 ± 0.08	0.28 ± 0.05	0.23 ± 0.05
$\chi^2/\text{d.o.f}$			$3138/3380$				$3134/3380$		

Note. The flux (2–15 keV) of the reflection component and the full model are presented in units of $10^{-9} \text{ erg s}^{-1} \text{ cm}^{-2}$.

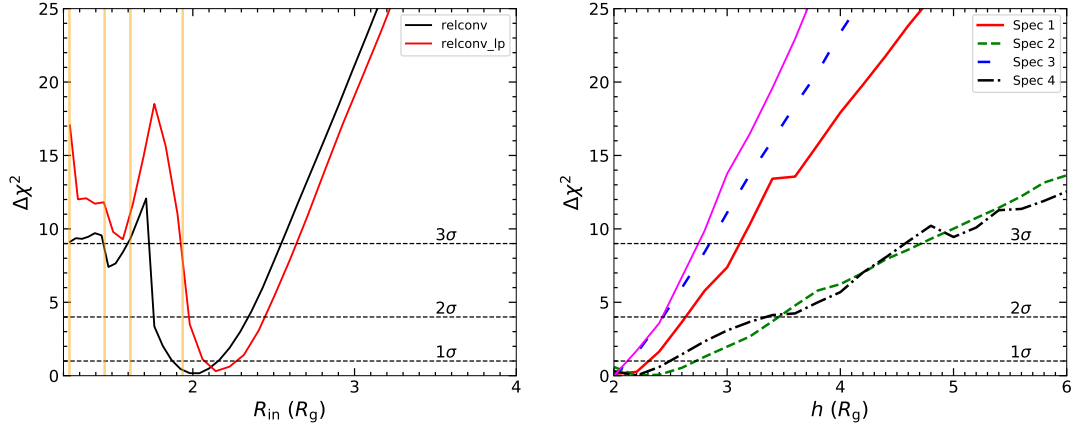


Figure 3-4 Left panel: The $\Delta\chi^2$ confidence contours of the inner disk radius for the two models. The orange vertical lines mark the radius of ISCO for $a_* = 0.998, 0.99, 0.98$ and 0.95 respectively (from left to right). Right panel: The $\Delta\chi^2$ confidence contours for the corona height (h) of the four spectra. In both panels, the horizontal dashed lines represent the 1 , 2 and 3σ confidence levels. Colors are coded as in Fig 3-5, while the magenta line represents the result when linking h between the four spectra.

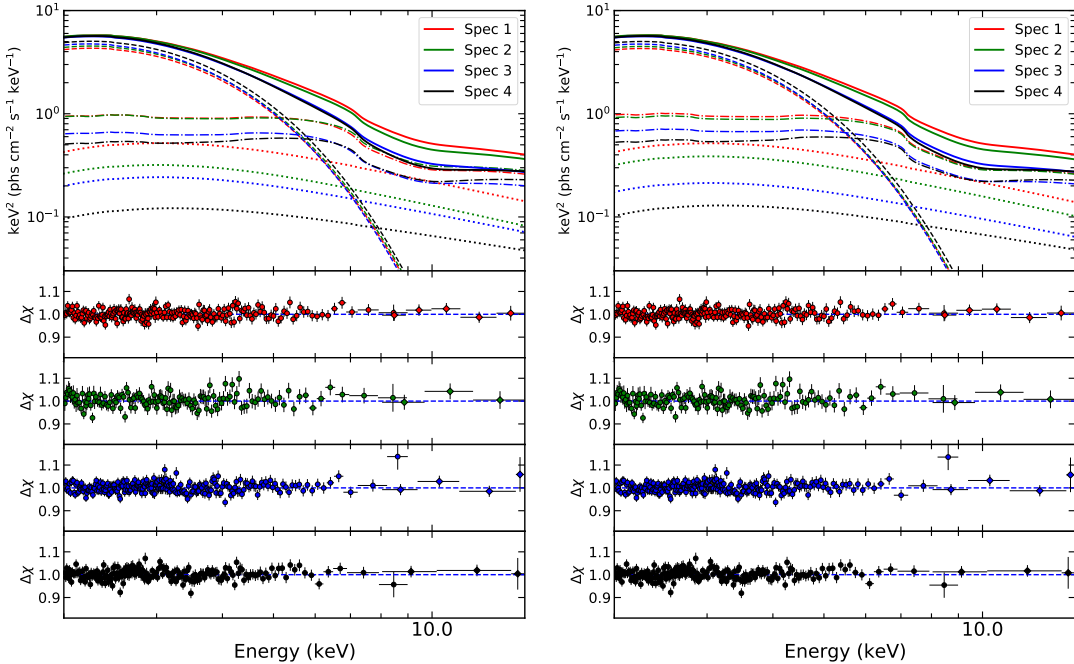


Figure 3-5 (Left): The best-fit models and the corresponding residuals to the four spectra with model `tbabs* (diskbb+nthcomp+relconv*reflionx)`. The LE and ME data are marked with filled circle and diamond markers respectively. (Right): The same as the left plot but with the relativistic broadening kernel replaced by `relconv_1p`. The full models are plotted in solid lines. The disk, power-law and reflection components are plotted in dashed, dotted and dash-dotted lines respectively.

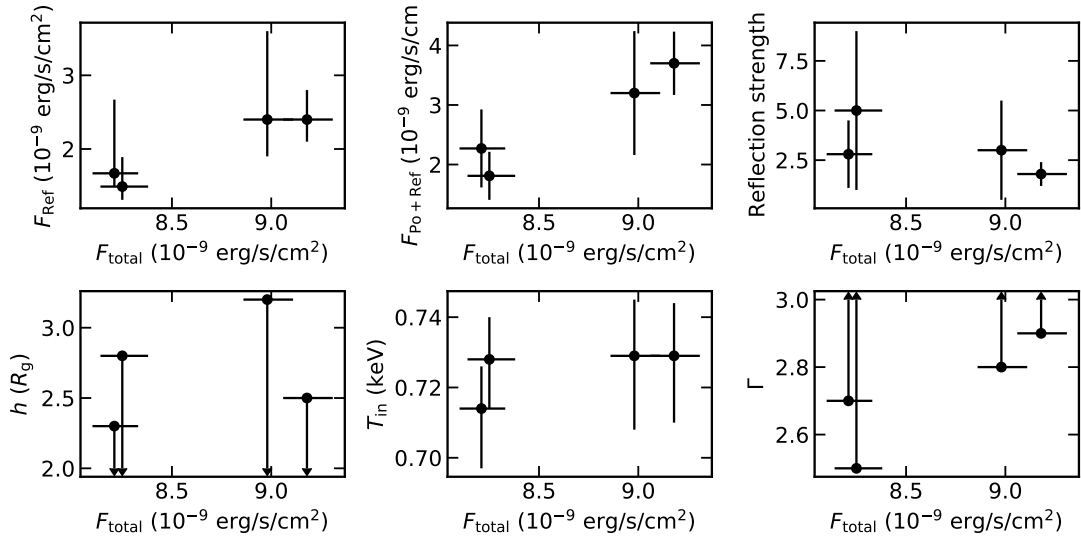


Figure 3-6 Relations of the some spectral parameters with the total X-ray flux in the energy range 2–15 keV. Lower and upper limits are marked with arrows.

broadband spectra, we incorporated contributions from disk thermal emission, power-law emission originating from the hot corona, and the relativistic reflection component from the optically thick accretion disk. Our analysis reveals that the fluctuations in the hard X-ray band flux (Fig. 3-5) are primarily driven by variations in the corona emission and the disk reflection component, while the disk thermal emission remains relatively stable.

3.5.1 The inner radius of the disk

After fitting the relativistic reflection model to the data, we ascertain that the disk might exhibit a slight truncation at $2 R_g$ when assuming a maximum black hole spin ($a_* = 0.998$)^①. The inner disk radius estimated from the normalization parameter of `diskbb` is approximately $4 \times (D/8 \text{ kpc})(10M_\odot/M_{\text{BH}}) R_g$ assuming a color correction factor of 1.7 and an inclination of 40 degrees. Utilizing the median values from the measurements of^[140] ($M = 7.5M_\odot$, $D = 10$ kpc) yields an inner radius of $6.6 R_g$. This estimate surpasses that obtained from modeling the relativistic reflection features. However, significant uncertainty persists in the current measurements of the system's distance and black hole mass. Considering the lower limit of the distance derived by^[187] (5kpc), we derive an inner radius size of $2.5R_g$, closely aligned with the measurement

^① If the spin is 0.95, which aligns with previous measurements using relativistic reflection^[6,143], the disk's truncation is consistent with non-truncation.

from relativistic reflection.

There appears to be a tentative trend suggesting that the disk inner radius, as measured with the disk component, is larger in the low flux state. However, the uncertainties are too significant to draw a robust conclusion. The change in disk flux within the 2–15 keV band is less than 15% from Spec 1 to Spec 4. The temperature of the inner edge of the disk remains similarly stable. Likewise, the inner radius of the disk, as measured by the reflection model, remains constant throughout our observation period. Even during the rapidly alternating flux states, the inner disk radius remains constant within the bounds of our measurement uncertainty.

3.5.2 The geometry of the corona during the state transition

In our analysis, we adopt a power-law-shaped emissivity profile and an emissivity with the lamppost geometry. Across all four spectra, the best-fit value of the power-law index (q) falls within the range of 4–5 and remains consistent. Notably, this index is steeper than the expectation from the Newtonian limit ($q = 3$). Such steepening can occur when the corona is positioned close to the black hole, causing photons to concentrate near the black hole due to light bending effects. This interpretation finds support in our results with `relconv_lp`, which yield an upper limit for the corona height of $3.2 R_g$.

Regarding the corona emission, we observe a notable decrease in its flux by a factor of 4 from Spec 1 to Spec 4, accompanied by a decrease in the reflection component by a factor of 1.6. An intriguing pattern is that the best-fit value of the reflection strength, defined as the ratio between the reflected and directly observed corona emission, appears to increase from the high flux to low flux states. However, due to considerable uncertainties, a definitive conclusion cannot be drawn. Considering that the corona height remains consistent across all four spectra, it is possible that the reflection strength remains constant. This suggests that the observed alternating states are likely a result of variations in the corona power.

However, it is impossible to see if the photon index changes between the low and high flux states. This is because we do not have data above 15 keV and the soft X-ray band is dominated by the disk emission.

3.5.3 The power of the corona

We conducted an analysis of GX 339–4 using *Insight*–HXMT data during its intermediate state. Throughout the observational period, GX 339–4 exhibited rapid alternations between high and low flux states in the hard X-ray band, while the soft X-ray emission remained relatively stable. Notably, the high flux state persisted only briefly, comparable to the orbital period of the telescope. Furthermore, the transition occurred between orbits of *Insight*–HXMT and was not captured by our observations. Additional details regarding the transition observation can be found in Appendix A, which covers the *Swift* observation.

The *Insight*–HXMT observations of GX 339–4 reveal signatures of both disk reflection and thermal emission from the inner accretion disk. A thorough analysis indicates that the thermal emission from the disk remains consistent throughout the state transition, in line with the observed stability of the soft X-ray emission (refer to Fig. 3–3). However, the variability observed in the hard X-ray flux transition is attributed to changes in the non-thermal emission, including both the power-law continuum from the corona and the reflected emission from the disk.

Detailed reflection modeling indicates that the inner geometry of the accretion region remains stable. Specifically, the inner radius of the accretion disk stays proximate to ISCO at approximately $2 R_g$. Assuming a maximum black hole (BH) spin, our findings imply a potential slight truncation of the disk. However, it's crucial to highlight that our measurement remains consistent with a non-truncated disk within a 3-sigma uncertainty range.

The geometry of the coronal region remains unchanged during the observed rapid alternations in flux states. Both the emissivity profiles of the disk, modeled using both a power law and a lamppost model, show no significant variations. Although there is tentative evidence indicating a higher reflection strength in the high flux state compared to the low flux state, the disparity is not statistically significant. These measurements are consistent within the ranges of uncertainty, suggesting a constant geometry of the corona in GX 339–4.

The rapid fluctuations observed in the coronal power law intensity by *Insight*–HXMT may be attributed to variations in the coronal heating mechanism. In BH XRBs, the hard X-ray continuum arises from the Compton scattering of lower-energy disk pho-

tons^[203]. To sustain the corona, a heating mechanism is necessary, with one widely accepted model involving the magnetic field. Pair production in the magnetosphere surrounding a black hole is thought to be a significant contributor to this process^[204]. While the disk appears relatively stable during the observed state transition, sudden alterations in the magnetic field could lead to increased release of accretion power from the disk to the corona.

Future X-ray observations focusing on these rapidly alternating flux states during the intermediate transition phase could provide valuable insights into this phenomenon. Observing the precise moments of these rapid state transitions is crucial for unraveling this mystery. However, most current X-ray missions lack the capability for non-stop monitoring due to their low-Earth orbits. Future X-ray missions, such as *Arcus*^[205], which operate on high Earth orbits, hold promise for continuously observing GX 339–4 over several days, enabling more comprehensive investigations.

3.5.4 The reflection component

The strong relativistic reflection features enable us to constrain important parameters like the radius of the disk inner edge and the corona height. Another vital parameter is the electron density of the accretion disk, which can significantly influence the fit in the soft X-ray band^[168]. Using the `reflionx` model, we obtain a constraint of $\log(n_e) < 20$ for the electron density. Alternatively, the `relxill1D` model^[113] offers a wider range of $15 < \log(n_e) < 19$. This model provides a more accurate treatment of atomic physics compared to `reflionx`. To evaluate the impact of different reflection models on our results, we apply the `relxill1lpD` model to the four spectra simultaneously. The best-fit parameters resulting from this analysis are listed in Tab. 3-3.

Comparing the fit results obtained with the `relxill1lpD` model to those with `reflionx`, we observe no significant alterations in the measurements of parameters such as the inner radius of the disk, the height of the corona, or the inclination angle. However, the constraint on the electron density is noticeably tighter, yielding an upper limit of $\log(n_e) = 16.7$. This finding generally aligns with the result obtained from the `reflionx` model (see Tab. 3-2) Additionally, we can estimate the electron density using the definition of the ionization parameter ($\xi = 4\pi F_{\text{irr}}/n$), where F_{irr} is the irradiating flux on the disk and n is the electron density. Following equation (8) in^[185], we obtain an electron density of approximately $\sim 10^{22} \text{ cm}^{-3}$ for Spec1, assuming a reflection

fraction $R = 1$. However, this value is several orders of magnitude higher than that derived from spectral fitting. The substantial discrepancy cannot be solely attributed to uncertainties in the irradiating flux or other parameters. Further analysis of reflection spectra in the soft state is required to elucidate the disparity between the two methods.

3.5.5 Compare with other sources

The rapid alternation between flux states observed in our study bears resemblance to the "flip-flop" transitions first identified in GX 339–4^[206]. These transitions manifest as abrupt shifts between higher and lower flux levels over short timescales, typically on the order of minutes. While flip-flops are relatively rare and have only been observed in a handful of sources (see Bogensberger et al. 2020^[201] and references therein), our findings differ from previous observations of flip-flops. Typically, flip-flops are detected during or after the very high state^[97,207], whereas the transitions observed in our study occur before the onset of the soft state. This distinction may explain the presence of strong reflection features in our data, which are not commonly observed in flip-flop events. Changes in power spectra and the occurrence of quasi-periodic oscillations (QPOs) are frequently associated with flip-flop transitions^[201,208]. However, we do not observe any QPOs, and the power spectra resemble those typical of a soft state, characterized by minimal power. Therefore, the transitions observed in our study share similarities with the "late flip-flops" observed in Swift J1658.2–4242^[201].

Spectral fitting of the flip-flops in Swift J1658.2–4242 has indicated that the change of the inner disk temperature is responsible for the spectral variability. In contrast, we observe nearly consistent temperatures for both the low and high flux states. The variability primarily arises from changes in coronal power, while the disk temperature remains stable. Analogous behaviors have been found during the soft state of certain X-ray binaries^[104,209].

3.6 Conclusions

During the 2021 outburst of GX 339–4, we found that the source rapidly alternates between a low and high flux state. Spectral analysis on its time-resolved spectra shows that:

1. The flux change is confined in the hard X-ray band (> 4 keV) and is regulated by the power-law emission and the reflected emission.

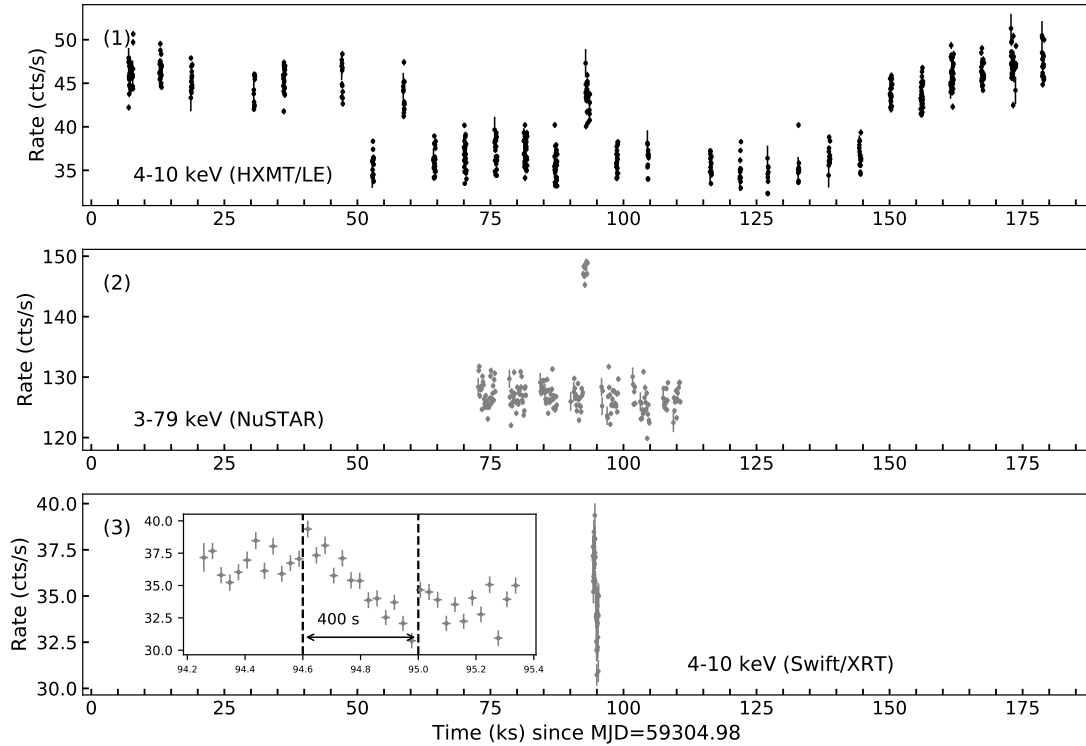


Figure 3-7 Lightcurves of GX 339–4 by *Insight–HXMT*, *NuSTAR* and *Swift*.

2. The strength of the disk thermal emission and the inner radius of the accretion disk do not change with the flux.
3. The corona is close to the black hole ($3 R_g$). There is no evidence for changes in the corona geometry when the flux changes, which suggests the change is in the intrinsic power of the corona.

3.7 Appendix

The *NuSTAR* lightcurve is extracted from the observation on 2021 April 1st with obsID: 90702303011. The data are first processed with the tool `nupipeline` ver 0.4.8. We then extract the lightcurve using the tool `nuproducts` with the source region being a 180 arcsec circle. The background product is extracted from a circular region with the same size near the source.

The *Swift/XRT* lightcurve is extracted from the observation (obsID: 00014218002) on the same day. Data are processed with tools `xrtpipeline` ver 0.13.5 and `xs-select`. Source lightcurve is extracted from a circular region of 100 arcsec and the background region is near the source with the same size.

Table 3-3 Best-fit values of the four spectra with the model `relxilllpD`.

Model	Parameter	Spec 1	Spec 2	Spec3	Spec 4
tbabs	N_{H} (10^{22} cm^{-2})		$0.93^{+0.07}_{-0.06}$		
diskbb	T_{in} (keV)	$0.731^{+0.016}_{-0.016}$	$0.728^{+0.019}_{-0.019}$	$0.704^{+0.012}_{-0.013}$	$0.718^{+0.013}_{-0.014}$
	Norm	2700^{+260}_{-200}	3000^{+350}_{-260}	3700^{+360}_{-300}	3600^{+350}_{-280}
<code>relxilllpD</code>	$h(R_g)$	< 2.5	< 3.1	< 2.1	< 2.6
	a_*			0.998^*	
	i (deg)			$39.5^{+2.7}_{-2.7}$	
	R_{in} (R_g)			$2.16^{+0.19}_{-0.11}$	
	$\log(n_e)$			< 16.7	
	$\log(\xi)$	$4.22^{+0.21}_{-0.11}$	$4.15^{+0.3}_{-0.11}$	$4.20^{+0.2}_{-0.26}$	$3.99^{+0.13}_{-0.25}$
	Γ	> 2.9	> 2.9	> 2.8	> 2.9
	Norm	10^{+120}_{-3}	6^{+8}_{-3}	50^{+70}_{-30}	9^{+2}_{-5}
nthcomp	Norm	$0.30^{+0.12}_{-0.12}$	$0.18^{+0.19}_{-0.18}$	< 0.2	< 0.1
$\chi^2/\text{d.o.f}$		3129/3380			

As shown in Fig. 3-7, the brief high flux state at 93 ks is captured by *Insight–HXMT*, *NuSTAR* and *Swift*. In particular, *Swift/XRT* captures the continuous flux drop from the high to the low flux state (panel (3) of Fig. 3-7), which takes around 400 s. However, the exact moment of the flux increase is not captured.

Chapter 4

High-density reflection spectroscopy of black hole X-ray binaries in the hard state

4.1 Introduction

The accretion process is widely regarded as the driving force behind numerous high-energy phenomena in the Universe, including active galactic nuclei (AGNs) and X-ray binaries (XRBs). Furthermore, it plays a pivotal role in our understanding of the growth of supermassive black holes (SMBHs) and galaxies^[38,210–211]. X-ray emissions serve as a potent tool for investigating the innermost regions of accreting black holes^[212–213].

One of the primary components in the X-ray spectra of black holes is the power-law continuum with a high-energy cutoff. This component is believed to originate from inverse Compton scattering of seed photons by a hot plasma, known as the corona, situated in close proximity to the black hole^[65,214]. The emission from this coronal region can illuminate the optically thick accretion disk, giving rise to reflected emission characterized by fluorescent emission, photoelectric absorption, and the Compton scattering hump^[105–106]. Owing to strong relativistic effects near the black hole, the observed reflected features exhibit significant skewing^[122,126,215] and harbor rich information about the spacetime geometry^[69,134–135,216] and the geometry of the disk-corona system^[120,217–218]. This technique has been effectively employed in numerous studies of both black hole XRBs and AGNs^[20,136,192,219].

Previous reflection models have typically assumed a disk electron density of $\log(n_e/\text{cm}^{-3}) = 15$. While this value is suitable for very massive black holes (e.g., $M_{\text{BH}} > 10^8 M_\odot$) found in AGNs^[220], standard disk models^[115] predict higher densities for less massive black holes. Reflection-based analyses of AGNs have revealed

that disk densities greater than $\log(n_e/\text{cm}^{-3}) = 15$ are sometimes necessary for supermassive black holes (SMBHs) with $M_{\text{BH}} < 10^7 M_\odot$, with the measured densities consistent with predictions of a radiation pressure-dominated disk^[7,11]. The adoption of a high-density reflection model has enabled the explanation of the "soft excess" feature observed in many Seyfert galaxies^[221] without the need for an additional component^[118]. Furthermore, the soft X-ray reverberation signature lends support to the reflection origin of the soft excess^[222–223].

Furthermore, an increased density within the disk could help resolve the puzzle of super-solar iron abundance observed in certain reflection spectral models^[6,8]. As the standard disk model suggests an inverse relationship between the disk density and the product of black hole mass and the square of the Eddington-scaled accretion rate ($M_{\text{BH}}\dot{m}^2$) for a disk dominated by radiation pressure (Eq. 4.1^[116]), we anticipate even greater densities within the accretion disks of XRBs, particularly in the hard state. While analyses of individual sources have supported this notion, the measured densities within the disks are generally lower than the theoretical predictions for disks dominated by radiation or gas pressure (refer to Fig. 8 of Jiang et al. 2019^[7]).

Previous high-density reflection modelling of black hole XRBs has only been conducted for a small number of sources^[6,8–9,13,167,224–231]. Moreover, on the $\log(n_e)$ – $\log(M_{\text{BH}}\dot{m}^2)$ diagram, there is still an obvious gap between the XRBs and AGNs sample (see Fig. 8 of Jiang et al. 2019^[7]). In this chapter, we undertake a systematic analysis on the broadband X-ray spectra of six black hole XRBs in the hard state that have not been investigated with high-density reflection models. The data selection and reduction are described in Sec. 4.2. Sec. 4.3 explains the spectral analysis. In Sec. 4.4 we discuss the results.

4.2 Observations and data reduction

We have chosen six black hole XRBs from the BlackCAT catalog^{①[39]}. These sources all have distance measurements available, allowing us to estimate their bolometric luminosities through broadband spectral fitting. Additionally, we have ensured that the sources were observed by *NuSTAR* to capture the Compton hump. Information about the selected sources is presented in Tab. 4-1. For those sources lacking measurements of their black hole mass, we have assumed a value of $10 \pm 1 M_\odot$ throughout this study to

^① <https://www.astro.puc.cl/BlackCAT/transients.php>

Table 4-1 Selected sources in this work

Source	Distance (kpc)	Mass (M_{\odot})	Inclination (°)	Ref
MAXI J1535–571	$4.1^{+0.6}_{-0.5}$	-	-	1
GRS 1739–278	6–8.5	-	-	2
GS 1354–64	25–61	-	< 79 (binary)	3
IGR J17091–3624	11–17	8.7–15.6	-	4,5
H 1743–322	8.5 ± 0.8	-	75 ± 3 (jet)	6
V404 Cyg	2.39 ± 0.14	$9.0^{+0.2}_{-0.6}$	67^{+3}_{-1} (binary)	7,8

Note. Selected sources and their properties. For references about the measurements of the distance, mass and inclination angle: (1) Chauhan et al. 2019^[234]; (2) Greiner et al. 1996^[235]; (3) Casares et al. 2009^[236]; (4) Rodriguez et al. 2011^[237]; (5) Iyer et al. 2015^[238]; (6) Steiner et al. 2012^[5]; (7) Miller-Jones et al. 2009^[239]; (8) Khargharia et al. 2010^[240]. Note that there is still debate on the distance of GS 1354–64 (also known as BW Cir). A smaller value has been reported by Gandhi et al. 2019^[241].

calculate the Eddington-scaled luminosity. We have selected *NuSTAR* observations in the hard state for each source, specifically targeting those displaying relativistic reflection features. A prominent characteristic of reflection by high-density accretion disks is the enhanced soft X-ray emission^[7]. Consequently, we have included contemporaneous (on the same day) *Swift* data whenever possible. Details of the selected observations are outlined in Tab. 4-2. Note that a few other sources may also meet our selection criteria, but they have already been investigated using reflection models incorporating variable electron density (e.g., GX 339–4, Jiang et al. 2019b^[6]; GRS 1716–249, Jiang et al. 2020^[9]; 4U 1630–47, King et al. 2014^[232], Connors et al. 2021^[167]; MAXI J1348–630, Chakraborty et al. 2021^[231]). These sources are excluded from the analysis in this study. MAXI J1820+070 also meets the selection criteria, but its accretion geometry is still under debate^[180,233]. We intend to explore this source in a future publication.

4.2.1 *NuSTAR*

We produce cleaned event files for both FPMA and FPMB using the tool `nupipeline` v0.4.9 and the calibration version 20220301. The source spectra are then extracted from circular regions centered on the sources with the `nuproducts` task. The background spectra are extracted from source-free areas with polygon regions created with `ds9`. Note that for V404 Cyg, five flux-resolved spectra are extracted from the two observations (see details in Sec. 4.6.2).

4.2.2 *Swift*

The *Swift*/XRT data are all in the Window Timing (WT) mode and are free from pile-up effects. The cleaned events files are produced using `xrtpipeline` v0.13.7 and the last calibration files as of September 2021. We extract the source spectra from circular regions centered on the source with a radius of 100 arcsec. The background regions are chosen to be annuli with an inner radius of 110 arcsec and an outer radius of 200 arcsec. We only include events with grade 0.

4.3 Spectral analysis

We perform spectral fittings using `XSPEC` v12.12.1^[154]. The *NuSTAR* data are utilized in the 3–79 keV band, while the *Swift* data cover the 1–10 keV band. To ensure statistical robustness, all data are grouped to maintain a minimum of 30 counts per bin. We adopt the element abundances from Wilm et al. 2000^[155] and the cross-sections from Verner et al. 1996^[156]. Model parameter values and uncertainties (unless stated otherwise, at a 90% confidence level) are determined using χ^2 statistics to obtain the best-fit results.

As the first step, we fit the broadband spectra of each source using a simple absorbed continuum model: `constant * tbabs * (diskbb + nthcomp)`. The `constant` model is utilized to account for the cross-normalization between instruments. Galactic interstellar medium absorption is modelled by `tbabs`^[155]. The `diskbb` component^[157] is employed to characterize the thermal emission from the multicolor accretion disk. Additionally, the coronal emission is modeled using the Comptonization model `nthcomp`^[55–56]. The data-to-model ratios for this fitting are displayed in Fig. 4-1. Common features observed in the plots of Fig. 4-1 include a broad line feature around 6–7 keV and a hump above 20 keV, which are recognized indica-

tors of a relativistic reflection component in the spectra^[159]. In certain instances, such as GRS 1739–278, a pronounced tail above 50keV is also observed. This high-energy excess may originate from additional emission from the jets. Alternatively, it could arise from the corona being a hybrid plasma containing both thermal and non-thermal particles^[242]. The presence of a non-thermal component can reduce the coronal temperature, resulting in the production of more hard X-ray photons compared to the pure thermal model^[57,243].

Next, we proceed to model the reflection features using relativistic reflection models: `constant * tbabs * (cflux * nthcomp + cflux * relconv * reflionx_HD)`. In this model, `reflionx_HD`^① represents a rest-frame disk reflection model computed with the `reflionx` code^[127]. The incident spectrum onto the accretion disk is assumed to be described by `nthcomp`. We link the photon index (Γ) and the coronal temperature (kT_e) parameters between `nthcomp` and `reflionx_HD`. Other free parameters of the reflection model include the ionization parameter $\xi = L/nr^2$ (where L is the ionizing luminosity from the primary source, n is the density, and r is the distance from the ionizing source), the iron abundance (A_{Fe}), and the electron density, which can vary between $\log(n_e/\text{cm}^{-3}) = 15\text{--}22$. The convolution kernel `relconv`^[60,126] is essential to incorporate relativistic effects. In this way, the model calculates the angle-averaged spectrum with only minor biases (smaller than the statistical errors) in the estimates of some parameters for low disk viewing angles^[244]. This model encompasses parameters such as the black hole spin (a_*), the disk inclination angle (i), the inner disk radius (R_{in}), and the emissivity profile. Here, we fix the spin parameter to constrain R_{in} . Specifically, the spin is fixed at $a_* = 0.2$ for H1743-322^[5], $a_* = 0$ for IGR J17091–3624 (see Sec. 4.6.2), and at the maximum value (0.998) for the other sources (see Sec. 4.6.2 for details). The inclination angle and the inner disk radius are left free during the fit. Regarding the emissivity profile, we employ a broken power-law profile. In cases where q_{out} and R_{br} are not constrained, a power-law emissivity ($q_{\text{in}} = q_{\text{out}}$) is used instead. Additionally, we incorporate a `cflux` model on each additive component to calculate the flux in the 0.1–100keV band. It’s important to note that in some instances, a distant reflection component, a disk thermal emission

^① The model is available for download from <https://www.michaelparker.space/reflionx-models>. The fits file used here is `reflionx_HD_nthcomp_v2.fits`.

component, or additional absorption components are necessary to adequately fit the data (see Fig. 4-10 and Sec. 4.6.2 for details).

To demonstrate the influence on the spectral parameter measurements resulting from incorporating a variable electron density, we further conduct fittings for each spectrum by setting $\log(n_e)$ to 15, a value commonly utilized by traditional reflection models. The best-fit parameters from these two sets of fittings are presented in Tab. 4-3 and Tab. 4-4. Additionally, we test the `relxill` model^[114] with $\log(n_e) = 15$ (refer to Sec. 4.6.1 and Tab. 4-5).

Figure 4-2 illustrates an example of high-density reflection observed in GRS 1739–278. The determined electron density for this source is $\log(n_e/\text{cm}^{-3}) = 19.0 \pm 0.4$. Allowing the electron density to vary as a free parameter improves the χ^2 by 60 with one additional degree of freedom (refer to Tab. 4-3 and Tab. 4-4). If the density were fixed at $\log(n_e/\text{cm}^{-3}) = 15$ (without re-fitting the spectrum), the reflection component in the soft X-ray band would appear suppressed, leading to an apparent excess in the residuals below 2 keV (refer to the third panel of Fig. 4-2). Conversely, increasing the density to $\log(n_e/\text{cm}^{-3}) = 22$ would noticeably strengthen the soft X-ray emission. This is attributed to the stronger free-free process on the disk with higher density, potentially resulting in an increase of the disk surface temperature (see the left panel of Fig. 4-6).

4.4 Results and Discussion

4.4.1 Comparisons with the low density model

In this section, we discuss the influence of the high-density reflection model on spectral parameters in comparison to the conventional low-density model. Fig. 4-3 presents the measurements of the disk ionization parameter, the iron abundance, and the reflection fraction. It is evident that when assuming a disk density of $\log(n_e/\text{cm}^{-3}) = 15$, the ionization parameter is consistently overestimated. This discrepancy likely arises because increasing the ionization parameter leads to stronger soft X-ray emissions in the reflected spectrum (see Fig. 3 of Garcia et al. 2013^[161]), thereby resembling the effects of high-density reflection (see Fig. 4 of Garcia et al. 2016^[113]).

When employing relativistic reflection models to analyze X-ray spectra of XRBs and AGNs, a super-solar iron abundance is often found^[192–193]. Some studies have suggested that high-density models might reduce the inferred iron abundance^[6,8]. How-

Table 4-2 Summary of observations analyzed in this work

Source	Obs ID (NuSTAR)	Exposure (ks)	Start date yyyy-mm-dd	Obs ID (Swift)	Exp. (ks) (Swift)
MAXI J1535–571	90301013002	10.3	2017-09-07		
GRS 1739–278	80002018002	29.7	2014-03-26	00033203003	1.9
GS 1354–64	90101006002	24.0	2015-06-13	00033811005	2.0
	90101006004	29.7	2015-07-11	00033811017	0.2
	90101006006	35.3	2015-08-06		
IGR J17091–3624	80001041002	43.3	2016-03-07	00031921099	1.5
	80202014002	20.2	2016-03-12	00031921104	1.9
	80202014004	20.7	2016-03-14	00031921106	1.0
H 1743–322	80001044002	50.4	2014-09-18		
	80001044004	61.1	2014-09-23		
	80001044006	25.7	2014-10-09		
	80002040002	28.3	2015-07-03		
	80202012002	65.9	2016-03-13		
	80202012004	65.7	2016-03-15		
	90401335002	38.4	2018-09-19		
	80202012006	65.7	2018-09-26		
V404 Cyg	90102007002	17.7	2015-06-24		
	90102007003	6.2	2015-06-25		

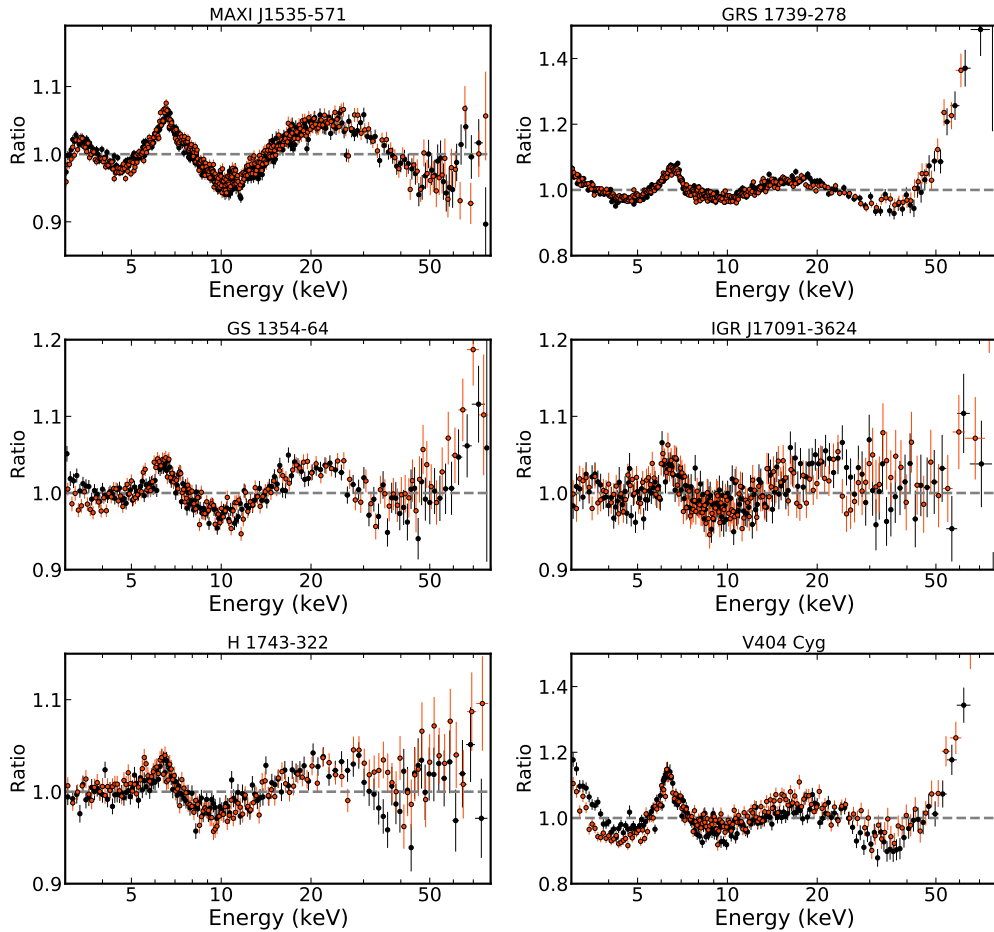


Figure 4-1 Data to model ratio when fitting with a simple absorbed continuum model: `constant * tbabs * (diskbb + nthcomp)`. Only one observation is shown for each source. The black and red colors represent data from FPMA and FPMB respectively. Data are rebinned for visual clarity.

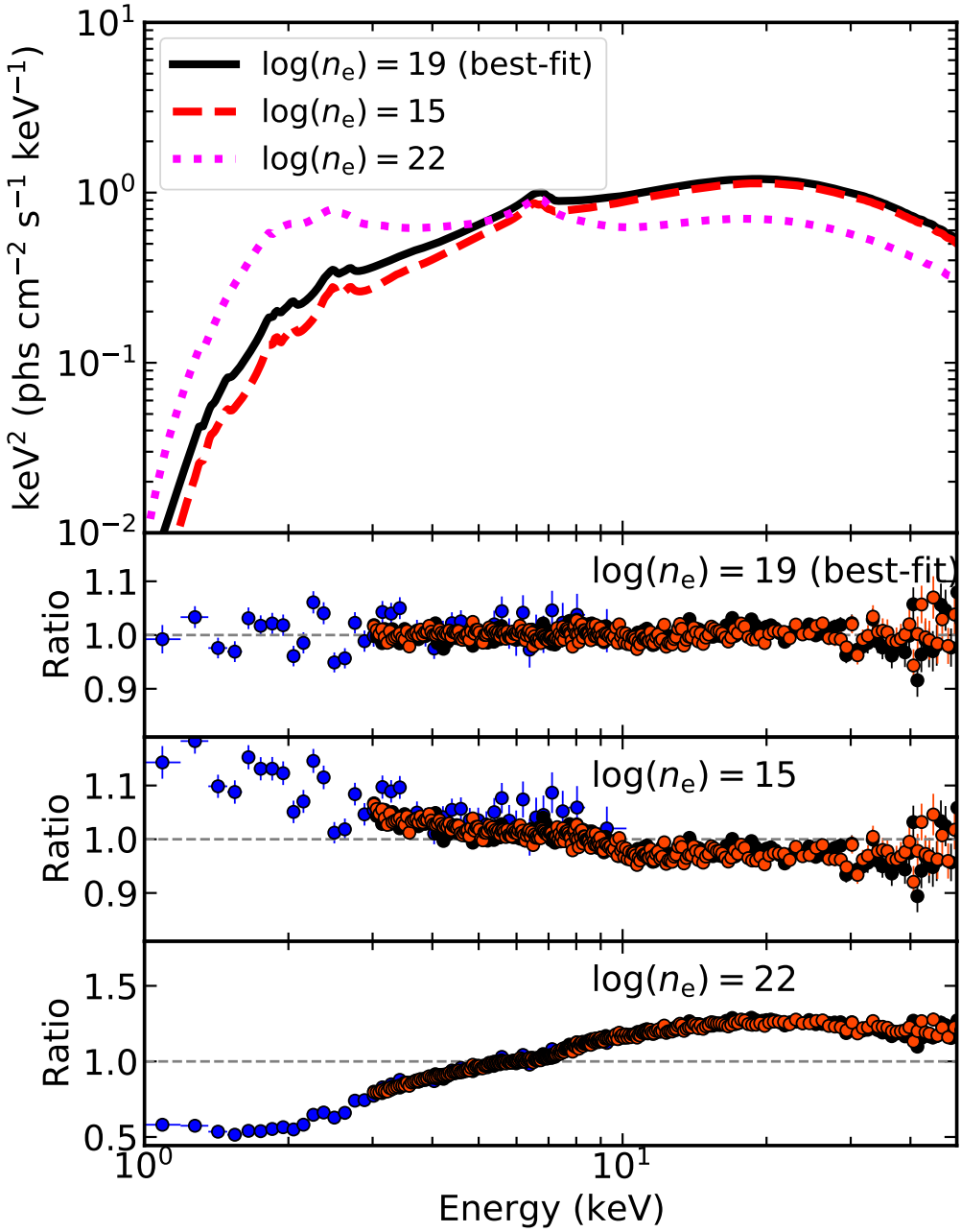


Figure 4-2 Upper: The black solid line shows the best-fit reflection component for GRS 1739–278 with a disk density of 10^{19} cm^{-3} . The red dashed and magenta dotted lines represent the cases when the density is set to 10^{15} cm^{-3} and 10^{22} cm^{-3} respectively without changing the other parameters. Lower three panels: The data to model ratios for the three cases in the upper panel. The blue, black and red data represent *Swift*-XRT, *NuSTAR*-FPMA and *NuSTAR*-FPMB respectively.

ever, we do not observe this effect in our dataset (see the middle panel of Fig. 4-3), possibly because the majority of our observations do not require a super-solar iron abundance, even when assuming $\log(n_e/\text{cm}^{-3}) = 15$.

We define the reflection strength parameter (R_{str}) as the ratio of energy flux between the reflected and coronal emissions in the 0.1–100 keV band. Fig. 4-3 demonstrates that, except for V 404Cyg, the model incorporating variable n_e consistently yields a higher reflection strength. As depicted in Fig. 4-2, the appearance of additional thermalized emission in the soft bands contributes to extra emission, possibly explaining the correlated increase in reflection strength with density.

It is crucial to assess whether the assumption of electron density affects the measurements of the inner disk radius. This is particularly important because black hole spin measurements via X-ray reflection spectroscopy rely on accurately determining the size of the Innermost Stable Circular Orbit (ISCO)^[134]. The constraints on R_{in} for each observation are illustrated in Fig. 4-4 by plotting the distribution of $\Delta\chi^2$ as a function of the inner disk radius. It reveals that allowing n_e to vary freely provides consistent measurements of R_{in} compared to the scenario with fixed n_e . This consistency is expected because R_{in} is primarily constrained by the red wing of the broad iron line due to the gravitational redshift effect, which is independent of the disk density.

4.4.2 Disk densities

In the left panel of Fig. 4-5, we illustrate our measurements of the disk density ($\log(n_e)$) versus $\log(M_{\text{BH}}\dot{m}^2)$. Previous studies in the literature of XRBs (the left cluster) and AGNs (the right cluster), which predominantly cover the parameter space of $\log(M_{\text{BH}}\dot{m}^2) < 0$ and $\log(M_{\text{BH}}\dot{m}^2) > 4$, are indicated in grey. Our data points fall within the gap $0 < \log(M_{\text{BH}}\dot{m}^2) < 3$. Overall, we observe that XRBs necessitate a significantly higher disk density compared to AGNs. Moreover, among our 21 spectra, 16 exhibit a disk density exceeding $\log(n_e) = 15$.

According to^[116], the density of radiation pressure-dominated standard disk^[115] follows:

$$n_e = \frac{1}{\sigma_T R_s} \frac{256\sqrt{2}}{27} \alpha^{-1} R^{3/2} \dot{m}^{-2} [1 - (R_{\text{in}}/R)^{1/2}]^{-2} [\xi'(1 - f)]^{-3} \quad (4.1)$$

where $\alpha = 0.1$ is the viscosity parameter, $\sigma_T = 6.64 \times 10^{-25} \text{ cm}^2$ is the cross-section for Thomson scattering, R_s is the Schwarzschild radius, R is the disc radius in units

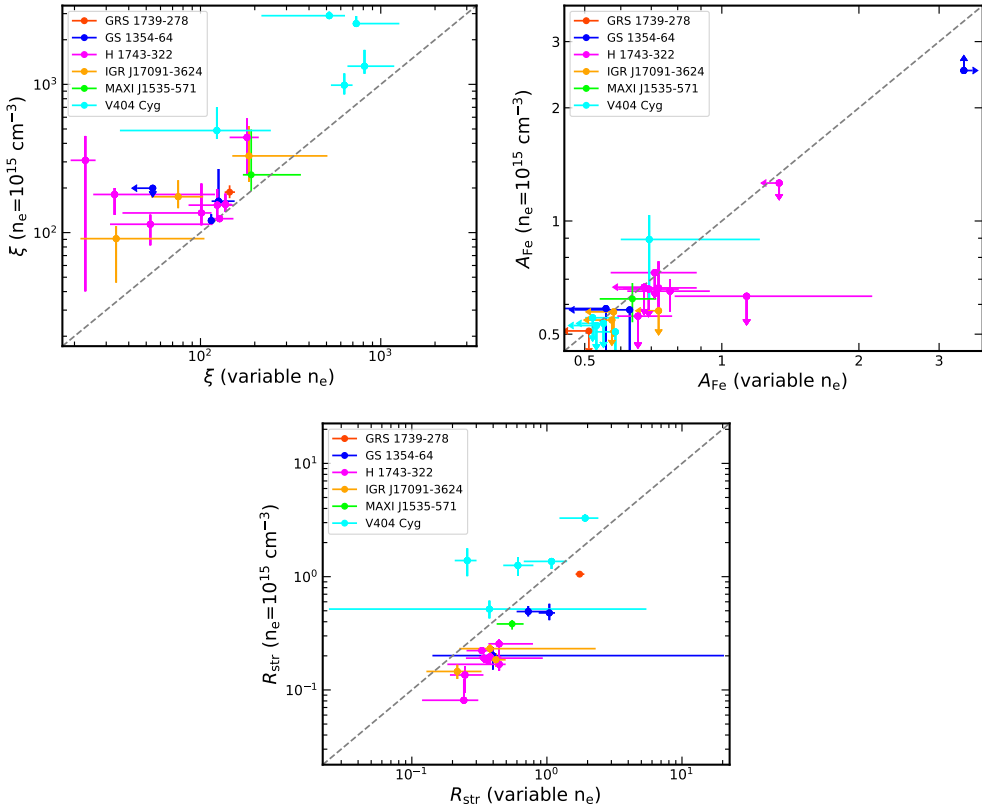


Figure 4-3 Comparison between the parameter measurements with the `reflectionx_HD` model that has a variable electron density and that with a fixed density at $\log(n_e/\text{cm}^{-3}) = 15$. The left panel is for the disk ionization parameter, the middle panel is for the iron abundance and the right panel is for the reflection strength (the energy flux ratio between the reflected and coronal emission in the 0.1–100 keV band). Colors are coded as in Fig. 4-5.

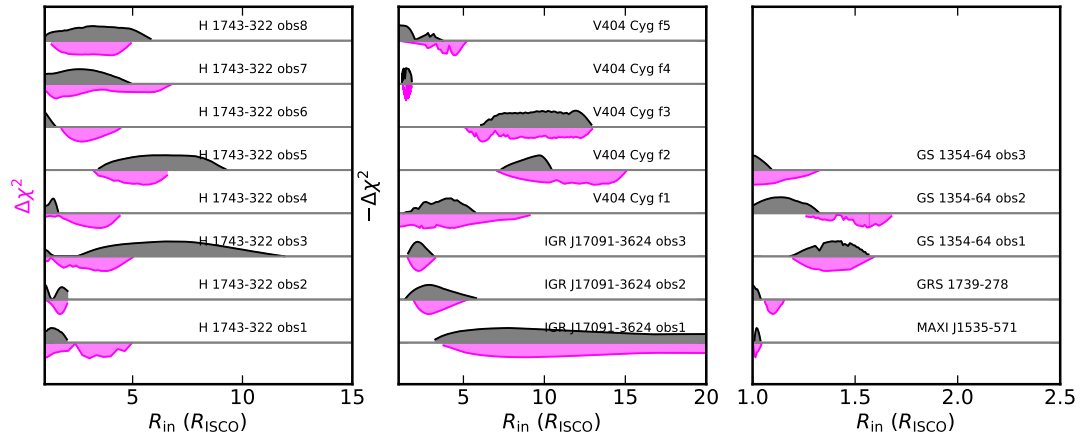


Figure 4-4 $\Delta\chi^2$ v.s. R_{in} for each observation obtained with `steppar` command in XSPEC. For the ISCO size, we assume $a_* = 0.2$ for H 1743–322^[5], $a_* = 0$ for IGR J17091–3624 (see Sec. 4.6.2) and $a_* = 0.998$ for the other sources. The horizontal grey lines represent the case $\Delta\chi^2 = 2.706$ (90% confidence level for one parameter of interest). Data are offset in the vertical direction for visual clarity. The regions between $\Delta\chi^2 - R_{\text{in}}$ and $\Delta\chi^2 = 2.706$ are shaded with magenta (n_e free) and grey ($n_e = 10^{15}$) colors. The grey areas result after a mirror symmetry transformation with respect to the horizontal lines. For sources with multiple observations, the sequence follows Tab. 4-2

of R_s , \dot{m} is the dimensionless mass accretion rate defined as $\dot{m} = L_{\text{bol}}/\eta L_{\text{Edd}}$ (η is the accretion efficiency that is 0.32 for $a_* = 0.998$ and 0.057 for $a_* = 0$, Thorne^[30]), ξ' is the conversion factor in the radiative diffusion equation that is chosen to be unity by^[115] and f is the fraction of accretion power transported from the disc to the corona. The solutions for different values of f are plotted in the left panel of Fig. 4-5. It's apparent that the majority of the AGN data (located in the lower right cluster) can be accounted for by these solutions, exhibiting a range of f values from 0.0 to 0.9 under the assumption of $\xi' = 1$. However, with the exception of a few observations featuring the highest accretion rates, most of the disk density measurements for black hole XRBs fall below the theoretical predictions.

We note that a considerable fraction (13/21) of our samples falls within the range of $L_{\text{bol}}/L_{\text{Edd}} < 10\%$. In such cases, the gas pressure may play a significant role in sustaining the disk, especially when f is large^[116]. According to^[116] the radius at which the radiation pressure (P_{rad}) equals the gas pressure (P_{gas}) is determined by:

$$\frac{R}{(1 - R^{-1/2})^{16/21}} = 40.5(\alpha M_{\text{BH}}/10M_{\odot})^{2/21}\dot{m}^{16/21}[\xi'(1 - f)]^{6/7} \quad (4.2)$$

On the left-hand side of this equation, the minimum is reached when $R \approx 5.7$. Con-

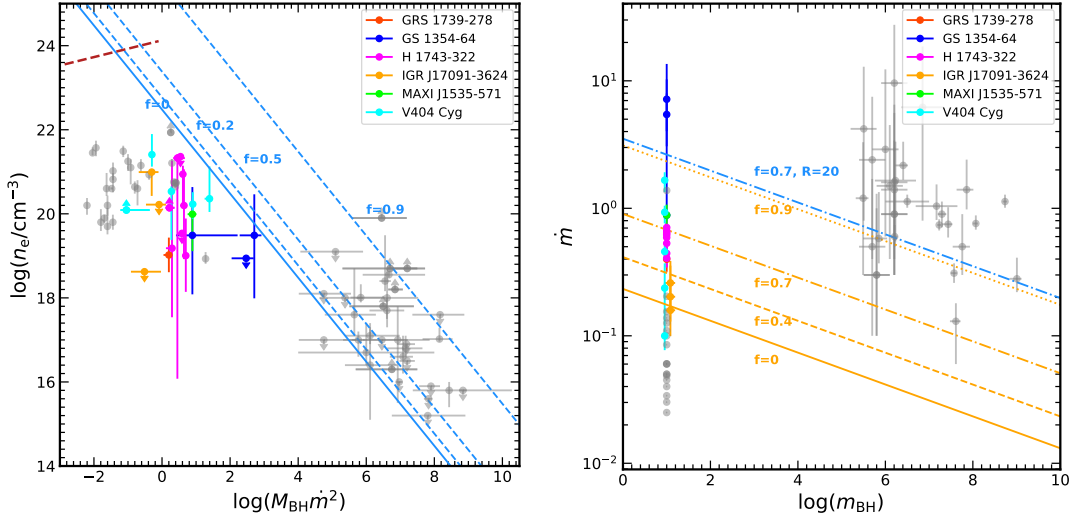


Figure 4-5 (Left) The variation of the disk electron density ($\log(n_e)$) with $\log(M_{\text{BH}}\dot{m}^2)$, where $\dot{m} = \dot{M}c^2/L_{\text{Edd}} = L_{\text{bol}}/\eta L_{\text{Edd}}$. The lines in light blue represent solutions of a radiation pressure-dominated disk for different values of f assuming $\xi' = 1$ and $R = R_s$. The dashed dark-red line represents the solution for a gas pressure-dominated disk with $f = 0$. (Right) The variation of the dimensionless mass accretion rate with the black hole mass. The orange lines show threshold mass accretion rates for a few values of f and $R = 5.7 R_s$, below which the disk is dominated by gas pressure. The line in light blue shows the solution for $f = 0.7$ and $R = 20 R_s$. The data in grey represent samples from Jiang et al.⁶ (GX 339-4), Jiang et al.⁷ (17 AGNs), Tomsick et al.⁸ (Cygnus X-1), Jiang et al.⁹ (GRS 1716-249), Liu et al.¹⁰ (GX 339-4) and Mallick et al.¹¹ (13 low-mass AGNs). Our results are marked with other colors.

sequently, given specific values for M_{BH} , f , and \dot{m} , the left-hand side can always be larger than the right-hand side, indicating dominance of gas pressure in the disk. In the right panel of Fig. 4-5, we show the threshold \dot{m} as a function of M_{BH} for several values of f . Based on the fitting of the AGN sample,^[11] found $f \approx 0.7$. As seen, the AGN sample is well above the threshold line for $f = 0.7$, suggesting that the radiation pressure should be important. However, this is not the case for our XRB sample, indicating the important role of gas pressure. In the left panel of Fig. 4-5, we also present the solution for a gas pressure-dominated disk, which still predicts a disk density larger than our measurements by two orders of magnitude. One possible explanation could be that the reflection model only probes the density of the disk surface. The current reflection models assume a uniform density in the vertical direction, which may not be the case in reality. Developing reflection models that consider the vertical density structure of the disk would be important to understand this issue.

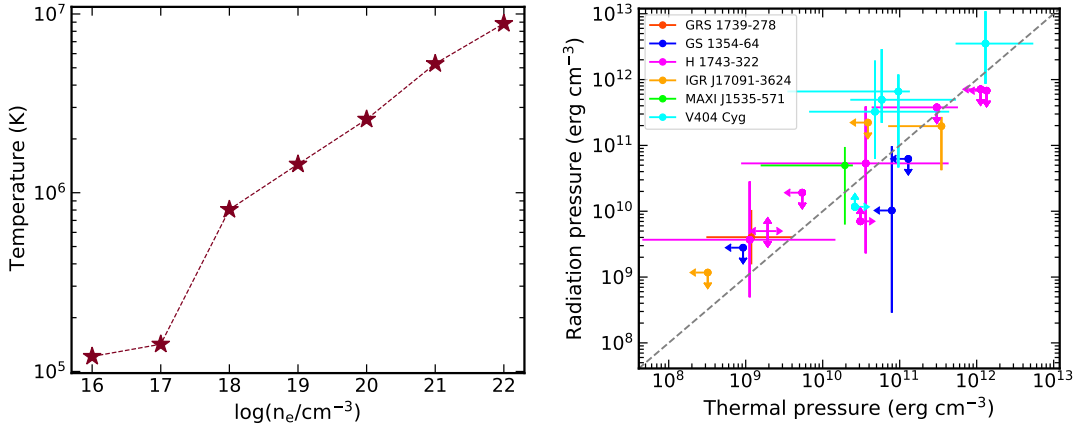


Figure 4-6 (Left) The temperature at the Thomson depth of $\tau = 1$ of the corona-illuminated disk as a function of the density. The coronal emission component and the disk properties are assumed to be the mean values from our samples ($\Gamma = 1.7$, $E_{\text{cut}}=100$ keV, $\xi=100$ erg cm s $^{-1}$ and $A_{\text{Fe}}=1$). The calculation is conducted with the `reflionx` code. (Right) The relation between the incident radiation pressure and the gas thermal pressure from this work. The grey line marks where $P_{\text{rad}} = P_{\text{th}}$.

In [11], the authors identify a equilibrium between the incident radiation pressure ($P_{\text{rad}} = L/4\pi r^2 c = \xi n_e/4\pi c$, where L represents the corona luminosity) and the thermal pressure of the disk gas ($P_{\text{th}} = n_e k_B T$). We investigate this scenario within our XRBs sample. The radiation pressure can be directly computed from the measured spectral parameters. To determine the gas thermal pressure, we utilize the `reflionx` code to derive the temperature at the Thomson depth $\tau = 1$ for $\log(n_e) = 16 - 22$ (see the left panel of Fig. 4-6). The parameters for the reflection calculation are set to the sample average: $\Gamma = 1.7$, $E_{\text{cut}}=100$ keV, $\xi=100$ erg cm s $^{-1}$ and $A_{\text{Fe}}=1$. The results are shown in the right panel of Fig. 4-6, where the dashed line represents $P_{\text{rad}} = P_{\text{th}}$. As observed, there indeed exists a equilibrium between the incident radiation pressure and the thermal pressure of the gas. It's important to note that in this comparison, we disregard the influence of the magnetic field and the radiation pressure from the disk.

4.4.3 Disk inner radius

The inner disk radius (R_{in}) is a crucial parameter for understanding the accretion process. The disk truncation scenario has been widely employed to explain the distinct states of XRBs^[62]. It is generally believed that the standard cold accretion disk is truncated at large radius in the low luminosity hard state^[15] while it extends to the innermost stable circular orbit (ISCO) in the high luminosity soft state^[101–102].

Nonetheless, ongoing debate persists regarding whether the disk is truncated in the bright hard state^[245–246]. We plot our reflection-based measurements of the inner disk radius against the Eddington-scaled luminosity in Fig. 4-7, alongside previous measurements in the hard state of GX 339–4, which stands as one of the most extensively studied sources concerning R_{in} (see also Fig. 8 of Wang et al. 2018^[22]). For GX 339–4, the measurements of R_{in} from timing mode data of *XMM-Newton* EPIC/pn consistently exceed those from *NuSTAR* or *RXTE* data. This may be due to the complex pile-up effects that are hard to eliminate (see the discussion in of Want et al. 2018^[22]).

Our measurements of R_{in} from six black hole XRBs in the hard state broadly align with the trend observed in GX 339–4, and we extend this trend to the regime where $L/L_{\text{Edd}} > 20\%$. We see that a small R_{in} ($< 10 R_g$) is required when $L/L_{\text{Edd}} > 1\%$ even though all the data in Fig. 4-7 are from the hard state. For $L/L_{\text{Edd}} > 10\%$, almost all measurements are consistent with R_{in} being smaller than twice the ISCO size (assuming $a_* = 0.998$). These results support the scenario that the inner disk radius can indeed reach the ISCO in the bright hard state. Although it appears that the H 1743-322 disk is truncated at a large radius in the hard state, the black hole in this system exhibits a low spin as measured by the independent continuum-fitting method ($a_* \sim 0.2$ ^[5]) and thus yielding a large ISCO size ($R_{\text{ISCO}} = 5.3 R_g$, see the magenta dashed line in Fig. 4-7). Things are more complicated for IGR J17091–3624 given that its black hole spin parameter is still uncertain (see Sec. 4.6.2).

4.4.4 Inclination angle

In our analysis, we consistently treat the inclination as a free parameter. This approach enables a comparison between the inclination angle derived from reflection modeling and those obtained through alternative methods, often pertaining to the inclination of the jet or the binary system. Notably, for GS 1354–64, only an upper limit of 79° has been established for its binary inclination based on the absence of X-ray eclipses^[236]. Conversely, a stringent constraint on the binary inclination of V 404Cyg (67^{+3}_{-1} ,^[240]) contrasts with the lower value derived from the reflection analysis.

Indeed, similar disparities between the inclination angles derived from reflection spectra and those obtained through other means have been observed in various sources. For instance, in the case of Cygnus X-1, reflection spectra consistently indicate an inclination around 40° ^[136,219,247], whereas its binary inclination is measured at $27.51^{+0.77}_{-0.57}$

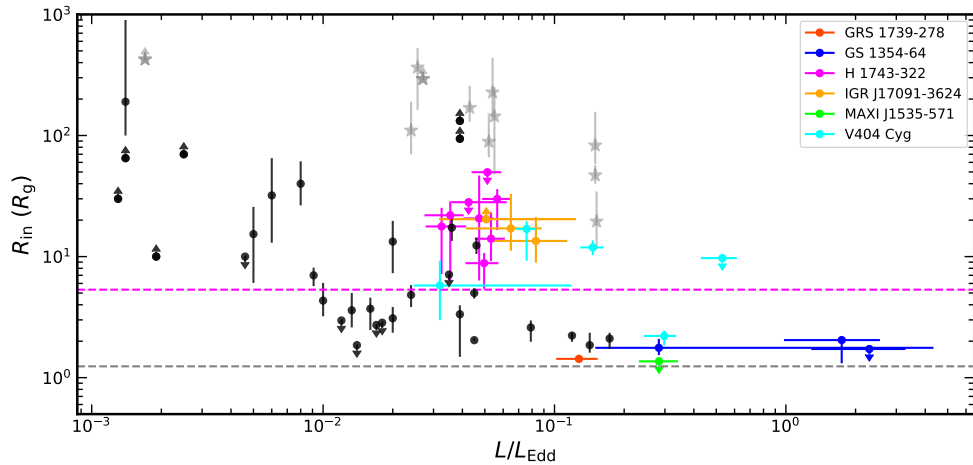


Figure 4-7 The evolution of the inner disk radius with the Eddington-scaled luminosity. Our results are color-coded as in Fig. 4-5. The data in black and grey are from previous measurements of GX 339–4^[12–22] where the grey stars mark the measurements with data in the timing mode of *XMM-Newton* EPIC/pn. The grey and magenta dashed horizontal lines represent the ISCO radii for $a_* = 0.998$ and 0.2 respectively.

◦[248]. It’s important to note that relativistic reflection spectra primarily probe the inner portion of the accretion disk, which may not necessarily align with the orbital inclination. This discrepancy can arise from the presence of a warped disk, where the orientation of the inner disk deviates from the orbital plane^[249]. Simulations suggest that such misalignments between the black hole spin axis and the orbital angular momentum could be common in black hole XRBs^[250–251]. While observational evidence of warped disks has been detected in a few sources, such as MAXI J1535–571^[252] and MAXI J1820+070^[253–254], the impact of a warped disk on relativistic reflection spectra warrants further investigation, although it falls outside the scope of this study.

For H 1743–322, Steiner et al. 2012^[5] determined an inclination angle of $75^\circ \pm 3^\circ$ for its large-scale ballistic jets, which are believed to align with the black hole spin axis. According to the Bardeen-Petterson effect^[255], the inner disk region should also align with the spin axis. However, the reflection model suggests a lower inclination angle of $30^\circ – 40^\circ$. We note that inclination angle measurements derived from reflection analysis can be affected by systematic uncertainties, such as uncertainties in the corona geometry or simplifications in the model calculations (see discussions in Bambi et al. 2021^[69]). In some cases, the systematic uncertainty can be as large as $\sim 30^\circ$ ^[256–257]. This could potentially explain the observed discrepancy.

4.4.5 Reflection strength

Note that the reflection strength (R_{str}) defined in this work differs from the reflection fraction (R_f) parameter in^[178]. R_f represents the ratio between the corona intensity shining on the disk and that reaching infinity, and it is determined by the accretion geometry. On the other hand, R_{str} could be influenced by the inclination between the line-of-sight and the black hole spin axis^[178]. Despite this distinction, in our sample, most sources exhibit inclinations in the range of 20°–30° (except for MAXI J1535–571). Therefore, R_{str} can still provide insight into the disk-corona geometry. In the left panel of Fig. 4–8, we illustrate the relationship between R_{str} and the Eddington-scaled X-ray luminosity from our analysis. We observe no strong correlation between the two parameters, with a Pearson correlation coefficient (r) of 0.32 ($1 - p = 75\%$). We further explore the correlation between the photon index and the reflection strength (see the middle panel of Fig. 4–8) but still find no strong correlation ($r = 0.22, 1 - p = 66\%$).

4.4.6 Photon index

It is well known in the literature that a positive statistical correlation exists between the Eddington ratio ($\lambda_{\text{Edd}} = L_{\text{bol}}/L_{\text{Edd}}$) and X-ray photon index (Γ) at high accretion rates in AGNs^[23,258–259] and XRBs^[260–262]. Conversely, at low accretion rates (e.g. $\lambda_{\text{Edd}} < 1\%$ ^[263–264]), a negative correlation is often observed^[265–266]. At extremely low accretion rates (e.g. $\lambda_{\text{Edd}} < 10^{-4}$), Γ has been found to saturate^[267–270]. This switch between correlation behaviors may suggest transition between different accretion modes^[271–272]. We investigate this correlation with our sample in the right panel of Fig. 4–8. All our data fall within the range of $\lambda_{\text{Edd}} > 1\%$ and are divided into two branches on the Γ - λ_{Edd} diagram. In the lower branch, the data for V 404Cyg are not from canonical outbursts but rather from strong repeated flaring events lasting less than 1 ks (see Sec. 4.6.2). Furthermore, these flaring events might be linked to transient jet activities rather than changes in the mass accretion rate^[273]. This may explain why Γ remains stable despite fluctuations in X-ray luminosity exceeding one order of magnitude. Apart from V 404Cyg, the data for GS 1354–64 also deviate from the trend observed in other sources. When considering only the upper branch, a strong positive correlation between the two parameters emerges ($r = 0.83, 1 - p = 99.96\%$). Additionally, we include in Fig. 4–8 the statistical relationship identified in AGNs by^[23], which aligns well with our upper branch. This suggests that variations in the mass ac-

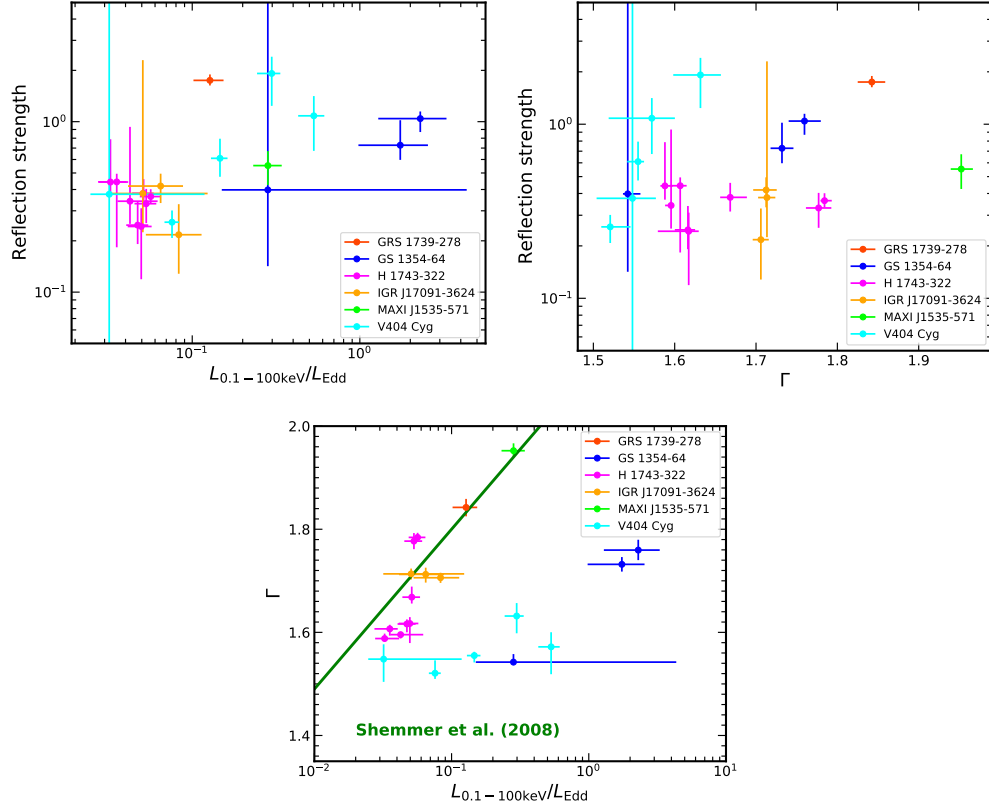


Figure 4-8 (Left) The relation between the reflection strength parameter (R_{str} , defined as the flux ratio between the reflected component and the power-law component in 0.1–100 keV band) and the Eddington-scaled luminosity. (Middle) The relation between R_{str} and the photon index Γ . (Right) The variation between the photon index Γ and Eddington-scaled luminosity. The line in green represents the statistical relation in AGNs found by^[23].

cretion rate influence the physical properties of the hot corona similarly in both XRBs and AGNs.

4.4.7 The corona properties in the compactness-temperature plane

The coronal properties can be studied on the compactness-temperature ($\ell-\Theta$) plane. The compactness is defined as:

$$\ell = \frac{L}{R} \frac{\sigma_T}{m_e c^3} \quad (4.3)$$

where L is the luminosity, R is the source radius assuming a spherical geometry, σ_T the Thomson cross section and m_e the electron mass. By examining a sample of *NuSTAR* measurements from both AGNs and black hole XRBs plotted on the compactness-temperature plane, Fabian et al. 2015^[54] observed that most of the measurements

are clustered near the limit set by electron-positron pair production^[274]. This clustering provides support for the significance of pair production in the corona. Pair production processes can lead to runaway production, effectively distributing energy and consequently limiting the coronal temperature below the pair production threshold^[57,67,275–276]. Additionally, the presence of many sources above the electron-electron coupling line suggests that energetic electrons may not undergo sufficient thermalization, indicating the potential existence of a magnetized and hybrid plasma containing both thermal and non-thermal particles^[277–278]. Incorporating a non-thermal component in the plasma would tend to reduce the temperature of the thermal component and result in a high-energy excess compared to spectra produced by purely thermal Comptonization. This characteristic aligns well with the data for GRS 1739–278, which exhibits the lowest observed coronal temperature in the sample. Fabian et al. 2017^[243] further investigated the hybrid plasma scenario using a sample of AGNs and found that a non-thermal fraction of 10%-30% could adequately account for the properties observed in most objects.

We illustrate the data from our sample on the compactness-temperature diagram alongside theoretical predictions from hybrid plasma models, aiming to elucidate the physical characteristics of the corona during the hard state (refer to Fig. 4-9). The computations of the theoretical lines are conducted using the `eqpair` model^{[57]①}. In this context, the non-thermal fraction, denoted as the ratio between the compactness parameter attributable to non-thermal components and the total heating power (ℓ_{nth}/ℓ_h), plays a pivotal role. For a constant heating power, an increase in the non-thermal fraction corresponds to a reduction in the equilibrium temperature. We assume a corona size of $10 R_g$, which is a reasonable value given existing measurements on AGNs with X-ray reflection modelling or reverberation analysis^[119,217,279].

In Fig. 4-9, it is evident that all our measurements fall below the theoretical line representing purely thermal plasma. Notably, a considerable portion (15 out of 21) of our dataset lies below the curve corresponding to $\ell_{\text{nth}}/\ell_h = 30\%$, indicating a potentially higher non-thermal contribution. It's worth mentioning that the hybrid plasma model has been previously employed in the analysis of various black hole XRBs^[242,280–283],

① The description of the model can be found here: <http://www.astro.yale.edu/coppi/eqpair/eqpair4.ps>. The model is available in XSPEC: <https://heasarc.gsfc.nasa.gov/xanadu/xspec/manual/XSmodelEqpair.html>

revealing that a substantial non-thermal fraction is necessary, particularly in the hard state^[284–286].

For individual sources, both GS 1354–64 and IGR J17091–3624 exhibit the anticipated trend for a pair-dominated plasma, wherein the coronal temperature decreases as the radiation compactness increases. Remarkably, even the flux-resolved data of V404Cyg adhere to this trend, despite the short timescale of the flaring activities analyzed here, lasting approximately a few kiloseconds (see Sec. 4.6.2). In the case of H 1743–322, two observations stand out as outliers with higher temperatures compared to the other six observations exhibiting a similar level of radiation compactness. This discrepancy may suggest a lower non-thermal fraction, although it is also plausible that the assumption of a $10R_g$ corona size is too conservative for these particular observations. However, this seems less likely given that the measurements of R_{in} for these two observations are consistent with the assumed corona size. It is noteworthy that these two outliers correspond to the so-called "failed" outbursts^[287], during which the source remains in the low hard state exclusively.

We delve deeper into the outliers observed in H 1743–322 by examining the correlation between X-ray and radio luminosity. This particular source exhibits a known transition between two distinct radio-X-ray correlations: the "radio loud" and "radio quiet" branches^[93]. Hence, we investigate whether our inferred high/low non-thermal fraction aligns with the source being situated on either the radio loud or radio quiet branch. This alignment might be expected if, for instance, the non-thermal fraction is linked to the properties of the jet. However, our analysis does not reveal such a correspondence. Only one of our outliers has a simultaneous radio observation, and it corresponds to the radio quiet branch (with a 1.28 GHz flux density of 0.88 ± 0.05 mJy; Williams et al.²⁸⁸), similar to several of the non-outliers.

4.5 Conclusion

In this work, we analyzed the broadband X-ray spectra of six stellar-mass black hole XRBs in the hard state with data from *NuSTAR* and *Swift*. The purpose is to test the effect of X-ray reflection by a high-density accretion disk. The main results are as follow:

- The model with the disk electron density fixed at 10^{15} cm^{-3} systematically overestimates the ionization degree of the disk atmosphere. The measurement of the

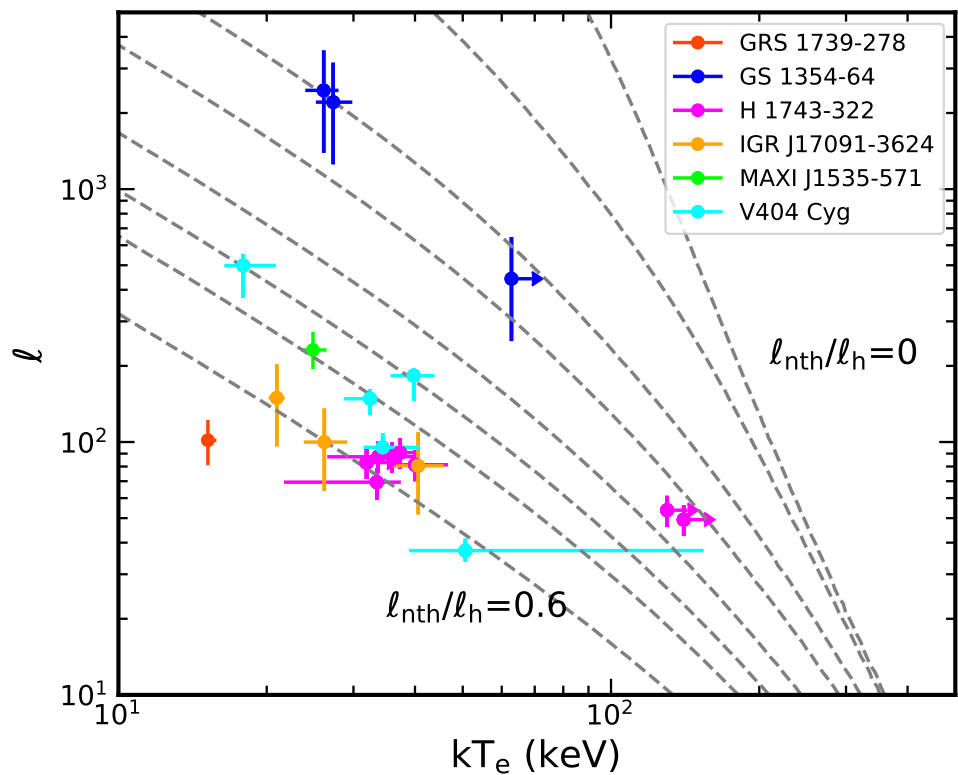


Figure 4-9 The relation between the coronal temperature and and the dimensionless compactness parameter from our analysis. The grey dashed lines are theoretical predictions of a hybrid plasma with $\ell_h/\ell_s = 1$, where ℓ_h is the total heating parameter and ℓ_s is the compactness of the soft photons. From right to left, the lines represent solutions with a non-thermal fraction (ℓ_{nth}/ℓ_h) of 0, 0.01, 0.05, 0.1, 0.2, 0.3, 0.4 and 0.6 respectively.

inner disk radius is not affected by the assumption of disk density.

- The X-ray spectra of black hole XRBs require a higher disk density than that of AGNs. For the selected observations in this work, the accretion disk should be dominated by gas pressure. However, the measured densities are lower than either the prediction of gas or radiation pressure-dominated disk. The discrepancy might represent the vertical density structure of the disk.
- From our analysis and previous measurements, we find that the inner disk radius can be close to the ISCO in the hard state.
- We find that the reflection strength is not correlated to the Eddington ratio or photon index. There is a strong correlation between the Eddington ratio and photon index which is in good agreement with the statistical relation found in AGNs.
- The coronal temperature is lower than the prediction of a purely thermal plasma and can be explained by a hybrid plasma with a non-thermal fraction around 30%.

4.6 Appendix

4.6.1 Modeling with `relxillcp`

Besides the `reflionx`-based models, the `relxill`^[14] model is also commonly used to fit relativistic reflection spectra. To compare our results with existed analysis in the literature, we replace the reflection component with the model `relxillcp` (Model 2), which is a flavor of the package `relxill` v1.4.3. This model assumes a electron density of the disk $\log(n_e/\text{cm}^{-3}) = 15^{\circledcirc}$. Moreover, relativistic effects are properly taken into account by combining the rest-frame reflection code `xillver`^[106,161] and the relativistic broadening code `relline`^[60,126]. The reflection fraction is set to -1 so the model returns only the reflection component. The best-fit parameters are shown in Tab. 4-5.

^① Note that the latest version of `relxillcp` allows a variable electron density in the range $\log(n_e/\text{cm}^{-3}) = 15\text{--}20$ (see <http://www.sternwarte.uni-erlangen.de/~dauser/research/relxill/>)

4.6.2 Spectral analysis results for individual sources

GRS 1739–278

GRS 1739–278 was initially discovered in 1996 by the *Granat* satellite^[289]. Its estimated distance ranges from 6 to 8.5 kpc^[235]. A *NuSTAR* observation of this source was previously analyzed by Miller et al. 2015^[290], albeit without the inclusion of *Swift* (*Swift*) data. In their study, both `reflionx` and `relxill`-based reflection models were tested, revealing a high black hole spin ($a_* = 0.8 \pm 0.2$), an intermediate inclination (20°–40°), and an inner disk radius close to the ISCO. Our reflection modeling yields similar measurements (refer to Tab 4-4 and Tab 4-5). The notably low temperature of the corona was previously identified by Miller et al. 2015^[290]. Another *NuSTAR* observation of GRS 1739–278 exists in the archive (obsID: 80101050002) from September 2015, but the reflection features in this observation are too weak^[291].

GS 1354–64

GS 1354–64, a Galactic black hole candidate, was first discovered in 1987^[292]. Despite extensive study, only a lower limit of approximately $8M_\odot$ has been determined for its black hole mass, and its distance remains uncertain, ranging from 25 to 61 kpc^[236]. The first two observations in June and July, as analyzed in our study, were previously examined by El-Batal et al. 2016^[293], albeit without including the *Swift* data. In their analysis,^[293], a substantial truncation of the accretion disk was observed in the June observation using a low-density `relxill` model, consistent with our findings presented in Table 4-5. Furthermore, the high disk inclination and small inner disk radius measured from the July observation align with previous investigations^[293–294].

IGR J17091–3624

GRJ17091–3624 is a Galactic black hole candidate located at a distance estimated to be between 11 kpc and 17 kpc^[237], although debates persist regarding its precise distance^[295]. The determination of its black hole spin parameter remains uncertain, with previous studies reporting conflicting results, including measurements indicating both negative spin^[296–297] and high spin ($a_* > 0.9$)^[298].

The three *NuSTAR* and *Swift* observations included in our analysis were previously

examined by Xu et al. 2017^[299] using low-density reflection models based on `relxill`. By assuming $a_* = 0.998$, Xu et al. 2017^[299] found evidence of a truncated disk ($R_{\text{in}} \sim 20R_g$) and an intermediate disk inclination angle ($i \sim 30^\circ - 40^\circ$), findings that are consistent with our analysis results (see Table 4-5).

V404 Cyg

V404 Cyg is a dynamically confirmed black hole X-ray binary situated at a distance of 2.39 ± 0.14 kpc^[239]. The estimated mass of the black hole in this system is approximately $9.0^{+0.2}_{-0.6} M_\odot$ ^[240]. The two observations of V404Cyg analyzed in this study exhibit significant flaring variability, as shown in Figure 2 of Walton et al. 2017^[273], with the count rate per focal plane module (FPM) ranging from 100 to more than 10^4 ct s⁻¹. Ref^[273] demonstrated the presence of strong relativistic reflection features in the X-ray spectra of V404 Cyg, indicating the possibility of constraining the black hole spin parameter by dividing the data according to flux levels and excluding data with deep absorption edges. We adopt a similar data processing approach to Walton et al. 2017^[273] and extract spectra for five flux levels, as outlined in Table 1 of^[273].

To model the spectra of V404 Cyg, additional components need to be incorporated, including a neutral local absorption layer, an ionized absorption layer, and a distant reflection component. The ionized absorption is characterized using a grid calculated with XSTAR^[300–301]. The complete Model 2 for this source is described as follows:

```
constant * tbabsgal * (tbabslocal * xstar * (cflux * nthcomp
+ cflux * relxillcp) + cflux * xillvercp). Here, the column density for Galactic absorption is fixed at  $10^{22}$  cm-2, while the absorption column locally to the source is treated as a free parameter. The ionization state of the distant reflection component (xillvercp) is set to  $\log(\xi) = 0$ , with the other parameters linked to the relativistic reflection component.
```

H 1743–322

H 1743–322 was discovered in 1977^[302]. It is located at 8.5 ± 0.8 kpc and the jet inclination is $75^\circ \pm 3^\circ$ ^[5]. The continuum fitting method indicates a black hole spin around $a_* \sim 0.2$ ^[5].^[303] estimated the black hole mass to be $11.21^{+1.65}_{-1.96} M_\odot$ using the two-component advective flow (TCAF) solution and the correlation between photon

index and frequency of the quasi-periodic oscillation (QPO).

There are eleven *NuSTAR* observation in the archive, three of which do not show reflection features. The other eight observations analyzed in this work are all in the hard state. The two observations from 2016 have been analyzed by^[304] and a truncated disk was found. However, our analysis with `relxillcp` model requires a disk extends to the ISCO. This difference is possibly due to the fact that we treat the inclination angle as a free parameter while in^[304] it is fixed at 75°. The two 2018 observations have also been analyzed with reflection models assuming a fixed inclination angle^[287] and again their measurements on R_{in} are larger than ours.

MAXI J1535–571

MAXI J1535–571 is a black hole candidate discovered in 2017^[305]. It is located at a distance of $4.1^{+0.6}_{-0.5}$ kpc^[234]. Previous reflection analysis indicates a high black hole spin and high inclination angle^[252,306]. Following^[306], we include a disk component and a distant reflection component to the full model to fit the *NuSTAR* data. The high inclination angle is well recovered with our fit (see Tab 4-5).

Table 4-3 Best-fit parameters with reflections that has variable electron density

Source	Date	nH	$R_{\text{in}} (R_{\odot})$	Γ	$\log(n_e)$	ξ	$kT_e (\text{keV})$	Incl (deg)	A_{Fe} (solar)	$\log(F_{\text{ref}})$	$\log(F_{\text{po}})$	χ^2/ν
GRS 1739-278	20140326	$3.15^{+0.12}_{-0.05}$	$1.43^{+0.08}_{-0.07}$	$1.842^{+0.016}_{-0.017}$	$19.0^{+0.4}_{-0.4}$	145.0^{+10}_{-10}	$15.2^{+0.6}_{-0.5}$	$24.2^{+2.5}_{-2.4}$	$0.500^{+0.011}_{-0.011}$	$-7.810^{+0.03}_{-0.023}$	$-8.053^{+0.015}_{-0.018}$	3431.9/3238
GS 1354-64	20150613	$1.18^{+0.07}_{-0.07}$	$1.76^{+0.3}_{-0.3}$	$1.542^{+0.016}_{-0.006}$	$19.5^{+1.1}_{-1.4}$	5.0^{+50}_{-P}	25^{+10}_{-10}	$5.0^{+P}_{-1.6}$	$-9.4^{+1.7}_{-0.5}$	$-8.960^{+0.07}_{-0.021}$	$-8.960^{+0.07}_{-0.021}$	2030.5/1872
GS 1354-64	20150711	$1.21^{+0.07}_{-0.07}$	$2.04^{+0.16}_{-0.7}$	$1.732^{+0.014}_{-0.014}$	$17.7^{+1.2}_{-P}$	115^{+6}_{-5}	$27.3^{+2.5}_{-2.1}$	20^{+9}_{-P}	$0.50^{+0.13}_{-0.06}$	$-8.40^{+0.15}_{-0.08}$	$-8.262^{+0.015}_{-0.015}$	3115.3/2918
GS 1354-64	20150806	$0.44^{+0.24}_{-0.19}$	$1.3^{+0.4}_{-P}$	$1.760^{+0.022}_{-0.019}$	$19.5^{+1}_{-1.5}$	130^{+50}_{-11}	$26.1^{+1.9}_{-2.2}$	22^{+8}_{-P}	$0.50^{+0.06}_{-P}$	$-8.197^{+0.029}_{-0.029}$	$-8.22^{+0.03}_{-0.02}$	2898.9/2821
IGR J17091	20160307	$1.79^{+0.07}_{-0.07}$	55^{+P}_{-34}	$1.713^{+0.011}_{-0.011}$	$18.0^{+0.64}_{-P}$	34^{+71}_{-13}	41^{+5}_{-15}	41^{+P}_{-18}	$0.50^{+0.07}_{-P}$	$-9.06^{+0.8}_{-0.23}$	$-8.641^{+0.012}_{-0.012}$	2821.7/2751
IGR J17091	20160312	$2.05^{+0.08}_{-0.15}$	17^{+16}_{-6}	$1.712^{+0.013}_{-0.016}$	$20.99^{+0.02}_{-0.02}$	75^{+28}_{-22}	$26.2^{+3.0}_{-2.4}$	$22.0^{+9.0}_{-P}$	$0.58^{+0.15}_{-P}$	$-8.92^{+0.07}_{-0.11}$	$-8.547^{+0.009}_{-0.009}$	2368.3/2409
IGR J17091	20160314	$1.57^{+0.19}_{-0.07}$	14^{+8}_{-5}	$1.71^{+0.01}_{-0.01}$	$18.0^{+2.3}_{-P}$	190^{+320}_{-320}	$21.0^{+0.8}_{-0.8}$	$17.3^{+7.7}_{-P}$	$0.50^{+0.08}_{-P}$	$-9.04^{+0.18}_{-0.18}$	$-8.372^{+0.11}_{-0.11}$	2305.0/2321
H 1743-322	20140918	$1.99^{+0.27}_{-0.04}$	6^{+22}_{-P}	$1.5956^{+0.029}_{-0.007}$	$21.33^{+0.09}_{-5}$	33^{+87}_{-8}	34^{+4}_{-12}	5^{+21}_{-P}	$0.65^{+0.12}_{-0.07}$	$-8.82^{+0.4}_{-0.13}$	$-8.357^{+0.025}_{-0.025}$	3039.2/3006
H 1743-322	20140923	$1.46^{+0.11}_{-0.5}$	$8.8^{+1.9}_{-3}$	$1.617^{+0.012}_{-0.004}$	$18.3^{+1.3}_{-P}$	180^{+30}_{-36}	33.7^{+4}_{-7}	28^{+4}_{-4}	$0.5^{+0.81}_{-P}$	$-8.87^{+0.11}_{-0.11}$	$-8.2562^{+0.022}_{-0.029}$	3324.7/3187
H 1743-322	20141009	$2.03^{+0.21}_{-0.23}$	21^{+26}_{-14}	$1.616^{+0.009}_{-0.016}$	$20.7^{+0.68}_{-P}$	53^{+64}_{-21}	49^{+P}_{-P}	17^{+6}_{-17}	$1.1^{+1.0}_{-0.3}$	$-8.89^{+0.14}_{-0.14}$	$-8.279^{+0.009}_{-0.009}$	2498.7/2605
H 1743-322	20150703	$2.41^{+0.17}_{-0.3}$	18^{+8}_{-11}	$1.588^{+0.011}_{-0.006}$	22.0^{+P}_{-P}	23.0^{+3}_{-4}	500^{+P}_{-360}	5^{+16}_{-P}	$0.71^{+0.17}_{-0.14}$	$-8.86^{+0.25}_{-0.08}$	$-8.505^{+0.005}_{-0.007}$	2387.6/2416
H 1743-322	20160313	$2.11^{+0.11}_{-0.12}$	30^{+6}_{-13}	$1.784^{+0.009}_{-0.005}$	$19.0^{+0.9}_{-0.9}$	137^{+12}_{-10}	37^{+3}_{-3}	27^{+3}_{-3}	$0.6^{+0.1}_{-P}$	$-8.68^{+0.04}_{-0.04}$	$-8.2400^{+0.003}_{-0.004}$	3212.4/3088
H 1743-322	20160315	$1.93^{+0.17}_{-0.18}$	14^{+9}_{-5}	$1.777^{+0.016}_{-0.016}$	$20.2^{+0.9}_{-1.3}$	128^{+25}_{-18}	36^{+5}_{-4}	31^{+3}_{-3}	$0.77^{+0.17}_{-0.17}$	$-8.74^{+0.09}_{-0.11}$	$-8.256^{+0.005}_{-0.005}$	3146.8/3060
H 1743-322	20180919	$2.59^{+0.16}_{-0.15}$	8^{+42}_{-P}	$1.668^{+0.021}_{-0.012}$	$20.9^{+0.2}_{-0.7}$	101^{+14}_{-64}	40^{+7}_{-4}	5^{+19}_{-P}	$0.69^{+0.11}_{-0.1}$	$-8.71^{+0.08}_{-0.08}$	$-8.288^{+0.005}_{-0.005}$	2870.0/2814
H 1743-322	20180926	$2.17^{+0.11}_{-0.14}$	22^{+7}_{-16}	$1.607^{+0.008}_{-0.013}$	$19.2^{+2.1}_{-1.6}$	124^{+29}_{-38}	500^{+P}_{-19}	19^{+6}_{-P}	$0.73^{+0.15}_{-0.12}$	$-8.82^{+0.08}_{-0.04}$	$-8.467^{+0.008}_{-0.008}$	3200.1/3019
MAXI J1535	20170907	$7.7^{+0.5}_{-0.2}$	$1.32^{+0.05}_{-P}$	$1.952^{+0.014}_{-0.013}$	$19.99^{+0.08}_{-0.09}$	190^{+170}_{-20}	$24.8^{+1.6}_{-1.8}$	$24.8^{+1.6}_{-2.4}$	$0.64^{+0.08}_{-0.1}$	$-7.46^{+0.09}_{-0.11}$	$-7.20^{+0.01}_{-0.01}$	3481.1/3131
V404 Cyg	20150624	$1.7^{+0.6}_{-0.5}$	$5.8^{+4}_{-2.8}$	$1.548^{+0.029}_{-0.024}$	21.7^{+P}_{-P}	123^{+122}_{-88}	51^{+104}_{-12}	27^{+10}_{-P}	$0.69^{+0.5}_{-0.09}$	$-8.0^{+1.2}_{-1.2}$	$-7.571^{+0.04}_{-0.04}$	2027.1/2057
V404 Cyg	20150624	$3.0^{+0.6}_{-0.5}$	$16.9^{+2.7}_{-8}$	$1.521^{+0.025}_{-0.011}$	$21.4^{+0.5}_{-0.3}$	520^{+120}_{-300}	34^{+7}_{-3}	5^{+9}_{-P}	$0.521^{+0.07}_{-0.019}$	$-7.75^{+0.05}_{-0.05}$	$-7.163^{+0.05}_{-0.05}$	2578.3/2545
V404 Cyg	20150624	$1.6^{+0.3}_{-0.9}$	$11.9^{+1.7}_{-1.6}$	$1.555^{+0.007}_{-0.013}$	$20.53^{+0.12}_{-1.2}$	731^{+537}_{-180}	$32.4^{+1.1}_{-4}$	18^{+4}_{-P}	$0.50^{+0.05}_{-P}$	$-7.19^{+0.11}_{-0.09}$	$-6.970^{+0.027}_{-0.027}$	2632.8/2627
V404 Cyg	20150624	$2.4^{+0.3}_{-1.5}$	$1.84^{+0.23}_{-0.24}$	$1.648^{+0.027}_{-0.023}$	$20.2^{+0.3}_{-0.3}$	610^{+130}_{-25}	40^{+4}_{-4}	$58.9^{+6}_{-1.1}$	$0.500^{+0.023}_{-P}$	$-6.62^{+0.09}_{-0.09}$	$-6.879^{+0.011}_{-0.09}$	2284.1/2296
V404 Cyg	20150624	$1.9^{+0.6}_{-0.4}$	6^{+4}_{-P}	$1.572^{+0.028}_{-0.025}$	$20.4^{+0.8}_{-0.3}$	810^{+380}_{-160}	$17.9^{+3.0}_{-1.5}$	23^{+7}_{-P}	$0.50^{+0.08}_{-P}$	$-6.41^{+0.11}_{-0.15}$	$-6.44^{+0.04}_{-0.12}$	2209.8/2156

Note: The flux of the power-law and reflection component are estimated in the 0.1–100 keV band. The symbol P denotes the lower or higher limits. Note that for V404 Cyg, the column density (nH) of the Galactic absorption is fixed at $1 \times 10^{22} \text{ cm}^{-2}$ and what shown in the table are for local absorption in the system (see Sec. 4.6.2).

Table 4-4 Best-fit parameters with reflionx that has $\log(n_e) = 15$

Source	Date	nH	$R_{\text{in}}(R_g)$	Γ	ξ	kT_e (keV)	Incl (deg)	A_{Fe} (solar)	$\log(F_{\text{ref}})$	$\log(F_{po})$	χ/ν
GRS 1739-278	20140326	$3.02^{+0.05}_{-0.04}$	$1.30^{+0.06}_{-P}$	$1.839^{+0.02}_{-0.012}$	190^{+21}_{-17}	$15.41^{+0.7}_{-0.23}$	$28.2^{+0.9}_{-1.2}$	$0.50^{+0.01}_{-P}$	$-8.045^{+0.016}_{-0.019}$	$-8.067^{+0.015}_{-0.007}$	3492.5/3239
GS 1354-64	20150613	$1.22^{+0.08}_{-0.04}$	$1.83^{+0.09}_{-0.05}$	$1.544^{+0.011}_{-0.01}$	140^{+60}_{-P}	500^{+P}_{-430}	20^{+15}_{-P}	$5.0^{+P}_{-2.5}$	$-9.66^{+0.07}_{-0.12}$	$-8.963^{+0.021}_{-0.022}$	2030.3/1873
GS 1354-64	20150711	$1.19^{+0.06}_{-0.06}$	$1.54^{+0.18}_{-P}$	$1.742^{+0.022}_{-0.015}$	120^{+13}_{-6}	$28.2^{+4}_{-2.3}$	40^{+14}_{-P}	$0.50^{+0.08}_{-P}$	$-8.57^{+0.05}_{-0.04}$	$-8.263^{+0.013}_{-0.022}$	3116.8/2919
GS 1354-64	20150806	$0.51^{+0.16}_{-0.17}$	$1.30^{+0.12}_{-P}$	$1.762^{+0.04}_{-0.03}$	163^{+106}_{-15}	$26.1^{+1.9}_{-2.7}$	33^{+3}_{-4}	$0.50^{+0.09}_{-P}$	$-8.521^{+0.028}_{-0.024}$	$-8.20^{+0.08}_{-0.05}$	2911.9/2822
IGR J17091	20160307	$1.76^{+0.04}_{-0.06}$	47^{+20}_{-29}	$1.707^{+0.012}_{-0.01}$	90^{+20}_{-45}	38^{+5}_{-4}	43^{+P}_{-12}	$0.50^{+0.05}_{-P}$	$-9.27^{+0.03}_{-0.08}$	$-8.638^{+0.012}_{-0.012}$	2824.3/2752
IGR J17091	20160312	$1.63^{+0.05}_{-0.05}$	17^{+22}_{-10}	$1.698^{+0.011}_{-0.01}$	175^{+51}_{-51}	$24.1^{+1.8}_{-1.5}$	28^{+10}_{-7}	$0.50^{+0.08}_{-P}$	$-9.29^{+0.06}_{-0.06}$	$-8.553^{+0.011}_{-0.011}$	2372.0/2410
IGR J17091	20160314	$1.55^{+0.06}_{-0.06}$	13^{+8}_{-8}	$1.70^{+0.01}_{-0.01}$	330^{+190}_{-190}	$20.9^{+0.8}_{-0.8}$	18^{+6}_{-7}	$0.50^{+0.07}_{-P}$	$-9.21^{+0.06}_{-0.06}$	$-8.372^{+0.011}_{-0.011}$	2305.7/2322
H 1743-322	20140918	$1.74^{+0.12}_{-0.18}$	5.3^{+16}_{-P}	$1.601^{+0.012}_{-0.003}$	180^{+19}_{-50}	$34.0^{+2.1}_{-12}$	22^{+12}_{-P}	$0.51^{+0.05}_{-P}$	$-9.087^{+0.011}_{-0.04}$	$-8.3677^{+0.018}_{-0.015}$	3039.5/3007
H 1743-322	20140923	$1.06^{+0.16}_{-0.16}$	5.4^{+5}_{-P}	$1.584^{+0.014}_{-0.014}$	440^{+150}_{-190}	26.6^{+7}_{-7}	32^{+4}_{-3}	$1.08^{+0.18}_{-P}$	$-9.33^{+0.19}_{-0.02}$	$-8.2416^{+0.018}_{-0.016}$	3325.4/3188
H 1743-322	20141009	$2.17^{+0.22}_{-0.22}$	40^{+13}_{-24}	$1.637^{+0.012}_{-0.012}$	114^{+18}_{-18}	99^{+P}_{-8}	29^{+18}_{-3}	$0.57^{+0.06}_{-P}$	$-9.16^{+0.07}_{-0.07}$	$-8.238^{+0.011}_{-0.011}$	2499.9/2606
H 1743-322	20150703	$1.72^{+0.22}_{-0.13}$	7^{+4}_{-P}	$1.583^{+0.011}_{-0.012}$	310^{+140}_{-270}	500^{+P}_{-390}	33^{+6}_{-3}	$0.50^{+0.23}_{-P}$	$-9.12^{+0.03}_{-0.12}$	$-8.528^{+0.019}_{-0.005}$	2389.9/2417
H 1743-322	20160313	$2.11^{+0.06}_{-0.14}$	38^{+10}_{-20}	$1.788^{+0.011}_{-0.011}$	155^{+28}_{-17}	39^{+4}_{-4}	33^{+8}_{-4}	$0.56^{+0.11}_{-P}$	$-8.976^{+0.03}_{-0.026}$	$-8.238^{+0.003}_{-0.003}$	3221.8/3089
H 1743-322	20160315	$2.31^{+0.05}_{-0.06}$	5.3^{+16}_{-P}	$1.822^{+0.004}_{-0.004}$	$124.1^{+2.5}_{-4}$	48^{+6}_{-3}	80^{+P}_{-7}	$0.65^{+0.05}_{-0.08}$	$-8.910^{+0.027}_{-0.028}$	$-8.2572^{+0.0028}_{-0.0028}$	3151.4/3061
H 1743-322	20180919	$2.48^{+0.2}_{-0.28}$	14^{+14}_{-P}	$1.679^{+0.019}_{-0.02}$	140^{+78}_{-23}	44^{+4}_{-7}	31^{+20}_{-6}	$0.51^{+0.15}_{-P}$	$-9.00^{+0.04}_{-0.04}$	$-8.293^{+0.006}_{-0.004}$	2876.7/2815
H 1743-322	20180926	$2.08^{+0.11}_{-0.07}$	17^{+16}_{-P}	$1.605^{+0.009}_{-0.009}$	150^{+43}_{-360}	500^{+P}_{-360}	24.7^{+6}_{-7}	$0.66^{+0.12}_{-0.1}$	$-9.24^{+0.04}_{-0.04}$	$-8.467^{+0.005}_{-0.005}$	3203.5/3020
MAXI J1535	20170907	$7.5^{+0.4}_{-0.6}$	$1.326^{+0.027}_{-0.025}$	$1.945^{+0.014}_{-0.021}$	245^{+250}_{-55}	$24.2^{+3}_{-1.7}$	$78.4^{+1.7}_{-1.0}$	$0.62^{+0.06}_{-0.08}$	$-7.62^{+0.03}_{-0.05}$	$-7.201^{+0.016}_{-0.013}$	3483.5/3132
V404 Cyg	20150624	$0.56^{+0.16}_{-P}$	$5.3^{+2.1}_{-2.0}$	$1.57^{+0.006}_{-0.005}$	490^{+220}_{-60}	80^{+114}_{-35}	29^{+5}_{-P}	$0.89^{+0.14}_{-0.07}$	$-7.88^{+0.07}_{-0.08}$	$-7.590^{+0.028}_{-0.004}$	2028.1/2058
V404 Cyg	20150624	$2.0^{+0.8}_{-0.5}$	$12.7^{+0.8}_{-2.7}$	$1.559^{+0.015}_{-0.009}$	2900^{+185}_{-130}	58^{+5}_{-9}	5^{+7}_{-P}	$0.52^{+0.04}_{-P}$	$-7.31^{+0.02}_{-0.09}$	$-7.46^{+0.11}_{-0.1}$	2589.0/2546
V404 Cyg	20150624	$0.3^{+0.4}_{-P}$	$12.0^{+2.0}_{-1.3}$	$1.577^{+0.005}_{-0.012}$	2570^{+320}_{-50}	$42.2^{+0.8}_{-1.6}$	11^{+8}_{-6}	$0.50^{+0.03}_{-P}$	$-7.051^{+0.06}_{-0.08}$	$-7.15^{+0.04}_{-0.09}$	2640.5/2628
V404 Cyg	20150624	$0.82^{+0.23}_{-0.07}$	$1.921^{+0.04}_{-0.018}$	$1.649^{+0.027}_{-0.004}$	10000^{+200}_{-130}	$43.8^{+0.5}_{-3}$	$58.7^{+0.3}_{-11}$	$0.500^{+0.027}_{-P}$	$-6.60^{+0.03}_{-0.03}$	$-7.12^{+0.01}_{-0.01}$	2288.2/2297
V404 Cyg	20150624	< 0.2	$1.9^{+1.3}_{-P}$	$1.660^{+0.007}_{-0.016}$	1330^{+380}_{-145}	$24.2^{+1.8}_{-0.9}$	$22.0^{+9}_{-2.5}$	$0.500^{+0.007}_{-P}$	$-6.398^{+0.016}_{-0.016}$	$-6.533^{+0.023}_{-0.028}$	2212.8/2157

Note: The flux of the power-law and reflection component are estimated in the 0.1–100 keV band. The symbol *P* denotes the lower or higher limits. Note that for V404 Cyg, the column density (nH) of the Galactic absorption is fixed at $1 \times 10^{22} \text{ cm}^{-2}$ and what shown in the table are for local absorption in the system (see Sec. 4.6.2).

Table 4-5 Best-fit parameters with $\text{relxi} \parallel \text{cp}$ that has $n_e = 10^{15} \text{ cm}^{-3}$

Source	Date	$n\text{H}$	$R_{\text{in}}(R_g)$	Γ	$\log(\xi)$	$kT_e \text{ (keV)}$	Incl (deg)	A_{Fe} (solar)	$\log(F_{\text{ref}})$	$\log(F_{\text{po}})$	χ^2/ν
GRS 1739-278	20140326	$2.87^{+0.05}_{-0.05}$	$1.30^{+0.03}_{-P}$	$1.61^{+0.02}_{-0.03}$	$3.544^{+0.028}_{-0.04}$	$20.0^{+1.8}_{-1.4}$	$25.9^{+2.4}_{-2.6}$	$2.3^{+0.5}_{-0.4}$	$-7.897^{+0.015}_{-0.015}$	$-8.71^{+0.05}_{-0.06}$	3409.5/3239
GS 1354-64	20150613	$1.20^{+0.08}_{-0.07}$	27^{+26}_{-10}	$1.525^{+0.01}_{-0.09}$	$2.71^{+0.24}_{-0.11}$	41^{+27}_{-8}	5^{+13}_{-P}	$0.7^{+0.5}_{-0.5}$	$-9.97^{+0.09}_{-0.16}$	$-8.933^{+0.017}_{-0.018}$	2049.0/1876
GS 1354-64	20150711	$1.07^{+0.06}_{-0.06}$	$1.60^{+0.01}_{-0.07}$	$1.705^{+0.013}_{-0.012}$	$2.49^{+0.06}_{-0.07}$	29^{+3}_{-3}	65^{+3}_{-7}	$0.50^{+0.05}_{-P}$	$-8.66^{+0.04}_{-0.04}$	$-8.251^{+0.016}_{-0.016}$	3117.3/2919
GS 1354-64	20150806	$1.00^{+0.11}_{-0.07}$	$1.42^{+0.21}_{-0.04}$	$1.751^{+0.01}_{-0.09}$	$2.71^{+0.04}_{-0.09}$	$26.6^{+2.1}_{-2.3}$	$73.4^{+1.2}_{-3.0}$	$0.50^{+0.04}_{-P}$	$-8.55^{+0.03}_{-0.05}$	$-8.19^{+0.01}_{-0.01}$	2901.7/2822
IGR J17091	20160307	$1.70^{+0.06}_{-0.06}$	19^{+22}_{-8}	$1.699^{+0.01}_{-0.011}$	$2.04^{+0.22}_{-0.21}$	60^{+18}_{-13}	34^{+6}_{-6}	$0.52^{+0.16}_{-P}$	$-9.42^{+0.05}_{-0.06}$	$-8.621^{+0.011}_{-0.01}$	2819.2/2752
IGR J17091	20160312	$1.56^{+0.05}_{-0.05}$	19^{+16}_{-11}	$1.684^{+0.01}_{-0.011}$	$2.83^{+0.11}_{-0.1}$	28^{+3}_{-3}	37^{+9}_{-7}	$0.52^{+0.22}_{-P}$	$-9.33^{+0.06}_{-0.06}$	$-8.552^{+0.014}_{-0.012}$	2367.5/2410
IGR J17091	20160314	$1.53^{+0.05}_{-0.05}$	18^{+10}_{-8}	$1.703^{+0.008}_{-0.012}$	$2.94^{+0.15}_{-0.12}$	$24.2^{+1.2}_{-2.2}$	28^{+7}_{-6}	$0.50^{+0.17}_{-P}$	$-9.18^{+0.04}_{-0.04}$	$-8.377^{+0.015}_{-0.008}$	2294.6/2322
H 1743-322	20140918	$1.44^{+0.09}_{-0.09}$	5.3^{+5}_{-P}	$1.559^{+0.008}_{-0.008}$	$3.10^{+0.18}_{-0.16}$	31^{+3}_{-3}	36^{+3}_{-7}	$1.5^{+0.6}_{-0.6}$	$-9.35^{+0.07}_{-0.08}$	$-8.350^{+0.007}_{-0.004}$	3042.7/3008
H 1743-322	20140923	$1.49^{+0.11}_{-0.09}$	$10.0^{+2.7}_{-2.0}$	$1.607^{+0.007}_{-0.006}$	$2.98^{+0.07}_{-0.08}$	$31.0^{+3.0}_{-2.2}$	$30.8^{+1.8}_{-2.1}$	$0.69^{+0.09}_{-0.09}$	$-9.13^{+0.05}_{-0.05}$	$-8.257^{+0.004}_{-0.005}$	3320.4/3189
H 1743-322	20141009	$1.8^{+0.3}_{-0.3}$	$5.3^{+3.3}_{-P}$	$1.611^{+0.02}_{-0.02}$	$2.86^{+0.16}_{-0.16}$	41^{+25}_{-25}	34^{+5}_{-5}	$0.82^{+0.05}_{-0.05}$	$-9.18^{+0.14}_{-0.14}$	$-8.296^{+0.008}_{-0.008}$	2503.7/2607
H 1743-322	20150703	$1.85^{+0.25}_{-0.12}$	5.3^{+8}_{-P}	$1.580^{+0.008}_{-0.011}$	$2.72^{+0.21}_{-0.17}$	400^{+P}_{-200}	34^{+4}_{-8}	$1.1^{+1.0}_{-0.3}$	$-9.47^{+0.08}_{-0.08}$	$-8.498^{+0.008}_{-0.008}$	2389.5/2417
H 1743-322	20160313	$1.56^{+0.08}_{-0.09}$	$5.3^{+1.3}_{-P}$	$1.725^{+0.007}_{-0.007}$	$3.17^{+0.08}_{-0.08}$	$30.4^{+2.6}_{-2.3}$	$33.5^{+2.2}_{-3.0}$	$1.23^{+0.6}_{-0.28}$	$-9.16^{+0.04}_{-0.05}$	$-8.244^{+0.004}_{-0.005}$	3212.6/3089
H 1743-322	20160315	$1.30^{+0.09}_{-0.08}$	$5.3^{+1.7}_{-P}$	$1.714^{+0.01}_{-0.01}$	$3.46^{+0.17}_{-0.17}$	$28.2^{+2.2}_{-2.2}$	33^{+3}_{-3}	$2.7^{+0.9}_{-1.2}$	$-9.17^{+0.07}_{-0.07}$	$-8.271^{+0.01}_{-0.01}$	3140.6/3061
H 1743-322	20180919	$1.92^{+0.12}_{-0.12}$	5.3^{+7}_{-P}	$1.608^{+0.012}_{-0.013}$	$3.21^{+0.22}_{-0.16}$	$30.2^{+4.4}_{-2.4}$	$38.8^{+1.3}_{-6}$	$1.9^{+0.5}_{-0.8}$	$-9.20^{+0.07}_{-0.07}$	$-8.290^{+0.008}_{-0.008}$	2878.5/2815
H 1743-322	20180926	$1.97^{+0.09}_{-0.1}$	15^{+15}_{-P}	$1.582^{+0.008}_{-0.004}$	$3.02^{+0.09}_{-0.14}$	400^{+P}_{-280}	23^{+6}_{-P}	$0.98^{+0.27}_{-0.13}$	$-9.41^{+0.05}_{-0.05}$	$-8.458^{+0.005}_{-0.006}$	3199.4/3020
MAXI J1535	20170907	$6.9^{+0.7}_{-0.6}$	4^{+5}_{-P}	$1.806^{+0.009}_{-0.009}$	$3.66^{+0.03}_{-0.04}$	$22.9^{+1.4}_{-1.1}$	$62.6^{+10}_{-2.4}$	$0.87^{+0.11}_{-0.08}$	$-7.29^{+0.07}_{-0.07}$	$-7.41^{+0.07}_{-0.09}$	3458.6/3132
V404 Cyg	20150624	$0.6^{+0.4}_{-0.3}$	$2.9^{+1.9}_{-P}$	$1.53^{+0.03}_{-0.03}$	$3.0^{+0.3}_{-0.2}$	62^{+300}_{-30}	35^{+20}_{-15}	$1.7^{+0.7}_{-0.8}$	$-7.94^{+0.05}_{-0.25}$	$-7.56^{+0.04}_{-0.03}$	2030.6/2058
V404 Cyg	20150624	< 0.07	$5.7^{+0.3}_{-0.3}$	$1.5542^{+0.018}_{-0.008}$	$3.076^{+0.009}_{-0.005}$	$50.0^{+9}_{-1,1}$	27^{+3}_{-3}	$1.003^{+0.04}_{-0.021}$	$-7.468^{+0.013}_{-0.014}$	$-7.220^{+0.005}_{-0.014}$	2611.6/2546
V404 Cyg	20150624	< 0.03	$7.1^{+1.2}_{-0.9}$	$1.5486^{+0.025}_{-0.007}$	$3.076^{+0.005}_{-0.003}$	$36.4^{+0.7}_{-0.9}$	$32.7^{+0.8}_{-0.7}$	$0.997^{+0.018}_{-0.009}$	$-7.149^{+0.007}_{-0.006}$	$-6.9573^{+0.0011}_{-0.015}$	2720.0/2628
V404 Cyg	20150624	< 0.2	$6.6^{+1.5}_{-0.5}$	$1.567^{+0.019}_{-0.009}$	$3.116^{+0.024}_{-0.014}$	$29.5^{+4}_{-1,8}$	$34.4^{+0.8}_{-1.0}$	$1.00^{+0.11}_{-0.08}$	$-6.809^{+0.025}_{-0.017}$	$-6.751^{+0.022}_{-0.019}$	2328.6/2297
V404 Cyg	20150624	< 0.1	$7.7^{+1.1}_{-1.0}$	$1.646^{+0.017}_{-0.013}$	$2.936^{+0.007}_{-0.003}$	$21.7^{+1.7}_{-0.3}$	$35.1^{+0.5}_{-0.6}$	$0.966^{+0.019}_{-0.017}$	$-6.544^{+0.008}_{-0.008}$	$-6.345^{+0.008}_{-0.008}$	2222.3/2157

Note: The power-law and reflection component are estimated in the 0.1–100 keV band. The symbol P denotes the lower or higher limits. Note that for V404 Cyg, the column density ($n\text{H}$) of the Galactic absorption is fixed at $1 \times 10^{22} \text{ cm}^{-2}$ and what shown in the table are for local absorption in the system (see Sec. 4.6.2).

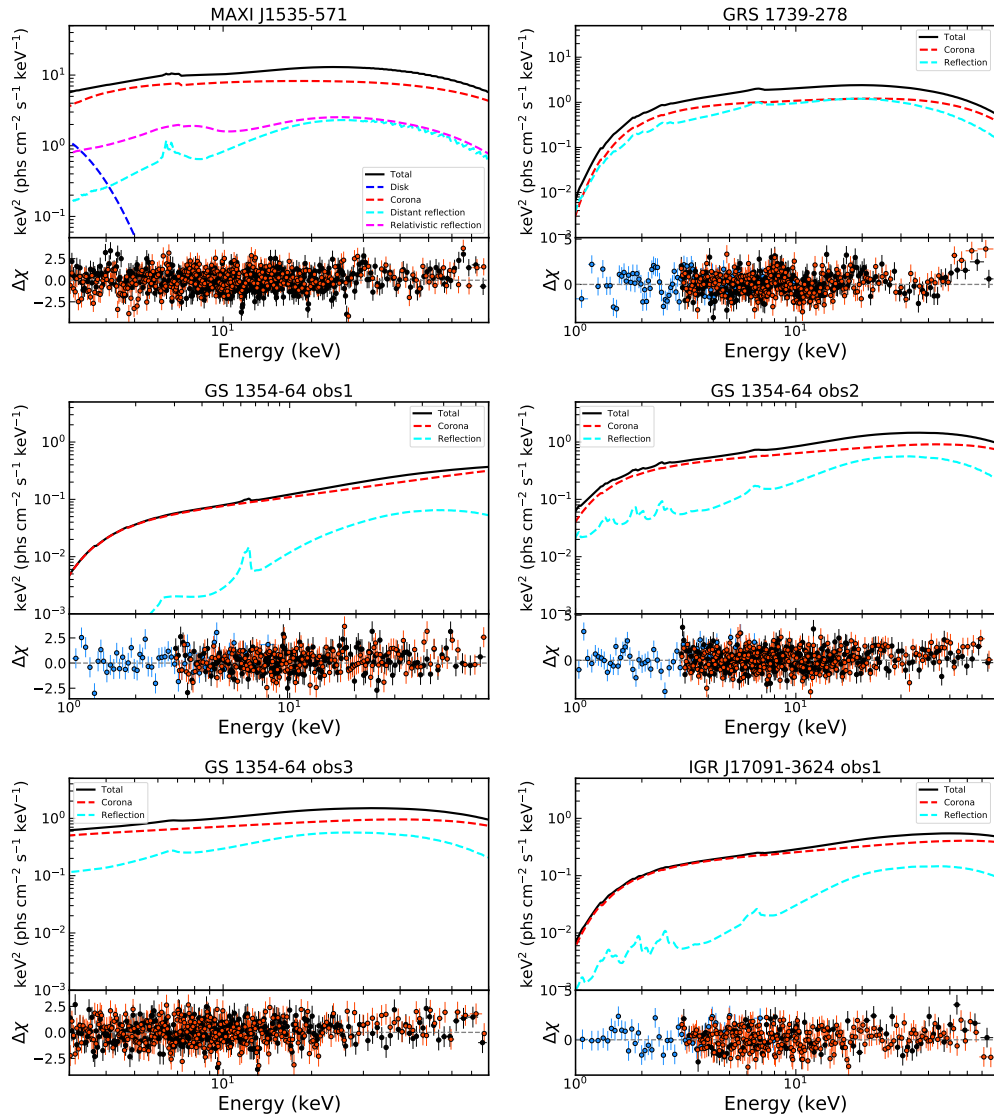


Figure 4-10 The best-fit model components (top panels) and the corresponding residual plots (bottom panels) for observations analyzed in this work.

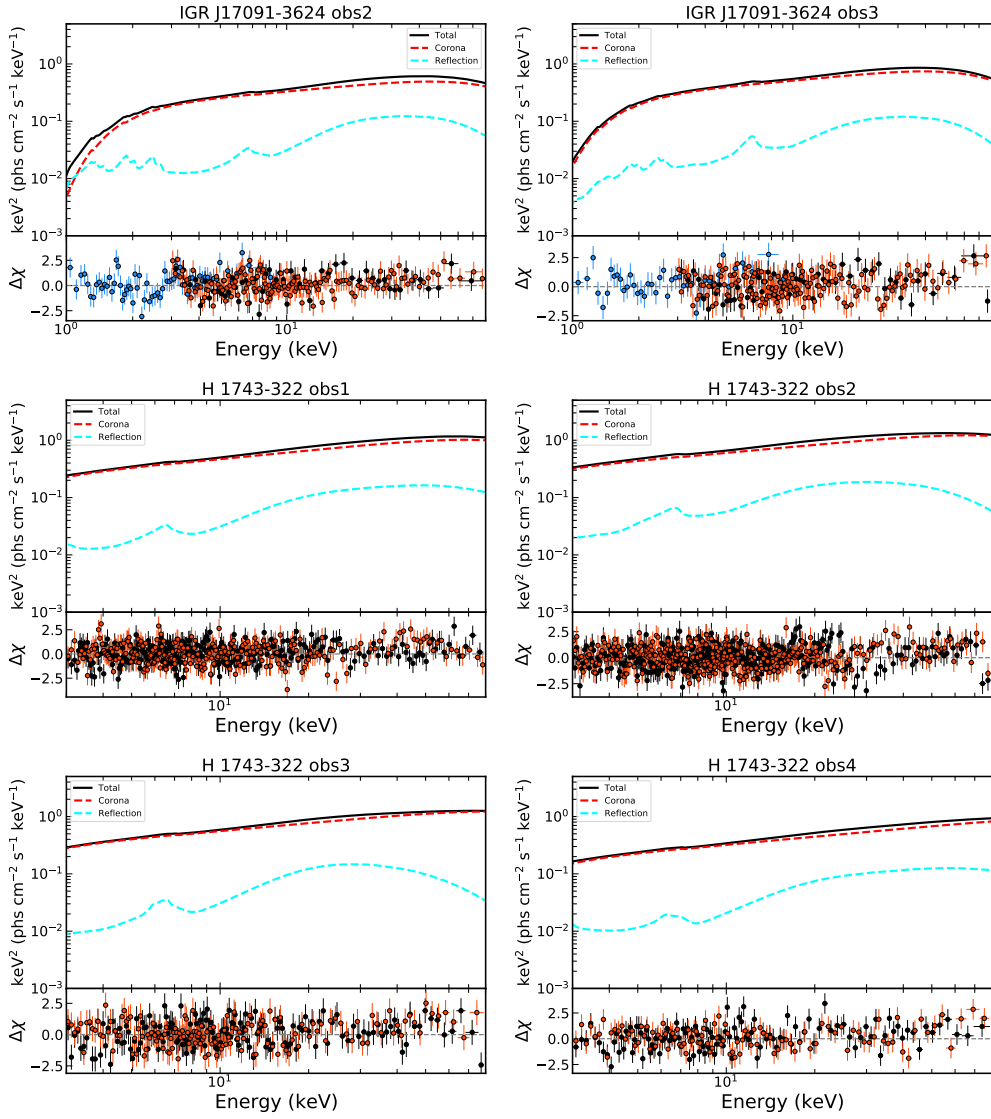


Figure 4-11 Figure 4-10 continued.

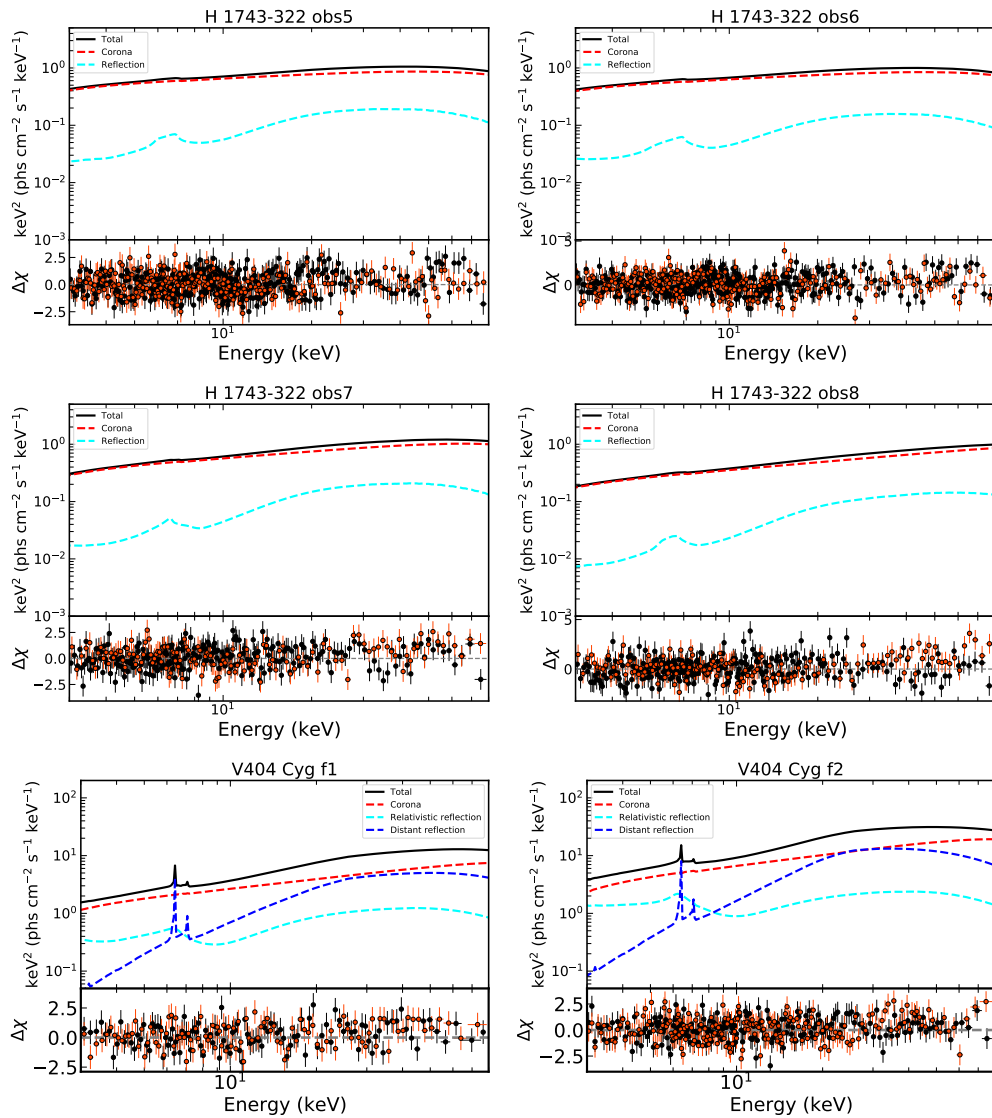


Figure 4-12 Figure 4-10 continued.

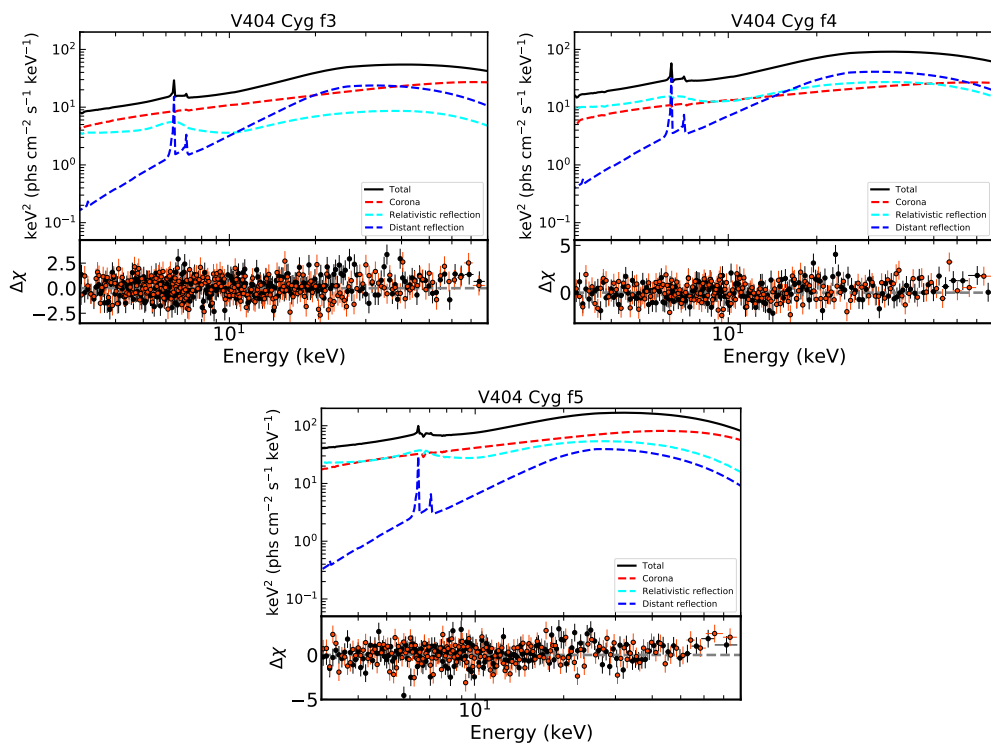


Figure 4-13 Figure 4-10 continued.

Chapter 5

The disk wind in GRS 1915+105 as seen by *Insight-HXMT*

5.1 Introduction

Ionized absorption winds have been commonly detected in the X-ray spectra of low mass X-ray binary systems^[307–311]. In many observations, these winds are found to be outflowing with respect to the central compact objects^[72,312–317]. The winds manifest as blueshifted narrow absorption lines, e.g., Fe XXV or Fe XXVI. The features are preferentially detected in high inclination systems (see Fig. 2 of Ponti et al. 2012^[1]), suggesting an equatorial geometry and an origin from the accretion disk.

Over the past two decades, our understanding has grown regarding the significance of disk winds in the accretion process of black holes. These winds can carry a mass comparable to or even larger than the accretion rate at the inner disk^[1,313]. The initiation of disk winds may coincide with state transitions in low-mass X-ray binaries^[72,74]. Observations indicating an inverse relationship between wind and jet activity^[75] suggest that the wind could serve as an alternative mechanism to suppress the jet (although see Homan et al. 2016^[76]). Furthermore, the detection of disk winds appears to be correlated with the spectral states of black hole transients. Most disk winds have been observed in the soft state^[1,81], with rare detections in the hard state^[307]. It remains unclear whether this scarcity in the hard state is due to non-launching of the wind (or its non-alignment with the line of sight)^[308,318], or if the wind is consistently launched but highly ionized^[83] or thermally unstable^[86,319].

Outflows may originate from various mechanisms such as thermal pressure^[77–78], magnetic pressure^[320], or radiation pressure^[321–322]. However, distinguishing between these launching mechanisms is challenging due to the complexities involved in determining the density and radial position of the disk wind. Additionally, multiple mech-

anisms could simultaneously drive the disk winds, and their relative significance may vary with the accretion state^[318].

Studying the disk wind in low mass X-ray binaries (LMXRBs) could potentially provide insights into the accretion environment within active galactic nuclei (AGNs). Recent research suggests a plausible link between the broad line region (BLR) observed in AGNs and the disk winds originating from stellar-mass black holes^[309,323]. If the wind carries substantial momentum, it may also play a role in providing feedback to the surrounding environment^[324].

GRS 1915+105 has been pivotal in advancing our understanding of disk winds. It stands out as one of the rare sources exhibiting evidence of magnetically driven disk winds^[317,325]. Furthermore, this source demonstrates a distinct separation between jets and disk winds^[75]. Additionally, the light curve of GRS 1915+105 often showcases significant amplitude variations on timescales ranging from tens of seconds to kiloseconds, providing an excellent opportunity to explore the correlation between the inner disk, outer disk, and jet^[72,315].

In this chapter, we analyze three observations (Fig. 5-1) of GRS 1915+105 by *Insight*–HXMT^[146] that show disk wind absorption signatures. The three observations show different variability patterns (see Fig. 5-2) but similar signatures of ionized absorption (see Fig. 5-3). With these data, we have the opportunity to study the disk wind, its variability on short (hundreds seconds) and long (months) timescales and its connection to different variability classes in GRS 1915+105.

5.2 Observations and data reduction

Insight–HXMT observed GRS 1915+105 three times during periods when the source exhibited a “soft state” in 2017 (as depicted in Fig. 5-1). The source maintained its spectral soft state for nearly a year, during which a persistent disk wind was observed^[311]. Further information regarding the three *Insight*–HXMT observations is provided in Tab. 5-1.

Insight-HXMT is the first Chinese X-ray telescope, which consists of low-energy (LE), medium-energy (ME) and high-energy (HE) detectors that cover the energy range of 1–250 keV^[147–150]. The lightcurves and spectra are extracted following the official user guide^① and using the software HXMTDAS ver 2.04. We estimate the background

① <http://www.hxmt.cn/SoftDoc/67.jhtml>

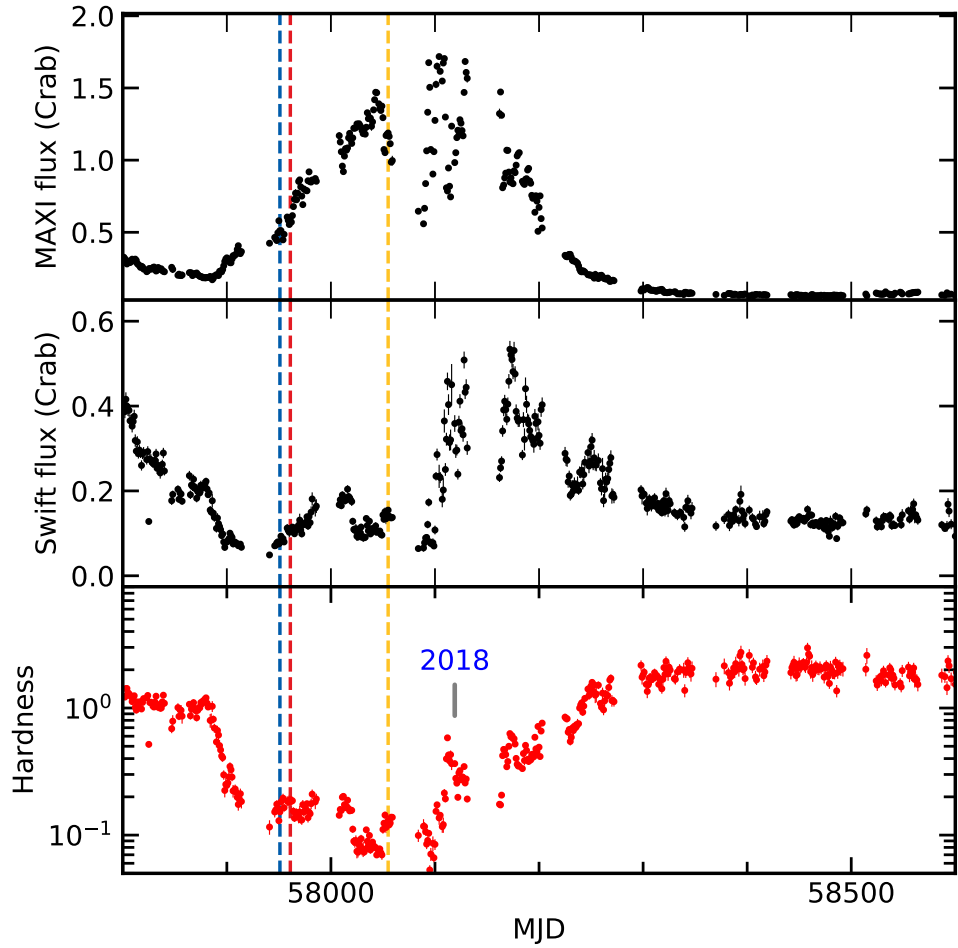


Figure 5-1 Light curves of GRS 1915+105 in Crab units by MAXI/GSC (2–20 keV) and Swift/BAT (15–50 keV). The hardness in the lower panel is defined as the ratio between the Swift and MAXI count rate in Crab units (Swift/MAXI). The vertical lines mark the three *Insight*–HXMT observations analyzed in this work.

using standalone scripts `hebkmap`, `mebkmap` and `lebkmap`^[151–153]. We screen good time intervals with the recommended criteria, i.e., the elevation angle > 10 degree, the geomagnetic cutoff rigidity > 8 GeV, the pointing offset angle < 0.1 and at least 300 s away from the South Atlantic Anomaly (SAA).

We fit data from *Insight*–HXMT Low Energy X-ray Telescope (LE) in the energy range 2–9 keV and Medium Energy X-ray Telescope (ME) in 10–20 keV. Data from the High Energy X-ray Telescope (HE) are not included because of the low source count rate and high background.

Table 5-1 *Insight–HXMT* observations of GRS 1915+105 analyzed in this paper

Reference name	Date ¹	obsID	Exposure (ks)	Flux ²	EW ³ (eV)
H1	20170717(18)	P0101330001	26.6	1.192 ± 0.01	$20.8^{+1.4}_{-1.9}$
H2	20170727	P0101310001	10.4	1.513 ± 0.03	$16.6^{+2.0}_{-2.7}$
H3	20171029(30)	P0101310002	23.3	2.583 ± 0.01	$27.7^{+1.2}_{-1.3}$

Note. (1) The observation date is presented in the form of yyyyymmdd. (2) The observed flux (in units of 10^{-8} erg cm $^{-2}$ s $^{-1}$ in 2–10 keV) is calculated from the best-fit model in XSPEC. (3) The equivalent width of the Fe XXVI Ly α absorption line.

5.3 Data analysis

The *Insight–HXMT* spectra of GRS 1915+105 are analyzed with XSPEC v12.10.1f^[154]. The cross section is set to be Verner et al. 1996^[156] and the element abundances to be Wilm et al. 2000^[155]. In this manuscript, the uncertainties are quoted at 90% confidence level.

5.3.1 The light curve

GRS 1915+105 is an exceptional source since it does not go into outbursts or trace certain patterns on the hardness intensity diagram (HID) compared to other canonical LMXRBs, such as GX 339-4. Since its discovery in 1992 by WATCH^[326], GRS 1915+105 has remained consistently bright. Its light curve can be categorized into 14 distinct classes based on variability patterns and color-color diagrams (CCDs)^[327–329]. In Fig. 5-2, we present typical light curves from three observations. During epochs 1 and 2, the LE count rate exhibits significant oscillations with an amplitude exceeding a factor of 3 over a timescale of 200 seconds. In contrast, epoch 3 does not display such pronounced variability. Comparing the light curves and CCD (not shown here) to the work of^[327], we determine that epochs 1 and 2 correspond to class κ , while epoch 3 corresponds to class δ .

5.3.2 The continuum and absorption lines

Model 1. As an initial step, we employ a broadband spectral fitting approach using a multicolor disk component (`diskbb`,^[157]) plus a Comptonized component (`nth-comp`^[55–56]). Additionally, we incorporate the `tbabs` model to account for absorption by the interstellar medium (ISM), with its column density linked across all observations.

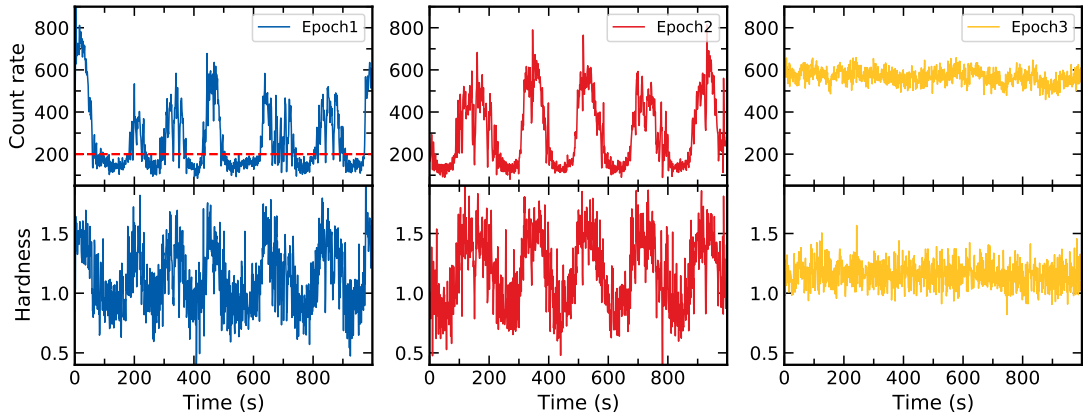


Figure 5-2 The LE (1–10 keV) light curve and the hardness ratio of GRS 1915+105 for the three epochs. For every epoch, only 1000 s (bin size 1 s) data are shown. The hardness ratio is defined as ratio between the count rates in the range of 4–10 keV and 1–4 keV. The red dashed line in the panel for Epoch 1 denotes the threshold used to divide this observation to low and high flux states (see Sec. 5.4.2).

The residuals from the best-fit are illustrated in the top panel of Fig. 5-3, revealing potential missing components in the current model. Notably, an excess below 3 keV and a hump in the iron band are evident. A deep trough at 7 keV indicates the presence of absorption by highly ionized iron species (e.g., Fe XXVI Ly α). Additionally, absorption attributed to Fe XXVI Ly β (at 8.25 keV) is detected with a significance of 4σ for epochs 1 and 3. Furthermore, the absorption line corresponding to Fe XXVI 1s–4p transition (at 8.7 keV) is notably significant only in epoch 3 (3σ).

Model 2. The prominent hump centered around 6.4 keV in Fig. 5-3 signifies the presence of a reflection component originating from the optically thick accretion disk surrounding the black hole, a characteristic feature commonly observed in the X-ray spectra of black hole X-ray binaries^[6,9,122,158,219]. To account for this, we introduce a relativistic reflection component (`relxill`,^[114]) into the model, along with two narrow negative Gaussian lines ($\sigma=10$ eV) to model the absorption by highly ionized iron. Although this model provides an acceptable fit ($\chi^2/\nu=3564/2906$), residual curvature is still noticeable in the 5–6 keV range (refer to the middle panel of Fig. 5-3).

Model 3. Lastly, we note that partially covered absorbers have previously been applied to fit the X-ray spectra of GRS 1915+105 during its flaring events^[330–331]. We also incorporate a partial covering absorption component (`pcfabs`) into the fitting of the three spectra. In this fit, we find that the `diskbb` component is not statistically

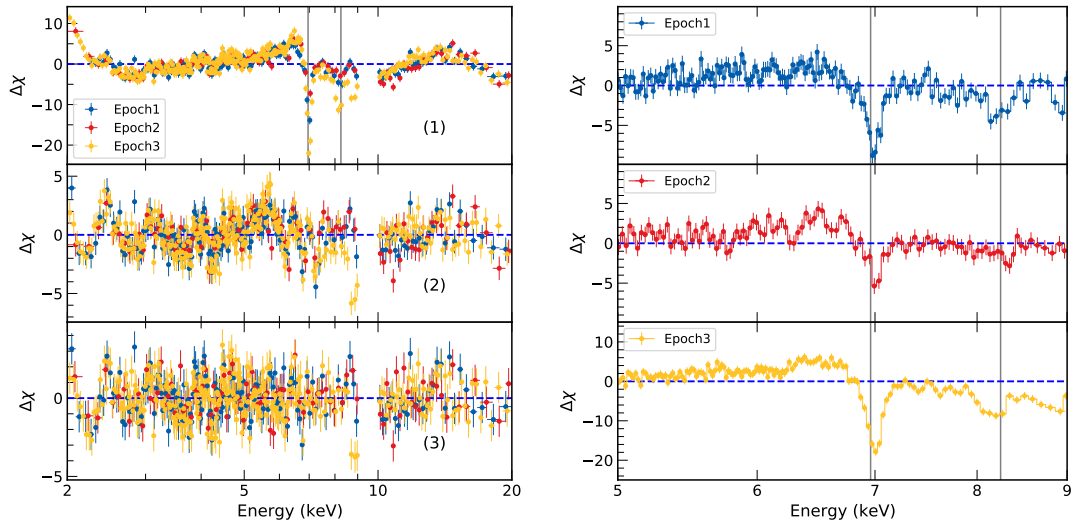


Figure 5-3 (Left 1): Residuals to an absorbed continuum model `tbabs*(diskbb + nthcomp)` for the three epochs. The two vertical grey lines mark the positions of absorption by Fe XXVI Ly α and Fe XXVI Ly β . (Left 2): Residuals to the model `tbabs*(diskbb + nthcomp + relxill)` with absorption lines fitted with two extra negative gaussian. (Left 3): Residuals to the model `tbabs*pcfabs*(nthcomp + gaussian)` with two additional absorption gaussian lines. (Right): A zoomed in version of panel 1 on the left with the three observations plotted separately. Data are rebinned for visual clarity.

required to fit the continuum since its inclusion only marginally improves the fit by $\Delta\chi^2 \sim 3$ compared to the model without it. Additionally, we discover that a gaussian line centered at 6.4 keV, rather than a `relxill` component, is sufficient to fit the reflection features present in the spectra. In XSPEC notation, the model used here is `tbabs*pcfabs*(nthcomp+gauss+gauss2+gauss3)`, where `gauss2` and `gauss3` are two negative gaussians to account for the iron absorption lines. This model yields improved fit statistics ($\chi^2/\nu = 3138/2911$) compared to the relativistic reflection model and exhibits fewer features in the residuals within the 5–6 keV range (refer to Fig. 5-3). The equivalent width (EW) of the Fe XXVI Ly α absorption line, as determined by this model, is presented in Tab. 5-1, indicating that the strongest absorption is observed during epoch 3.

Note that the broadband X-ray spectra of the three observations exhibit complexity, and the objective of this paper does not involve an in-depth exploration of their nature. Our focus lies in fitting the broadband X-ray spectra to unveil absorption features attributable to the disk wind and ascertain the most suitable model for describing the

continuum. Consequently, the best-fit parameters of the continuum model should be regarded as phenomenological outcomes.

5.3.3 The absorption wind

Time-averaged analysis

To derive the physical properties such as ionization state and column density of the disk wind based on the absorption signatures, we employ XSTAR (version 2.2) code^[300–301] to calculate a grid model. This grid model is constructed assuming the absorption-corrected best-fit continuum model obtained from *Model 1* (refer to Sec. 5.3.2). We set the turbulent velocity to 1000 km s^{-1} and the density (n) to 10^{12} cm^{-3} . Applying the grid model to the three observations, we model the continuum with partially absorbed corona emission. The final model in XSPEC notation is: `tbabsxs-tarpcfabs*(nthcomp+gauss)` (*Model 4*). We simultaneously fit the three observations with the column density (N_{H}) of `tbabs` and the cross normalization constant between LE and ME tied across observations. Note that this single-zone absorption model already yields an acceptable fit ($\chi^2/\text{d.o.f}=3201/2914$).

We further investigate whether a second layer of absorption is necessary to adequately fit the spectra. Including a second XSTAR layer improves the χ^2 by 70 with nine additional degrees of freedom. However, we observe that for epochs 1 and 2, the column density of the second layer is constrained to the lower limit and has negligible impact on the continuum. Additionally, the outflowing velocity and ionization state remain unconstrained. The improvement in χ^2 primarily arises from the spectrum of epoch 3. Therefore, we introduce this second layer only for epoch 3 while keeping a single layer of absorption for epochs 1 and 2. We present the best-fit parameters for both the single-zone and two-zone models in Tab. 5-2, facilitating a straightforward comparison of parameter changes resulting from the inclusion of a second absorption zone. The parameters in Tab. 5-2 reveal that the second absorber of epoch 3 has a notably high outflow velocity (approximately 0.05 c). However, a detailed examination of the absorption lines generated by the second layer indicates that it still accounts for the absorption line at 7 keV. The high outflow velocity simply shifts the energy of the Fe XXV line (6.70 keV) to 7 keV. Multiple absorption zones have been observed in other LMXRBs^[309]. Typically, the higher velocity components are associated with higher ionization states,

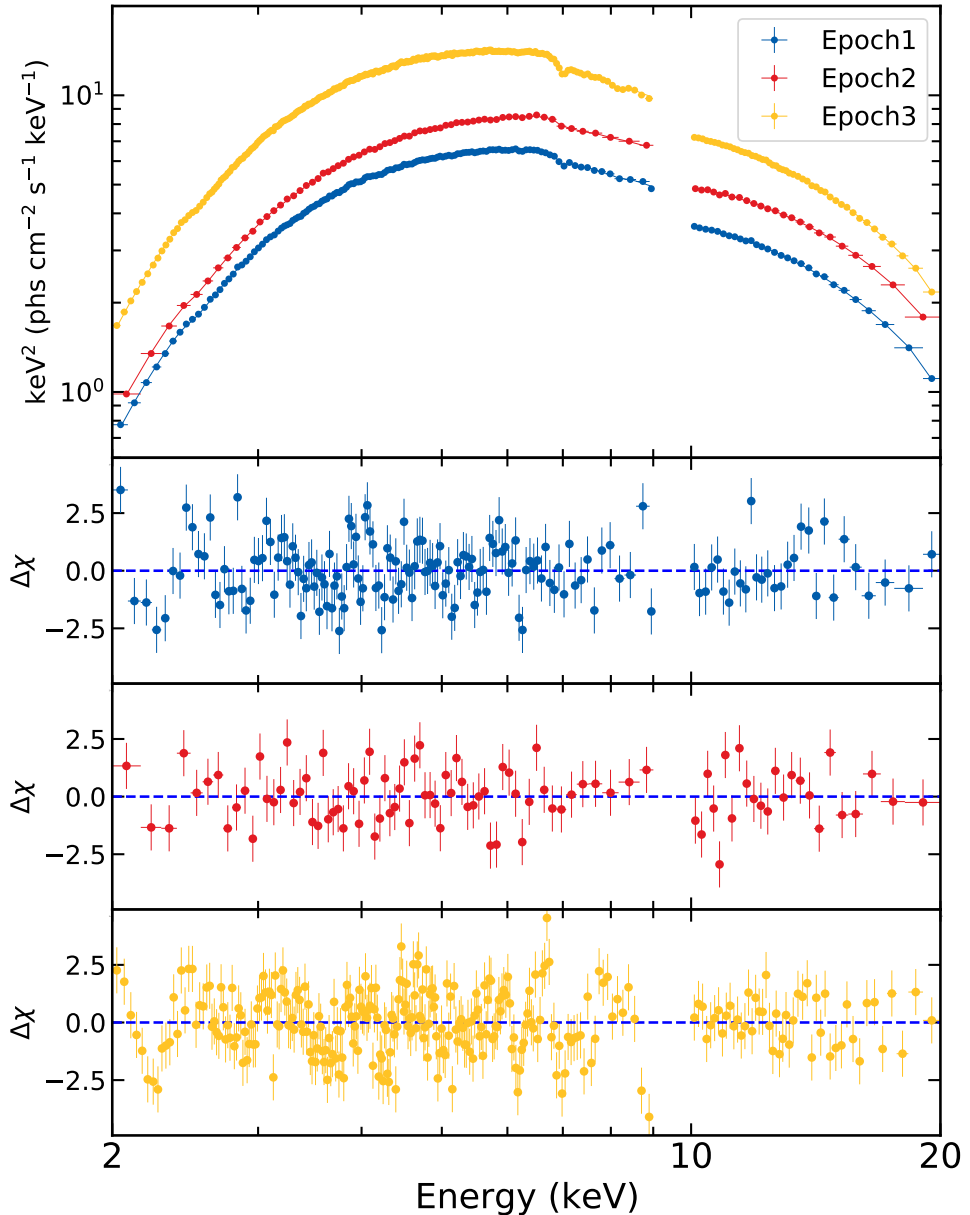


Figure 5-4 Spectra and residuals for the best-fit model `tbabs*xstar*pcfabs (nthcomp + gauss)` for the three epochs. The spectra are corrected for the effective area of the instruments but not unfolded from the response. Data are rebinned for visual clarity.

contrary to our fit. Therefore, the findings of the two-zone model should be interpreted with caution, and we only present the unfolded spectra and residuals for the single-zone model in Fig. 5-4. Our discussion will also concentrate on the single-zone model.

From the best-fit parameters of the single-zone model, it is evident that the wind is outflowing from the X-ray source with a velocity of approximately 1000 km s^{-1} . Moreover, notable variations in the column density of the disk wind are observed. Specifically, epoch 3 exhibits the highest column density, consistent with the analysis of the equivalent width of the absorption line. Additionally, the absorption-corrected ionizing flux increases by a factor of 2 from epoch 1 to epoch 3. Assuming a constant density and location of the disk wind, the ionization parameter ($\xi = L/nr^2$) should increase by $\Delta \log(\xi) = 0.3$. The measured variation of the ionization parameter aligns with this value, albeit the relatively large upper error bar for epoch 1 (refer to Tab. 5-2). This trend is also observed in the two-zone model, although the substantial uncertainty in the ionization parameter for epoch 3 precludes definitive conclusions.

Flux-resolved analysis

The light curve in Fig. 5-2 illustrates that the count rate of GRS 1915+105 undergoes fluctuations by a factor of 3 over a timescale of approximately 200 s for epoch 1 and 2. It is crucial to test whether the physical properties, such as the ionization parameter, of the disk wind respond to these rapid variations in the ionizing continuum. Considering that epoch 1 has the longest exposure, we segment this observation into low flux and high flux states, employing a threshold of 200 counts/s for LE (indicated by the red line in Fig. 5-2).

Initially, we employ *Model 2* to fit the flux-resolved spectra, aiming to determine the equivalent width of the Fe XXVI Ly α absorption line in the low and high flux intervals. The analysis reveals that the equivalent width evolves from $21.4^{+3.0}_{-2.6} \text{ eV}$ for the low flux state to $15.9^{+2.6}_{-0.9} \text{ eV}$ for the high flux state. This suggests a lower ionic column density of Fe XXVI Ly α in the high flux state, which could be attributed to a change in the line-of-sight column density of the wind or to the increased stripping of iron ions due to the stronger ionizing flux in the high state. It's important to note that the degeneracy between these two scenarios may result in parameter degeneracy when fitting with a photoionization model.

Table 5-2 Best-fit values.

Component	Parameter	Single zone			Two zones	
		Epoch 1	Epoch 2	Epoch 3	Epoch 1	Epoch 2
TBABS	N_{H} (10^{22} cm^{-2})	$6.21^{+0.09}_{-0.24}$			$6.01^{+0.17}_{-0.21}$	
XSTAR	N_{H} (10^{22} cm^{-2})	$7.9^{+1.6}_{-1.1}$	$6.5^{+2.1}_{-1.3}$	$12.7^{+0.4}_{-0.3}$	$6.4^{+2.1}_{-1.3}$	$10.6^{+2.1}_{-4.0}$
	$\log(\xi)$	$4.28^{+0.2}_{-0.07}$	$4.33^{+0.26}_{-0.13}$	$4.623^{+0.05}_{-0.029}$	$4.28^{+0.18}_{-0.06}$	$4.33^{+0.24}_{-0.12}$
	v (km s^{-1})	900^{+400}_{-300}	1200^{+700}_{-700}	1300^{+200}_{-200}	900^{+400}_{-300}	1300^{+700}_{-700}
XSTAR	N_{H} (10^{22} cm^{-2})	-	-	-	-	700^{+500}_{-500}
	$\log(\xi)$	-	-	-	-	$0.77^{+0.20}_{-0.24}$
	v (km s^{-1})	-	-	-	-	$3.40^{+0.24}_{-0.12}$
PCFABS	N_{H} (10^{22} cm^{-2})	$11.6^{+0.6}_{-0.9}$	$11.9^{+0.6}_{-0.7}$	$11.9^{+0.5}_{-1.0}$	$10.6^{+0.8}_{-0.8}$	$11.1^{+0.7}_{-0.7}$
	f_c	$0.374^{+0.04}_{-0.017}$	$0.459^{+0.04}_{-0.018}$	$0.369^{+0.03}_{-0.017}$	$0.41^{+0.04}_{-0.03}$	$0.472^{+0.04}_{-0.022}$
NTHCOMP	Γ	$2.401^{+0.026}_{-0.017}$	$2.293^{+0.009}_{-0.023}$	$2.632^{+0.017}_{-0.026}$	$2.40^{+0.05}_{-0.03}$	$2.302^{+0.06}_{-0.026}$
	kT_e (keV)	$3.34^{+0.04}_{-0.04}$	$3.34^{+0.04}_{-0.04}$	$3.69^{+0.05}_{-0.04}$	$3.34^{+0.04}_{-0.04}$	$3.36^{+0.04}_{-0.06}$
	kT_{bb} (keV)	$1.07^{+0.09}_{-0.07}$	$0.94^{+0.18}_{-0.06}$	$1.12^{+0.06}_{-0.03}$	$1.07^{+0.06}_{-0.07}$	$0.98^{+0.13}_{-0.1}$
	Norm	$3.26^{+0.13}_{-0.12}$	$4.6^{+0.4}_{-0.4}$	$7.52^{+0.14}_{-0.2}$	$3.23^{+0.14}_{-0.22}$	$4.32^{+0.6}_{-0.25}$
GAUSS	E_{line} (keV)	6.4^*	6.4^*	6.4^*	6.4^*	6.4^*
	EW (keV)	$0.17^{+0.05}_{-0.05}$	$0.29^{+0.07}_{-0.05}$	$0.101^{+0.03}_{-0.016}$	$0.17^{+0.05}_{-0.05}$	$0.29^{+0.06}_{-0.06}$
	Norm ($10^{-2} \text{ Phs cm}^{-2} \text{ s}^{-1}$)	$3.0^{+0.3}_{-0.4}$	$6.9^{+0.5}_{-0.6}$	$4.1^{+0.4}_{-0.3}$	$3.1^{+0.3}_{-0.6}$	$6.6^{+0.7}_{-1.2}$
	$\chi^2/\text{d.o.f}$			$3201.4/2914$		$3153.7/2911$

Note. Best-fit parameters for the model tbabs*xstar*pcfabs (nthcomp + gauss). The gauss component is used to fit possible reflected emission from the accretion disk. Note that there is a second layer of xstar for epoch 3 in the “Two zones” case. Parameters with * are fixed during the fit.

Subsequently, we conduct simultaneous fitting of both spectra with *Model 4* using new XSTAR grids calculated with the low and high flux spectral continuum. It's important to note that, despite significant variation in the ionizing flux, it is reasonable to assume that the absorption gas is in ionization equilibrium, as the recombination timescale can be well below 1 s for typical wind densities^[332]. In this scenario, when allowing the column density and outflowing velocity of XSTAR to vary freely between the two spectra, consistent results are obtained (N_{H} is $8.4^{+2.4}_{-2.5} \times 10^{22} \text{ cm}^{-2}$ in the low flux state and $6.4^{+2.7}_{-1.5} \times 10^{22} \text{ cm}^{-2}$ in the high flux state). However, the ionization parameter ($\log(\xi)$) is only loosely constrained (low: $4.18^{+0.09}_{-0.15}$, high: $4.05^{+0.14}_{-0.12}$), possibly due to the degeneracy discussed earlier. Additionally, we consider the possibility that the same wind is observed in both low and high flux states by linking the column density and velocity of the XSTAR model. This assumption is reasonable given that the traveling timescale of the wind is much longer than the 200 s timescale we are considering^[308]. The change in fit statistics is minor ($\Delta\chi^2 = 1$) compared to the previous case where N_{H} and v are not linked between the two spectra. The results of this model are presented in Tab. 5-3 and Fig. 5-5.

5.4 Discussion and conclusions

5.4.1 Long timescale variability of the disk wind

In the three soft spectra of GRS 1915+105, we detect the presence of a highly ionized ($\log(\xi) > 4.2$) and high column ($N_{\text{H}} \sim 10^{23} \text{ cm}^{-2}$) absorption wind along the line of sight. Over a period of three months, we find that the ionization state of the disk wind correlates with changes in the ionizing flux, indicating a photoionization origin. Notably, Neilsen et al. 2018^[311] identified a persistent accretion disk wind in GRS 1915+105 using *NICER* observations spanning from June to November 2017, which overlaps well with the time frame of the three observations under study. Neilsen et al. 2018^[311] found that the Fe XXV absorption line is less common than Fe XXVI, with the ionization parameter ξ expected to exceed 10^4 based on simple line ratio analysis. Our analysis of *Insight*–HXMT data confirms these findings. Another intriguing observation by^[311] is that the column density of Fe XXVI remains relatively stable across the five-month period, suggesting either a consistent total column density or a balance between variations in total column density and ionization state. However, our

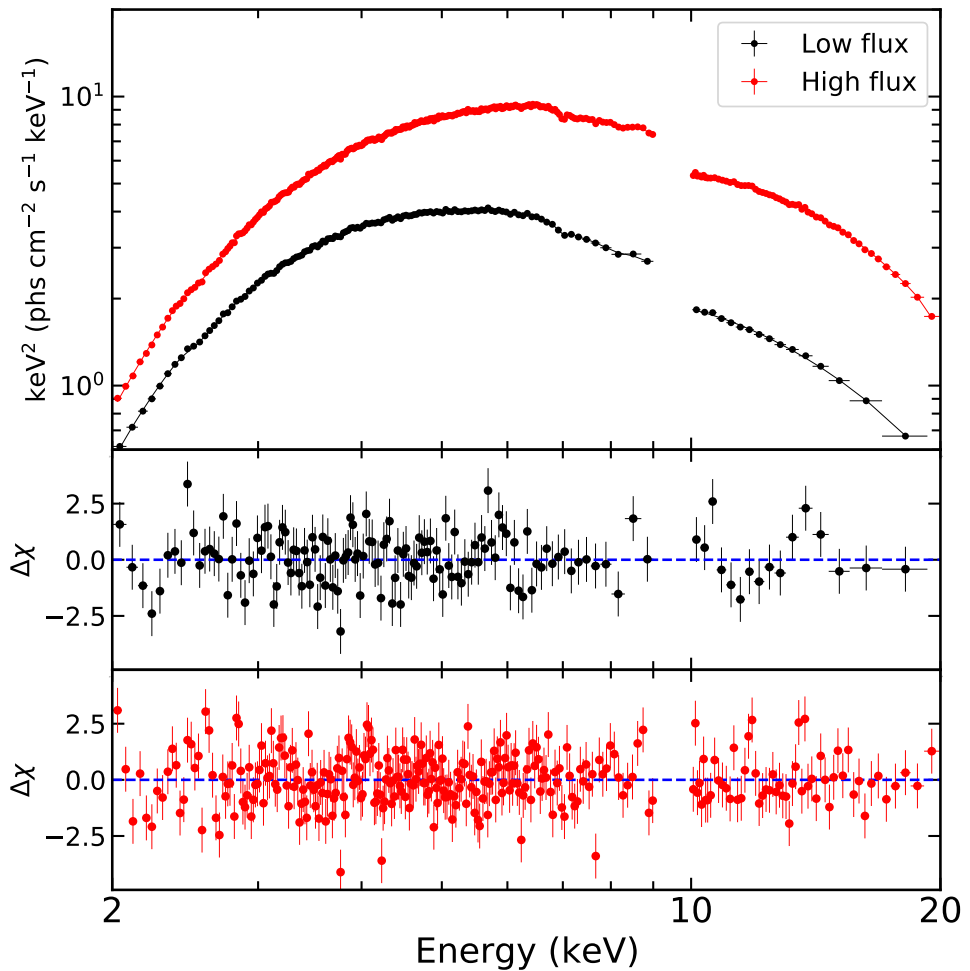


Figure 5-5 Spectra and residuals for the low and high flux data of epoch 1. The spectra are corrected for the effective area and are only shown for demonstration purposes. Data are rebinned for visual clarity.

Table 5-3 Best-fit values.

Component	Parameter	Low Flux	High Flux
TBABS	N_{H} (10^{22} cm^{-2})	$5.6^{+0.4}_{-0.8}$	
XSTAR	N_{H} (10^{22} cm^{-2})	$7.6^{+1.5}_{-2.0}$	
	$\log(\xi)$	$4.15^{+0.08}_{-0.14}$	$4.12^{+0.08}_{-0.13}$
	v (km s^{-1})	1000^{+360}_{-360}	
PCFABS	N_{H} (10^{22} cm^{-2})	$9.7^{+2.5}_{-2.4}$	$7.9^{+1.4}_{-1.3}$
	f_c	$0.39^{+0.14}_{-0.08}$	$0.45^{+0.15}_{-0.09}$
NTHCOMP	Γ	$2.76^{+0.11}_{-0.10}$	$2.35^{+0.16}_{-0.13}$
	kT_e (keV)	$3.76^{+0.36}_{-0.22}$	$3.33^{+0.23}_{-0.15}$
	kT_{bb} (keV)	$1.08^{+0.09}_{-0.09}$	$1.35^{+0.15}_{-0.23}$
	Norm	$2.38^{+0.24}_{-0.20}$	$3.23^{+0.57}_{-0.23}$
GAUSS	E_{line} (keV)	6.4^*	6.4^*
	EW (keV)	$0.046^{+0.029}_{-0.029}$	$0.08^{+0.05}_{-0.05}$
	Norm	$0.50^{+0.26}_{-0.18}$	$1.8^{+2.1}_{-1.3}$
$(10^{-2} \text{ Phs/cm}^2/\text{s})$		$\chi^2/\text{d.o.f}$	
		2024/1904	

Note. Best-fit parameters for the low and high flux state spectra with *Model 4*.

Parameters with * are fixed during the fit.

analysis reveals a clear change in both the total column density and ionization state (in the single zone model) of the absorber from epoch 1 to epoch 3, supporting the latter scenario. The tentative evidence of over-ionization observed in the analysis of short timescale variability of the wind (see Sec. 5.4.2) further reinforces this interpretation. It is conceivable that as the X-ray irradiation on the outer disk intensifies, more material is lifted from the disk into the line of sight. However, the increased ionizing flux also leads to greater ionization of the wind, ultimately maintaining a relatively steady ionic column of Fe XXVI.

Epoch 3 exhibits a distinct variability pattern compared to epochs 1 and 2. However, we do not observe any discernible impact of this difference on the behavior of the disk wind. The higher column density and ionization parameter observed in epoch 3 appear to be primarily a consequence of more intense X-ray illumination. In our analysis employing a two-zone model, we identify a rapid absorber in epoch 3 with an outflow velocity of approximately $0.05c$. Nevertheless, it's worth noting that the detection of this fast absorber lacks strong conviction, as it predominantly fits the same absorption

line (at 7 keV) as the slower component, with no other detectable signatures.

5.4.2 Short timescale variability of the disk wind

The flux-resolved spectra offer insights into the variability of the disk wind on timescales of hundreds of seconds. As shown in Fig. 5-5, the spectra illustrate that the source exhibits a harder spectral state during periods of higher flux. Moreover, spectral analysis indicates a harder power-law emission during these high-flux states (refer to Tab. 5-3).

A preliminary analysis of line widths suggests a marginal significance in the change of equivalent width of the Fe XXVI line at a 90% confidence level (refer to Sec. 5.3.3). The reduction in equivalent width observed during high-flux intervals implies an increase in ionization of the wind as X-ray luminosity rises. As previously mentioned, the source spectrum becomes harder during higher flux states, resulting in a greater abundance of high-energy photons capable of fully stripping the Fe XXVI ions.

The variability of the disk wind in GRS 1915+105 on short timescales, ranging from seconds to kiloseconds, has been investigated using a flux-resolved approach in ρ , β , γ , and θ states^[72,308,315]. To the best of our knowledge, this study represents the first examination of disk wind variability in the κ state. Our findings align with those of Ueda et al. 2010^[308], where a weaker absorption line is observed when the hard X-ray flux is stronger, strongly suggesting photoionization of the disk wind. In Lee et al. 2002^[307], it was reported that the variation amplitude of the ionization parameter of the disk wind was much higher than that of the ionizing flux, indicating changes in the density of the disk wind on kilosecond timescales. Similarly, Neilsen et al. 2011^[72] identified density variations on timescales as short as 5 seconds in the ρ state. However, our flux-resolved analysis did not reveal any evidence of variation in the ionization parameter with changes in the source flux (refer to Tab. 5-3). This suggests that we are seeing changes in the density of the disk wind on a timescale of 200 seconds.

5.4.3 Driving mechanism and mass outflow

The accretion disk wind can be launched by various mechanisms, including radiation, thermal, or magnetic pressure. However, the high ionization state we have observed effectively rules out radiation pressure as the dominant driving mechanism. This is because radiation pressure primarily operates through UV absorption lines and is

typically effective only when the ionization parameter ($\log(\xi)$) is less than 3^[321,333]. Thermally driven winds, on the other hand, can only be launched from relatively large distances, typically on the order of 10^4 gravitational radii (r_g)^[77,334]. Therefore, accurately locating the wind's origin is essential for determining its driving mechanism.

The upper limit of the wind location can be estimated by simple geometric consideration. Since the wind thickness ΔR can not exceed its distance to the central black r , we would have:

$$r < \frac{L_{\text{ion}}}{N_{\text{H}}\xi} \quad (5.1)$$

if assuming $N_{\text{H}} = n\Delta R$ and including the definition of ionization parameter. In this way, the maximum of the radial location will be $8 \times 10^4 R_g$, $11 \times 10^4 R_g$ and $5 \times 10^4 R_g$ for absorbers of epoch 1, 2 and 3, respectively. A lower limit can be placed if we assume that the outflow velocity of the wind is larger than the local escape velocity:

$$r_{\min} = 2GM_{\text{BH}}v_{\text{out}}^{-2} \quad (5.2)$$

This gives a lower boundary of $11 \times 10^4 R_g$, $5 \times 10^4 R_g$ and $8 \times 10^4 R_g$ for epoch 1, 2 and 3 for a black hole mass of $12.4 M_{\odot}$ ^[335]. We note that this is only a loose constraint. The wind can be much closer than this lower boundary if a substantial amount of its velocity is perpendicular to the line of sight. Therefore, the lower limit can be further relaxed to be reconciled with the upper limit. These estimates indicate a launching radius about $10^4 \sim 10^5 R_g$ for the disk wind. This range aligns well with the predictions of a thermally driven wind, suggesting that magnetic pressure is not necessary to explain the wind's behavior.

We can also estimate the mass outflow rate of the disk wind via:

$$\dot{M}_{\text{wind}} = f\mu 4\pi r^2 nm_{\text{p}} v \frac{\Omega}{4\pi} = f\mu \Omega m_{\text{p}} v \left(\frac{L_{\text{ion}}}{\xi} \right) \quad (5.3)$$

where $\Omega/4\pi$ is the covering factor, f is volume filling factor, m_{p} is the proton mass and μ is the mean atomic weight ($\mu = 1.23$ with solar abundances). Assuming the parameters of epoch 3, this gives

$$\dot{M}_{\text{wind}} = 3.1 \times 10^{19} f \left(\frac{\Omega}{4\pi} \right) \text{ g s}^{-1} \quad (5.4)$$

The mass accretion rate is estimated as $M_{\text{acc}} = L/\eta c^2 = 5.6 \times 10^{18} \text{ g s}^{-1}$, where the efficiency is set to $\eta = 0.1$. This comparison shows that, as the covering factor and volume filling factor approach unity, the mass outflow carried by the wind can be

comparable or even larger than the mass accretion rate in the inner disk. The importance of disk wind in the understanding of accretion process is obvious.

Chapter 6

Summary and future work

6.1 Summary of previous research

In this thesis, I have studied the X-ray spectra of several black hole X-ray binaries with the purpose to understand the following aspects: (1) the accretion geometry (or disk-corona geometry) at different accretion states; (2) the microphysics of the accretion disk such as the electron density; (3) the disk wind outflow in X-ray binaries. The first two aspects are studied making use of the relativistic reflection component in the X-ray spectrum. The analysis takes the advantage of recent X-ray missions (e.g., *NuSTAR* and *Insight–HXMT*) that can provide a broadband coverage to capture the full features of the coronal emission (e.g., the photon index and the high-energy cutoff) and the reflection component (e.g., the broad iron line profile and the Compton hump).

Using a sample of black hole X-ray binaries, including MAXI J1535–571, GRS 1739–278, GS 1354–64, IGR J17091–3624, H 1743–322, and V404 Cyg, observed by *NuSTAR* and *Swift* in the hard state, the reflection analysis suggests that the inner edge of the optically thick accretion disk can already be at the ISCO if the accretion rate is high enough (Chapter 4). This conclusion is strengthened by high-cadence observations for the hard-to-soft state transition of GX 339-4 by *Insight–HXMT*. The observation strategy of *Insight–HXMT* makes it possible to provide daily monitoring of the week-long state transition. In addition, the three instruments onboard *Insight–HXMT* cover a wide energy band (1–250 keV) and provide good energy resolution around the iron line (150 eV at 6 keV). These properties make this dataset perfect for applying the reflection analysis to understand the evolution of the disk-corona system during the state transition. The fact that we find the disk to be stable during state transition has important physical implications. It raises questions about the commonly accepted disk truncation scenario to explain the state transition^[133] and also requires a

new explanation of what is happening during the transition. Our spectral analysis is only sensitive to the location of the optically thick accretion disk, but it is difficult to reveal the structure of the corona. The very steep emissivity profile suggests the corona to be compact and close to the black hole, so the strong light bending can concentrate the photons in the inner part of the disk. The steepening of the photon index and the decreasing scattering fraction possibly indicate that the coronal optical depth to the disk photons is decreasing along with the state transition. It should be noted that recent investigations of timing properties (e.g., rms spectra or lag spectra) of BH XRBs provide tentative evidence that the coronal geometry indeed changes during the state transition. Phenomenologically, Wang et al. (2022)^[2] found that the time lag between the direct coronal photons and reflected photons increases along with the state transition, indicating a corona expanding in the vertical direction. Fitting the rms and lag spectra with more physical models has also shown that the corona changes configuration and size (e.g., Zhang et al., 2022^[171]). These analyses, combined with ours, suggest that changes in coronal properties are responsible for the state transition. However, current spectral and timing models are subject to a number of uncertainties. More work in the future is required to validate (or disprove) this idea. Moreover, at the end of the state transition of GX 339–4, we find that the source alternating rapidly between a high and a low flux states, which is a result of changing of the coronal power by a factor of 3 on a timescale of a few minutes.

The hard state sample also allows us to measure the density of the accretion disk. We find that the disk density of XRBs is higher than the previously assumed value in reflection models. High-density reflection models are required to correctly model their X-ray spectra. More importantly, we find that the vertical density structure is important for XRBs in the hard state. This is revealed by the fact that the density on the disk surface measured with our reflection model is systematically lower than that of the theoretical value at the disk mid plane. Physically we also expect a density gradient since the disk is mainly supported by gas pressure ($P = nkT$, n is the density) in the vertical direction in the hard state. This lead to a new concern of current reflection models in the sense that they all assumed a constant density in the vertical direction, possibly to simplify the calculation. This might be appropriate for high accretion rate AGNs (e.g., narrow line Seyfert 1s) because radiation pressure is more important in these sources. A gradient of

the density will significantly changes the ionization structure in the vertical direction, therefore altering the line emission and Comptonization within the disk. Moreover, ionizing instability will cause two distinctive layers on the disk surface: an upper layer with low density, high temperature and high ionization and a low layer with high density, low temperature and low ionization^[336]. The transition between the two layers will be sharp (see Figure 1.23 of Done et al. 2010^[337]). In this sense, the density structure is important for both XRBs and AGNs. Implementation of the density structure in reflection models is required in the future.

The *Insight*–HXMT observations of GRS 1915+105 during its spectrally soft state enable us to study the evolution of the disk wind on a timescale of months. Moreover, the source was captured during one of its exotic variability states^[327], which makes it possible to also study the response of the disk wind on a short timescale of 200 s. The wind responds to the ionizing continuum on both long and short timescales. With geometric considerations, we can only roughly estimate the launching radius of the wind, making it difficult to understand the launching mechanism.

6.2 Future work

6.2.1 Spectral-timing study of the state transition

As mentioned above, the energy spectrum is only sensitive to the geometry of the cold accretion disk, but the timing properties hold the potential to reveal the coronal structure. Therefore, a natural extension of our work in the future is to combine the constraining power of both spectral and timing analysis. The dataset presented in Chapter 2 would be a good candidate for this, given that *Insight*–HXMT has good time resolution. It has to be noted although there is little debate about the spectral components for XRBs, a few distinctive models exist to explain their X-ray timing products such `reltrans`^[131] and `vkompthdk`^[338].

6.2.2 Disk density at soft state

As of now, the density of the accretion disk has been studied in AGNs^[7,11] and hard state of XRBs^[6]. The soft state remains largely unexplored, mainly because the lack of appropriate reflection models. In the soft state of BH XRBs, the disk thermal emission is strong, with a peak temperature around 1 keV. This strong thermal emission will for sure contribute to ionize the disk atmosphere. Therefore, the ionizing continuum should be

a combination of the coronal emission from above the disk and thermal emission within the disk. Such models are still in lack (see more discussions in Sec 6.2.3 below).

6.2.3 Improving reflection models

There are four vital ingredients for calculating the full relativistic reflection spectrum: (1) the local spectrum (2) the corona geometry, (3) the disk structure and (4) the relativistic effects. The commonly used models today implement a optically thick geometrically thin accretion disk (e.g., the Novikov-Thorne disk^[339]). This assumption can be met if the mass accretion rate is at a moderate value (e.g., $5\% < \lambda_{\text{Edd}} < 30\%$)^[340]. At higher accretion rates, the disk might be puffed up to form a thick disk which may bias our measurements if a thin disk model is used to fit the data^[341]. As for the relativistic effects, standard reflection models usually employ the Kerr metric to describe the spacetime near the black hole. Metrics beyond Kerr have also been implemented, with the purpose to test the prediction of general relativity^[135–136].

Significant uncertainties still exist for the calculation of the local reflection spectrum. The first one is the vertical density structure as mentioned in Sec. 6.1. For future work, I will improve current reflection codes by incorporating a density profile along the vertical direction. The density profile will be derived from predictions of accretion theories^[115] or calculations of hydrostatic equilibrium^[342]. The second source of uncertainty comes from the “hot disk” effect as discussed in Sec. 6.2.2. Current reflection models typically incorporate the “cold disk” assumption, assuming an effective temperature of approximately 10 eV for the disk. This assumption is in agreement with observations of AGNs but the disk temperatures of XRBs can often be considerably hotter ($\sim 1 \text{ keV}$,^[4]). The hot disk could provide additional and sometimes stronger thermal emission than the coronal emission to ionize the disk surface and impacts the reflection spectrum. Stronger Compton process is also expected in this case. Such effects are particularly important for XRBs in the intermediate state and the thermally dominant soft state. The impact has been partly included in the `reflionx` model^[168] and studied in some sources^[13]. The major caveat of the previous `reflionx` model and related studies in this context is that the disk was assumed to emit a single-temperature blackbody emission. In reality, the accretion disk exhibits a multi-temperature blackbody spectrum, with higher temperatures closer to the central black hole. This will lead to a radius-dependent ionization state of the disk. I plan to develop a relativistic reflection

model based on the previous `reflionx` model, taking into account multi-temperature nature of the disk. In this way, the thermal emission from the disk is self-consistently considered, without the need to include an additional thermal component in data analysis. The model will be the first self-consistent reflection model specifically designed for XRBs. I will apply the model to *NuSTAR/Insight–HXMT* observations of XRBs to: (1) study the long-debating disk-corona geometry during the state transition (2) measure more properly the black hole spins in XRBs and compare to gravitational wave sources in order to understand the interplay between different evolutionary channels (3) measure the disk density in the soft state.

The geometry of the corona in accreting systems remains poorly understood. However, it is important for modeling the reflection component as it determines how the disk is illuminated (see Figure 1-11). Previous reflection analyses have addressed this by adopting simple geometrical assumptions, such as a lamppost positioned above the black hole^[60] or by fitting the illumination pattern with a phenomenological profile, often a simple power-law. These simplified assumptions generally yield good fits to the data^[4]. Nevertheless, this unknown geometry also involves significant uncertainties in interpreting the data, which can exceed the statistical uncertainties derived from data fitting. For example, in Liu et al. 2019^[136], it is shown that the measurements of spacetime metric of Cygnus X-1 strongly depends on the assumption of the illumination pattern. In some cases, the measurements of the disk inclination angle can vary by up to 30° when different coronal geometry assumptions are employed^[256].

6.2.4 Spectra-polarimetric study of accreting systems

The Imaging X-ray Polarimetry Explorer (IXPE) mission, launched in 2021, offers additional insights into the coronal geometry. The two quantities measured by IXPE, the polarization degree (PD) and polarization angle (PA), reveal the level of asymmetry and the main orientation of the emitting region. The first IXPE visit of Cygnus X-1 in the hard state already found that the corona should have a slab geometry (extended in the radial direction^[64], but see Dexter & Begelman 2024^[343]), although the exact configuration has not been figured out. This geometric information can be incorporated into the reflection analysis to mitigate systematic uncertainties. Furthermore, the reflection component itself exhibits unique polarization characteristics, such as depolarized fluorescent lines^[344]. However, the reflection component has been largely ignored in

polarimetry studies because the lack of proper models. Moreover, in Cygnus X-2, it is already found that including the polarization of the reflection component can impact the interpretation of the measurements (Liu et al. in prep).

Therefore, combining the constraining power of spectroscopic and polarimetric measurements based on X-ray reflection spectroscopy has the potential to unveil the coronal geometry. Such reflection models should incorporate specific coronal geometries, such as a wedge-shaped corona around the disk or a cone-shaped corona aligned with the spin axis with sizes or opening angles as free parameters^[345]. The calculation of how the corona illuminates the accretion disk and produce the reflection spectrum can be performed using ray-tracing code such as `blacklamp`^[346] and the improved local reflection models mentioned in above sections. Additionally, the polarization properties of the coronal emission and reflection component with the chosen geometries can be computed using codes like `MONK`^[347] and `STOKES`^[348]. There are other codes that can do similar tasks, such as the `KerrC`^[345] code and the `KYN` package^[124].

Bibliography

- [1] Ponti G, Fender R P, Begelman M C, et al. Ubiquitous equatorial accretion disc winds in black hole soft states[J/OL]. *MNRAS*, 2012, 422(1): L11-L15. DOI: [10.1111/j.1745-3933.2012.01224.x](https://doi.org/10.1111/j.1745-3933.2012.01224.x).
- [2] Wang J, Kara E, Lucchini M, et al. The NICER “Reverberation Machine”: A Systematic Study of Time Lags in Black Hole X-Ray Binaries[J/OL]. *ApJ*, 2022, 930(1): 18. DOI: [10.3847/1538-4357/ac6262](https://doi.org/10.3847/1538-4357/ac6262).
- [3] Fabian A C, Iwasawa K, Reynolds C S, et al. Broad Iron Lines in Active Galactic Nuclei[J/OL]. *PASP*, 2000, 112(775): 1145-1161. DOI: [10.1086/316610](https://doi.org/10.1086/316610).
- [4] Liu H, Bambi C, Jiang J, et al. The Hard-to-soft Transition of GX 339-4 as Seen by Insight-HXMT[J/OL]. *ApJ*, 2023, 950(1): 5. DOI: [10.3847/1538-4357/acca17](https://doi.org/10.3847/1538-4357/acca17).
- [5] Steiner J F, McClintock J E, Reid M J. The Distance, Inclination, and Spin of the Black Hole Microquasar H1743-322[J/OL]. *ApJ*, 2012, 745(1): L7. DOI: [10.1088/2041-8205/745/1/L7](https://doi.org/10.1088/2041-8205/745/1/L7).
- [6] Jiang J, Fabian A C, Wang J, et al. High-density reflection spectroscopy: I. A case study of GX 339-4[J/OL]. *MNRAS*, 2019, 484(2): 1972-1982. DOI: [10.1093/mnras/stz095](https://doi.org/10.1093/mnras/stz095).
- [7] Jiang J, Fabian A C, Dauser T, et al. High Density Reflection Spectroscopy - II. The density of the inner black hole accretion disc in AGN[J/OL]. *MNRAS*, 2019, 489(3): 3436-3455. DOI: [10.1093/mnras/stz2326](https://doi.org/10.1093/mnras/stz2326).
- [8] Tomsick J A, Parker M L, García J A, et al. Alternative Explanations for Extreme Supersolar Iron Abundances Inferred from the Energy Spectrum of Cygnus X-1 [J/OL]. *ApJ*, 2018, 855(1): 3. DOI: [10.3847/1538-4357/aaaab1](https://doi.org/10.3847/1538-4357/aaaab1).

- [9] Jiang J, Fürst F, Walton D J, et al. A NuSTAR view of GRS 1716-249 in the hard and intermediate states[J/OL]. MNRAS, 2020, 492(2): 1947-1956. DOI: [10.1093/mnras/staa017](https://doi.org/10.1093/mnras/staa017).
- [10] Liu H, Bambi C, Jiang J, et al. The hard to soft transition of GX 339-4 as seen by Insight-HXMT[A]. 2022: arXiv:2211.09543. arXiv: [2211.09543](https://arxiv.org/abs/2211.09543).
- [11] Mallick L, Fabian A C, García J A, et al. High-density disc reflection spectroscopy of low-mass active galactic nuclei[J/OL]. MNRAS, 2022, 513(3): 4361-4379. DOI: [10.1093/mnras/stac990](https://doi.org/10.1093/mnras/stac990).
- [12] Miller J M, Homan J, Steeghs D, et al. A Long, Hard Look at the Low/Hard State in Accreting Black Holes[J/OL]. ApJ, 2006, 653(1): 525-535. DOI: [10.1086/508644](https://doi.org/10.1086/508644).
- [13] Reis R C, Fabian A C, Ross R R, et al. A systematic look at the very high and low/hard state of GX339-4: constraining the black hole spin with a new reflection model[J/OL]. MNRAS, 2008, 387(4): 1489-1498. DOI: [10.1111/j.1365-2966.2008.13358.x](https://doi.org/10.1111/j.1365-2966.2008.13358.x).
- [14] Tomsick J A, Kalemci E, Kaaret P, et al. Broadband X-Ray Spectra of GX 339-4 and the Geometry of Accreting Black Holes in the Hard State[J/OL]. ApJ, 2008, 680(1): 593-601. DOI: [10.1086/587797](https://doi.org/10.1086/587797).
- [15] Tomsick J A, Yamaoka K, Corbel S, et al. Truncation of the Inner Accretion Disk Around a Black Hole at Low Luminosity[J/OL]. ApJ, 2009, 707(1): L87-L91. DOI: [10.1088/0004-637X/707/1/L87](https://doi.org/10.1088/0004-637X/707/1/L87).
- [16] Shidatsu M, Ueda Y, Tazaki F, et al. X-Ray and Near-Infrared Observations of GX 339-4 in the Low/Hard State with Suzaku and IRSF[J/OL]. PASJ, 2011, 63: S785-S801. DOI: [10.1093/pasj/63.sp3.S785](https://doi.org/10.1093/pasj/63.sp3.S785).
- [17] Kolehmainen M, Done C, Díaz Trigo M. The soft component and the iron line as signatures of the disc inner radius in Galactic black hole binaries[J/OL]. MNRAS, 2014, 437(1): 316-326. DOI: [10.1093/mnras/stt1886](https://doi.org/10.1093/mnras/stt1886).

- [18] Petrucci P O, Cabanac C, Corbel S, et al. The return to the hard state of GX 339-4 as seen by Suzaku[J/OL]. *A&A*, 2014, 564: A37. DOI: [10.1051/0004-6361/201322268](https://doi.org/10.1051/0004-6361/201322268).
- [19] Plant D S, Fender R P, Ponti G, et al. The truncated and evolving inner accretion disc of the black hole GX 339-4[J/OL]. *A&A*, 2015, 573: A120. DOI: [10.1051/0004-6361/201423925](https://doi.org/10.1051/0004-6361/201423925).
- [20] García J A, Steiner J F, McClintock J E, et al. X-Ray Reflection Spectroscopy of the Black Hole GX 339–4: Exploring the Hard State with Unprecedented Sensitivity[J/OL]. *ApJ*, 2015, 813(2): 84. DOI: [10.1088/0004-637X/813/2/84](https://doi.org/10.1088/0004-637X/813/2/84).
- [21] Basak R, Zdziarski A A. Spectral analysis of the XMM-Newton data of GX 339-4 in the low/hard state: disc truncation and reflection[J/OL]. *MNRAS*, 2016, 458 (2): 2199-2214. DOI: [10.1093/mnras/stw420](https://doi.org/10.1093/mnras/stw420).
- [22] Wang-Ji J, García J A, Steiner J F, et al. The Evolution of GX 339-4 in the Low-hard State as Seen by NuSTAR and Swift[J/OL]. *ApJ*, 2018, 855(1): 61. DOI: [10.3847/1538-4357/aaa974](https://doi.org/10.3847/1538-4357/aaa974).
- [23] Shemmer O, Brandt W N, Netzer H, et al. The Hard X-Ray Spectrum as a Probe for Black Hole Growth in Radio-Quiet Active Galactic Nuclei[J/OL]. *ApJ*, 2008, 682(1): 81-93. DOI: [10.1086/588776](https://doi.org/10.1086/588776).
- [24] Sitzungsberichte der Königlich Preußischen Akademie der Wissenschaften [J/OL]. *Naturwissenschaften*, 1915, 3(33): 436-436. DOI: [10.1007/BF01546184](https://doi.org/10.1007/BF01546184).
- [25] Chruściel P T, Costa J L, Heusler M. Stationary Black Holes: Uniqueness and Beyond[J/OL]. *Living Reviews in Relativity*, 2012, 15(1): 7. DOI: [10.12942/lrr-2012-7](https://doi.org/10.12942/lrr-2012-7).
- [26] Schwarzschild K. Über das Gravitationsfeld eines Massenpunktes nach der Einsteinschen Theorie[J]. *Sitzungsberichte der Königlich Preussischen Akademie der Wissenschaften*, 1916: 189-196.

- [27] Kerr R P. Gravitational Field of a Spinning Mass as an Example of Algebraically Special Metrics[J/OL]. *Phys. Rev. Lett.*, 1963, 11(5): 237-238. DOI: [10.1103/PhysRevLett.11.237](https://doi.org/10.1103/PhysRevLett.11.237).
- [28] Haardt F, Maraschi L. A Two-Phase Model for the X-Ray Emission from Seyfert Galaxies[J/OL]. *ApJ*, 1991, 380: L51. DOI: [10.1086/186171](https://doi.org/10.1086/186171).
- [29] Pounds K. Searching for Black Holes in Space. The Key Role of X-Ray Observations[J/OL]. *Space Sci. Rev.*, 2014, 183(1-4): 5-19. DOI: [10.1007/s11214-013-0011-9](https://doi.org/10.1007/s11214-013-0011-9).
- [30] Thorne K S. Disk-Accretion onto a Black Hole. II. Evolution of the Hole[J/OL]. *ApJ*, 1974, 191: 507-520. DOI: [10.1086/152991](https://doi.org/10.1086/152991).
- [31] Seyfert C K. Nuclear Emission in Spiral Nebulae.[J/OL]. *ApJ*, 1943, 97: 28. DOI: [10.1086/144488](https://doi.org/10.1086/144488).
- [32] Antonucci R. Unified models for active galactic nuclei and quasars.[J/OL]. *ARA&A*, 1993, 31: 473-521. DOI: [10.1146/annurev.aa.31.090193.002353](https://doi.org/10.1146/annurev.aa.31.090193.002353).
- [33] Kormendy J, Richstone D. Inward Bound—The Search For Supermassive Black Holes In Galactic Nuclei[J/OL]. *ARA&A*, 1995, 33: 581. DOI: [10.1146/annurev.aa.33.090195.003053](https://doi.org/10.1146/annurev.aa.33.090195.003053).
- [34] Magorrian J, Tremaine S, Richstone D, et al. The Demography of Massive Dark Objects in Galaxy Centers[J/OL]. *AJ*, 1998, 115(6): 2285-2305. DOI: [10.1086/300353](https://doi.org/10.1086/300353).
- [35] Ferrarese L, Merritt D. A Fundamental Relation between Supermassive Black Holes and Their Host Galaxies[J/OL]. *ApJ*, 2000, 539(1): L9-L12. DOI: [10.1086/631283](https://doi.org/10.1086/631283).
- [36] Gebhardt K, Bender R, Bower G, et al. A Relationship between Nuclear Black Hole Mass and Galaxy Velocity Dispersion[J/OL]. *ApJ*, 2000, 539(1): L13-L16. DOI: [10.1086/312840](https://doi.org/10.1086/312840).
- [37] Kormendy J, Ho L C. Coevolution (Or Not) of Supermassive Black Holes and Host Galaxies[J/OL]. *ARA&A*, 2013, 51(1): 511-653. DOI: [10.1146/annurev-astro-082708-101811](https://doi.org/10.1146/annurev-astro-082708-101811).

- [38] Fabian A C. Observational Evidence of Active Galactic Nuclei Feedback[J/OL]. *ARA&A*, 2012, 50: 455-489. DOI: [10.1146/annurev-astro-081811-125521](https://doi.org/10.1146/annurev-astro-081811-125521).
- [39] Corral-Santana J M, Casares J, Muñoz-Darias T, et al. BlackCAT: A catalogue of stellar-mass black holes in X-ray transients[J/OL]. *A&A*, 2016, 587: A61. DOI: [10.1051/0004-6361/201527130](https://doi.org/10.1051/0004-6361/201527130).
- [40] Heger A, Fryer C L, Woosley S E, et al. How Massive Single Stars End Their Life[J/OL]. *ApJ*, 2003, 591(1): 288-300. DOI: [10.1086/375341](https://doi.org/10.1086/375341).
- [41] Matsuoka M, Kawasaki K, Ueno S, et al. The MAXI Mission on the ISS: Science and Instruments for Monitoring All-Sky X-Ray Images[J/OL]. *PASJ*, 2009, 61: 999. DOI: [10.1093/pasj/61.5.999](https://doi.org/10.1093/pasj/61.5.999).
- [42] Tetarenko B E, Sivakoff G R, Heinke C O, et al. WATCHDOG: A Comprehensive All-sky Database of Galactic Black Hole X-ray Binaries[J/OL]. *ApJS*, 2016, 222(2): 15. DOI: [10.3847/0067-0049/222/2/15](https://doi.org/10.3847/0067-0049/222/2/15).
- [43] Moravec E, Svoboda J, Borkar A, et al. Do radio active galactic nuclei reflect X-ray binary spectral states?[J/OL]. *A&A*, 2022, 662: A28. DOI: [10.1051/0004-6361/202142870](https://doi.org/10.1051/0004-6361/202142870).
- [44] Arcodia R, Ponti G, Merloni A, et al. Do stellar-mass and super-massive black holes have similar dining habits?[J/OL]. *A&A*, 2020, 638: A100. DOI: [10.1051/0004-6361/202037969](https://doi.org/10.1051/0004-6361/202037969).
- [45] Merloni A, Heinz S, di Matteo T. A Fundamental Plane of black hole activity [J/OL]. *MNRAS*, 2003, 345(4): 1057-1076. DOI: [10.1046/j.1365-2966.2003.07017.x](https://doi.org/10.1046/j.1365-2966.2003.07017.x).
- [46] Narayan R, McClintock J E. Advection-dominated accretion and the black hole event horizon[J/OL]. *New A Rev.*, 2008, 51(10-12): 733-751. DOI: [10.1016/j.newar.2008.03.002](https://doi.org/10.1016/j.newar.2008.03.002).
- [47] Yuan F, Narayan R. Hot Accretion Flows Around Black Holes[J/OL]. *ARA&A*, 2014, 52: 529-588. DOI: [10.1146/annurev-astro-082812-141003](https://doi.org/10.1146/annurev-astro-082812-141003).

- [48] Narayan R. Low-Luminosity Accretion in Black Hole X-Ray Binaries and Active Galactic Nuclei[J/OL]. *Ap&SS*, 2005, 300(1-3): 177-188. DOI: [10.1007/s10509-005-1178-7](https://doi.org/10.1007/s10509-005-1178-7).
- [49] Frank J, King A, Raine D J. Accretion Power in Astrophysics: Third Edition[M]. 2002.
- [50] Lightman A P, Shapiro S L. Spectrum and polarization of X-rays from accretion disks around black holes.[J/OL]. *ApJ*, 1975, 198: L73-L75. DOI: [10.1086/181815](https://doi.org/10.1086/181815).
- [51] Elvis M, Maccacaro T, Wilson A S, et al. Seyfert galaxies as X-ray sources. [J/OL]. *MNRAS*, 1978, 183: 129-157. DOI: [10.1093/mnras/183.2.129](https://doi.org/10.1093/mnras/183.2.129).
- [52] Eardley D M, Lightman A P, Shapiro S L. Cygnus X-1: a two-temperature accretion disk model which explains the observed hard X-ray spectrum.[J/OL]. *ApJ*, 1975, 199: L153-L155. DOI: [10.1086/181871](https://doi.org/10.1086/181871).
- [53] Petrucci P O, Haardt F, Maraschi L, et al. Testing Comptonization Models Using BeppoSAX Observations of Seyfert 1 Galaxies[J/OL]. *ApJ*, 2001, 556(2): 716-726. DOI: [10.1086/321629](https://doi.org/10.1086/321629).
- [54] Fabian A C, Lohfink A, Kara E, et al. Properties of AGN coronae in the NuSTAR era[J/OL]. *MNRAS*, 2015, 451(4): 4375-4383. DOI: [10.1093/mnras/stv1218](https://doi.org/10.1093/mnras/stv1218).
- [55] Zdziarski A A, Johnson W N, Magdziarz P. Broad-band γ -ray and X-ray spectra of NGC 4151 and their implications for physical processes and geometry.[J/OL]. *MNRAS*, 1996, 283(1): 193-206. DOI: [10.1093/mnras/283.1.193](https://doi.org/10.1093/mnras/283.1.193).
- [56] Źycki P T, Done C, Smith D A. The 1989 May outburst of the soft X-ray transient GS 2023+338 (V404 Cyg)[J/OL]. *MNRAS*, 1999, 309(3): 561-575. DOI: [10.1046/j.1365-8711.1999.02885.x](https://doi.org/10.1046/j.1365-8711.1999.02885.x).
- [57] Coppi P S. The Physics of Hybrid Thermal/Non-Thermal Plasmas[C]//Poutanen J, Svensson R. Astronomical Society of the Pacific Conference Series: Vol. 161 High Energy Processes in Accreting Black Holes. 1999: 375.

- [58] Merloni A, Fabian A C. Accretion disc coronae as magnetic reservoirs[J/OL]. MNRAS, 2001, 321(3): 549-552. DOI: [10.1046/j.1365-8711.2001.04060.x](https://doi.org/10.1046/j.1365-8711.2001.04060.x).
- [59] Matt G, Perola G C, Piro L. The iron line and high energy bump as X-ray signatures of cold matter in Seyfert 1 galaxies.[J]. A&A, 1991, 247: 25.
- [60] Dauser T, Garcia J, Wilms J, et al. Irradiation of an accretion disc by a jet: general properties and implications for spin measurements of black holes[J/OL]. MNRAS, 2013, 430(3): 1694-1708. DOI: [10.1093/mnras/sts710](https://doi.org/10.1093/mnras/sts710).
- [61] Markoff S, Nowak M A, Wilms J. Going with the Flow: Can the Base of Jets Subsume the Role of Compact Accretion Disk Coronae?[J/OL]. ApJ, 2005, 635 (2): 1203-1216. DOI: [10.1086/497628](https://doi.org/10.1086/497628).
- [62] Esin A A, McClintock J E, Narayan R. Advection-Dominated Accretion and the Spectral States of Black Hole X-Ray Binaries: Application to Nova Muscae 1991 [J/OL]. ApJ, 1997, 489(2): 865-889. DOI: [10.1086/304829](https://doi.org/10.1086/304829).
- [63] Liu B F, Qiao E. Accretion around black holes: The geometry and spectra[J/OL]. iScience, 2022, 25(1): 103544. DOI: [10.1016/j.isci.2021.103544](https://doi.org/10.1016/j.isci.2021.103544).
- [64] Krawczynski H, Muleri F, Dovčiak M, et al. Polarized x-rays constrain the disk-jet geometry in the black hole x-ray binary Cygnus X-1[J/OL]. Science, 2022, 378(6620): 650-654. DOI: [10.1126/science.add5399](https://doi.org/10.1126/science.add5399).
- [65] Haardt F, Maraschi L. X-Ray Spectra from Two-Phase Accretion Disks[J/OL]. ApJ, 1993, 413: 507. DOI: [10.1086/173020](https://doi.org/10.1086/173020).
- [66] Haardt F, Maraschi L, Ghisellini G. A Model for the X-Ray and Ultraviolet Emission from Seyfert Galaxies and Galactic Black Holes[J/OL]. ApJ, 1994, 432: L95. DOI: [10.1086/187520](https://doi.org/10.1086/187520).
- [67] Stern B E, Poutanen J, Svensson R, et al. On the Geometry of the X-Ray-Emitting Region in Seyfert Galaxies[J/OL]. ApJ, 1995, 449: L13. DOI: [10.1086/309617](https://doi.org/10.1086/309617).
- [68] Reynolds C S, Nowak M A. Fluorescent iron lines as a probe of astrophysical black hole systems[J/OL]. Phys. Rep., 2003, 377(6): 389-466. DOI: [10.1016/S0370-1573\(02\)00584-7](https://doi.org/10.1016/S0370-1573(02)00584-7).

- [69] Bambi C, Brenneman L W, Dauser T, et al. Towards Precision Measurements of Accreting Black Holes Using X-Ray Reflection Spectroscopy[J/OL]. *Space Sci. Rev.*, 2021, 217(5): 65. DOI: [10.1007/s11214-021-00841-8](https://doi.org/10.1007/s11214-021-00841-8).
- [70] Beloborodov A M. Plasma Ejection from Magnetic Flares and the X-Ray Spectrum of Cygnus X-1[J/OL]. *ApJ*, 1999, 510(2): L123-L126. DOI: [10.1086/311810](https://doi.org/10.1086/311810).
- [71] Poutanen J, Veledina A, Beloborodov A M. Polarized X-Rays from Windy Accretion in Cygnus X-1[J/OL]. *ApJ*, 2023, 949(1): L10. DOI: [10.3847/2041-8213/acd33e](https://doi.org/10.3847/2041-8213/acd33e).
- [72] Neilsen J, Remillard R A, Lee J C. The Physics of the “Heartbeat” State of GRS 1915+105[J/OL]. *ApJ*, 2011, 737(2): 69. DOI: [10.1088/0004-637X/737/2/69](https://doi.org/10.1088/0004-637X/737/2/69).
- [73] Dubus G, Done C, Tetarenko B E, et al. The impact of thermal winds on the outburst lightcurves of black hole X-ray binaries[J/OL]. *A&A*, 2019, 632: A40. DOI: [10.1051/0004-6361/201936333](https://doi.org/10.1051/0004-6361/201936333).
- [74] Shields G A, McKee C F, Lin D N C, et al. Compton-heated Winds and Coronae above Accretion Disks. III. Instability and Oscillations[J/OL]. *ApJ*, 1986, 306: 90. DOI: [10.1086/164322](https://doi.org/10.1086/164322).
- [75] Neilsen J, Lee J C. Accretion disk winds as the jet suppression mechanism in the microquasar GRS 1915+105[J/OL]. *Nature*, 2009, 458(7237): 481-484. DOI: [10.1038/nature07680](https://doi.org/10.1038/nature07680).
- [76] Homan J, Neilsen J, Allen J L, et al. Evidence for Simultaneous Jets and Disk Winds in Luminous Low-mass X-Ray Binaries[J/OL]. *ApJ*, 2016, 830(1): L5. DOI: [10.3847/2041-8205/830/1/L5](https://doi.org/10.3847/2041-8205/830/1/L5).
- [77] Begelman M C, McKee C F, Shields G A. Compton heated winds and coronae above accretion disks. I. Dynamics.[J/OL]. *ApJ*, 1983, 271: 70-88. DOI: [10.1086/161178](https://doi.org/10.1086/161178).
- [78] Done C, Tomaru R, Takahashi T. Thermal winds in stellar mass black hole and neutron star binary systems[J/OL]. *MNRAS*, 2018, 473(1): 838-848. DOI: [10.1093/mnras/stx2400](https://doi.org/10.1093/mnras/stx2400).

- [79] Liu H, Fu Y, Bambi C, et al. The Disk Wind in GRS 1915+105 as Seen by Insight-Hard X-Ray Modulation Telescope[J/OL]. *ApJ*, 2022, 933(2): 122. DOI: [10.3847/1538-4357/ac74b1](https://doi.org/10.3847/1538-4357/ac74b1).
- [80] Miller J M, Raymond J, Fabian A, et al. The magnetic nature of disk accretion onto black holes[J/OL]. *Nature*, 2006, 441(7096): 953-955. DOI: [10.1038/nature04912](https://doi.org/10.1038/nature04912).
- [81] Miller J M, Raymond J, Reynolds C S, et al. The Accretion Disk Wind in the Black Hole GRO J1655-40[J/OL]. *ApJ*, 2008, 680(2): 1359-1377. DOI: [10.1086/588521](https://doi.org/10.1086/588521).
- [82] Tomaru R, Done C, Mao J. What powers the wind from the black hole accretion disc in GRO J1655-40?[J/OL]. *MNRAS*, 2023, 518(2): 1789-1801. DOI: [10.1093/mnras/stac3210](https://doi.org/10.1093/mnras/stac3210).
- [83] Shidatsu M, Done C. Application of the Thermal Wind Model to Absorption Features in the Black Hole X-Ray Binary H1743-322[J/OL]. *ApJ*, 2019, 885(2): 112. DOI: [10.3847/1538-4357/ab46b3](https://doi.org/10.3847/1538-4357/ab46b3).
- [84] Miller J M, Raymond J, Fabian A C, et al. The Disk-wind-Jet Connection in the Black Hole H 1743-322[J/OL]. *ApJ*, 2012, 759(1): L6. DOI: [10.1088/2041-8205/759/1/L6](https://doi.org/10.1088/2041-8205/759/1/L6).
- [85] Ponti G, Bianchi S, Muñoz-Darias T, et al. On the Fe K absorption - accretion state connection in the Galactic Centre neutron star X-ray binary AX J1745.6-2901[J/OL]. *MNRAS*, 2015, 446(2): 1536-1550. DOI: [10.1093/mnras/stu1853](https://doi.org/10.1093/mnras/stu1853).
- [86] Petrucci P O, Bianchi S, Ponti G, et al. Expected evolution of disk wind properties along an X-ray binary outburst[J/OL]. *A&A*, 2021, 649: A128. DOI: [10.1051/0004-6361/202039524](https://doi.org/10.1051/0004-6361/202039524).
- [87] Lasota J P. The disc instability model of dwarf novae and low-mass X-ray binary transients[J/OL]. *New A Rev.*, 2001, 45(7): 449-508. DOI: [10.1016/S1387-6473\(01\)00112-9](https://doi.org/10.1016/S1387-6473(01)00112-9).

- [88] Dubus G, Hameury J M, Lasota J P. The disc instability model for X-ray transients: Evidence for truncation and irradiation[J/OL]. *A&A*, 2001, 373: 251-271. DOI: [10.1051/0004-6361:20010632](https://doi.org/10.1051/0004-6361:20010632).
- [89] Belloni T, Homan J, Casella P, et al. The evolution of the timing properties of the black-hole transient GX 339-4 during its 2002/2003 outburst[J/OL]. *A&A*, 2005, 440(1): 207-222. DOI: [10.1051/0004-6361:20042457](https://doi.org/10.1051/0004-6361:20042457).
- [90] Muñoz-Darias T, Motta S, Belloni T M. Fast variability as a tracer of accretion regimes in black hole transients[J/OL]. *MNRAS*, 2011, 410(1): 679-684. DOI: [10.1111/j.1365-2966.2010.17476.x](https://doi.org/10.1111/j.1365-2966.2010.17476.x).
- [91] Heil L M, Uttley P, Klein-Wolt M. Power colours: simple X-ray binary variability comparison[J/OL]. *MNRAS*, 2015, 448(4): 3339-3347. DOI: [10.1093/mnras/stv191](https://doi.org/10.1093/mnras/stv191).
- [92] Yan Z, Xie F G, Zhang W. Coronal Properties of Black Hole X-Ray Binaries in the Hard State as Seen by NuSTAR and Swift[J/OL]. *ApJ*, 2020, 889(1): L18. DOI: [10.3847/2041-8213/ab665e](https://doi.org/10.3847/2041-8213/ab665e).
- [93] Coriat M, Corbel S, Prat L, et al. Radiatively efficient accreting black holes in the hard state: the case study of H1743-322[J/OL]. *MNRAS*, 2011, 414(1): 677-690. DOI: [10.1111/j.1365-2966.2011.18433.x](https://doi.org/10.1111/j.1365-2966.2011.18433.x).
- [94] Muñoz-Darias T, Casares J, Mata Sánchez D, et al. Regulation of black-hole accretion by a disk wind during a violent outburst of V404 Cygni[J/OL]. *Nature*, 2016, 534(7605): 75-78. DOI: [10.1038/nature17446](https://doi.org/10.1038/nature17446).
- [95] Muñoz-Darias T, Jiménez-Ibarra F, Panizo-Espinar G, et al. Hard-state Accretion Disk Winds from Black Holes: The Revealing Case of MAXI J1820+070[J/OL]. *ApJ*, 2019, 879(1): L4. DOI: [10.3847/2041-8213/ab2768](https://doi.org/10.3847/2041-8213/ab2768).
- [96] Panizo-Espinar G, Armas Padilla M, Muñoz-Darias T, et al. Discovery of optical and infrared accretion disc wind signatures in the black hole candidate MAXI J1348-630[J/OL]. *A&A*, 2022, 664: A100. DOI: [10.1051/0004-6361/202243426](https://doi.org/10.1051/0004-6361/202243426).

- [97] Casella P, Belloni T, Homan J, et al. A study of the low-frequency quasi-periodic oscillations in the X-ray light curves of the black hole candidate <ASTROBJ>XTE J1859+226</ASTROBJ>[J/OL]. *A&A*, 2004, 426: 587-600. DOI: [10.1051/0004-6361:20041231](https://doi.org/10.1051/0004-6361:20041231).
- [98] Casella P, Belloni T, Stella L. The ABC of Low-Frequency Quasi-periodic Oscillations in Black Hole Candidates: Analogies with Z Sources[J/OL]. *ApJ*, 2005, 629(1): 403-407. DOI: [10.1086/431174](https://doi.org/10.1086/431174).
- [99] Fender R P, Belloni T M, Gallo E. Towards a unified model for black hole X-ray binary jets[J/OL]. *MNRAS*, 2004, 355(4): 1105-1118. DOI: [10.1111/j.1365-2966.2004.08384.x](https://doi.org/10.1111/j.1365-2966.2004.08384.x).
- [100] Sánchez-Sierras J, Muñoz-Darias T. Near-infrared emission lines trace the state-independent accretion disc wind of the black hole transient MAXI J1820+070 [J/OL]. *A&A*, 2020, 640: L3. DOI: [10.1051/0004-6361/202038406](https://doi.org/10.1051/0004-6361/202038406).
- [101] Gierliński M, Done C. Black hole accretion discs: reality confronts theory[J/OL]. *MNRAS*, 2004, 347(3): 885-894. DOI: [10.1111/j.1365-2966.2004.07266.x](https://doi.org/10.1111/j.1365-2966.2004.07266.x).
- [102] Steiner J F, McClintock J E, Remillard R A, et al. The Constant Inner-disk Radius of LMC X-3: A Basis for Measuring Black Hole Spin[J/OL]. *ApJ*, 2010, 718(2): L117-L121. DOI: [10.1088/2041-8205/718/2/L117](https://doi.org/10.1088/2041-8205/718/2/L117).
- [103] De Marco B, Zdziarski A A, Ponti G, et al. The inner flow geometry in MAXI J1820+070 during hard and hard-intermediate states[J/OL]. *A&A*, 2021, 654: A14. DOI: [10.1051/0004-6361/202140567](https://doi.org/10.1051/0004-6361/202140567).
- [104] Buisson D J K, Fabian A C, Gandhi P, et al. MAXI J1820+070 with NuSTAR - II. Flaring during the hard to soft state transition with a long soft lag[J/OL]. *MNRAS*, 2021, 500(3): 3976-3986. DOI: [10.1093/mnras/staa3510](https://doi.org/10.1093/mnras/staa3510).
- [105] George I M, Fabian A C. X-ray reflection from cold matter in Active Galactic Nuclei and X-ray binaries.[J/OL]. *MNRAS*, 1991, 249: 352. DOI: [10.1093/mnras/249.2.352](https://doi.org/10.1093/mnras/249.2.352).

- [106] García J, Kallman T R. X-ray Reflected Spectra from Accretion Disk Models. I. Constant Density Atmospheres[J/OL]. *ApJ*, 2010, 718(2): 695-706. DOI: [10.1088/0004-637X/718/2/695](https://doi.org/10.1088/0004-637X/718/2/695).
- [107] Mushotzky R F. The X-ray spectrum and time variability of narrow emission line galaxies.[J/OL]. *ApJ*, 1982, 256: 92-102. DOI: [10.1086/159886](https://doi.org/10.1086/159886).
- [108] Pounds K A, Nandra K, Stewart G C, et al. Iron features in the X-ray spectra of three Seyfert galaxies.[J/OL]. *MNRAS*, 1989, 240: 769-783. DOI: [10.1093/mnras/240.4.769](https://doi.org/10.1093/mnras/240.4.769).
- [109] Nandra K, Pounds K A, Stewart G C, et al. Detection of iron features in the X-ray spectrum of the Seyfert I galaxy MCG -6-30-15.[J/OL]. *MNRAS*, 1989, 236: 39P-46. DOI: [10.1093/mnras/236.1.39P](https://doi.org/10.1093/mnras/236.1.39P).
- [110] Ricci C, Ueda Y, Paltani S, et al. Iron $K\alpha$ emission in type-I and type-II active galactic nuclei[J/OL]. *MNRAS*, 2014, 441(4): 3622-3633. DOI: [10.1093/mnras/stu735](https://doi.org/10.1093/mnras/stu735).
- [111] Lightman A P, White T R. Effects of Cold Matter in Active Galactic Nuclei: A Broad Hump in the X-Ray Spectra[J/OL]. *ApJ*, 1988, 335: 57. DOI: [10.1086/166905](https://doi.org/10.1086/166905).
- [112] Pounds K A, Nandra K, Stewart G C, et al. X-ray reflection from cold matter in the nuclei of active galaxies[J/OL]. *Nature*, 1990, 344(6262): 132-133. DOI: [10.1038/344132a0](https://doi.org/10.1038/344132a0).
- [113] García J A, Fabian A C, Kallman T R, et al. The effects of high density on the X-ray spectrum reflected from accretion discs around black holes[J/OL]. *MNRAS*, 2016, 462(1): 751-760. DOI: [10.1093/mnras/stw1696](https://doi.org/10.1093/mnras/stw1696).
- [114] García J, Dauser T, Lohfink A, et al. Improved Reflection Models of Black Hole Accretion Disks: Treating the Angular Distribution of X-Rays[J/OL]. *ApJ*, 2014, 782(2): 76. DOI: [10.1088/0004-637X/782/2/76](https://doi.org/10.1088/0004-637X/782/2/76).
- [115] Shakura N I, Sunyaev R A. Black holes in binary systems. Observational appearance.[J]. *A&A*, 1973, 24: 337-355.

- [116] Svensson R, Zdziarski A A. Black Hole Accretion Disks with Coronae[J/OL]. ApJ, 1994, 436: 599. DOI: [10.1086/174934](https://doi.org/10.1086/174934).
- [117] Mallick L, Alston W N, Parker M L, et al. A high-density relativistic reflection origin for the soft and hard X-ray excess emission from Mrk 1044[J/OL]. MNRAS, 2018, 479(1): 615-634. DOI: [10.1093/mnras/sty1487](https://doi.org/10.1093/mnras/sty1487).
- [118] García J A, Kara E, Walton D, et al. Implications of the Warm Corona and Relativistic Reflection Models for the Soft Excess in Mrk 509[J/OL]. ApJ, 2019, 871(1): 88. DOI: [10.3847/1538-4357/aaf739](https://doi.org/10.3847/1538-4357/aaf739).
- [119] Wilkins D R, Fabian A C. Determination of the X-ray reflection emissivity profile of 1H 0707-495[J/OL]. MNRAS, 2011, 414(2): 1269-1277. DOI: [10.1111/j.1365-2966.2011.18458.x](https://doi.org/10.1111/j.1365-2966.2011.18458.x).
- [120] Wilkins D R, Fabian A C. Understanding X-ray reflection emissivity profiles in AGN: locating the X-ray source[J/OL]. MNRAS, 2012, 424(2): 1284-1296. DOI: [10.1111/j.1365-2966.2012.21308.x](https://doi.org/10.1111/j.1365-2966.2012.21308.x).
- [121] Cunningham C T. The effects of redshifts and focusing on the spectrum of an accretion disk around a Kerr black hole.[J/OL]. ApJ, 1975, 202: 788-802. DOI: [10.1086/154033](https://doi.org/10.1086/154033).
- [122] Fabian A C, Rees M J, Stella L, et al. X-ray fluorescence from the inner disc in Cygnus X-1.[J/OL]. MNRAS, 1989, 238: 729-736. DOI: [10.1093/mnras/238.3.729](https://doi.org/10.1093/mnras/238.3.729).
- [123] Laor A. Line Profiles from a Disk around a Rotating Black Hole[J/OL]. ApJ, 1991, 376: 90. DOI: [10.1086/170257](https://doi.org/10.1086/170257).
- [124] Dovčiak M, Karas V, Yaqoob T. An Extended Scheme for Fitting X-Ray Data with Accretion Disk Spectra in the Strong Gravity Regime[J/OL]. ApJS, 2004, 153(1): 205-221. DOI: [10.1086/421115](https://doi.org/10.1086/421115).
- [125] Brenneman L W, Reynolds C S. Constraining Black Hole Spin via X-Ray Spectroscopy[J/OL]. ApJ, 2006, 652(2): 1028-1043. DOI: [10.1086/508146](https://doi.org/10.1086/508146).

- [126] Dauser T, Wilms J, Reynolds C S, et al. Broad emission lines for a negatively spinning black hole[J/OL]. MNRAS, 2010, 409(4): 1534-1540. DOI: [10.1111/j.1365-2966.2010.17393.x](https://doi.org/10.1111/j.1365-2966.2010.17393.x).
- [127] Ross R R, Fabian A C. A comprehensive range of X-ray ionized-reflection models [J/OL]. MNRAS, 2005, 358(1): 211-216. DOI: [10.1111/j.1365-2966.2005.08797.x](https://doi.org/10.1111/j.1365-2966.2005.08797.x).
- [128] Bambi C, Cárdenas-Avendaño A, Dauser T, et al. Testing the Kerr Black Hole Hypothesis Using X-Ray Reflection Spectroscopy[J/OL]. ApJ, 2017, 842(2): 76. DOI: [10.3847/1538-4357/aa74c0](https://doi.org/10.3847/1538-4357/aa74c0).
- [129] Niedźwiecki A, Życki P T. On the variability and spectral distortion of fluorescent iron lines from black hole accretion discs[J/OL]. MNRAS, 2008, 386(2): 759-780. DOI: [10.1111/j.1365-2966.2008.12735.x](https://doi.org/10.1111/j.1365-2966.2008.12735.x).
- [130] Niedźwiecki A, Szanecki M, Zdziarski A A. Improved spectral models for relativistic reflection[J/OL]. MNRAS, 2019, 485(2): 2942-2955. DOI: [10.1093/mnras/stz487](https://doi.org/10.1093/mnras/stz487).
- [131] Ingram A, Mastroserio G, Dauser T, et al. A public relativistic transfer function model for X-ray reverberation mapping of accreting black holes[J/OL]. MNRAS, 2019, 488(1): 324-347. DOI: [10.1093/mnras/stz1720](https://doi.org/10.1093/mnras/stz1720).
- [132] Zdziarski A A, Gierliński M. Radiative Processes, Spectral States and Variability of Black-Hole Binaries[J/OL]. Progress of Theoretical Physics Supplement, 2004, 155: 99-119. DOI: [10.1143/PTPS.155.99](https://doi.org/10.1143/PTPS.155.99).
- [133] Done C, Gierliński M, Kubota A. Modelling the behaviour of accretion flows in X-ray binaries. Everything you always wanted to know about accretion but were afraid to ask[J/OL]. A&A Rev., 2007, 15(1): 1-66. DOI: [10.1007/s00159-007-006-1](https://doi.org/10.1007/s00159-007-006-1).
- [134] Reynolds C S. Measuring Black Hole Spin Using X-Ray Reflection Spectroscopy [J/OL]. Space Sci. Rev., 2014, 183(1-4): 277-294. DOI: [10.1007/s11214-013-006-6](https://doi.org/10.1007/s11214-013-006-6).

- [135] Bambi C. Testing black hole candidates with electromagnetic radiation[J/OL]. *Reviews of Modern Physics*, 2017, 89(2): 025001. DOI: [10.1103/RevModPhys.89.025001](https://doi.org/10.1103/RevModPhys.89.025001).
- [136] Liu H, Abdikamalov A B, Ayzenberg D, et al. Testing the Kerr hypothesis using x-ray reflection spectroscopy with NuSTAR data of Cygnus X-1 in the soft state [J/OL]. *Phys. Rev. D*, 2019, 99(12): 123007. DOI: [10.1103/PhysRevD.99.123007](https://doi.org/10.1103/PhysRevD.99.123007).
- [137] Wilkins D R, Gallo L C. Driving extreme variability: the evolving corona and evidence for jet launching in Markarian 335[J/OL]. *MNRAS*, 2015, 449(1): 129-146. DOI: [10.1093/mnras/stv162](https://doi.org/10.1093/mnras/stv162).
- [138] Wang J, Kara E, Steiner J F, et al. Relativistic Reflection and Reverberation in GX 339-4 with NICER and NuSTAR[J/OL]. *ApJ*, 2020, 899(1): 44. DOI: [10.3847/1538-4357/ab9ec3](https://doi.org/10.3847/1538-4357/ab9ec3).
- [139] Szanecki M, Niedźwiecki A, Done C, et al. Geometry of the X-ray source 1H 0707-495[J/OL]. *A&A*, 2020, 641: A89. DOI: [10.1051/0004-6361/202038303](https://doi.org/10.1051/0004-6361/202038303).
- [140] Zdziarski A A, Ziolkowski J, Mikołajewska J. The X-ray binary GX 339-4/V821 Ara: the distance, inclination, evolutionary status, and mass transfer[J/OL]. *MNRAS*, 2019, 488(1): 1026-1034. DOI: [10.1093/mnras/stz1787](https://doi.org/10.1093/mnras/stz1787).
- [141] Miller J M, Fabian A C, Reynolds C S, et al. Evidence of Black Hole Spin in GX 339-4: XMM-Newton/EPIC-pn and RXTE Spectroscopy of the Very High State [J/OL]. *ApJ*, 2004, 606(2): L131-L134. DOI: [10.1086/421263](https://doi.org/10.1086/421263).
- [142] Liu H, Jiang J, Zhang Z, et al. Rapidly alternating flux states of GX 339-4 during its 2021 outburst captured by Insight-HXMT[J/OL]. *MNRAS*, 2022, 513(3): 4308-4317. DOI: [10.1093/mnras/stac1178](https://doi.org/10.1093/mnras/stac1178).
- [143] Parker M L, Tomsick J A, Kennea J A, et al. NuSTAR and Swift Observations of the Very High State in GX 339-4: Weighing the Black Hole with X-Rays[J/OL]. *ApJ*, 2016, 821(1): L6. DOI: [10.3847/2041-8205/821/1/L6](https://doi.org/10.3847/2041-8205/821/1/L6).

- [144] Fürst F, Nowak M A, Tomsick J A, et al. The Complex Accretion Geometry of GX 339-4 as Seen by NuSTAR and Swift[J/OL]. *ApJ*, 2015, 808(2): 122. DOI: [10.1088/0004-637X/808/2/122](https://doi.org/10.1088/0004-637X/808/2/122).
- [145] Sridhar N, García J A, Steiner J F, et al. Evolution of the Accretion Disk-Corona during the Bright Hard-to-soft State Transition: A Reflection Spectroscopic Study with GX 339-4[J/OL]. *ApJ*, 2020, 890(1): 53. DOI: [10.3847/1538-4357/ab64f5](https://doi.org/10.3847/1538-4357/ab64f5).
- [146] Zhang S, Lu F J, Zhang S N, et al. Introduction to the hard x-ray modulation telescope[C/OL]//Takahashi T, den Herder J W A, Bautz M. Society of Photo-Optical Instrumentation Engineers (SPIE) Conference Series: Vol. 9144 Space Telescopes and Instrumentation 2014: Ultraviolet to Gamma Ray. 2014: 914421. DOI: [10.1117/12.2054144](https://doi.org/10.1117/12.2054144).
- [147] Chen Y, Cui W, Li W, et al. The Low Energy X-ray telescope (LE) onboard the Insight-HXMT astronomy satellite[J/OL]. *Science China Physics, Mechanics, and Astronomy*, 2020, 63(4): 249505. DOI: [10.1007/s11433-019-1469-5](https://doi.org/10.1007/s11433-019-1469-5).
- [148] Cao X, Jiang W, Meng B, et al. The Medium Energy X-ray telescope (ME) onboard the Insight-HXMT astronomy satellite[J/OL]. *Science China Physics, Mechanics, and Astronomy*, 2020, 63(4): 249504. DOI: [10.1007/s11433-019-506-1](https://doi.org/10.1007/s11433-019-506-1).
- [149] Liu C, Zhang Y, Li X, et al. The High Energy X-ray telescope (HE) onboard the Insight-HXMT astronomy satellite[J/OL]. *Science China Physics, Mechanics, and Astronomy*, 2020, 63(4): 249503. DOI: [10.1007/s11433-019-1486-x](https://doi.org/10.1007/s11433-019-1486-x).
- [150] Zhang S N, Li T, Lu F, et al. Overview to the Hard X-ray Modulation Telescope (Insight-HXMT) Satellite[J/OL]. *Science China Physics, Mechanics, and Astronomy*, 2020, 63(4): 249502. DOI: [10.1007/s11433-019-1432-6](https://doi.org/10.1007/s11433-019-1432-6).
- [151] Liao J Y, Zhang S, Lu X F, et al. Background model for the high-energy telescope of Insight-HXMT[J/OL]. *Journal of High Energy Astrophysics*, 2020, 27: 14-23. DOI: [10.1016/j.jheap.2020.04.002](https://doi.org/10.1016/j.jheap.2020.04.002).

- [152] Guo C C, Liao J Y, Zhang S, et al. The background model of the medium energy X-ray telescope of Insight-HXMT[J/OL]. *Journal of High Energy Astrophysics*, 2020, 27: 44-50. DOI: [10.1016/j.jheap.2020.02.008](https://doi.org/10.1016/j.jheap.2020.02.008).
- [153] Liao J Y, Zhang S, Chen Y, et al. Background model for the Low-Energy Telescope of Insight-HXMT[J/OL]. *Journal of High Energy Astrophysics*, 2020, 27: 24-32. DOI: [10.1016/j.jheap.2020.02.010](https://doi.org/10.1016/j.jheap.2020.02.010).
- [154] Arnaud K A. XSPEC: The First Ten Years[C]//Jacoby G H, Barnes J. Astronomical Society of the Pacific Conference Series: Vol. 101 Astronomical Data Analysis Software and Systems V. 1996: 17.
- [155] Wilms J, Allen A, McCray R. On the Absorption of X-Rays in the Interstellar Medium[J/OL]. *ApJ*, 2000, 542(2): 914-924. DOI: [10.1086/317016](https://doi.org/10.1086/317016).
- [156] Verner D A, Ferland G J, Korista K T, et al. Atomic Data for Astrophysics. II. New Analytic FITS for Photoionization Cross Sections of Atoms and Ions[J/OL]. *ApJ*, 1996, 465: 487. DOI: [10.1086/177435](https://doi.org/10.1086/177435).
- [157] Mitsuda K, Inoue H, Koyama K, et al. Energy spectra of low-mass binary X-ray sources observed from Tenma.[J]. *PASJ*, 1984, 36: 741-759.
- [158] Miller J M, Parker M L, Fuerst F, et al. NuSTAR Spectroscopy of GRS 1915+105: Disk Reflection, Spin, and Connections to Jets[J/OL]. *ApJ*, 2013, 775(2): L45. DOI: [10.1088/2041-8205/775/2/L45](https://doi.org/10.1088/2041-8205/775/2/L45).
- [159] Ross R R, Fabian A C, Young A J. X-ray reflection spectra from ionized slabs [J/OL]. *MNRAS*, 1999, 306(2): 461-466. DOI: [10.1046/j.1365-8711.1999.02528.x](https://doi.org/10.1046/j.1365-8711.1999.02528.x).
- [160] Fabian A C, Parker M L, Wilkins D R, et al. On the determination of the spin and disc truncation of accreting black holes using X-ray reflection[J/OL]. *MNRAS*, 2014, 439(3): 2307-2313. DOI: [10.1093/mnras/stu045](https://doi.org/10.1093/mnras/stu045).
- [161] García J, Dauser T, Reynolds C S, et al. X-Ray Reflected Spectra from Accretion Disk Models. III. A Complete Grid of Ionized Reflection Calculations[J/OL]. *ApJ*, 2013, 768(2): 146. DOI: [10.1088/0004-637X/768/2/146](https://doi.org/10.1088/0004-637X/768/2/146).

- [162] Sridhar N, Sironi L, Beloborodov A M. Comptonization by reconnection plasmoids in black hole coronae I: Magnetically dominated pair plasma[J/OL]. MNRAS, 2021, 507(4): 5625-5640. DOI: [10.1093/mnras/stab2534](https://doi.org/10.1093/mnras/stab2534).
- [163] Sridhar N, Sironi L, Beloborodov A M. Comptonization by reconnection plasmoids in black hole coronae II: Electron-Ion plasma[J/OL]. MNRAS, 2022. DOI: [10.1093/mnras/stac2730](https://doi.org/10.1093/mnras/stac2730).
- [164] Steiner J F, García J A, Eikmann W, et al. Self-consistent Black Hole Accretion Spectral Models and the Forgotten Role of Coronal Comptonization of Reflection Emission[J/OL]. ApJ, 2017, 836(1): 119. DOI: [10.3847/1538-4357/836/1/119](https://doi.org/10.3847/1538-4357/836/1/119).
- [165] García J A, Dauser T, Ludlam R, et al. Relativistic X-Ray Reflection Models for Accreting Neutron Stars[J/OL]. ApJ, 2022, 926(1): 13. DOI: [10.3847/1538-4357/ac3cb7](https://doi.org/10.3847/1538-4357/ac3cb7).
- [166] Connors R M T, García J A, Dauser T, et al. Evidence for Returning Disk Radiation in the Black Hole X-Ray Binary XTE J1550-564[J/OL]. ApJ, 2020, 892(1): 47. DOI: [10.3847/1538-4357/ab7afc](https://doi.org/10.3847/1538-4357/ab7afc).
- [167] Connors R M T, García J A, Tomsick J, et al. Reflection Modeling of the Black Hole Binary 4U 1630-47: The Disk Density and Returning Radiation[J/OL]. ApJ, 2021, 909(2): 146. DOI: [10.3847/1538-4357/abdd2c](https://doi.org/10.3847/1538-4357/abdd2c).
- [168] Ross R R, Fabian A C. X-ray reflection in accreting stellar-mass black hole systems[J/OL]. MNRAS, 2007, 381(4): 1697-1701. DOI: [10.1111/j.1365-2966.2007.12339.x](https://doi.org/10.1111/j.1365-2966.2007.12339.x).
- [169] Del Santo M, Malzac J, Jourdain E, et al. Spectral variability of GX339-4 in a hard-to-soft state transition[J/OL]. MNRAS, 2008, 390(1): 227-234. DOI: [10.1111/j.1365-2966.2008.13672.x](https://doi.org/10.1111/j.1365-2966.2008.13672.x).
- [170] Motta S, Belloni T, Homan J. The evolution of the high-energy cut-off in the X-ray spectrum of GX 339-4 across a hard-to-soft transition[J/OL]. MNRAS, 2009, 400(3): 1603-1612. DOI: [10.1111/j.1365-2966.2009.15566.x](https://doi.org/10.1111/j.1365-2966.2009.15566.x).

- [171] Zhang Y, Méndez M, García F, et al. The evolution of the corona in MAXI J1535-571 through type-C quasi-periodic oscillations with Insight-HXMT[J/OL]. MNRAS, 2022, 512(2): 2686-2696. DOI: [10.1093/mnras/stac690](https://doi.org/10.1093/mnras/stac690).
- [172] McConnell M L, Zdziarski A A, Bennett K, et al. The Soft Gamma-Ray Spectral Variability of Cygnus X-1[J/OL]. ApJ, 2002, 572(2): 984-995. DOI: [10.1086/340436](https://doi.org/10.1086/340436).
- [173] Miller J M, D'Aì A, Bautz M W, et al. On Relativistic Disk Spectroscopy in Compact Objects with X-ray CCD Cameras[J/OL]. ApJ, 2010, 724(2): 1441-1455. DOI: [10.1088/0004-637X/724/2/1441](https://doi.org/10.1088/0004-637X/724/2/1441).
- [174] García J A, Tomsick J A, Sridhar N, et al. The 2017 Failed Outburst of GX 339-4: Relativistic X-Ray Reflection near the Black Hole Revealed by NuSTAR and Swift Spectroscopy[J/OL]. ApJ, 2019, 885(1): 48. DOI: [10.3847/1538-4357/ab384f](https://doi.org/10.3847/1538-4357/ab384f).
- [175] Kubota A, Tanaka Y, Makishima K, et al. Evidence for a Black Hole in the X-Ray Transient GRS 1009-45[J/OL]. PASJ, 1998, 50: 667-673. DOI: [10.1093/pasj/50.6.667](https://doi.org/10.1093/pasj/50.6.667).
- [176] Rodriguez J, Corbel S, Tomsick J A. Spectral Evolution of the Microquasar XTE J1550-564 over Its Entire 2000 Outburst[J/OL]. ApJ, 2003, 595(2): 1032-1038. DOI: [10.1086/377478](https://doi.org/10.1086/377478).
- [177] Wang J, Mastroserio G, Kara E, et al. Disk, Corona, Jet Connection in the Intermediate State of MAXI J1820+070 Revealed by NICER Spectral-timing Analysis[J/OL]. ApJ, 2021, 910(1): L3. DOI: [10.3847/2041-8213/abec79](https://doi.org/10.3847/2041-8213/abec79).
- [178] Dauser T, García J, Walton D J, et al. Normalizing a relativistic model of X-ray reflection. Definition of the reflection fraction and its implementation in relxill [J/OL]. A&A, 2016, 590: A76. DOI: [10.1051/0004-6361/201628135](https://doi.org/10.1051/0004-6361/201628135).
- [179] You B, Tuo Y, Li C, et al. Insight-HXMT observations of jet-like corona in a black hole X-ray binary MAXI J1820+070[J/OL]. Nature Communications, 2021, 12: 1025. DOI: [10.1038/s41467-021-21169-5](https://doi.org/10.1038/s41467-021-21169-5).

- [180] Buisson D J K, Fabian A C, Barret D, et al. MAXI J1820+070 with NuSTAR I. An increase in variability frequency but a stable reflection spectrum: coronal properties and implications for the inner disc in black hole binaries[J/OL]. MNRAS, 2019, 490(1): 1350-1362. DOI: [10.1093/mnras/stz2681](https://doi.org/10.1093/mnras/stz2681).
- [181] García F, Méndez M, Karpouzas K, et al. A two-component Comptonization model for the type-B QPO in MAXI J1348-630[J/OL]. MNRAS, 2021, 501(3): 3173-3182. DOI: [10.1093/mnras/staa3944](https://doi.org/10.1093/mnras/staa3944).
- [182] García F, Karpouzas K, Méndez M, et al. The evolving properties of the corona of GRS 1915+105: a spectral-timing perspective through variable-Comptonization modelling[J/OL]. MNRAS, 2022, 513(3): 4196-4207. DOI: [10.1093/mnras/stac1202](https://doi.org/10.1093/mnras/stac1202).
- [183] Méndez M, Karpouzas K, García F, et al. Coupling between the accreting corona and the relativistic jet in the microquasar GRS 1915+105[J/OL]. Nature Astronomy, 2022, 6: 577-583. DOI: [10.1038/s41550-022-01617-y](https://doi.org/10.1038/s41550-022-01617-y).
- [184] Peirano V, Méndez M, García F, et al. Dual-corona Comptonization model for the type-b quasi-periodic oscillations in GX 339-4[J/OL]. MNRAS, 2023, 519 (1): 1336-1348. DOI: [10.1093/mnras/stac3553](https://doi.org/10.1093/mnras/stac3553).
- [185] Zdziarski A A, De Marco B. Two Major Constraints on the Inner Radii of Accretion Disks[J/OL]. ApJ, 2020, 896(2): L36. DOI: [10.3847/2041-8213/ab9899](https://doi.org/10.3847/2041-8213/ab9899).
- [186] Ludlam R M, Miller J M, Cackett E M. Reapproaching the Spin Estimate of GX 339-4[J/OL]. ApJ, 2015, 806(2): 262. DOI: [10.1088/0004-637X/806/2/262](https://doi.org/10.1088/0004-637X/806/2/262).
- [187] Heida M, Jonker P G, Torres M A P, et al. The Mass Function of GX 339-4 from Spectroscopic Observations of Its Donor Star[J/OL]. ApJ, 2017, 846(2): 132. DOI: [10.3847/1538-4357/aa85df](https://doi.org/10.3847/1538-4357/aa85df).
- [188] Zhou M, Ayzenberg D, Bambi C, et al. Modeling uncertainties in X-ray reflection spectroscopy measurements I: Impact of higher order disk images[J/OL]. Phys. Rev. D, 2020, 101(4): 043010. DOI: [10.1103/PhysRevD.101.043010](https://doi.org/10.1103/PhysRevD.101.043010).
- [189] Cárdenas-Avendaño A, Zhou M, Bambi C. Modeling uncertainties in x-ray reflection spectroscopy measurements. II. Impact of the radiation from the plunging

- region[J/OL]. Phys. Rev. D, 2020, 101(12): 123014. DOI: [10.1103/PhysRevD.101.123014](https://doi.org/10.1103/PhysRevD.101.123014).
- [190] Tripathi A, Zhang Y, Abdikamalov A B, et al. Testing General Relativity with NuSTAR Data of Galactic Black Holes[J/OL]. ApJ, 2021, 913(2): 79. DOI: [10.3847/1538-4357/abf6cd](https://doi.org/10.3847/1538-4357/abf6cd).
- [191] Dauser T, Svoboda J, Schartel N, et al. Spectral analysis of 1H 0707-495 with XMM-Newton[J/OL]. MNRAS, 2012, 422(3): 1914-1921. DOI: [10.1111/j.1365-2966.2011.20356.x](https://doi.org/10.1111/j.1365-2966.2011.20356.x).
- [192] Jiang J, Parker M L, Fabian A C, et al. The 1.5 Ms observing campaign on IRAS 13224-3809 - I. X-ray spectral analysis[J/OL]. MNRAS, 2018, 477(3): 3711-3726. DOI: [10.1093/mnras/sty836](https://doi.org/10.1093/mnras/sty836).
- [193] García J A, Kallman T R, Bautista M, et al. The Problem of the High Iron Abundance in Accretion Disks around Black Holes[C]//Astronomical Society of the Pacific Conference Series: Vol. 515 Workshop on Astrophysical Opacities. 2018: 282.
- [194] Uttley P, Wilkinson T, Cassatella P, et al. The causal connection between disc and power-law variability in hard state black hole X-ray binaries[J/OL]. MNRAS, 2011, 414(1): L60-L64. DOI: [10.1111/j.1745-3933.2011.01056.x](https://doi.org/10.1111/j.1745-3933.2011.01056.x).
- [195] Ross R R, Fabian A C, Ballantyne D R. Multiple X-ray reflection from ionized slabs[J/OL]. MNRAS, 2002, 336(1): 315-318. DOI: [10.1046/j.1365-8711.2002.05758.x](https://doi.org/10.1046/j.1365-8711.2002.05758.x).
- [196] Riaz S, Szanecki M, Niedźwiecki A, et al. Impact of the Returning Radiation on the Analysis of the Reflection Spectra of Black Holes[J/OL]. ApJ, 2021, 910(1): 49. DOI: [10.3847/1538-4357/abe2a3](https://doi.org/10.3847/1538-4357/abe2a3).
- [197] Dauser T, García J A, Joyce A, et al. The effect of returning radiation on relativistic reflection[J/OL]. MNRAS, 2022, 514(3): 3965-3983. DOI: [10.1093/mnras/stac1593](https://doi.org/10.1093/mnras/stac1593).

- [198] Reynolds C S, Brenneman L W, Lohfink A M, et al. A Monte Carlo Markov Chain Based Investigation of Black Hole Spin in the Active Galaxy NGC 3783 [J/OL]. *ApJ*, 2012, 755(2): 88. DOI: [10.1088/0004-637X/755/2/88](https://doi.org/10.1088/0004-637X/755/2/88).
- [199] Ingram A R, Motta S E. A review of quasi-periodic oscillations from black hole X-ray binaries: Observation and theory[J/OL]. *New A Rev.*, 2019, 85: 101524. DOI: [10.1016/j.newar.2020.101524](https://doi.org/10.1016/j.newar.2020.101524).
- [200] Kara E, Steiner J F, Fabian A C, et al. The corona contracts in a black-hole transient[J/OL]. *Nature*, 2019, 565(7738): 198-201. DOI: [10.1038/s41586-018-0803-x](https://doi.org/10.1038/s41586-018-0803-x).
- [201] Bogensberger D, Ponti G, Jin C, et al. An underlying clock in the extreme flip-flop state transitions of the black hole transient Swift J1658.2-4242[J/OL]. *A&A*, 2020, 641: A101. DOI: [10.1051/0004-6361/202037657](https://doi.org/10.1051/0004-6361/202037657).
- [202] Anders E, Grevesse N. Abundances of the elements: Meteoritic and solar[J/OL]. *Geochim. Cosmochim. Acta*, 1989, 53(1): 197-214. DOI: [10.1016/0016-7037\(89\)90286-X](https://doi.org/10.1016/0016-7037(89)90286-X).
- [203] Maisack M, Johnson W N, Kinzer R L, et al. OSSE Observations of NGC 4151 [J/OL]. *ApJ*, 1993, 407: L61. DOI: [10.1086/186806](https://doi.org/10.1086/186806).
- [204] Hirotani K, Okamoto I. Pair Plasma Production in a Force-free Magnetosphere around a Supermassive Black Hole[J/OL]. *ApJ*, 1998, 497(2): 563-572. DOI: [10.1086/305479](https://doi.org/10.1086/305479).
- [205] Smith R K. The Arcus soft x-ray grating spectrometer explorer[C/OL]//Society of Photo-Optical Instrumentation Engineers (SPIE) Conference Series: Vol. 11444 Society of Photo-Optical Instrumentation Engineers (SPIE) Conference Series. 2020: 114442C. DOI: [10.1117/12.2576047](https://doi.org/10.1117/12.2576047).
- [206] Miyamoto S, Kimura K, Kitamoto S, et al. X-Ray Variability of GX 339-4 in Its Very High State[J/OL]. *ApJ*, 1991, 383: 784. DOI: [10.1086/170837](https://doi.org/10.1086/170837).
- [207] Takizawa M, Dotani T, Mitsuda K, et al. Spectral and Temporal Variability in the X-Ray Flux of GS 1124-683, Nova Muscae 1991[J/OL]. *ApJ*, 1997, 489(1): 272-283. DOI: [10.1086/304759](https://doi.org/10.1086/304759).

- [208] Nespoli E, Belloni T, Homan J, et al. A transient variable 6 Hz QPO from GX 339-4[J/OL]. *A&A*, 2003, 412: 235-240. DOI: [10.1051/0004-6361:20031423](https://doi.org/10.1051/0004-6361:20031423).
- [209] Churazov E, Gilfanov M, Revnivtsev M. Soft state of Cygnus X-1: stable disc and unstable corona[J/OL]. *MNRAS*, 2001, 321(4): 759-766. DOI: [10.1046/j.1365-8711.2001.04056.x](https://doi.org/10.1046/j.1365-8711.2001.04056.x).
- [210] King A. Black Holes, Galaxy Formation, and the $M_{BH}-\sigma$ Relation[J/OL]. *ApJ*, 2003, 596(1): L27-L29. DOI: [10.1086/379143](https://doi.org/10.1086/379143).
- [211] Alexander D M, Hickox R C. What drives the growth of black holes?[J/OL]. *New A Rev.*, 2012, 56(4): 93-121. DOI: [10.1016/j.newar.2011.11.003](https://doi.org/10.1016/j.newar.2011.11.003).
- [212] Mushotzky R F, Done C, Pounds K A. X-ray spectra and time variability of active galactic nuclei.[J/OL]. *ARA&A*, 1993, 31: 717-717. DOI: [10.1146/annurev.aa.31.090193.003441](https://doi.org/10.1146/annurev.aa.31.090193.003441).
- [213] McHardy I M, Koerding E, Knigge C, et al. Active galactic nuclei as scaled-up Galactic black holes[J/OL]. *Nature*, 2006, 444(7120): 730-732. DOI: [10.1038/nature05389](https://doi.org/10.1038/nature05389).
- [214] Shapiro S L, Lightman A P, Eardley D M. A two-temperature accretion disk model for Cygnus X-1: structure and spectrum.[J/OL]. *ApJ*, 1976, 204: 187-199. DOI: [10.1086/154162](https://doi.org/10.1086/154162).
- [215] Bambi C. Black Holes: A Laboratory for Testing Strong Gravity[M/OL]. 2017. DOI: [10.1007/978-981-10-4524-0](https://doi.org/10.1007/978-981-10-4524-0).
- [216] Reynolds C S. Observational Constraints on Black Hole Spin[J/OL]. *ARA&A*, 2021, 59: 117-154. DOI: [10.1146/annurev-astro-112420-035022](https://doi.org/10.1146/annurev-astro-112420-035022).
- [217] Fabian A C, Zoghbi A, Ross R R, et al. Broad line emission from iron K- and L-shell transitions in the active galaxy 1H0707-495[J/OL]. *Nature*, 2009, 459 (7246): 540-542. DOI: [10.1038/nature08007](https://doi.org/10.1038/nature08007).
- [218] Fabian A C, Zoghbi A, Wilkins D, et al. 1H 0707-495 in 2011: an X-ray source within a gravitational radius of the event horizon[J/OL]. *MNRAS*, 2012, 419(1): 116-123. DOI: [10.1111/j.1365-2966.2011.19676.x](https://doi.org/10.1111/j.1365-2966.2011.19676.x).

- [219] Walton D J, Tomsick J A, Madsen K K, et al. The Soft State of Cygnus X-1 Observed with NuSTAR: A Variable Corona and a Stable Inner Disk[J/OL]. *ApJ*, 2016, 826(1): 87. DOI: [10.3847/0004-637X/826/1/87](https://doi.org/10.3847/0004-637X/826/1/87).
- [220] Jiang J, Walton D J, Fabian A C, et al. A relativistic disc reflection model for 1H0419-577: Multi-epoch spectral analysis with XMM-Newton and NuSTAR [J/OL]. *MNRAS*, 2019, 483(3): 2958-2967. DOI: [10.1093/mnras/sty3228](https://doi.org/10.1093/mnras/sty3228).
- [221] Arnaud K A, Branduardi-Raymont G, Culhane J L, et al. EXOSAT observations of a strong soft X-ray excess in MKN 841.[J/OL]. *MNRAS*, 1985, 217: 105-113. DOI: [10.1093/mnras/217.1.105](https://doi.org/10.1093/mnras/217.1.105).
- [222] De Marco B, Ponti G, Cappi M, et al. Discovery of a relation between black hole mass and soft X-ray time lags in active galactic nuclei[J/OL]. *MNRAS*, 2013, 431(3): 2441-2452. DOI: [10.1093/mnras/stt339](https://doi.org/10.1093/mnras/stt339).
- [223] Kara E, Fabian A C, Cackett E M, et al. The closest look at 1H0707-495: X-ray reverberation lags with 1.3 Ms of data[J/OL]. *MNRAS*, 2013, 428(4): 2795-2804. DOI: [10.1093/mnras/sts155](https://doi.org/10.1093/mnras/sts155).
- [224] Reis R C, Fabian A C, Ross R R, et al. Determining the spin of two stellar-mass black holes from disc reflection signatures[J/OL]. *MNRAS*, 2009, 395(3): 1257-1264. DOI: [10.1111/j.1365-2966.2009.14622.x](https://doi.org/10.1111/j.1365-2966.2009.14622.x).
- [225] Reis R C, Miller J M, Fabian A C, et al. Multistate observations of the Galactic black hole XTE J1752-223: evidence for an intermediate black hole spin[J/OL]. *MNRAS*, 2011, 410(4): 2497-2505. DOI: [10.1111/j.1365-2966.2010.17628.x](https://doi.org/10.1111/j.1365-2966.2010.17628.x).
- [226] Steiner J F, Reis R C, McClintock J E, et al. The spin of the black hole microquasar XTE J1550-564 via the continuum-fitting and Fe-line methods[J/OL]. *MNRAS*, 2011, 416(2): 941-958. DOI: [10.1111/j.1365-2966.2011.19089.x](https://doi.org/10.1111/j.1365-2966.2011.19089.x).
- [227] Reis R C, Miller J M, Reynolds M T, et al. Suzaku Observation of the Black Hole Candidate Maxi J1836-194 in a Hard/Intermediate Spectral State[J/OL]. *ApJ*, 2012, 751(1): 34. DOI: [10.1088/0004-637X/751/1/34](https://doi.org/10.1088/0004-637X/751/1/34).
- [228] Steiner J F, Reis R C, Fabian A C, et al. A broad iron line in LMC X-1[J/OL]. *MNRAS*, 2012, 427(3): 2552-2561. DOI: [10.1111/j.1365-2966.2012.22128.x](https://doi.org/10.1111/j.1365-2966.2012.22128.x).

- [229] Walton D J, Reis R C, Cackett E M, et al. The similarity of broad iron lines in X-ray binaries and active galactic nuclei[J/OL]. *MNRAS*, 2012, 422(3): 2510-2531. DOI: [10.1111/j.1365-2966.2012.20809.x](https://doi.org/10.1111/j.1365-2966.2012.20809.x).
- [230] Chiang C Y, Reis R C, Walton D J, et al. Re-examining the XMM-Newton spectrum of the black hole candidate XTE J1652-453[J/OL]. *MNRAS*, 2012, 425(4): 2436-2442. DOI: [10.1111/j.1365-2966.2012.21591.x](https://doi.org/10.1111/j.1365-2966.2012.21591.x).
- [231] Chakraborty S, Ratheesh A, Bhattacharyya S, et al. NuSTAR monitoring of MAXI J1348-630: evidence of high density disc reflection[J/OL]. *MNRAS*, 2021, 508(1): 475-488. DOI: [10.1093/mnras/stab2530](https://doi.org/10.1093/mnras/stab2530).
- [232] King A L, Walton D J, Miller J M, et al. The Disk Wind in the Rapidly Spinning Stellar-mass Black Hole 4U 1630-472 Observed with NuSTAR[J/OL]. *ApJ*, 2014, 784(1): L2. DOI: [10.1088/2041-8205/784/1/L2](https://doi.org/10.1088/2041-8205/784/1/L2).
- [233] Zdziarski A A, You B, Szanecki M, et al. Insight-HXMT, NuSTAR, and INTEGRAL Data Show Disk Truncation in the Hard State of the Black Hole X-Ray Binary MAXI J1820+070[J/OL]. *ApJ*, 2022, 928(1): 11. DOI: [10.3847/1538-4357/ac54a7](https://doi.org/10.3847/1538-4357/ac54a7).
- [234] Chauhan J, Miller-Jones J C A, Anderson G E, et al. An H I absorption distance to the black hole candidate X-ray binary MAXI J1535-571[J/OL]. *MNRAS*, 2019, 488(1): L129-L133. DOI: [10.1093/mnrasl/slz113](https://doi.org/10.1093/mnrasl/slz113).
- [235] Greiner J, Dennerl K, Predehl P. ROSAT observation of GRS 1739-278.[J]. *A&A*, 1996, 314: L21-L24.
- [236] Casares J, Orosz J A, Zurita C, et al. Refined Orbital Solution and Quiescent Variability in the Black Hole Transient GS 1354-64 (= BW Cir)[J/OL]. *ApJS*, 2009, 181(1): 238-243. DOI: [10.1088/0067-0049/181/1/238](https://doi.org/10.1088/0067-0049/181/1/238).
- [237] Rodriguez J, Corbel S, Caballero I, et al. First simultaneous multi-wavelength observations of the black hole candidate IGR J17091-3624. ATCA, INTEGRAL, Swift, and RXTE views of the 2011 outburst[J/OL]. *A&A*, 2011, 533: L4. DOI: [10.1051/0004-6361/201117511](https://doi.org/10.1051/0004-6361/201117511).

- [238] Iyer N, Nandi A, Mandal S. Determination of the Mass of IGR J17091-3624 from “Spectro-temporal” Variations during the Onset Phase of the 2011 Outburst [J/OL]. ApJ, 2015, 807(1): 108. DOI: [10.1088/0004-637X/807/1/108](https://doi.org/10.1088/0004-637X/807/1/108).
- [239] Miller-Jones J C A, Jonker P G, Dhawan V, et al. The First Accurate Parallax Distance to a Black Hole[J/OL]. ApJ, 2009, 706(2): L230-L234. DOI: [10.1088/0004-637X/706/2/L230](https://doi.org/10.1088/0004-637X/706/2/L230).
- [240] Khargharia J, Froning C S, Robinson E L. Near-infrared Spectroscopy of Low-mass X-ray Binaries: Accretion Disk Contamination and Compact Object Mass Determination in V404 Cyg and Cen X-4[J/OL]. ApJ, 2010, 716(2): 1105-1117. DOI: [10.1088/0004-637X/716/2/1105](https://doi.org/10.1088/0004-637X/716/2/1105).
- [241] Gandhi P, Rao A, Johnson M A C, et al. Gaia Data Release 2 distances and peculiar velocities for Galactic black hole transients[J/OL]. MNRAS, 2019, 485 (2): 2642-2655. DOI: [10.1093/mnras/stz438](https://doi.org/10.1093/mnras/stz438).
- [242] Parker M L, Tomsick J A, Miller J M, et al. NuSTAR and Suzaku Observations of the Hard State in Cygnus X-1: Locating the Inner Accretion Disk[J/OL]. ApJ, 2015, 808(1): 9. DOI: [10.1088/0004-637X/808/1/9](https://doi.org/10.1088/0004-637X/808/1/9).
- [243] Fabian A C, Lohfink A, Belmont R, et al. Properties of AGN coronae in the NuSTAR era - II. Hybrid plasma[J/OL]. MNRAS, 2017, 467(3): 2566-2570. DOI: [10.1093/mnras/stx221](https://doi.org/10.1093/mnras/stx221).
- [244] Tripathi A, Liu H, Bambi C. Impact of the reflection model on the estimate of the properties of accreting black holes[J/OL]. MNRAS, 2020, 498(3): 3565-3577. DOI: [10.1093/mnras/staa2618](https://doi.org/10.1093/mnras/staa2618).
- [245] Dziełak M A, Zdziarski A A, Szanecki M, et al. Comparison of spectral models for disc truncation in the hard state of GX 339-4[J/OL]. MNRAS, 2019, 485(3): 3845-3856. DOI: [10.1093/mnras/stz668](https://doi.org/10.1093/mnras/stz668).
- [246] Mahmoud R D, Done C, De Marco B. Reverberation reveals the truncated disc in the hard state of GX 339-4[J/OL]. MNRAS, 2019, 486(2): 2137-2152. DOI: [10.1093/mnras/stz933](https://doi.org/10.1093/mnras/stz933).

- [247] Tomsick J A, Nowak M A, Parker M, et al. The Reflection Component from Cygnus X-1 in the Soft State Measured by NuSTAR and Suzaku[J/OL]. *ApJ*, 2014, 780(1): 78. DOI: [10.1088/0004-637X/780/1/78](https://doi.org/10.1088/0004-637X/780/1/78).
- [248] Miller-Jones J C A, Bahramian A, Orosz J A, et al. Cygnus X-1 contains a 21-solar mass black hole—Implications for massive star winds[J/OL]. *Science*, 2021, 371(6533): 1046-1049. DOI: [10.1126/science.abb3363](https://doi.org/10.1126/science.abb3363).
- [249] Pringle J E. Self-induced warping of accretion discs[J/OL]. *MNRAS*, 1996, 281 (1): 357-361. DOI: [10.1093/mnras/281.1.357](https://doi.org/10.1093/mnras/281.1.357).
- [250] Brandt W N, Podsiadlowski P. The Effects of High-Velocity Supernova Kicks on the Orbital Properties and Sky Distributions of Neutron Star Binaries[A]. 1994: astro-ph/9412023. arXiv: [astro-ph/9412023](https://arxiv.org/abs/astro-ph/9412023).
- [251] Fragos T, Tremmel M, Rantsiou E, et al. Black Hole Spin-Orbit Misalignment in Galactic X-ray Binaries[J/OL]. *ApJ*, 2010, 719(1): L79-L83. DOI: [10.1088/2041-8205/719/1/L79](https://doi.org/10.1088/2041-8205/719/1/L79).
- [252] Miller J M, Gendreau K, Ludlam R M, et al. A NICER Spectrum of MAXI J1535-571: Near-maximal Black Hole Spin and Potential Disk Warping[J/OL]. *ApJ*, 2018, 860(2): L28. DOI: [10.3847/2041-8213/aacc61](https://doi.org/10.3847/2041-8213/aacc61).
- [253] Poutanen J, Veledina A, Berdyugin A V, et al. Black hole spin–orbit misalignment in the x-ray binary MAXI J1820+070[J/OL]. *Science*, 2022, 375(6583): 874-876. DOI: [10.1126/science.abl4679](https://doi.org/10.1126/science.abl4679).
- [254] Thomas J K, Charles P A, Buckley D A H, et al. Large optical modulations during 2018 outburst of MAXI J1820 + 070 reveal evolution of warped accretion disc through X-ray state change[J/OL]. *MNRAS*, 2022, 509(1): 1062-1074. DOI: [10.1093/mnras/stab3033](https://doi.org/10.1093/mnras/stab3033).
- [255] Bardeen J M, Petterson J A. The Lense-Thirring Effect and Accretion Disks around Kerr Black Holes[J/OL]. *ApJ*, 1975, 195: L65. DOI: [10.1086/181711](https://doi.org/10.1086/181711).
- [256] García J A, Steiner J F, Grinberg V, et al. Reflection Spectroscopy of the Black Hole Binary XTE J1752-223 in Its Long-stable Hard State[J/OL]. *ApJ*, 2018, 864(1): 25. DOI: [10.3847/1538-4357/aad231](https://doi.org/10.3847/1538-4357/aad231).

- [257] Connors R M T, García J A, Tomsick J, et al. The Long-stable Hard State of XTE J1752-223 and the Disk Truncation Dilemma[J/OL]. *ApJ*, 2022, 935(2): 118. DOI: [10.3847/1538-4357/ac7ff2](https://doi.org/10.3847/1538-4357/ac7ff2).
- [258] Risaliti G, Young M, Elvis M. The Sloan Digital Sky Survey/XMM-Newton Quasar Survey: Correlation Between X-Ray Spectral Slope and Eddington Ratio [J/OL]. *ApJ*, 2009, 700(1): L6-L10. DOI: [10.1088/0004-637X/700/1/L6](https://doi.org/10.1088/0004-637X/700/1/L6).
- [259] Brightman M, Silverman J D, Mainieri V, et al. A statistical relation between the X-ray spectral index and Eddington ratio of active galactic nuclei in deep surveys [J/OL]. *MNRAS*, 2013, 433(3): 2485-2496. DOI: [10.1093/mnras/stt920](https://doi.org/10.1093/mnras/stt920).
- [260] Kubota A, Makishima K. The Three Spectral Regimes Found in the Stellar Black Hole XTE J1550-564 in Its High/Soft State[J/OL]. *ApJ*, 2004, 601(1): 428-438. DOI: [10.1086/380433](https://doi.org/10.1086/380433).
- [261] Wu Q, Gu M. The X-Ray Spectral Evolution in X-Ray Binaries and Its Application to Constrain the Black Hole Mass of Ultraluminous X-Ray Sources[J/OL]. *ApJ*, 2008, 682(1): 212-217. DOI: [10.1086/588187](https://doi.org/10.1086/588187).
- [262] You B, Dong Y, Yan Z, et al. X-Ray Spectral Correlations in a Sample of Low-mass Black Hole X-Ray Binaries in the Hard State[J/OL]. *ApJ*, 2023, 945(1): 65. DOI: [10.3847/1538-4357/acba11](https://doi.org/10.3847/1538-4357/acba11).
- [263] Yuan F, Taam R E, Misra R, et al. Accretion Disk Spectra of the Brightest Ultraluminous X-Ray Source in M82[J/OL]. *ApJ*, 2007, 658(1): 282-287. DOI: [10.1086/511301](https://doi.org/10.1086/511301).
- [264] Constantin A, Green P, Aldcroft T, et al. Probing the Balance of AGN and Star-forming Activity in the Local Universe with ChaMP[J/OL]. *ApJ*, 2009, 705(2): 1336-1355. DOI: [10.1088/0004-637X/705/2/1336](https://doi.org/10.1088/0004-637X/705/2/1336).
- [265] Gu M, Cao X. The anticorrelation between the hard X-ray photon index and the Eddington ratio in low-luminosity active galactic nuclei[J/OL]. *MNRAS*, 2009, 399(1): 349-356. DOI: [10.1111/j.1365-2966.2009.15277.x](https://doi.org/10.1111/j.1365-2966.2009.15277.x).

- [266] Díaz Y, Hernández-García L, Arévalo P, et al. Constraining the X-ray reflection in low accretion rate AGN using XMM-Newton, NuSTAR and Swift[A]. 2022: arXiv:2210.15376. arXiv: [2210.15376](https://arxiv.org/abs/2210.15376).
- [267] Corbel S, Tomsick J A, Kaaret P. On the Origin of Black Hole X-Ray Emission in Quiescence: Chandra Observations of XTE J1550-564 and H1743-322[J/OL]. ApJ, 2006, 636(2): 971-978. DOI: [10.1086/498230](https://doi.org/10.1086/498230).
- [268] Sobolewska M A, Papadakis I E, Done C, et al. Evidence for a change in the X-ray radiation mechanism in the hard state of Galactic black holes[J/OL]. MNRAS, 2011, 417(1): 280-288. DOI: [10.1111/j.1365-2966.2011.19209.x](https://doi.org/10.1111/j.1365-2966.2011.19209.x).
- [269] Göltekin K, Cackett E M, Miller J M, et al. A Chandra Survey of Supermassive Black Holes with Dynamical Mass Measurements[J/OL]. ApJ, 2012, 749(2): 129. DOI: [10.1088/0004-637X/749/2/129](https://doi.org/10.1088/0004-637X/749/2/129).
- [270] Plotkin R M, Gallo E, Jonker P G. The X-Ray Spectral Evolution of Galactic Black Hole X-Ray Binaries toward Quiescence[J/OL]. ApJ, 2013, 773(1): 59. DOI: [10.1088/0004-637X/773/1/59](https://doi.org/10.1088/0004-637X/773/1/59).
- [271] Cao X F, Wu Q, Dong A J. Different X-Ray Spectral Evolution for Black Hole X-Ray Binaries in Dual Tracks of Radio-X-Ray Correlation[J/OL]. ApJ, 2014, 788(1): 52. DOI: [10.1088/0004-637X/788/1/52](https://doi.org/10.1088/0004-637X/788/1/52).
- [272] Yang Q X, Xie F G, Yuan F, et al. Correlation between the photon index and X-ray luminosity of black hole X-ray binaries and active galactic nuclei: observations and interpretation[J/OL]. MNRAS, 2015, 447(2): 1692-1704. DOI: [10.1093/mnras/stu2571](https://doi.org/10.1093/mnras/stu2571).
- [273] Walton D J, Mooley K, King A L, et al. Living on a Flare: Relativistic Reflection in V404 Cyg Observed by NuSTAR during Its Summer 2015 Outburst[J/OL]. ApJ, 2017, 839(2): 110. DOI: [10.3847/1538-4357/aa67e8](https://doi.org/10.3847/1538-4357/aa67e8).
- [274] Ricci C, Ho L C, Fabian A C, et al. BAT AGN Spectroscopic Survey - XII. The relation between coronal properties of active galactic nuclei and the Eddington ratio[J/OL]. MNRAS, 2018, 480(2): 1819-1830. DOI: [10.1093/mnras/sty1879](https://doi.org/10.1093/mnras/sty1879).

- [275] Svensson R. Steady mildly relativistic thermal plasmas - Processes and properties [J/OL]. MNRAS, 1984, 209: 175-208. DOI: [10.1093/mnras/209.2.175](https://doi.org/10.1093/mnras/209.2.175).
- [276] Zdziarski A A. Power-law X-ray and gamma-ray emission from relativistic thermal plasmas[J/OL]. ApJ, 1985, 289: 514-525. DOI: [10.1086/162912](https://doi.org/10.1086/162912).
- [277] Zdziarski A A, Lightman A P, Maciolek-Niedzwiecki A. Acceleration Efficiency in Nonthermal Sources and the Soft Gamma Rays from NGC 4151 Observed by OSSE and SIGMA[J/OL]. ApJ, 1993, 414: L93. DOI: [10.1086/187004](https://doi.org/10.1086/187004).
- [278] Grove J E, Johnson W N, Kroeger R A, et al. Gamma-Ray Spectral States of Galactic Black Hole Candidates[J/OL]. ApJ, 1998, 500(2): 899-908. DOI: [10.1086/305746](https://doi.org/10.1086/305746).
- [279] Emmanoulopoulos D, Papadakis I E, Dovčiak M, et al. General relativistic modelling of the negative reverberation X-ray time delays in AGN[J/OL]. MNRAS, 2014, 439(4): 3931-3950. DOI: [10.1093/mnras/stu249](https://doi.org/10.1093/mnras/stu249).
- [280] Gierliński M, Zdziarski A A, Poutanen J, et al. Radiation mechanisms and geometry of Cygnus X-1 in the soft state[J/OL]. MNRAS, 1999, 309(2): 496-512. DOI: [10.1046/j.1365-8711.1999.02875.x](https://doi.org/10.1046/j.1365-8711.1999.02875.x).
- [281] Zdziarski A A, Grove J E, Poutanen J, et al. OSSE and RXTE Observations of GRS 1915+105: Evidence for Nonthermal Comptonization[J/OL]. ApJ, 2001, 554(1): L45-L48. DOI: [10.1086/320932](https://doi.org/10.1086/320932).
- [282] Droulans R, Belmont R, Malzac J, et al. Variability and Spectral Modeling of the Hard X-ray Emission of GX 339-4 in a Bright Low/Hard State[J/OL]. ApJ, 2010, 717(2): 1022-1036. DOI: [10.1088/0004-637X/717/2/1022](https://doi.org/10.1088/0004-637X/717/2/1022).
- [283] Zdziarski A A, Jourdain E, Lubiński P, et al. Hybrid Comptonization and Electron-Positron Pair Production in the Black-hole X-Ray Binary MAXI J1820+070[J/OL]. ApJ, 2021, 914(1): L5. DOI: [10.3847/2041-8213/ac0147](https://doi.org/10.3847/2041-8213/ac0147).
- [284] Wardziński G, Zdziarski A A, Gierliński M, et al. X-ray and γ -ray spectra and variability of the black hole candidate GX 339-4[J/OL]. MNRAS, 2002, 337(3): 829-839. DOI: [10.1046/j.1365-8711.2002.05914.x](https://doi.org/10.1046/j.1365-8711.2002.05914.x).

- [285] Nowak M A, Hanke M, Trowbridge S N, et al. Corona, Jet, and Relativistic Line Models for Suzaku/RXTE/Chandra-HETG Observations of the Cygnus X-1 Hard State[J/OL]. *ApJ*, 2011, 728(1): 13. DOI: [10.1088/0004-637X/728/1/13](https://doi.org/10.1088/0004-637X/728/1/13).
- [286] Del Santo M, Belloni T M, Tomsick J A, et al. Spectral and timing evolution of the bright failed outburst of the transient black hole Swift J174510.8-262411 [J/OL]. *MNRAS*, 2016, 456(4): 3585-3595. DOI: [10.1093/mnras/stv2901](https://doi.org/10.1093/mnras/stv2901).
- [287] Stiele H, Kong A K H. A Multi-instrument Study of the 2018 Hard-state-only Outburst of H1743-322[J/OL]. *ApJ*, 2021, 914(2): 93. DOI: [10.3847/1538-4357/abfaa5](https://doi.org/10.3847/1538-4357/abfaa5).
- [288] Williams D R A, Motta S E, Fender R, et al. The 2018 outburst of BHXB H1743-322 as seen with MeerKAT[J/OL]. *MNRAS*, 2020, 491(1): L29-L33. DOI: [10.1093/mnrasl/slz152](https://doi.org/10.1093/mnrasl/slz152).
- [289] Paul J, Bouchet L, Churazov E, et al. GRS 1739-278[J]. *IAU Circ.*, 1996, 6348: 1.
- [290] Miller J M, Tomsick J A, Bachetti M, et al. New Constraints on the Black Hole Low/Hard State Inner Accretion Flow with NuSTAR[J/OL]. *ApJ*, 2015, 799(1): L6. DOI: [10.1088/2041-8205/799/1/L6](https://doi.org/10.1088/2041-8205/799/1/L6).
- [291] Fürst F, Tomsick J A, Yamaoka K, et al. GRS 1739-278 Observed at Very Low Luminosity with XMM-Newton and NuSTAR[J/OL]. *ApJ*, 2016, 832(2): 115. DOI: [10.3847/0004-637X/832/2/115](https://doi.org/10.3847/0004-637X/832/2/115).
- [292] Makino F. 4U 0115+63 and X-Ray Nova[J]. *IAU Circ.*, 1987, 4342: 1.
- [293] El-Batal A M, Miller J M, Reynolds M T, et al. NuSTAR Observations of the Black Hole GS 1354-645: Evidence of Rapid Black Hole Spin[J/OL]. *ApJ*, 2016, 826(1): L12. DOI: [10.3847/2041-8205/826/1/L12](https://doi.org/10.3847/2041-8205/826/1/L12).
- [294] Xu Y, Nampalliwar S, Abdikamalov A B, et al. A Study of the Strong Gravity Region of the Black Hole in GS 1354-645[J/OL]. *ApJ*, 2018, 865(2): 134. DOI: [10.3847/1538-4357/aadb9d](https://doi.org/10.3847/1538-4357/aadb9d).

- [295] Altamirano D, Belloni T, Linares M, et al. The Faint “Heartbeats” of IGR J17091-3624: An Exceptional Black Hole Candidate[J/OL]. *ApJ*, 2011, 742(2): L17. DOI: [10.1088/2041-8205/742/2/L17](https://doi.org/10.1088/2041-8205/742/2/L17).
- [296] Rao A, Vadawale S V. Why is IGR J17091-3624 So Faint? Constraints on Distance, Mass, and Spin from “Phase-resolved” Spectroscopy of the “Heartbeat” Oscillations[J/OL]. *ApJ*, 2012, 757(1): L12. DOI: [10.1088/2041-8205/757/1/L12](https://doi.org/10.1088/2041-8205/757/1/L12).
- [297] Wang Y, Méndez M, Altamirano D, et al. The reflection component in the average and heartbeat spectra of the black hole candidate IGR J17091-3642 during the 2016 outburst[J/OL]. *MNRAS*, 2018, 478(4): 4837-4850. DOI: [10.1093/mnras/sty1372](https://doi.org/10.1093/mnras/sty1372).
- [298] Reis R C, Miller J M, King A L, et al. IGR J17091-3624 might harbor a rapidly rotating black hole as well as a persistent ultra-fast outflow[J]. *The Astronomer’s Telegram*, 2012, 4382: 1.
- [299] Xu Y, García J A, Fürst F, et al. Spectral and Timing Properties of IGR J17091-3624 in the Rising Hard State During Its 2016 Outburst[J/OL]. *ApJ*, 2017, 851(2): 103. DOI: [10.3847/1538-4357/aa9ab4](https://doi.org/10.3847/1538-4357/aa9ab4).
- [300] Kallman T, Bautista M. Photoionization and High-Density Gas[J/OL]. *ApJS*, 2001, 133(1): 221-253. DOI: [10.1086/319184](https://doi.org/10.1086/319184).
- [301] Kallman T R, Palmeri P, Bautista M A, et al. Photoionization Modeling and the K Lines of Iron[J/OL]. *ApJS*, 2004, 155(2): 675-701. DOI: [10.1086/424039](https://doi.org/10.1086/424039).
- [302] Kaluzienski L J, Holt S S. Variable X-Ray Sources[J]. *IAU Circ.*, 1977, 3099: 3.
- [303] Molla A A, Chakrabarti S K, Debnath D, et al. Estimation of Mass of Compact Object in H 1743-322 from 2010 and 2011 Outbursts using TCAF Solution and Spectral Index-QPO Frequency Correlation[J/OL]. *ApJ*, 2017, 834(1): 88. DOI: [10.3847/1538-4357/834/1/88](https://doi.org/10.3847/1538-4357/834/1/88).

- [304] Chand S, Agrawal V K, Dewangan G C, et al. 2016 Outburst of H 1743-322: XMM-Newton and NuSTAR View[J/OL]. *ApJ*, 2020, 893(2): 142. DOI: [10.3847/1538-4357/ab829a](https://doi.org/10.3847/1538-4357/ab829a).
- [305] Negoro H, Kawase T, Sugizaki M, et al. Further brightening of the X-ray transient MAXI J1535-571, suggesting the presence of a black hole[J]. *The Astronomer's Telegram*, 2017, 10708: 1.
- [306] Xu Y, Harrison F A, García J A, et al. Reflection Spectra of the Black Hole Binary Candidate MAXI J1535-571 in the Hard State Observed by NuSTAR[J/OL]. *ApJ*, 2018, 852(2): L34. DOI: [10.3847/2041-8213/aaa4b2](https://doi.org/10.3847/2041-8213/aaa4b2).
- [307] Lee J C, Reynolds C S, Remillard R, et al. High-Resolution Chandra HETGS and Rossi X-Ray Timing Explorer Observations of GRS 1915+105: A Hot Disk Atmosphere and Cold Gas Enriched in Iron and Silicon[J/OL]. *ApJ*, 2002, 567 (2): 1102-1111. DOI: [10.1086/338588](https://doi.org/10.1086/338588).
- [308] Ueda Y, Honda K, Takahashi H, et al. Suzaku Observation of GRS 1915+105: Evolution of Accretion Disk Structure during Limit-cycle Oscillation[J/OL]. *ApJ*, 2010, 713(1): 257-268. DOI: [10.1088/0004-637X/713/1/257](https://doi.org/10.1088/0004-637X/713/1/257).
- [309] Miller J M, Fabian A C, Kaastra J, et al. Powerful, Rotating Disk Winds from Stellar-mass Black Holes[J/OL]. *ApJ*, 2015, 814(2): 87. DOI: [10.1088/0004-637X/814/2/87](https://doi.org/10.1088/0004-637X/814/2/87).
- [310] Díaz Trigo M, Boirin L. Accretion disc atmospheres and winds in low-mass X-ray binaries[J/OL]. *Astronomische Nachrichten*, 2016, 337(4-5): 368. DOI: [10.1002/asna.201612315](https://doi.org/10.1002/asna.201612315).
- [311] Neilsen J, Cackett E, Remillard R A, et al. A Persistent Disk Wind in GRS 1915+105 with NICER[J/OL]. *ApJ*, 2018, 860(2): L19. DOI: [10.3847/2041-8213/aaca96](https://doi.org/10.3847/2041-8213/aaca96).
- [312] Miller J M, Raymond J, Homan J, et al. Simultaneous Chandra and RXTE Spectroscopy of the Microquasar H1743-322: Clues to Disk Wind and Jet Formation from a Variable Ionized Outflow[J/OL]. *ApJ*, 2006, 646(1): 394-406. DOI: [10.1086/504673](https://doi.org/10.1086/504673).

- [313] Ueda Y, Yamaoka K, Remillard R. GRS 1915+105 in “Soft State”: Nature of Accretion Disk Wind and Origin of X-ray Emission[J/OL]. *ApJ*, 2009, 695(2): 888-899. DOI: [10.1088/0004-637X/695/2/888](https://doi.org/10.1088/0004-637X/695/2/888).
- [314] Blum J L, Miller J M, Cackett E, et al. Suzaku Observations of the Black Hole H1743-322 in Outburst[J/OL]. *ApJ*, 2010, 713(2): 1244-1248. DOI: [10.1088/0004-637X/713/2/1244](https://doi.org/10.1088/0004-637X/713/2/1244).
- [315] Neilsen J, Petschek A J, Lee J C. Accretion disc wind variability in the states of the microquasar GRS 1915+105[J/OL]. *MNRAS*, 2012, 421(1): 502-511. DOI: [10.1111/j.1365-2966.2011.20329.x](https://doi.org/10.1111/j.1365-2966.2011.20329.x).
- [316] King A L, Miller J M, Raymond J, et al. An Extreme X-Ray Disk Wind in the Black Hole Candidate IGR J17091-3624[J/OL]. *ApJ*, 2012, 746(2): L20. DOI: [10.1088/2041-8205/746/2/L20](https://doi.org/10.1088/2041-8205/746/2/L20).
- [317] Miller J M, Raymond J, Fabian A C, et al. The Accretion Disk Wind in the Black Hole GRS 1915+105[J/OL]. *ApJ*, 2016, 821(1): L9. DOI: [10.3847/2041-8205/821/1/L9](https://doi.org/10.3847/2041-8205/821/1/L9).
- [318] Neilsen J, Homan J. A Hybrid Magnetically/Thermally Driven Wind in the Black Hole GRO J1655-40?[J/OL]. *ApJ*, 2012, 750(1): 27. DOI: [10.1088/0004-637X/750/1/27](https://doi.org/10.1088/0004-637X/750/1/27).
- [319] Chakravorty S, Lee J C, Neilsen J. The effects of thermodynamic stability on wind properties in different low-mass black hole binary states[J/OL]. *MNRAS*, 2013, 436(1): 560-569. DOI: [10.1093/mnras/stt1593](https://doi.org/10.1093/mnras/stt1593).
- [320] Fukumura K, Kazanas D, Shrader C, et al. Magnetic origin of black hole winds across the mass scale[J/OL]. *Nature Astronomy*, 2017, 1: 0062. DOI: [10.1038/s41550-017-0062](https://doi.org/10.1038/s41550-017-0062).
- [321] Proga D, Kallman T R. On the Role of the Ultraviolet and X-Ray Radiation in Driving a Disk Wind in X-Ray Binaries[J/OL]. *ApJ*, 2002, 565(1): 455-470. DOI: [10.1086/324534](https://doi.org/10.1086/324534).
- [322] Higginbottom N, Proga D. Coronae and Winds from Irradiated Disks in X-Ray Binaries[J/OL]. *ApJ*, 2015, 807(1): 107. DOI: [10.1088/0004-637X/807/1/107](https://doi.org/10.1088/0004-637X/807/1/107).

- [323] Tremaine S, Shen Y, Liu X, et al. Relativistic Redshifts in Quasar Broad Lines [J/OL]. *ApJ*, 2014, 794(1): 49. DOI: [10.1088/0004-637X/794/1/49](https://doi.org/10.1088/0004-637X/794/1/49).
- [324] King A L, Miller J M, Raymond J, et al. Regulation of Black Hole Winds and Jets across the Mass Scale[J/OL]. *ApJ*, 2013, 762(2): 103. DOI: [10.1088/0004-637X/762/2/103](https://doi.org/10.1088/0004-637X/762/2/103).
- [325] Ratheesh A, Tombesi F, Fukumura K, et al. A variable magnetic disc wind in the black hole X-ray binary GRS 1915+105?[J/OL]. *A&A*, 2021, 646: A154. DOI: [10.1051/0004-6361/202038621](https://doi.org/10.1051/0004-6361/202038621).
- [326] Castro-Tirado A J, Brandt S, Lund N. GRS 1915+105[J]. *IAU Circ.*, 1992, 5590: 2.
- [327] Belloni T, Klein-Wolt M, Méndez M, et al. A model-independent analysis of the variability of GRS 1915+105[J]. *A&A*, 2000, 355: 271-290.
- [328] Klein-Wolt M, Fender R P, Pooley G G, et al. Hard X-ray states and radio emission in GRS 1915+105[J/OL]. *MNRAS*, 2002, 331(3): 745-764. DOI: [10.1046/j.1365-8711.2002.05223.x](https://doi.org/10.1046/j.1365-8711.2002.05223.x).
- [329] Hannikainen D C, Rodriguez J, Vilhu O, et al. Characterizing a new class of variability in GRS 1915+105 with simultaneous INTEGRAL/RXTE observations [J/OL]. *A&A*, 2005, 435(3): 995-1004. DOI: [10.1051/0004-6361:20042250](https://doi.org/10.1051/0004-6361:20042250).
- [330] Neilsen J, Homan J, Steiner J F, et al. A NICER View of a Highly Absorbed Flare in GRS 1915+105[J/OL]. *ApJ*, 2020, 902(2): 152. DOI: [10.3847/1538-4357/ab598](https://doi.org/10.3847/1538-4357/ab598).
- [331] Kong L D, Zhang S, Chen Y P, et al. Insight-HXMT Observations of a Possible Fast Transition from the Jet- to Wind-dominated State during a Huge Flare of GRS 1915+105[J/OL]. *ApJ*, 2021, 906(1): L2. DOI: [10.3847/2041-8213/abd03d](https://doi.org/10.3847/2041-8213/abd03d).
- [332] Kallman T R, Bautista M A, Goriely S, et al. Spectrum Synthesis Modeling of the X-Ray Spectrum of GRO J1655-40 Taken During the 2005 Outburst[J/OL]. *ApJ*, 2009, 701(2): 865-884. DOI: [10.1088/0004-637X/701/2/865](https://doi.org/10.1088/0004-637X/701/2/865).

- [333] Proga D. Numerical Simulations of Mass Outflows Driven from Accretion Disks by Radiation and Magnetic Forces[J/OL]. ApJ, 2003, 585(1): 406-417. DOI: [10.1086/345897](https://doi.org/10.1086/345897).
- [334] Woods D T, Klein R I, Castor J I, et al. X-Ray-heated Coronae and Winds from Accretion Disks: Time-dependent Two-dimensional Hydrodynamics with Adaptive Mesh Refinement[J/OL]. ApJ, 1996, 461: 767. DOI: [10.1086/177101](https://doi.org/10.1086/177101).
- [335] Reid M J, McClintock J E, Steiner J F, et al. A Parallax Distance to the Micro-quasar GRS 1915+105 and a Revised Estimate of its Black Hole Mass[J/OL]. ApJ, 2014, 796(1): 2. DOI: [10.1088/0004-637X/796/1/2](https://doi.org/10.1088/0004-637X/796/1/2).
- [336] Done C, Nayakshin S. Can the soft excess in AGN originate from disc reflection? [J/OL]. MNRAS, 2007, 377(1): L59-L63. DOI: [10.1111/j.1745-3933.2007.00303.x](https://doi.org/10.1111/j.1745-3933.2007.00303.x).
- [337] Done C. Observational characteristics of accretion onto black holes[A/OL]. 2010: arXiv:1008.2287. arXiv: [1008.2287](https://arxiv.org/abs/1008.2287).
- [338] Karpouzas K, Méndez M, Ribeiro E M, et al. The Comptonizing medium of the neutron star in 4U 1636 - 53 through its lower kilohertz quasi-periodic oscillations[J/OL]. MNRAS, 2020, 492(1): 1399-1415. DOI: [10.1093/mnras/stz3502](https://doi.org/10.1093/mnras/stz3502).
- [339] Novikov I D, Thorne K S. Astrophysics of black holes.[C]//Black Holes (Les Astres Occlus). 1973: 343-450.
- [340] Penna R F, McKinney J C, Narayan R, et al. Simulations of magnetized discs around black holes: effects of black hole spin, disc thickness and magnetic field geometry[J/OL]. MNRAS, 2010, 408(2): 752-782. DOI: [10.1111/j.1365-2966.2010.17170.x](https://doi.org/10.1111/j.1365-2966.2010.17170.x).
- [341] Riaz S, Ayzenberg D, Bambi C, et al. Reflection spectra of thick accretion discs [J/OL]. MNRAS, 2020, 491(1): 417-426. DOI: [10.1093/mnras/stz3022](https://doi.org/10.1093/mnras/stz3022).
- [342] Nayakshin S, Kazanas D, Kallman T R. Thermal Instability and Photoionized X-Ray Reflection in Accretion Disks[J/OL]. ApJ, 2000, 537(2): 833-852. DOI: [10.1086/309054](https://doi.org/10.1086/309054).

- [343] Dexter J, Begelman M C. A relativistic outflow model of the X-ray polarization in Cyg X-1[J/OL]. MNRAS, 2024, 528(1): L157-L160. DOI: [10.1093/mnrasl/slad182](https://doi.org/10.1093/mnrasl/slad182).
- [344] Matt G. X-ray polarization properties of a centrally illuminated accretion disc. [J/OL]. MNRAS, 1993, 260: 663-674. DOI: [10.1093/mnras/260.3.663](https://doi.org/10.1093/mnras/260.3.663).
- [345] Krawczynski H, Beheshtipour B. New Constraints on the Spin of the Black Hole Cygnus X-1 and the Physical Properties of its Accretion Disk Corona[J/OL]. ApJ, 2022, 934(1): 4. DOI: [10.3847/1538-4357/ac7725](https://doi.org/10.3847/1538-4357/ac7725).
- [346] Bambi C, Abdikamalov A B, Liu H, et al. Testing General Relativity with Black Hole X-Ray Data and ABHModels[A/OL]. 2023: arXiv:2307.12755. arXiv: [2307.12755](https://arxiv.org/abs/2307.12755).
- [347] Zhang W, Dovčiak M, Bursa M. Constraining the Size of the Corona with Fully Relativistic Calculations of Spectra of Extended Coronae. I. The Monte Carlo Radiative Transfer Code[J/OL]. ApJ, 2019, 875(2): 148. DOI: [10.3847/1538-4357/ab1261](https://doi.org/10.3847/1538-4357/ab1261).
- [348] Goosmann R W, Gaskell C M. Modeling optical and UV polarization of AGNs. I. Imprints of individual scattering regions[J/OL]. A&A, 2007, 465(1): 129-145. DOI: [10.1051/0004-6361:20053555](https://doi.org/10.1051/0004-6361:20053555).

Acknowledgements

I would like to express my sincere gratitude to my Ph.D. advisor, Professor Cosimo Bambi, for his invaluable guidance and unwavering support throughout my academic journey, as well as for his willingness to answer any of my questions at any time. Additionally, I would like to thank Dr. Jiachen Jiang for providing amazing ideas, and for engaging in weekly discussions about science.

I am grateful to Dr. Michael Parker, Dr. Javier Garcia, Dr. James Steiner, Dr. Adam Ingram, Prof. Andrew Fabian, Dr. John Tomsick, Dr. Dominic Walton, Prof. Andrew Young, Prof. Ranjeev Misra, Dr. Divya Rawat, and Prof. Erin Kara for carefully reading my papers and providing valuable insights. Additionally, I want to extend special thanks to Dr. Long Ji, Prof. Shu Zhang, and Prof. Shuangnan Zhang for their support in accessing *Insight*–HXMT data, without which this thesis may not exist. I am also grateful to Dr. Yuexin Zhang and Yerong Xu for checking my timing products and high-resolution analysis.

My thanks also go to other members of the high-energy group at Fudan, who are also my friends and office mates, including Zuobin Zhang, Menglei Zhou, Songcheng Li, Shafqat Riaz, Gitika Mall, Debroy Das, Shuitongze Zhao, Jiale Gu, Kexin Huang, and Yimin Huang.

Three years of my Ph.D. have been affected by COVID-19, making it a truly challenging time. I am sincerely grateful to the staff and students at Fudan University who have made tireless efforts to maintain normalcy in our lives.

复旦大学 学位论文独创性声明

本人郑重声明：所呈交的学位论文，是本人在导师的指导下，独立进行研究工作所取得的成果。论文中除特别标注的内容外，不包含任何其他个人或机构已经发表或撰写过的研究成果。对本研究做出重要贡献的个人和集体，均已在论文中作了明确的声明并表示了谢意。本声明的法律结果由本人承担。

作者签名：_____ 日期：_____

复旦大学 学位论文使用授权声明

本人完全了解复旦大学有关收藏和利用博士、硕士学位论文的规定，即：学校有权收藏、使用并向国家有关部门或机构送交论文的印刷本和电子版本；允许论文被查阅和借阅；学校可以公布论文的全部或部分内容，可以采用影印、缩印或其它复制手段保存论文。涉密学位论文在解密后遵守此规定。

作者签名：_____ 导师签名：_____ 日期：_____